



**GENETIC UNITS BASED RESERVOIR CHARACTERIZATION USING A
NORMALIZED PORE THROAT RADIUS
FOR THE CLASTIC SYSTEM: NIGER DELTA AS FIELD CASE STUDY**

**A DISSERTATION
SUBMITTED TO THE DEPARTMENT OF PETROLEUM ENGINEERING
AND THE COMMITTEE ON GRADUATE STUDIES
OF AFRICAN UNIVERSITY OF SCIENCE & TECHNOLOGY (AUST)
IN PARTIAL FULFILLMENT OF THE REQUIREMENTS
FOR THE DEGREE OF
DOCTOR OF PHILOSOPHY**

By

Onuh, Haruna Monday, M.Sc.

DECEMBER 2016

**GENETIC UNITS BASED RESERVOIR CHARACTERIZATION USING
THE NORMALIZED PORE THROAT RADIUS FOR
THE CLASTIC SYSTEM: NIGER DELTA AS FIELD CASE STUDY**

By

Onuh, Haruna Monday

RECOMMENDED:

Chair: Prof. David Ogbe

Prof. Djebbar Tiab

Dr. Alpheus Igbokoyi

APPROVED:

Chief Academic Officer

Date: 12th December, 2016

I certify that I have read this thesis and that in my opinion
it is fully adequate, in scope and in quality,
as a dissertation for the degree of Doctor of Philosophy.

Prof. David O. Ogbe
(Principal Advisor)

I certify that I have read this thesis and that in my opinion
it is fully adequate, in scope and in quality,
as a dissertation for the degree of Doctor of Philosophy.

Prof. Tiab Djebbar

I certify that I have read this thesis and that in my opinion
it is fully adequate, in scope and in quality,
as a dissertation for the degree of Doctor of Philosophy.

Dr. Alpheus Igbokoyi

I certify that I have read this thesis and that in my opinion
it is fully adequate, in scope and in quality,
as a dissertation for the degree of Doctor of Philosophy.

Approved for the University Committee on Graduate Studies:

© Copyright 2016
By
Onuh, Haruna M.

Acknowledgement

First and foremost I would like to thank my parents who have been a pillar of strength throughout my life. To my wife – my most adorned pearl of inestimable value, for her support and prayers for me every step of the way, I will be forever grateful for your love and guidance. For always being there for me, my gratitude goes to Prof. Wumi Iledare and Mrs. Regina Akubo, for always asking about my thesis, thereby motivating me to keep working hard. Their support has provided me the driving force in my life.

I feel a deep sense of gratitude towards my research advisor Prof. David O. Ogbe for his support, supervision, and assistance in this project. My special thanks go to Prof Djebbar Tiab, Dr. Alpheus Igbokoyi and Engr. Nwosu Chikezie for their willingness to serve on my project committee. I am sincerely in debt to them for all their guidance, inspiration, constructive criticism and scholastic advice. Also, I am grateful to the management and staff of Shell Nigeria for the opportunity as a graduate research petrophysicist, granting me access to hard and soft dataset and resources for this work.

The financial support from the Petroleum Technology Development Fund (PTDF) and the African University of Science and Technology are greatly acknowledged.

Special thanks to all my most cherished family and loved ones for their prayers and support. To my friends and colleagues in Halliburton Energy Services Limited (HESLN) that offered their contributions throughout my program and to this project. I am honored meeting you all during this phase of my life

Finally, I thank God Almighty for his grace, immeasurable favor and most of all his peace throughout my program and the completion of this project. In him and through him, I have accomplished all that I set out to do. For all the blessings and guidance without which nothing that I have achieved could have been done, I bless his name.

Abstract

Globally, 30–50% of hydrocarbon volumes in silici-clastic reservoirs are contained within the thin-bedded pay. In the Niger Delta deep water assets, over 30% of in-place volumes are found within the complex turbidites. The presence of multi-pore architecture within such facies makes their description from petrophysics very complex. With the quest for hydrocarbon prospects in frontier deep water settings characterized by such complex rock fabric, detailed reservoir characterization is essential for accurate field management and production optimization.

The focus of this work is to characterize complex reservoir pore systems at core scale based on genetic reservoir unit averages and to provide improved models for petrophysical evaluation using a normalized pore throat radius ($\overline{R_{tot}}$) approach for clastic reservoirs. New methods are presented for modelling permeability in rocks with multimodal pore throat size distributions using Niger Delta field as case study. The statistical significance of the coefficients in the proposed relationships for various genetic reservoir units was verified using α -level of 0.05; and the results indicate that the proposed model is very unlikely to have occurred by chance.

Two methodologies are presented for upscaling from core plug to log scale—genetic unit averages of pseudo normalized pore throat radius as input parameter to the proposed model. This study also presents improved methodology for generating capillary pressures from NMR T_2 relaxation time using a genetic unit based averages of the kappa scaling parameter proposed by Volokitin et al. The improved methodology is also applicable to conventional geophysical logs for estimating capillary pressure in the absence of NMR T_2 data.

Comparative analyses indicate that the proposed methodology is an excellent improvement over existing methods (e.g., Reservoir Quality Index, Leverett J-Function, Stratigraphic Modified Lorenz Plot) for characterizing hydraulic flow units. Additionally, efficiency of the proposed methodology is demonstrated by comparison of estimated permeabilities versus core permeabilities from four depobelts in the Niger Delta. Permeabilities were derived from existing methodologies including Genetic Unit Averages of FZI's, Neural Network Permeability, NMR based Schlumberger Doll Research (SDR) and Coates correlations. It is concluded that the proposed methodology is a superior and practical tool for reservoir characterization.

Table of Contents

Acknowledgement.....	v
Abstract.....	vi
Table of Contents.....	viii
List of Figures.....	xiii
List of Tables.....	xxvi
Chapter 1	1
Introduction	1
1.1 Statement of the Problem.....	1
1.2 Literature Review.....	19
1.3 Objectives of the Study.....	23
1.4 Organization of the Thesis.....	24
Chapter 2	26
Overview of the Niger Delta Geology.....	26
2.1 Petroleum Geology of the Niger Delta.....	26
2.2 Genetic Reservoir Units within the Niger Delta Province.....	28
2.2.1 Channel Sandstone.....	28
2.2.2 Channel Heterolithic.....	30
2.2.3 Upper Shoreface Sandstone.....	31
2.2.4 Lower Shoreface Heterolithic.....	33
2.2.5 Marine Shale.....	34
2.2.6 Coastal Plain Sandstone.....	35
2.2.7 Coastal Plain Heterolithic.....	36
2.2.8 Coastal Plain Shale.....	37
Chapter 3	39
Theory of Capillary Pressure Modelling (CPM).....	39

3.1	Capillary Curves Measurement Techniques	39
3.2	Capillary Pressure Petrophysical Models	42
3.3	Applications of Capillary Pressure Model to Reservoir Understanding	46
3.3.1	Exploration and Geological Applications	46
3.3.2	Reservoir Engineering	47
3.4	Capillary Curve Corrections and Conversions	49
3.4.1	Closure Correction	49
3.4.2	Stress Correction	50
3.4.3	Clay-Bound-Water or Shaliness Correction	51
3.5	Capillary Curve Fitting and Smoothing	53
3.5.1	J. Leverett Function	55
3.5.2	Thomeer Function	56
3.5.3	Trigonometric Tangent Function	57
3.5.4	Brook's Corey Function	58
3.5.5	Lambda Function	59
3.5.6	Entry Height Functions	59
3.5.7	Exponential Function	60
3.5.8	Hyperbola Function	60
3.5.9	Polynomial Function	61
3.5.10	Sigmoidal Function	61
3.6	Permeability Modelling from Capillary Pressures/Saturation Curves	62
3.6.1	Integrating the Area under the Capillary Curve (Kozeny Methodology)	63
3.6.2	Purcell Parameter	65
3.6.3	Thomeer Parameter	65
3.6.4	Swamson's Methodology for Correlation with Capillary Curve Data	68
3.6.5	Windland's Empirical Relationship for Permeability Modelling	70

3.6.6	Pittman’s Methodology for Correlation with Capillary Curve Data	71
3.6.7	Permeability Correlations for the Niger Delta Reservoirs	72
CHAPTER 4	75
Theory of Nuclear Magnetic Resonance (NMR)	75
4.1	Theoretical Background	75
4.2	Genetic Units Averages of Kappa for Capillary Pressure Estimation from NMR measurements	81
4.3	NMR-Log Interpretation	85
4.4	Lithology Independent NMR Total Porosity	87
4.5	Construction of Capillary curves (P_c) from NMR T_2 distribution	87
4.6	Estimating NMR-Derived Permeability in Sandstones	90
CHAPTER 5	92
Material and Methodology	92
5.1	Sample Selection and Data Analysis	92
5.2	Genetic Reservoir Units Definition: Sedimentologic Characterization and Rock Type Definition	106
5.3	Pore Throat Size Histogram Analysis	108
5.4	Pressure Range Setting and Curve Fitting	111
5.5	Permeability Modelling from Capillary Pressure	113
CHAPTER 6	123
Data Analysis, Results, and Discussions	123
6.1	Introduction	123
6.2	Statistical Significance of Model Coefficients for the Proposed Genetic Unit Based Permeability Model	124
6.3	Proposed Model Calibration using NMR T_2 transversal relaxation time	127
6.3.1	Capillary Pressures and Pore Throat Distribution from NMR measurement ...	127
6.3.2	Flow Unit Based Analytical Methodology for NMR-P_c Calibration	138

6.3.3	NMR-Pc Calibration: Application to Reservoir Characterization Using the Niger Delta Deepwater Turbidites as Case Study	143
6.3.4	Genetic Unit Averages of Pseudo-Normalized Pore Throats and Model Upscaling	165
6.4	Statistical Analysis and Uncertainty Modelling in Permeability Derived from the Proposed Model	184
CHAPTER 7	187
Improved RQI, Leverett J-function and SMLP Concept using the Normalized Pore Throat (R_{tot})	187	
7.1	The Reservoir Quality Indicator (RQI) Concept	187
7.1.1	Integrating the R_{tot} with the RQI Concept	189
7.1.2	Case Study of the Clastic Turbidite Reservoirs	190
7.2	The Leverett J-Function	205
7.2.1	Integrating the R_{tot} with the Leverett J-Function	207
7.2.2	Case Study of the Clastic Turbidite Reservoirs	207
7.3.	Improved Stratigraphic Modified Lorenz Plot (SMLP) Concept Using the Proposed Normalized Pore Throat (R_{tot}) Model	215
7.3.1	Methodology for Hydraulic Flow Units Characterization Using the SMLP ...	218
7.3.2	Case Study 1 of the Tidal Channel Sandstone Reservoir (Zone 1)	221
7.3.3	Case Study of the Fluvial Channel Sandstone Reservoir (Zone 2)	228
7.4	Application of the Normalized Pore Throat Methodology in 3D Reservoir Characterization Studies	233
7.4.1	Field Overview and Location of Study Area	233
7.4.2	Reservoir and Fluid Characterization of the Study Area	234
7.4.3	Results and Analysis	239
7.4.4	Implication of the $\overline{R_{tot}}$ based Modified RQI Methodology in 3D Simulation Studies 244	
CHAPTER 8	253
Contribution to Knowledge	253

8.1 Major Contributions	253
8.2 Published research articles	254
8.3 Publications In-view	255
CHAPTER 9	256
Summary, Conclusions and Recommendations	256
9.1 Summary and Conclusions	256
9.2 Recommendations	259
Nomenclature	260
References	264
Appendix A	270
A1: Sample Dataset for Model Development	270

List of Figures

Figure 1.1: Core interpretation: visible & ultra-violet images of the Mud-Rich Thin Beds-Deep Water; showing the diagenetic influence of clay minerals responsible for the complex lithologies.	2
Figure 1.2: Core interpretation: visible and ultra-violet image of the Inter-Channel Thin Beds.....	3
Figure 1. 3: Capillary Behaviors and Log Responses of the Channel Storey Axis (CSA), Margins (CSM), and Inter-Channel Thin Beds-Deep Water.	4
Figure 1. 4: Porosity, Permeability and Pore Throat Size Distribution of the Inter-Channel Thin Beds.....	5
Figure 1.5: Pore Throat Size Distribution of the Channel Storey Margin/Axis and Thin Beds.	6
Figure 1.6: Petrographic analysis of the Mud-Rich Thin Beds-Deep Water Niger Delta, indicating a dominant 95% silt and clay composition.....	7
Figure 1.7: Petrographic analysis of the Inter-Channel Thin Beds-Deep Water Niger Delta, indicating a 63% silt and clay composition	8
Figure 1.8: Petrographic analysis of the Inter-Channel Thin Beds-Deep Water Niger Delta.....	9
Figure 1.9: Plot of permeability versus porosity showing a large data scatter, which indicates that permeability is not only dependent on porosity, but other RQI parameters.....	10
Figure 1.10: Empirical Correlation for Permeability Prediction for the Canyon Reservoirs, Deep Water – Niger Delta, obtained from core analysis dataset.....	11
Figure 1.11: Plot of capillary pressure versus saturation exhibiting diversity in equivalent pore throat size distribution and heterogeneity within the total dataset	12
Figure 1.12: Study area showing the depositional belts, structural play segments and well locations – onshore and offshore Niger Delta (courtesy Shell Nigeria)	13

Figure 3. 1: Semilog plot of mercury injection-capillary pressure data. Katz and Thompson (1987), defined the threshold pressure graphically as the inflection point at which the curve becomes convex upward. The displacement pressure (P_d) was defined by Schowalter (1979) as the pressure at a mercury saturation of 10%. 44

Figure 3.2: Schematic diagram of a Capillary Pressure Curve and hydrocarbon column 54

Figure 3.3: A log-log hyperbolic plot of mercury injection data [after Thomeer (1960) and Swanson (1981)]. Thomeer used the values of the asymptotes in his mathematical description. The 45°-line is tangent to the hyperbola at the apex 66

Figure 4. 1: The NMR-measurement process (after Freedman 2006)..... 76

Figure 4.2: NMR T_2 distribution of typical water-saturated sandstone (after Freedman 2006) 80

Figure 4.3: Magnetization decay as a function of the pore size, indicating the relationship between T_2 values and pore bodies. Low T_2 values are associated with the smaller pores and vice versa. This serve as the basis for assuming that only small pores (with shorter T_2 's) contribute to the irreducible water saturation 82

Figure 4.4: NMR T_2 conversion to pore-body size distribution assuming spherical pore bodies using dataset from the Channel Storey Margin unit. The rock surface relaxivity, $\rho = 10 \mu\text{m/s}$ was obtained from the Sørland *et al.* (2007) relationship..... 85

Figure 5. 1: Workflow adopted for the study. 93

Figure 5. 2: Uncorrected pore throat size distribution demonstrating a relationship between the rock units and capillary parameters. Petrophysical and geologic rock quality increases from the purple (Heterolithic units) to the red (Fluvial Channel units) 95

Figure 5.3: Corrected pore throat size distribution demonstrating a relationship between the rock units and capillary parameters. Petrophysical and geologic rock quality increases from the purple (Heterolithic units) to the red (Fluvial Channel units).....	96
Figure 5. 4: Core permeability versus porosity for the different genetic reservoir units demonstrating a relationship between the various rock units and petrophysical attributes. Reservoir quality increases from the purple (Heterolithic units) to the red (Fluvial Channel units)	97
Figure 5.5: Corrected capillary pressure curves demonstrating a relationship between the various rock units and capillary parameters. Petrophysical and geologic rock quality increases from the purple (Heterolithic units) to the red (Fluvial Channel units)	98
Figure 5.6: Regional distribution of Expansive Clay (EC) and Non Expansive Clay (NEC) minerals in the Niger Delta (obtained from table 1.1); indicating the strong dominance of expansive clay group with depth	100
Figure 5.7: Niger Delta Regional Distribution of Kaolinite and Illite/Smectite Clay Minerals, indicating increasing dominance of the expansive illite and mixed illite/smectite group as a function of depth (obtained from table 1.1).....	101
Figure 5.8: Air/Brine Capillary Pressure curves for Sand 'X', obtained from Field 'Y', Deep Water – Niger Delta. This presents typical reference sample used for CBW correction.....	102
Figure 5.9: Mercury Injection Capillary Pressure curves for Sand 'X', obtained from Field 'Y', Deep Water – Niger Delta. Capillary curves were corrected for CBW effects using the air/brine data (figure 5.8)	103
Figure 5.10: Capillary pressure curves exhibiting the effect of CBW correction on MICP dataset. Reduction in wetting phase saturation (red curves) indicate the effect of CBW since mercury as the wetting fluid does not interact with the clay within the plug samples.....	104

Figure 5.11: Capillary pressure curves exhibiting the effect of insitu stress correction on MICP dataset. Reduction in wetting phase saturation (red curves) indicate the effect of relieved insitu stress at reservoir conditions..... 105

Figure 5.12: Petrophysical Data Log (PDL) view showing various hydrocarbon pay zones and interpretations for Field W (offshore Niger Delta) with capillary pressures core analysis data points 107

Figure 5.13: Pore throat size distribution for individual sample within the Channel Heterolithics unit. This demonstrates a heterogeneous unit with dominant micropores 109

Figure 5.14: Plot of cumulative pore throat distribution for Channel Heterolithics rock unit demonstrating a bimodal distribution and dominant micropores population 110

Figure 5.15: Plot of permeability versus porosity for the Channel Heterolithics rock unit demonstrating poor rock properties with average permeability of 10 mD 113

Figure 5.16: Plot of permeability versus macroporosity ($\phi_i \sum_i S_{wi}$) for Channel Heterolithic rock unit demonstrating improved correlation compared to typical porosity/permeability plots, due to influence incremental wetting phase saturation (S_{wi}) at every capillary pressure step ... 114

Figure 5.17: Plot of permeability versus macropore normalized pore throat radius $\left[\phi_i \sum_i S_{wi} (R_{pi})_{Mac} \right]$ for the Channel Heterolithic genetic reservoir unit, indicating higher correlation coefficient due to influence of pore throat radius (R_{pi}) at every capillary pressure step 115

Figure 5.18: Matrix Plot of Input Parameters (ϕ and k) demonstrating relationship with capillary pressure parameters (Sw_{irr} , P_e and N) for the Channel Heterolithic genetic unit..... 116

Figure 5.19: Capillary pressure versus water saturation curve fit for the Fluvial Channel sand unit indicating appreciable match between measured and calculated capillary curves 117

Figure 5.20: Plot of core permeability versus core porosity for Fluvial Channel sands showing very good reservoir properties associated with the unit. The large scatter shows the influence of other rock parameter other than porosity on permeability 118

Figure 5.21: Plot of core permeability versus total normalized pore throat radius $\left[\phi \sum_i S_{wi} (R_{pi})_{Mac} \right]$ for Fluvial Channel sands showing very good reservoir properties associated with the unit. Observable improvement in correlation coefficient is attributed to influence of pore throat radius (R_{pi}) at every capillary pressure step. 119

Figure 5.22: Plot of core permeability versus total normalized pore throat radius ($\overline{R_{tot}}$) for all the genetic units classified in the study, indicating the proposed model and improved correlation 122

Figure 6.1: Plot of measured permeability versus $\overline{R_{tot}}$ predicted permeability based on SCAL dataset from three (3) depobelts, indicating good correlation. 126

Figure 6.2: Mercury Injection Capillary pressure curves obtained at a confining stress (1,850-1,950 psi), indicating 11 special core analysis samples from various genetic reservoir units from the Deep Water turbidite environment..... 128

Figure 6.3: Pore throat size distribution obtained from mercury injection capillary pressure dataset with the red arrow indicating macropores greater than 100 microns for the Deep Water turbidites dataset (offshore Niger Delta)..... 129

Figure 6.4: Plot of Pore Throat Size Distribution predicted from NMR capillary pressure for $kappa = 10$ (Olubunmi and Nwosu; 2011.). Red arrow indicates the deficiency of the model in modelling macropores with reference to laboratory measured MICP data (figure 6.3)... 130

Figure 6.5: Pore Throat Size Distribution predicted from NMR capillary pressures for $kappa = 7$ and 5. Red arrow indicates the deficiency of the model in modelling macropores with reference to laboratory measured MICP data (Figure 6.3). 131

Figure 6.6: Pore throat size distribution derived from NMR Capillary Pressures for $\kappa = 3$ and 2 (current study). Red arrow indicates the capability of the proposed model in modelling pore distribution with reference to laboratory measured MICP data (Figure 6.3)..... 132

Figure 6.7: Mercury Injection Capillary pressure curves versus inverse NMR T_2 distribution for samples dataset from indicating nonlinearity in relationship..... 134

Figure 6.8: Mercury Injection Capillary pressure curves versus inverse NMR T_2 distribution for samples dataset from indicating nonlinearity in relationship..... 135

Figure 6.9: Mercury Injection Capillary pressure curves versus inverse NMR T_2 distribution for samples dataset from indicating nonlinearity in relationship..... 136

Figure 6.10: Mercury Injection Capillary pressure curves versus NMR predicted capillary pressures for the dataset indicating poor correlation at pressures below the imposed cut offs for the entry pressures and transition zone..... 137

Figure 6.11: Illustration of T_2 cutoff estimation process with NMR core measurements. (A) is the incremental distribution and (B) is the cumulative distribution (after Songhua *et al.*, 1998). 139

Figure 6.12: Sample 1 – 5 employed for the study. This present petrographic grain analysis, NMR T_2 distribution and MICP distribution demonstrating various rock quality indicators; relationship between pore bodies and pore throats for various genetic reservoir units, within the Deep Water Niger Delta. 144

Figure 6.13: Sample 6 – 11 employed for the study. This present petrographic grain analysis, NMR T_2 distribution and MICP distribution demonstrating various rock quality indicators; relationship between pore bodies and pore throats for various genetic reservoir units, within the Deep Water Niger Delta. 145

Figure 6.14: Normalized cumulative reservoir quality index (RQI_{nc}) versus depth indicating four (4) possible zones. 148

Figure 6.15: Laboratory capillary pressure curves indicating a relationship between the various hydraulic flow units/genetic rock units and capillary parameters. Reservoir quality properties increase from the black curve (HFU 1 – Mud Rich Thin Bed units) with high irreducible water saturation and entry pressures to the green curve (HFU 4 – Channel Storey Axis units) with low S_{wirr} and P_{entry} 149

Figure 6.16: Plot of mercury injection capillary pressure and inverse NMR T_2 relaxation for the Channel Storey Axis unit for a fully saturated sample. This indicates a fair relationship between capillary parameters that requires a recalibration for improved fit. 150

Figure 6.17: NMR T_2 relaxation plot for the Channel Storey Axis unit for a fully saturated sample. The green dash lines indicates the cut offs for estimating the FFI, BVI, corresponding S_{wirr} and total porosity determined from the cumulative porosity (sum of amplitudes) spectrum. 151

Figure 6.18: Measured capillary pressure (black) and NMR capillary pressure (red) for the Mud Rich Thin Bed Unit indicating a closer match between the entry pressures with much discrepancy with saturation (S_{wirr}). The semi-log plot (below) scales the plot for better estimates of entry/displacement pressures. 153

Figure 6.19: Measured capillary pressure (black) and NMR capillary pressure (red) for the Inter-Channel Thin Bed Unit indicating a closer match between the entry pressures with much discrepancy with saturation (S_{wirr}). The semi-log plot (below) scales the plot for better estimates of entry/displacement pressures. 154

Figure 6.20: Measured capillary pressure (black) and NMR capillary pressure (red) for the Channel Storey Margin Unit indicating a closer match between the entry pressures with much discrepancy with saturation (S_{wirr}). The semi-log plot (below) scales the plot for better estimates of entry/displacement pressures. 155

Figure 6.21: Measured capillary pressure (black) and NMR capillary pressure (red) for the Channel Storey Axis Unit indicating a closer match between the entry pressures with much

discrepancy with saturation (S_{wirr}). The semi-log plot (below) scales the plot for better estimates of entry/displacement pressures.	156
Figure 6.22: S_{w-LAB} versus S_{w-NMR} for all samples within the Channel Storey Margin unit. The black thick line represents the average curve.	158
Figure 6.23: Plot of S_{w-LAB} versus S_{w-NMR} for all samples within the various genetic reservoir units. The red thick line indicates a possible averaging with various scaling factors for each unit.	159
Figure 6.24: Calibrated P_c -NMR and P_c -LAB for the Mud Rich Thin Bed (Top) and Inter-Channel Thin Beds (Bottom) units indicating a good match in capillary attributes (entry pressures and irreducible water saturation).	161
Figure 6.25: Calibrated P_c -NMR and P_c -LAB for the Channel Storey Margin (Top) and the Channel Storey Axis (Bottom) units indicating a good match in capillary attributes (entry pressures and irreducible water saturation)	162
Figure 6.26: Petrophysical data view of two prolific hydrocarbon bearing zones within the low contrast and low resistive thin bedded turbidites. Track 5 presents a comparison of various permeability models indicating a good correlation between the proposed model and core derived permeabilites using 75 samples.	163
Figure 6.27: Plot of core permeability versus porosity for field X-turbiditic environment (genetic unit averages of R_{tot}). Relationship is biased to the normalized pore throat radius which demonstrates a strong correlation.	166
Figure 6.28: Petrophysical Data Log for Field W- Continental/Fluvial environment indicating cored intervals and varying facies association.	171
Figure 6.29: Petrophysical Data Log view for Field X- Turbiditic/Deep Water environment indicating cored interval and varying facies association.	172
Figure 6.30: Petrophysical Data Log (PDL) view for Field Y- Coastal/Distributary environment showing cored interval and varying facies association.	173

Figure 6.31: Plot of measured permeability versus $\overline{R_{tot}}$ predicted permeability for Field 'W'- Continental/Fluvial environment indicating appreciable correlation.....	174
Figure 6.32: Plot of measured permeability versus $\overline{R_{tot}}$ predicted permeability for Field 'X'- Turbiditic/Deep Water environment indicating appreciable correlation.....	175
Figure 6.33: Plot of measured permeability versus $\overline{R_{tot}}$ predicted permeability for Field 'Y'- Coastal/Distributary environment indicating appreciable correlation.....	176
Figure 6.34: Plot of measured permeability versus $\overline{R_{tot}}$ predicted permeability for Field 'Z'- Tidal/Estuarine environment indicating appreciable correlation.....	177
Figure 6.35: Plot of measured permeability versus FZI predicted permeability for Field 'W'- Continental/Fluvial environment. Highlighted in red indicates deviation and over-estimation of predicted permeabilities within the poorer rock facies within the unit.	178
Figure 6.36: Plot of measured permeability versus FZI predicted permeability for Field 'Y'- Tidal/Estuarine environment. Large scatter indicates poorer correlation within the unit.	179
Figure 6.37: Plot of measured permeability versus FZI predicted permeability for Field 'Z'- Coastal/Distributary environment. Highlighted in red demonstrates the model deficiency in capturing extreme values of connections of permeabilities within the unit.....	180
Figure 7. 1: PDL view for Zone 1 (Deep Water – Niger Delta) indicating the cored interval, complex turbiditic sequence of the submarine canyons and the four (4) facies association.	191
Figure 7.2: PDL view for Zone 2 (Deep Water – Niger Delta) indicating the cored interval, complex turbiditic sequence of the submarine canyons and the four (4) facies association.	192
Figure 7.3: Plot of permeability versus porosity for all samples; the non-linear relationship results in very low correlation coefficient which is evident in complex shaley sandstone.....	193

Figure 7.4: Plot of capillary pressure versus wetting phase saturation indicating the four (4) distinct genetic units with increasing macropores from rock unit I to IV, and decreasing reservoir quality from rock unit IV to I.194

Figure 7.5: PDL view for Zone 1 (Deep Water – Niger Delta). Track 3 presents the Normalized Modified RQI plot versus depth for flow zones delineation. This presents seven flow zones indicating consistency between the geologic rock facies classification and petrophysical units.196

Figure 7.6: Normalized Cumulative Modified RQI versus depth within the cored section indicating seven reservoir flow units.197

Figure 7.7: Facies biased Normalized Cumulative Modified RQI versus depth within the cored section. This shows four units which bears correlation with the rock-type-based reservoir zonation and petrophysically based flow units.198

Figure 7.8: Log-log plot of RQI (after Ameafule *et al.*) versus ϕ_z for all samples, indicating their average FZI per unit as obtained from the intercept of each straight line at $\phi_z = 1$199

Figure 7.9: Log-log plot of $RQI_{\overline{R_{tot}}}$ (proposed model) versus ϕ_z for all samples, indicating their average FZI per unit as obtained from the intercept of each straight line at $\phi_z = 1$200

Figure 7.10: Log-log plot of RQI versus ϕ_z (top plot, A) and $RQI_{\overline{R_{tot}}}$ versus ϕ_z (bottom plot, B) for the Channel Storey Axis unit, indicating improved R^2 of 78% for the modified RQI over 31% indicates the efficacy of the proposed model for hydraulic flow zonation.201

Figure 7.11: Plot of irreducible water saturation versus FZI (after Ameafule *et al.*) for all samples. Higher FZI's corresponds to rock units with megapores and lower irreducible saturation. 203

Figure 7.12: Plot of irreducible water saturation versus $FZI_{\overline{R_{tot}}}$ (proposed modified RQI) for all samples. Higher FZI's correspond to rock units with megapores and lower irreducible water saturation.204

Figure 7.13: Plot of J-function (after Leverett J.) versus normalized wetting phase saturation for all samples, with color codes indicating the four (4) genetic unit classifications. Plot

demonstrates deficiency in delineating the various facies association within the complex turbidites.	208
Figure 7.14: Plot of modified J-function (proposed model) versus normalized wetting phase saturation for all samples, with color codes indicating the four (4) genetic unit classifications. Plot demonstrates the capability of the proposed model in delineating various facies association within the turbiditic system.	209
Figure 7.15: Log-log plot of J-function (after Leverett J.) versus normalized wetting phase saturation for all samples, indicating the pore size distribution index (λ) for the four (4) genetic units. The figure indicates difficulty in delineating the MRTB from the ICTB rock units.	212
Figure 7.16: Log-log plot of Modified J-function (proposed model) versus normalized wetting phase saturation for all samples, indicating the pore size distribution index (λ) for the four (4) genetic units. Plot indicates a differentiation between the MRTB and ICTB rock units.	213
Figure 7.17: Stratigraphic Flow Profile for Zone 1 (Continental/Fluvial Environment) – Field “K” indicating a low resistive and low contrast pay reservoir with cored interval and facies association. The flow capacity track indicates multiple hydraulic units which is evident from the GR signature depicting a complex diagenetic effect.	216
Figure 7.18: Stratigraphic Flow Profile for Zone 2 (Continental/Fluvial Environment) – Field “K” indicating the cored interval and multiple hydraulic units; and sand-shale intercalation evident of possible flow baffles within the highly permeable reservoir.....	217
Figure 7.19: Porosity-Permeability plot for various genetic reservoir units for Zone 1 – Field “K” indicating nine (9) genetic reservoir units based on core description.	222
Figure 7.20: Log-log plot of RQI versus normalized porosity indicated various flow units for Zone 1 indicating eight (8) hydraulic flow units.	223
Figure 7.21: Stratigraphic Plot demonstrating hydraulic flow unit results from the proposed approach (blue color) and SMLP (black color) for Zone 1 – Field “K”.....	224

Figure 7.22: Plots of Stratigraphic flow profile (left) and SMLP (right) demonstrating hydraulic flow unit results from the proposed approach and SMLP for Zone 1 – Field “K”. Highlighted in red are reservoir seals. The green highlight demonstrates the efficacy of the modified SMLP in delineating the reservoir seal beyond the resolution of the existing SMLP method. This evidently captures the geologic control on flows on flow properties.225

Figure 7.23: Plot of mercury injection capillary pressure curves (top) and Pore Throat Size Distribution (bottom) obtained within Zone 1 – Field “K”, showing relationship between plot as a function of identified flow units.227

Figure 7.24: Porosity-Permeability plot for various genetic reservoir units for Zone 2 – Field “K” indicating ten (10) genetic units as interpreted from detailed core description.228

Figure 7.25: Log-log plot of RQI versus normalized porosity indicating various flow units for Zone 2, indicating ten (10) flow units with distinct FZI value, where normalized porosity = 1.229

Figure 7.26: Plots of stratigraphic flow profile (left) and SMLP (right) demonstrating hydraulic flow unit results from the proposed approach and SMLP for Zone 2 – Field “K”, indicating the presence of ten (10) hydraulic units within the reservoir system.230

Figure 7.27: Plot of mercury injection capillary pressure curves (top) and Pore Throat Size Distribution (bottom) obtained within Zone 2 – Field “K”, showing relationship between plot as a function of identified flow units.231

Figure 7.28: Base map of the study area with well locations.....233

Figure 7.29: Lithostratigraphic correlation indicating the four (4) facies assemblage interpreted from core description, ditch cuttings analysis and well logs for the shoreface reservoir.234

Figure 7.30: Fluid differentiation plot indicating OOWC established from interplay between resistivity and density/neutron logs, and correlating with RFT fluid gradient analysis.....235

Figure 7.31: Field wide fluid differentiation plot indicating OOWC established from interplay between resistivity and density/neutron logs.....236

Figure 7. 32: Plot of oil production rates (FOPR) versus time (years) obtained from dynamic reservoir modelling, with proposed model (red) and FZI-based method (blue).242

Figure 7. 33: Lithostratigraphic correlation presenting a fairly homogeneous setting. Inset map underneath indicates line of cross-section E–W.245

Figure 7. 34: Plot of core derived permeability versus porosity from the reservoir interval indicating excellent reservoir quality.246

Figure 7. 35: Petrophysical Data Log View for Well-A2 indicating improved correlation between the measured dataset and proposed model (green) with Timur-Coates (red).248

Figure 7. 36: Lithostratigraphic correlation of the reservoir unit indicating variation between the proposed methodology (green) and Timur-Coates approach (red). Highlighted in red presents preliminary model calibration to measured data.248

Figure 7. 37: 3D dynamic simulation results for pressures and saturation match.....250

Figure 7. 38: 3D dynamic simulation results for pressures and saturation match. The black dots, blue and red lines represents historical/measured data, Timur Coates and the proposed $(\overline{R_{tot}})$ results respectively. The proposed model indicate appreciable match than the Timur Coates model.251

List of Tables

Table 1. 1: X-ray Diffraction (XRD) data of sidewall core samples of the study area	15
Table 3. 1: Comparison of techniques for measuring drainage capillary curves	40
Table 3. 2: Typical values for interfacial tension (σ) and contact angle (θ) in laboratory system	41
Table 4. 1: Surface to volume ratio of simple pore-body geometries (modified after Chicheng et al., 2013)	84
Table 5. 1: Data Inventory for Reservoir Modelling	94
Table 5.2: Relationship between Brooks Corey & Petrophysical Properties for the Genetic Units	120
Table 6. 1: Proposed Model Coefficients for Various Genetic Units	123
Table 6.2: Statistical Significance of Coefficients for the Proposed Permeability Models	125
Table 6.3: Pore throat ranges of petrofacies	146
Table 6.4: Genetic Units Classification for the Turbidite/Deep Water Environment developed for the study	147
Table 6.5: Averages of Genetic Unit based Kappa Values for NMR Capillary Pressure Modelling for the Turbidites/Deep Water Environment	152
Table 6.6: shows the results for the estimated coefficients	160
Table 6.7: Statistical analysis for various permeability models using NMR T_2 data	164
Table 6.8: R_{tot} for the Continental/Fluvial Depositional Environment of the study area	167
Table 6.9: R_{tot} for Turbiditic/Deep Water depositional environment of the study area	167

Table 6.10: R_{tot} for Coastal/Distributary depositional environment of the study area	168
Table 6.11: R_{tot} for Tidal/Estuarine depositional environment of the study area	168
Table 6.12: Statistical Error Analysis of Permeability Models in the Continental/Fluvial Depositional Environment of the study area.....	181
Table 6.13: Statistical Error Analysis of Permeability Models in Tidal/Estuarine Depositional Environment of the study area.....	182
Table 6.14: Statistical error analysis of permeability models in Coastal/Distributary depositional environment of the study area.	183
Table 6.15: Statistical Analysis for Permeability Models	185
Table 6.16: Statistical analysis for various permeability models using NMR T_2 data	186
Table 7. 1: Summaries of FZI's and HFU's for turbiditic shaley-sand system.....	210
Table 7.2: Summaries of FZI's, J^* and λ for turbiditic shaley-sand dataset	214
Table 7.3: Reservoir and PVT properties obtained from Well A-002 indicating an under- saturated black oil reservoir.....	237
Table 7.4: Project (top) and Model (bottom) dimensions obtained from the interpreted seismic seggy volume post stack migrated.	238
Table 7.5: Histogram and Function Plot Analysis of the FZI Model and the Proposed Normalized Pore Throat (R_{tot}) Method.	239
Table 7.6: Volumetric comparison between the booked STOIP and model estimated STOIP indicating reasonable percentage difference.	241
Table 7.7: Reservoir model Initialization indicating STOIP and average reservoir properties..	241
Table 7.8: Relationship between Volumetric Estimation Methods Assessed in the Study.	242
Table 7. 9: Reservoir and Fluid Properties.....	244
Table 7. 10: Initialized reservoir properties from existing model after Timur-Coates.	247
Table 7. 11: Simulation Result Comparison for Cumulative Oil and Water Production.....	252

Chapter 1

Introduction

1.1 Statement of the Problem

Reservoir characterization has been a major research subject in reservoir engineering and formation evaluation since the 1960s, as a key input linking geology and petrophysics into reserves optimization. In today's economic climate with an increasing challenge to find new reserves in frontier basins, it is more important than ever to emphasize the value petrophysics adds to our business. The most commonly encountered and probably the most challenging task confronting reservoir modelling is arriving at a realistic realization which best describes both the static and dynamic features of the reservoir. This involves the proper understanding of their *insitu* petrophysical properties. Detailed knowledge of these properties such as permeability, initial saturation, capillary pressures and relative permeability are crucial to performance prediction and effective reservoir management. Inaccurate prediction of such petrophysical properties; or nature of their distribution within the turbiditic clastic environment can result in significant cost due to inefficient completions, interventions/work-overs, or reserves exploitation. When a good history-matched model results in a bad forecast, question your petrophysical data (Hani Qutob *et al.*, 2013).

The detailed characterization of complex reservoir units, typical of the thin bedded canyon turbidites system within the clastic environment is essential for accurate reservoir modelling. The presence of multi-pore systems within these systems, however, makes their description from petrophysics quite challenging.

Globally, 10 – 50% of hydrocarbon volumes in silici-clastic reservoirs are contained in the thin-bedded pay, with over 30% of in-place volumes within the mud-rich and inter-channel thin-bedded turbidites in the Niger Delta deep water asset (M. Kittridge, M. Winkler, and C. Nwosu; Shell international, 2009). Figure 1.1 through 1.8 demonstrates core imaging, well log responses, NMR T_2 transversal distribution, capillary behavior, petrographic and X-Ray Diffraction (XRD) analysis of the formations within the study area. This depicts a dominant very fine sand, silt and clay depositional fabric within the turbidites.

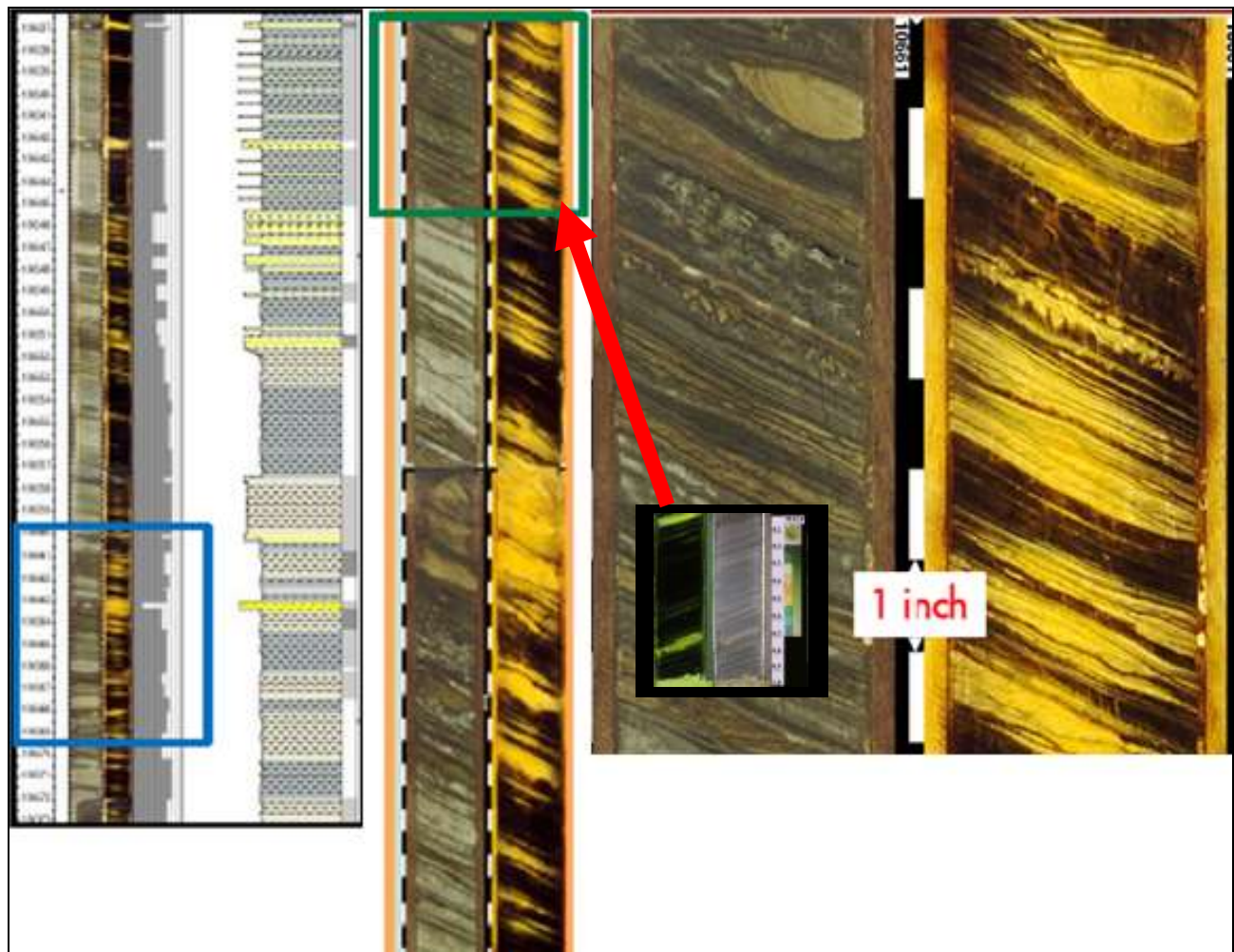


Figure 1.1: Core interpretation: visible & ultra-violet images of the Mud-Rich Thin Beds-Deep Water; showing the diagenetic influence of clay minerals responsible for the complex lithologies.

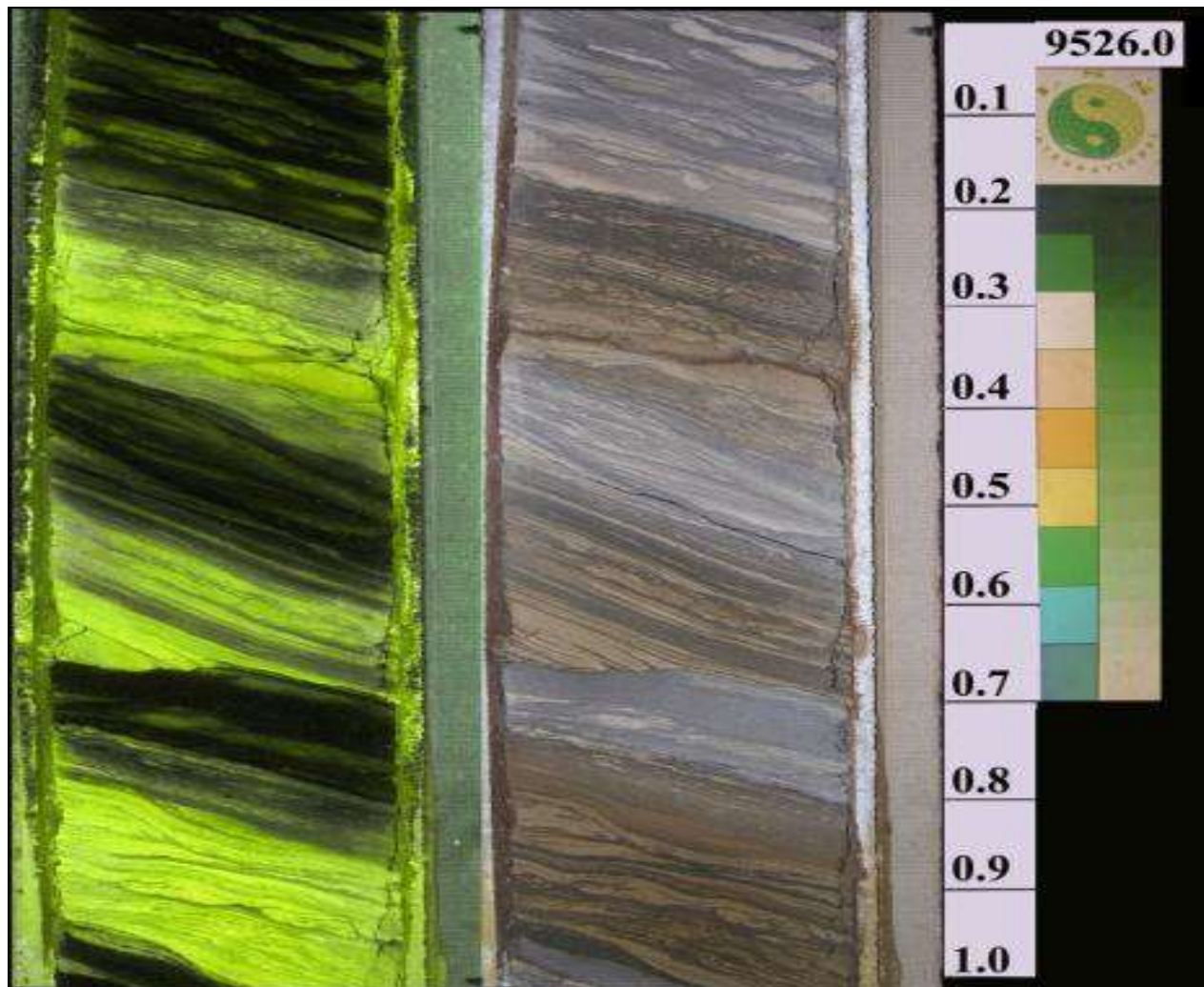


Figure 1.2: Core interpretation: visible and ultra-violet image of the Inter-Channel Thin Beds.

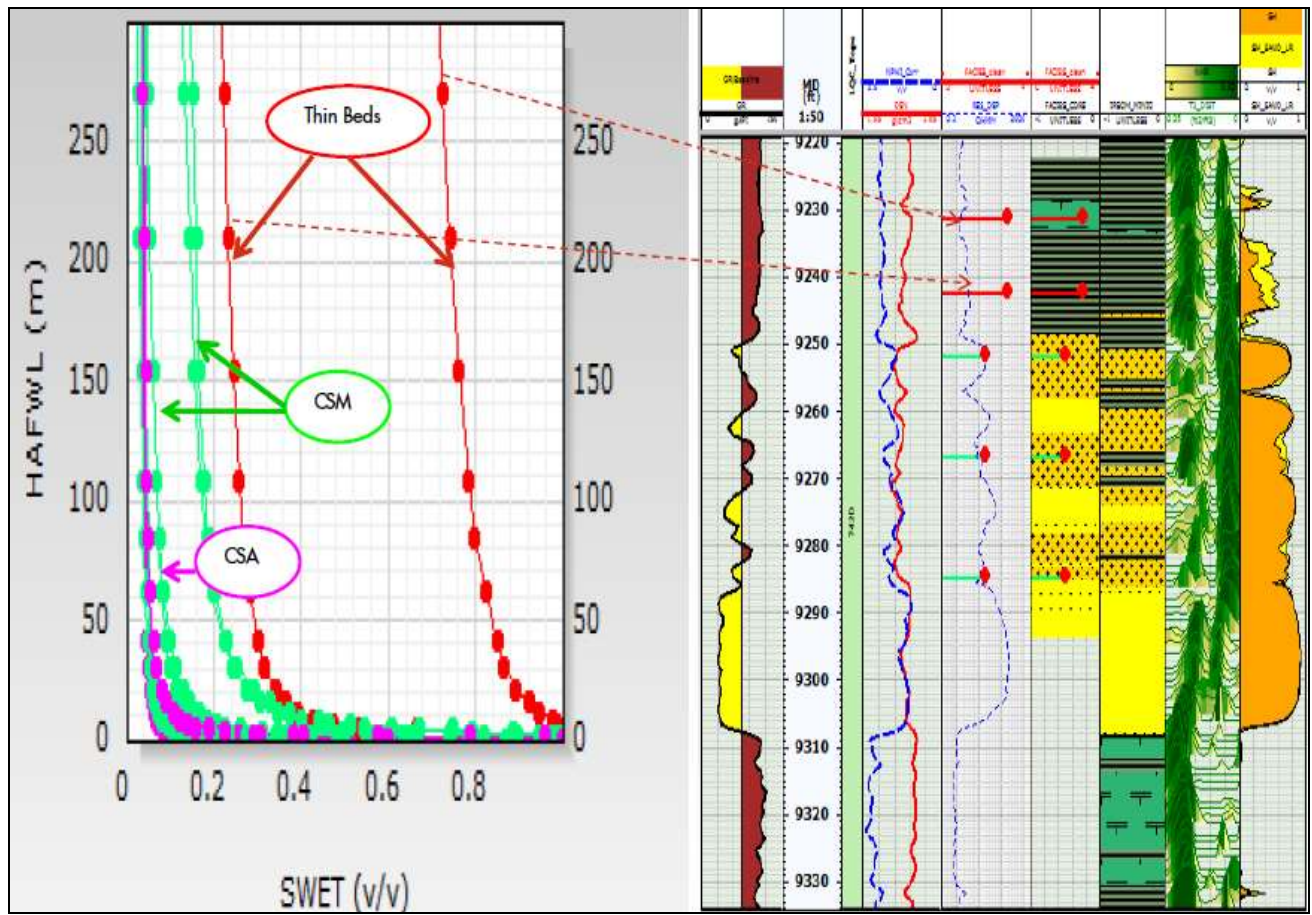


Figure 1. 3: Capillary Behaviors and Log Responses of the Channel Storey Axis (CSA), Margins (CSM), and Inter-Channel Thin Beds-Deep Water.

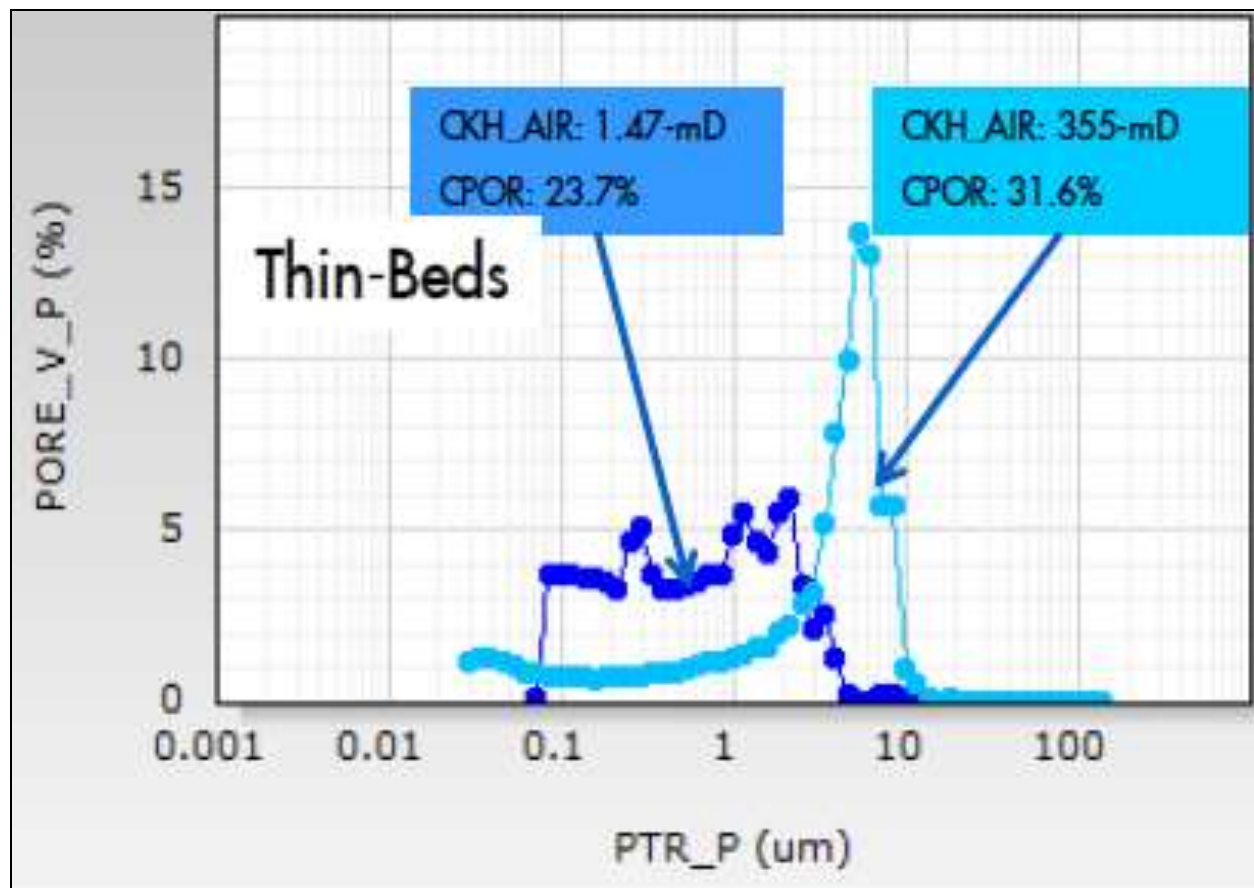


Figure 1. 4: Porosity, Permeability and Pore Throat Size Distribution of the Inter-Channel Thin Beds.

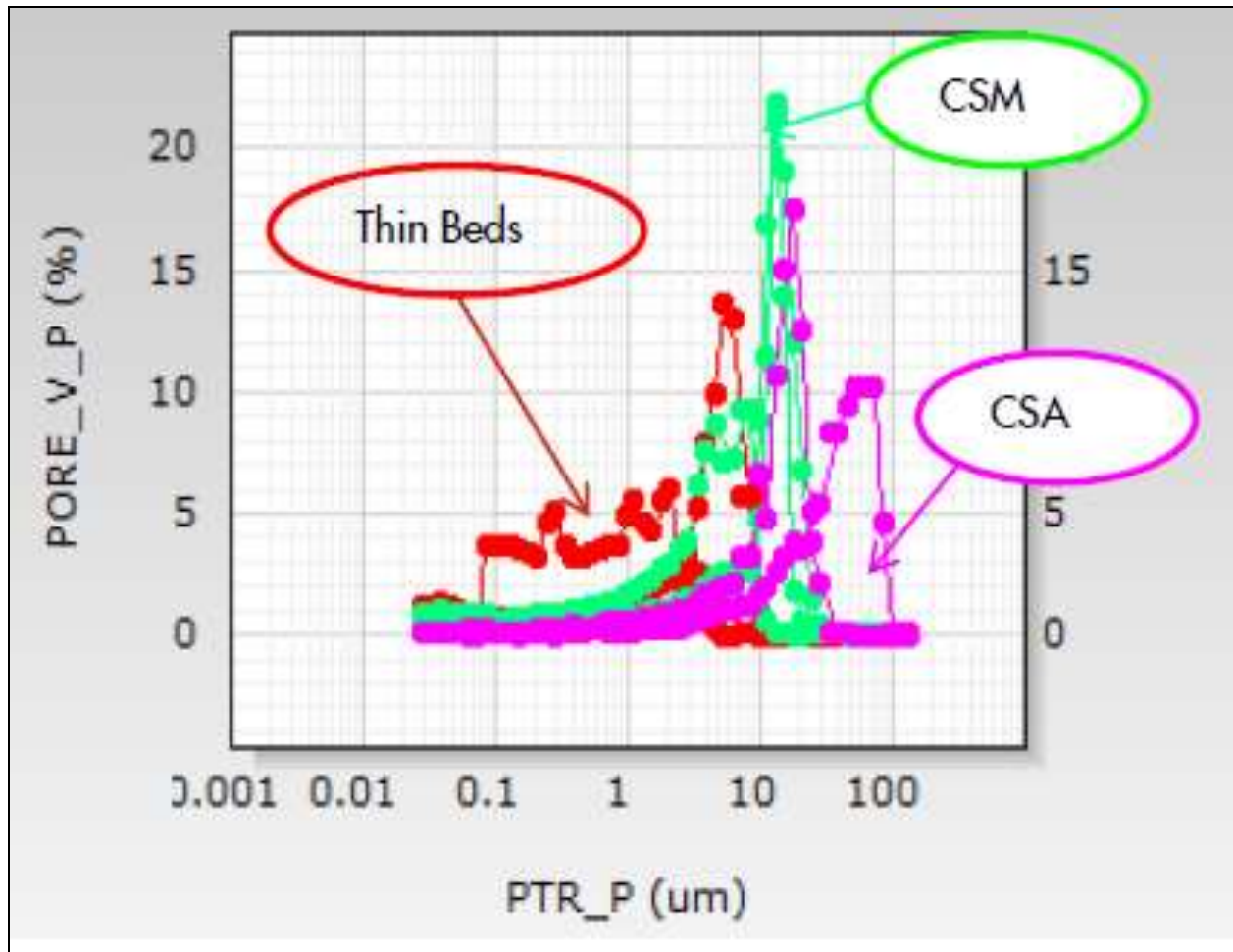


Figure 1.5: Pore Throat Size Distribution of the Channel Storey Margin/Axis and Thin Beds.

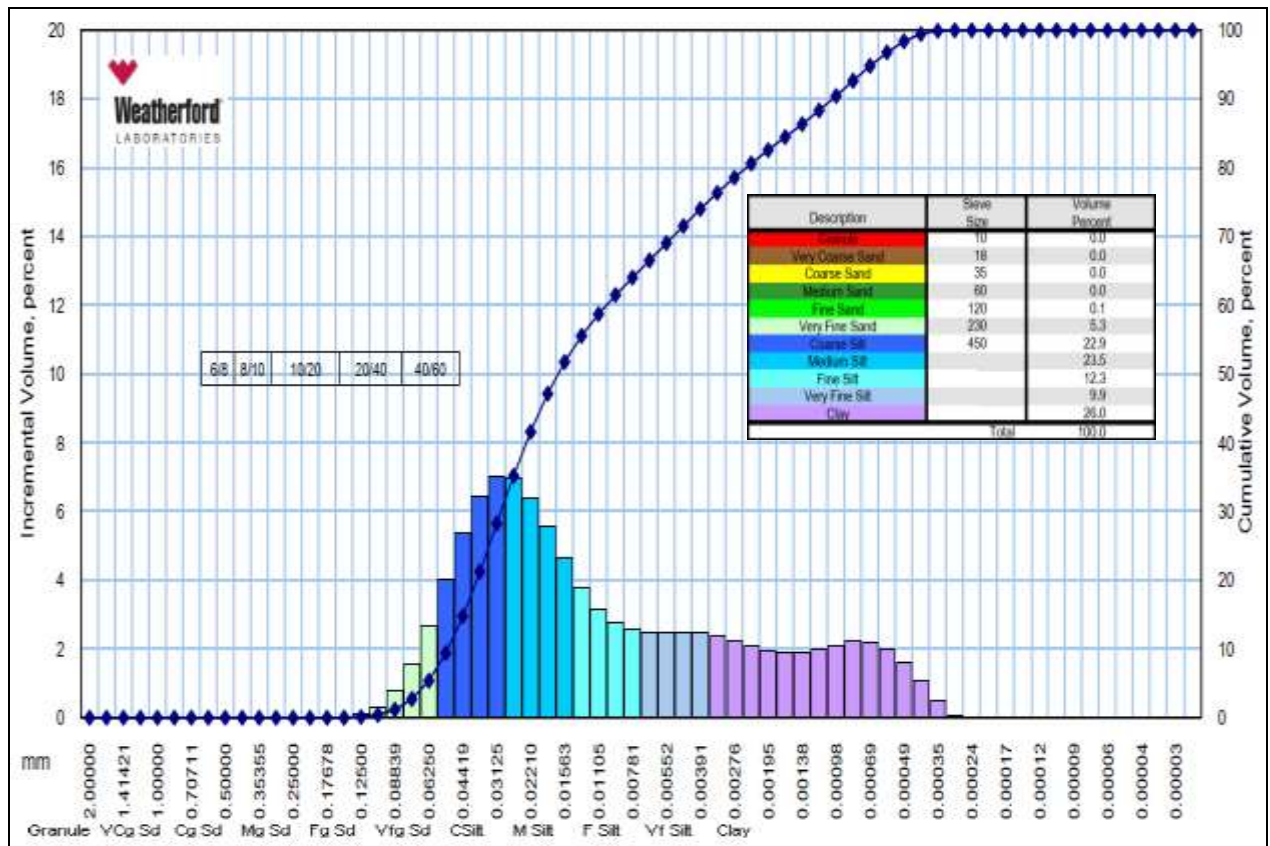


Figure 1.6: Petrographic analysis of the Mud-Rich Thin Beds-Deep Water Niger Delta, indicating a dominant 95% silt and clay composition

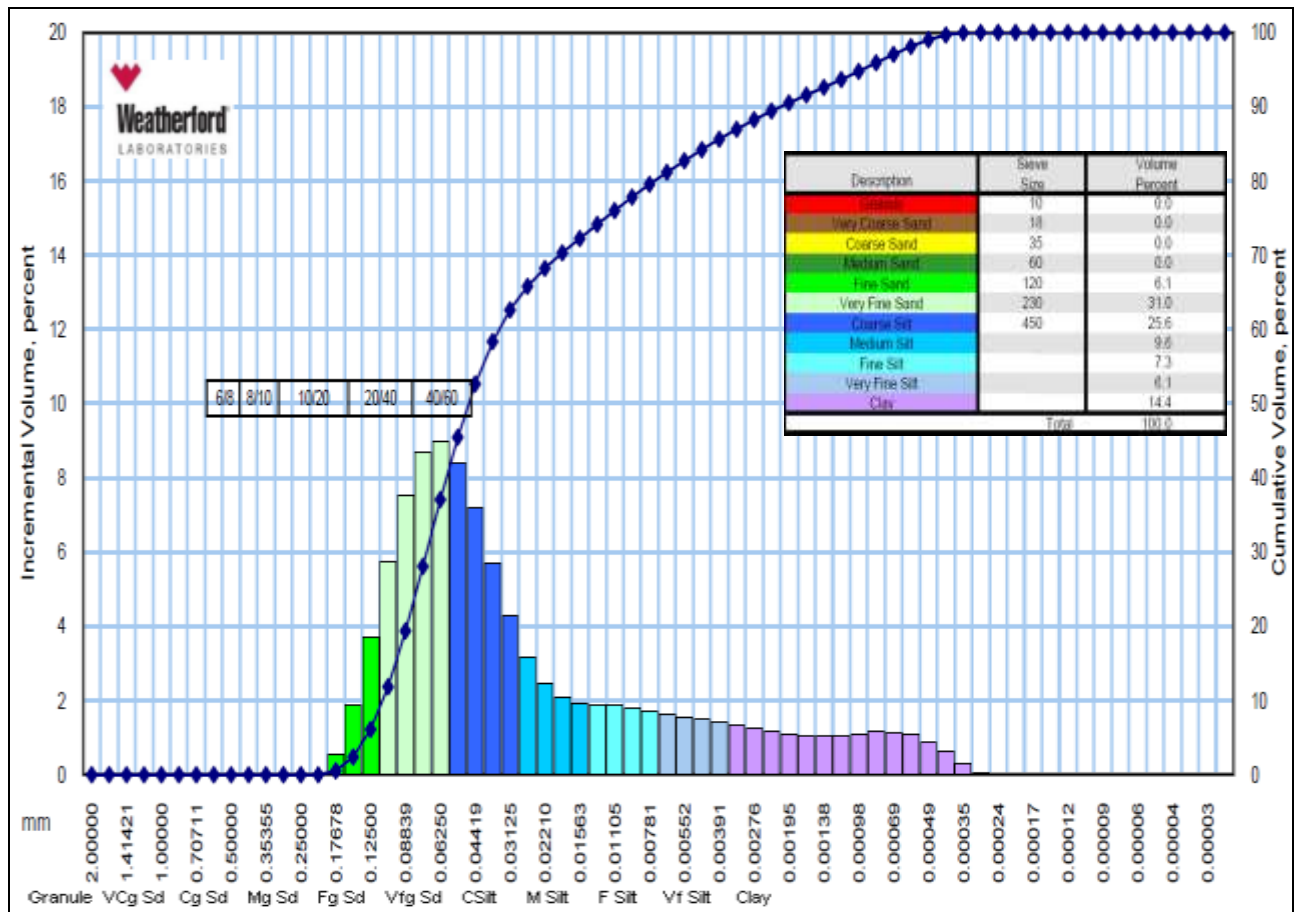


Figure 1.7: Petrographic analysis of the Inter-Channel Thin Beds-Deep Water Niger Delta, indicating a 63% silt and clay composition

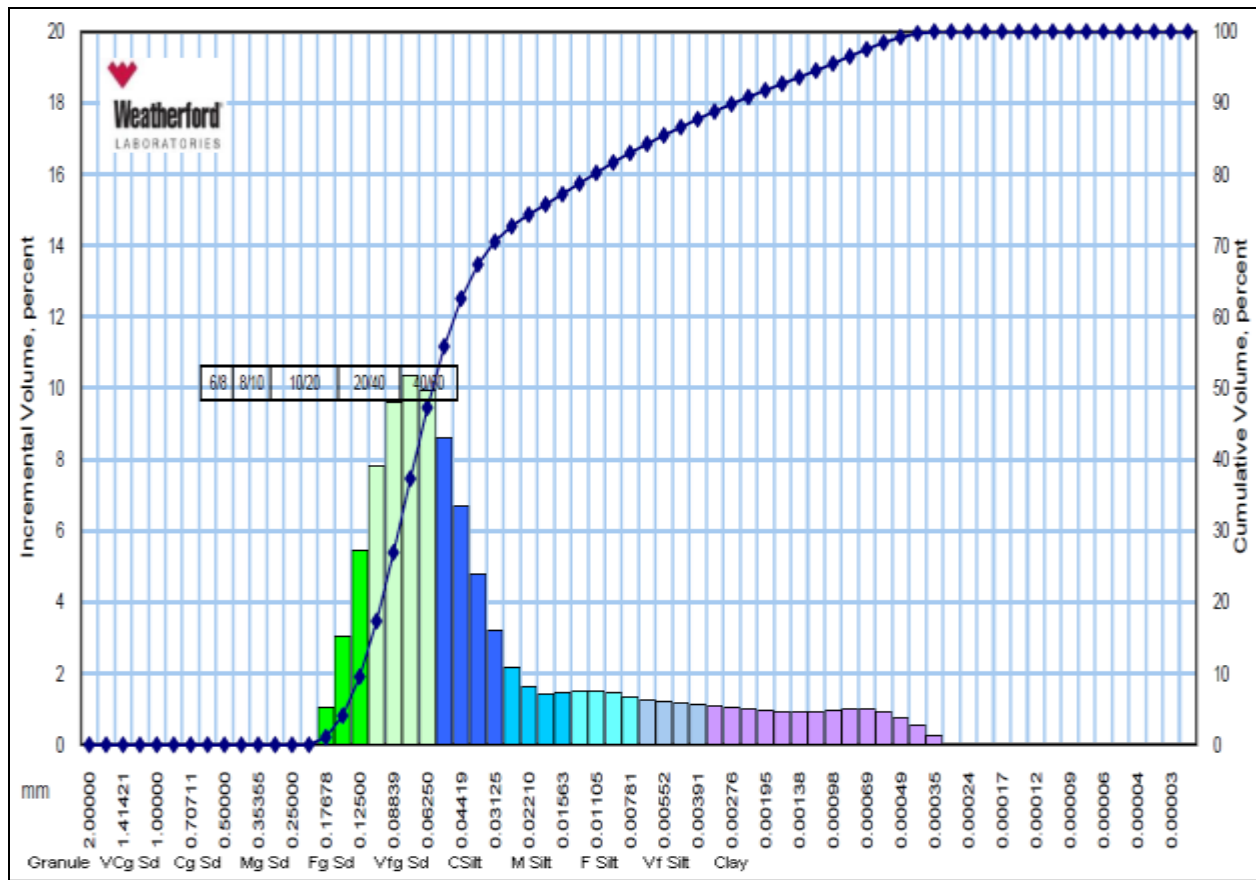


Figure 1.8: Petrographic analysis of the Inter-Channel Thin Beds-Deep Water Niger Delta

The large-scale heterogeneity resulting from the complex geology is a key factor that controls the size of the reservoir bodies and their connections. Nadeau *et al.* (1999, 2005) demonstrated the effective mechanism by which the precipitation of relatively minor amounts (even less than 5%) of neoformed illite-smectite within shales could result in pronounced reductions in permeability by blocking the effective pore network in clastic systems. This is demonstrated in the lack of relationship between porosity and permeability, as exemplified by the spread observed in the measured permeability as a function of porosity that commonly span orders of magnitude for a given porosity within one geological sequence or reservoir. Figure 1.9 and 1.10 shows a plot of core-measured porosity and permeability indicating a large scatter in the data.

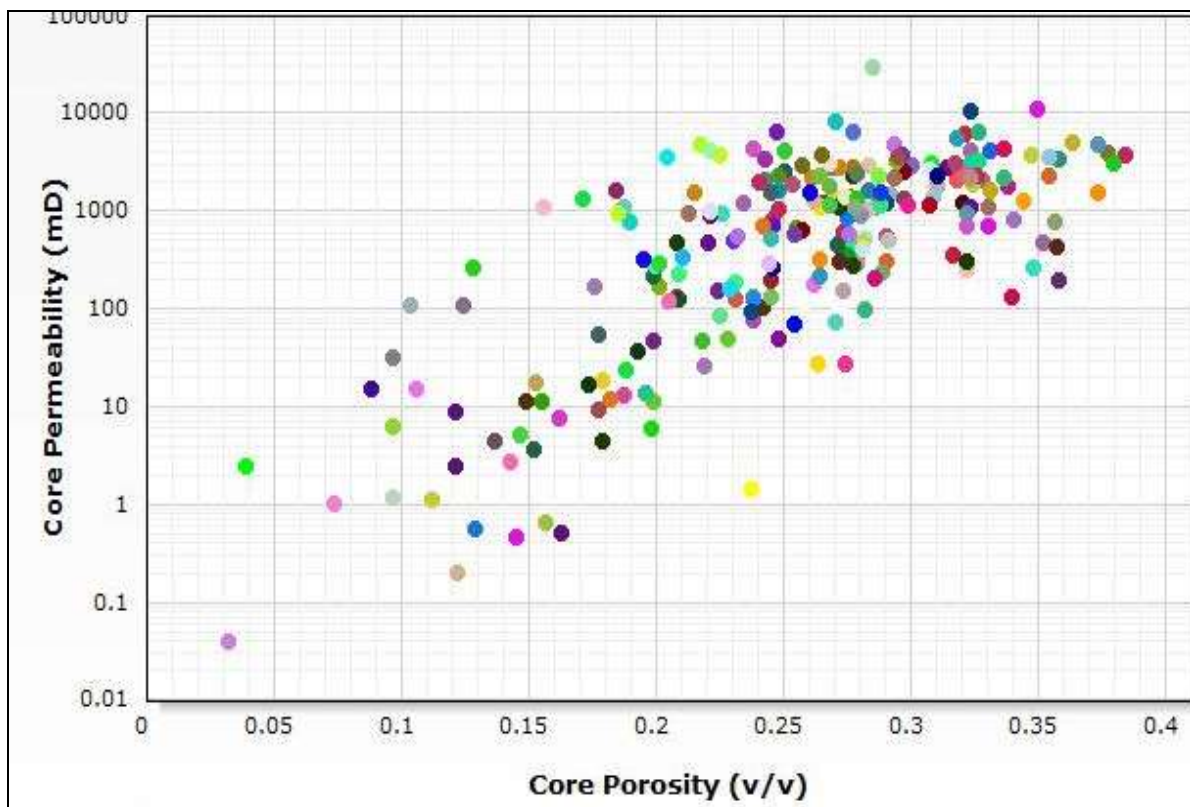


Figure 1.9: Plot of permeability versus porosity showing a large data scatter, which indicates that permeability is not only dependent on porosity, but other RQI parameters

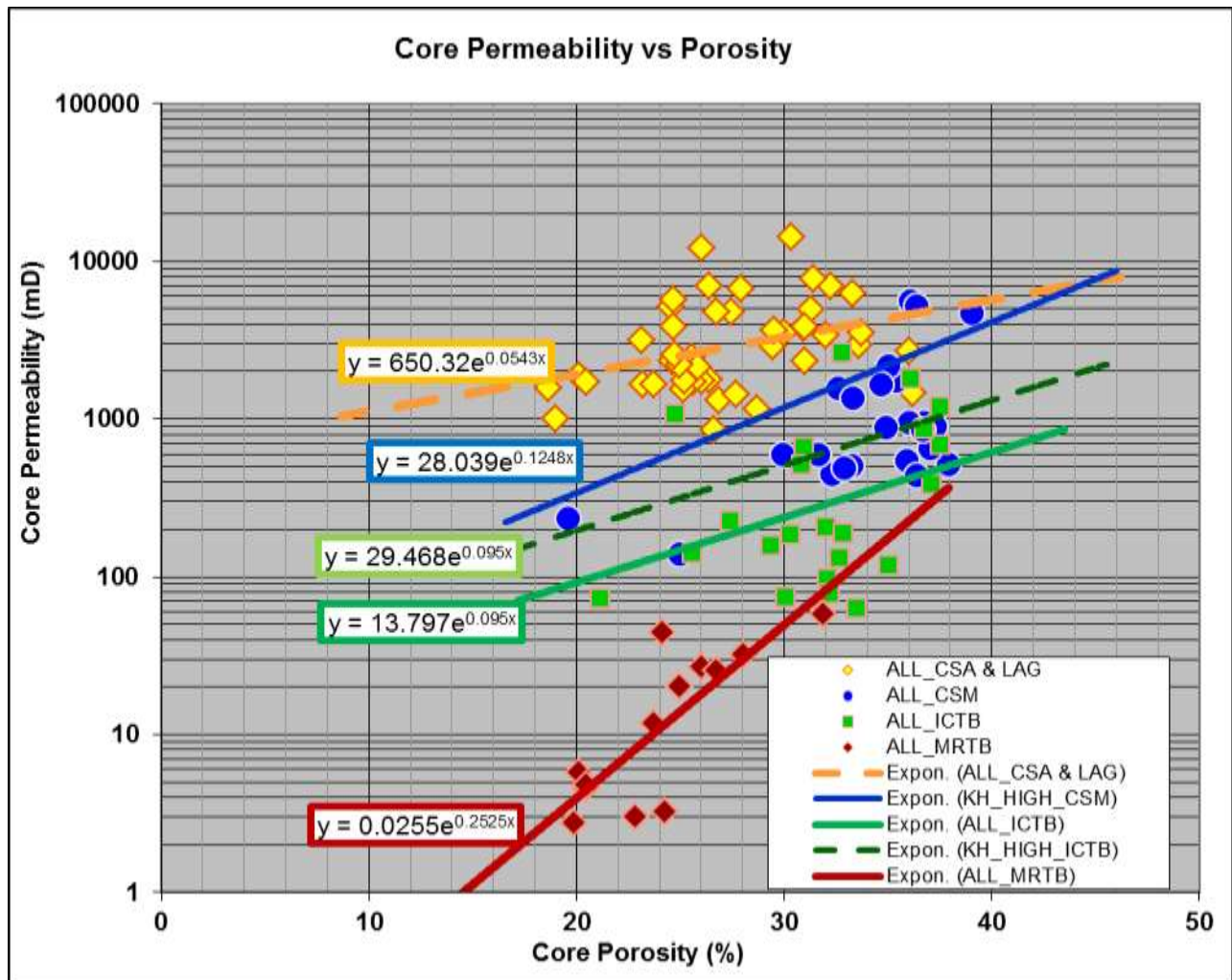


Figure 1.10: Empirical Correlation for Permeability Prediction for the Canyon Reservoirs, Deep Water – Niger Delta, obtained from core analysis dataset

Figure 1.10 presents a core derived facies based porosity-permeability relationship for estimating permeabilities in one the most prolific Niger Delta Deep Water asset. The heterogeneity within the various facies definition demonstrates that rock permeability is not only dependent on porosity, but other reservoir quality and flow unit indicator parameters. This poses challenges to formation evaluation in uncored areas away from well control in deeper objective sands.

Capillary pressure profiles generated using mercury porosimeter has many pressure stabilization points that cover wide ranges of pore sizes. Capillary properties also exhibit similar complexity. Mercury intrusion experiments – also called mercury porosimetry – are widely used for the determination of these total pore volumes and pore size distributions for porous materials. Figure 1.11 shows core-derived capillary pressure curves which exhibit a wide range in shapes and a corresponding diversity in equivalent pore throat size distributions.

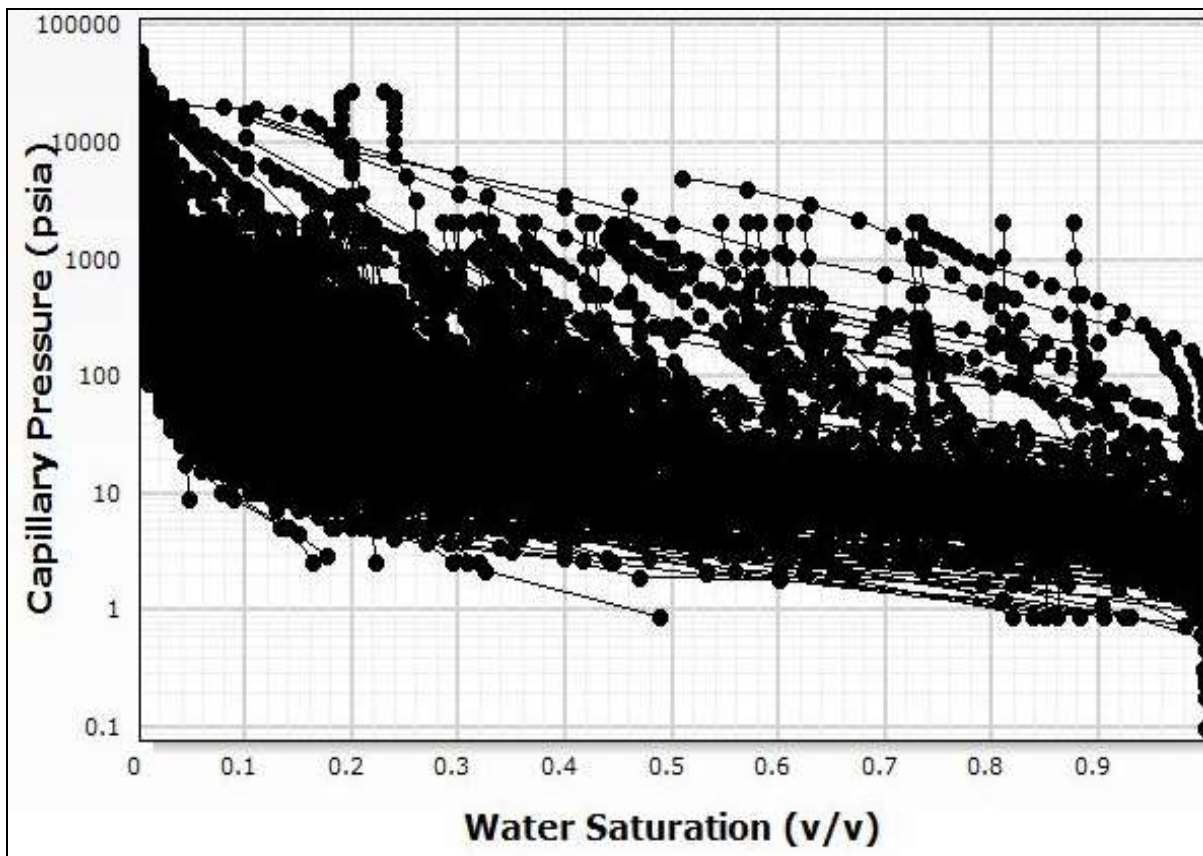


Figure 1.11: Plot of capillary pressure versus saturation exhibiting diversity in equivalent pore throat size distribution and heterogeneity within the total dataset

The study area (figure 1.12) encompasses the Tertiary Niger Delta silici-clastic (Akata-Agbada) petroleum system. It consists of (6) depositional belts (depobelts) containing sediments generally described as an upward and updip (south-to-north) transition from marine deep water and pro-delta sediments (Akata Formation), through alternating sand/shale paralic deposits (Agbada Formation), to continental deposits (Benin Formation) [Ejedawe, *et al.*, 1984]. The onshore extensional depobelts: Northern Delta, Greater Ughelli, Central Swamp, Coastal Swamp and Shallow Offshore; and the Deep Water Offshore compressional regime (Knox and Omatsola, 1989).

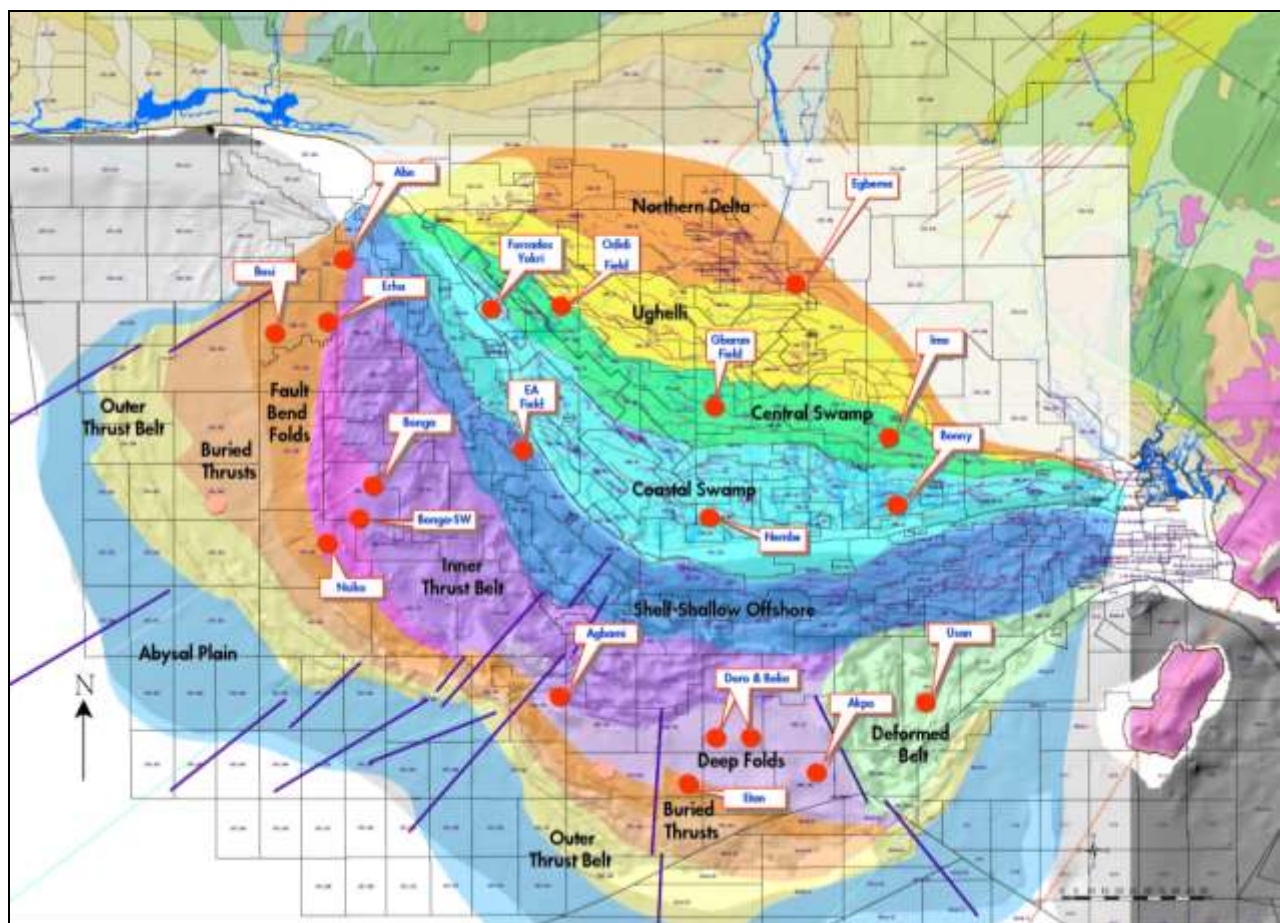


Figure 1.12: Study area showing the depositional belts, structural play segments and well locations – onshore and offshore Niger Delta (courtesy Shell Nigeria)

The sedimentary architecture usually overprinted by late diagenesis results in the intrinsic complexities which poses major problems to explorationist and petroleum engineers in modelling these systems. Although the average permeabilities exhibited by most clastic reservoirs is relatively high, the low permeabilities of the component shale strata results in low sweep efficiency and transmissibility, and may form effective flow baffles. These clay breaks are expected to have a relatively low correlatability (Weber, 1971), although they may extend up to 3,200 feet in length perpendicular to channel axis (Oomkens, 1974). The variation in clay groups as a function of depth within various depobelts, suggest that the diagenetic overprint affecting the clastic rocks of the Niger Delta are both of environmental and sedimentary origin.

In 2005, the Shell's internal second interim report of regional distribution of clay minerals in Niger Delta formed the basis to account for diagenetic overprints of dominant expansive clay groups and minerals at depths where most prolific reservoirs are located. X-ray Diffraction (XRD) data of sidewall core samples from a well within the study area as shown in table 1.1 was used to assess the relationship between expansive and non-expansive clay minerals at comparable depths. The shales were delineated from adjacent sandstone units using a combination of petrographic analysis, core description, gamma-ray logs, NMR T_2 spectrum and composite logs, while log sections with questionable attributes as captured by the caliper log were filtered-out thus building a reliable and high-confidence database of shale properties.

Table 1.1 indicate the dominant minerals within the study area as: Non-expandable clays (NEC) of kaolinite-dickite-halloysite (K+D+H) series with chlorite; Expandable clays (EC) of mixed-layer clays comprising essentially interstratified illite/smectite of montmorillonite character with sepiolite and palygorskite; and varying proportions of muscovite (mica). The clay type within the system; often lining the pore walls and obstructing the pore throats, controls the pore throat size distribution, and invariably the capillary pressures.

Table 1. 1: X-ray Diffraction (XRD) data of sidewall core samples of the study area

Depth (ftah)	Depth (ftss)	K+D+H (wt%)	Chlorite (wt%)	Total NEC (wt%)	S+P (wt%)	Illite+I/S (wt%)	Total EC (wt%)	Muscovite Mica (wt%)
6890.00	6699.02	37	33	70	0	21	21	7
7190.00	6997.57	38	28	66	10	16	26	8
7490.00	7298.03	36	29	65	13	12	25	10
7670.00	7477.93	33	18	51	20	29	49	-
7850.00	7657.82	26	25	51	26	12	38	11
9230.00	9037.46	5	10	15	71	5	76	9
9650.00	9458.39	1	20	21	33	33	66	11
9950.00	9758.70	0	31	31	15	54	69	-
10610.00	10416.56	0	20	20	39	41	80	-
11630.00	11450.22	0	18	18	57	25	82	-
12170.00	11847.27	0	17	17	34	49	83	-

S+P=Sepiolite+Palygorskite

K+D+H = Kaolinite+Dickite+Halloysite

I/S=Mixed Illite Smectite of Montmorillonite Character

Total Expandible Clay (EC) = S+P + Illite+I/S

Total Non Expandible Clay (NEC) = K+D+H + Chlorite

Courtesy: Shell Petroleum Development Company (SPDC) Geological Integration Team, 2009.

In a quest to model these extreme values of connections of petrophysical properties – permeabilities, for the various genetic reservoir units within the silici-clastic system, the study presents the development and validation of a statistically derived genetic units-based normalized pore throat radius ($\overline{R_{tot}}$) method for improved reservoir characterization and permeability modeling from mercury injection capillary pressure (MICP) dataset at core scale. The last form of our proposed model allows us to compute absolute permeability as a function of porosity, the incremental pore volume, and basic pore size characteristics. The foundations of the proposed model are the classic I.N. Hulea and C.A. Nicholls (2012) workflow for the carbonate system, but with some key differences. The proposed model incorporates characteristic lambda-most applicable to the dataset (which is controlled asymptotically to the irreducible water saturation, S_{wirr}) and Brooks-Corey power-law models for capillary pressure behavior modelling; extensive capillary pressure data correction and normalization to capture the potential impact of insitu stress & clay damage on plug samples; and sedimentologic classification of genetic reservoir unit (lithofacies association) classification for the Tertiary Niger Delta clastic system.

This presents a new method for relating permeability to pore throat sizes that is more versatile than the existing methods of Swanson (1981), Pittman (1992), J.O. Amaefule (1997) and C.I. Uguru (2005), because of its applicability to all pore throat size distribution – unimodal or multimodal, and captures other reservoir quality and flow unit indicator parameters. A cut-off of 2 microns was applicable for delineating the macro from micro pores. The present studies demonstrates that classifying macro and micro pores before modelling is vital for permeability modelling and improvement on existing workflow/methodologies for the clastic systems.

The proposed method demonstrates that a normalized pore throat radius parameter forms a straight line relationship with permeability over six (6) orders of magnitude of permeability. It appears to be a fundamental property for all pore systems so far examined.

A method for upscaling from core to well log scale is presented; for application in uncored well intervals for various depositional environments within the study area. This seeks to develop genetic unit averages of pseudo normalized pore throat radius as input parameter to the proposed model for improved permeability modelling. The proposed $\overline{R_{tot}}$ model has been validated using approximately 1,000 core and well logs dataset at same formation depth interval and well-centric and 3D reservoir scale.

Furthermore, an alternative approach to derive capillary pressure curves from Nuclear Magnetic Resonance, NMR T_2 distributions, developed by Volokitin *et al.* (1999), has been tested in one of the Niger Delta key reservoirs in the Deep Water Turbidite North Field and compared to mercury injection capillary pressure (MICP) data from a full-bore core across the reservoir. The hypothesis is the resulting relationship between the NMR T_2 distribution and pore-throat distribution embedded within a proportionality factor termed kappa, κ . This study demonstrates that a constant kappa scaling factor, $\kappa = 3$ psi Hg.sec as proposed by Volokitin is insufficient in modelling capillary pressures from NMR T_2 logs for the complex turbidites. Kappa scaling factor vary as a function of pore size/grain sorting, petrofacies and influence of clay diagenesis within the clastic system. Genetic unit based averages of kappa for NMR T_2 -Pc calibration has been developed for application in the absence of core analysis dataset for the clastic reservoirs.

Comparison between the derived capillary pressure curves and the SCAL (MICP) data provide confidence that this technique is applicable in the absence of SCAL data.

The proposed model was also validated at log scale using 75 plug samples and NMR log from same well within the Deep Water canyon reservoirs, Niger Delta Province. This was compared to existing NMR based works of Schlumberger Doll Research group (SDR) and Coates. The SDR and Coates over-estimates the permeability of most of the permeable horizon in comparison with the corrected permeabilities from measured cores, resulting in a high average absolute relative error as well as maximum error compared to the proposed model.

The efficacy of the proposed model was validated using the hydraulic flow unit characterization concept. The proposed model was modified by incorporating the normalized pore throat term into existing hydraulic unit characterization methods: RQI, Leverett J-function, and the stratigraphic modified Lorenz plot (SMLP) methodologies. Various case studies from the Deep Water and Continental setting were used to assess the viability of the modified models. The proposed model demonstrates improved efficacy and capabilities in delineating challenging petrofacies unit for improved reservoir modelling and definition of reservoir speed zones and flow baffles. A flow based 3D reservoir simulation has been performed using the proposed model and compared with the existing genetic units based permeability model for the Niger Delta system. Considering all other things being equal during simulation studies, the proposed model outperforms existing works as captured in the model's transmissibility, improved recoveries & simulation run time, and reduced convergence problems.

1.2 Literature Review

Capillary behavior is one of the most important factors that determine hydrocarbon distribution in subsurface reservoirs. An understanding of capillary pressures is vital for optimal evaluation and production of hydrocarbon accumulations. A capillary curve represents the pore geometry of a rock sample which specifically indicates the size distribution and connections of the pore throats and their associated effective pore volumes (Purcell, 1949; Thomeer, 1960 & 1983). These characteristics of a pore network also define its permeability. Therefore, it is no surprise that many investigators have proposed techniques to derive permeability from capillary curves (Purcell, 1949; Thomeer, 1983; McGeogh *et al.*, 1992; Huet *et al.*, 2005).

For a given dataset containing porosity, permeability and capillary pressure curves for different plug samples, a multivariate regression can be used to obtain an equation linking all the parameters. For the core-derived relationship to remain valid, a constant genetic unit's distribution must be established. However, it is a good practice to still measure permeability (and porosity) on the same sample used for capillary curve measurements. Moreover, it should be noted that permeability is a tensor, which implies it is not the same in all directions. For instance, horizontal permeability is usually higher than vertical permeability. Consequently, all that can be achieved from capillary pressure curves is the order of magnitude of some "average permeabilities".

Emerging research in reservoir characterization is to estimate a precise porosity-permeability relationship for particular pore types or genetic reservoir units and relationship that results from petrographic observation of multiple pore types alongside capillary pressure and air permeability data. Pore throat size distribution derived from capillary pressures is usually correlated with the petrographically observed pore types.

Subsurface engineers and geoscientist are interested in how permeability and porosity relates to pore aperture size and its distribution, primarily so they can estimate permeability. Exploration geologists also explore the pore aperture size derived from mercury injection results to evaluate the sealing capacity of cap rocks (e.g., Smith, 1966; Berg, 1975; Swanson, 1981; Pittman, 1992; Purcell, 1994; Hulea, 2011).

In a water-saturated rock, hydrocarbon migration and entrapment result from the opposing interplay of buoyancy and capillary pressures. Following expulsion from a source rock, hydrocarbons migrate through carrier beds when a hydrocarbon filament has been established through the pores of the rock. If one can determine the pressure required to set up a connected hydrocarbon filament through the largest interconnected water-saturated pore throats, one can calculate the vertical hydrocarbon column required for hydrocarbon migration (Schowalter, 1979). This displacement pressure is important to hydrocarbon migration and entrapment.

The pore aperture size that corresponds to displacement pressure is determined from a mercury injection test. However, often, one may want to know this information when mercury injection tests are unavailable because of cost management, lack of cores, or insufficient core material (e.g., small chips or thin slabs) to permit sampling. Therefore, a readily available estimation of entry/displacement pressure, from other data such as porosity and permeability, would be helpful.

If the petrophysical properties of the rocks are to be distributed between well control points in 3D models in an intelligent way, then the interplay of depositional and diagenetic controls on rock properties needs to be understood. To address these types of petrophysical and geological complexities, methods have been developed in the oil and gas industry that generally fall under the heading of Rock Typing. Most published

literatures on rock typing methods are case studies of a reservoir or field. Good examples include papers by Cantrell and Hagerty (2003) on the Arab reservoir of Ghawar field by Hollis *et al.* (2010) for the Natih Formation of North Oman and by Skalinski *et al.* (2005) on the Tengiz Field. Increasingly mercury-air capillary pressure data is used as one of the distinguishing criteria for reservoir Rock Type definition. This data can be measured relatively cheaply on core plugs and converted directly to pore throat size distributions – a key characteristic of the pore system.

Some studies lay particular emphasis on capillary pressure data for Rock Type definition (Al Aruri *et al.*, 1998, Skalinski *et al.*, 2005) while others use the capillary pressure data as just one of several criteria for Rock Type definition (Cantrell and Hagerty, 2003; Hollis *et al.*, 2010).

The wider implication of the workflow presented is that they offer better integration between methods used for saturation prediction and methods used for permeability prediction – something that is desirable for all subsurface studies. This workflow is also used to address how best to upscale permeability when transferring data from core to log and 3D grid cell scale. The analogous behavior of capillary pressure and inverse T_2 decay versus saturation data provides a method for deriving synthetic capillary pressure information directly from NMR logs even if core data are not available. The estimations of irreducible water saturation and synthetic capillary pressure profiles from NMR logs have many benefits. One benefit is the enhanced accuracy of permeability estimations by using synthetic bulk volume irreducible in the bound water model.

In this work, I always compare MICP data points with the geological data available from core & petrographic description, as well as routine porosity and permeability data. In this way, my aim is to understand the spatial organization of rock property variability across a range of scales (centimeter to meter scale) and can place “spot data” within a wider context. Rock type is hereby defined as a representative unit or volume of rock that has a distinctive pore type network whose spatial distribution is related to one or a combination of genetic processes and whose petrophysical character is predictably expressed in terms of porosity, permeability and capillary properties (unique water saturation for a given height above free water level). Hence both geological (spatial) and petrophysical criteria are used to define a rock type. Ultimately, rock type definition for this study is an iterative process, taking into account geological and petrophysical considerations and at the same time views the wider reservoir engineering considerations of what matters most for fluid flow and recovery. This bears the view that rock types are best defined based on porosity, permeability and drainage capillary pressure data and that once defined, the rock–fluid interaction aspects can then be investigated.

1.3 Objectives of the Study

The present study proposes the development of genetic units (lithofacies association) based semi-analytical, statistically derived methodology for improved reservoir characterization using pore parameters from mercury injection capillary pressures for the clastic system with Niger Delta as field case study.

The main objectives are highlighted below:

- Develop a methodology for relating permeability to pore throat sizes that is more versatile than the existing methods of Swanson (1981), Pittman (1992), Amaefule (1997) and Uguru (2005).
- Characterizing the complex reservoir pore systems at core plug scale based on genetic reservoir unit (lithofacies association) averages, to provide improved models for permeability prediction, using a normalized pore throat radius ($\overline{R_{tot}}$) approach for the clastic reservoirs.
- Demonstrate an upscaling procedure from core plug to log scale—based on the relationship between the NMR transversal T_2 distribution and pore-throat distribution embedded within the proportionality parameter term kappa, κ , developed after Volokitin *et al.* for estimating drainage capillary pressure curves.
- Develop pseudo normalized pore throat radius as input to the $\overline{R_{tot}}$ parameter without measured core and NMR T_2 distribution datasets.
- Demonstrate the implication of the proposed normalized pore throat radius for hydraulic flow unit characterization in comparison with existing methods: RQI, Leverett J-Function and SMLP and their implications in flow based 3D reservoir simulation studies.

- Proposed model validation at core and well logs in comparison with existing works: Genetic Unit Averages of FZI's and Neural Networks Permeability for the Niger Delta, NMR based Schlumberger-Doll-Research (SDR) group and Timur-Coates correlations for the Niger Delta.

1.4 Organization of the Thesis

The contents of this dissertation are organized and reported in nine (9) chapters and three appendixes as highlighted below:

- Chapter two covers an overview of the Niger Delta Petroleum Geology with particular emphasis on the genetic units as applied in this work.
- Chapter three covers the theory of mercury injection capillary pressures and capillary pressure modelling (CPM), which captures an overview of its application to reservoir and production engineering as well as exploration and geosciences; various mercury air capillary pressure corrections and conversions; mercury air capillary pressure curve fitting & smoothing; and finally existing correlations and models for estimating permeability from capillary pressures.
- Chapter four highlights the theory of Nuclear Magnetic Resonance (NMR) logs. This includes the theoretical background; NMR log interpretation; total porosity determination from lithology independent NMR logs; methodology involved in constructing synthetic capillary curves from NMR T_2 distribution; and existing correlation/models for estimating permeability from NMR logs in sandstone reservoirs.

- Chapter five discusses data analysis and various corrections applied, methodology and workflow involved to achieve the above stated objectives.
- Chapter six covers analysis of the results obtained and discussion of the results. This presents a pseudo normalized pore throat radius based on recalibration of the kappa proportionality constant after Volokitin *et al.* for application without core and well log dataset. It details the various validation employed to substantiate the developed empirical model, and the use of special core analysis (SCAL) & routine core analysis (RCA) dataset that were not used in the model building phase for validation purposes and NMR logs in uncored well intervals. It also includes the discussion of the results and compares with existing permeability correlation for the Niger-Delta Deep Water reservoir.
- Chapter 7 presents the applicability of the proposed normalized pore throat based methodology for hydraulic unit characterization. The concepts of RQI, Leverett J-Function and stratigraphic modified Lorenz plot (SMLP) were modified and analyzed to validate the efficacy of the proposed method. This resulted in improved flow unit definitions and reservoir parameters estimation. Application to 3D reservoir modelling demonstrates improved characterization for field development and EOR purposes.
- Chapter 8 presents a summary of my contributions to knowledge, published research articles as well as publications in view.
- Finally, Chapter 9 covers the summary, conclusions, and recommendations for further studies.

Chapter 2

Overview of the Niger Delta Geology

2.1 Petroleum Geology of the Niger Delta

The Cenozoic Niger Delta is one of the world's largest Tertiary delta systems and an extremely prolific hydrocarbon province situated at the intersection of the Benue Trough and the South Atlantic Ocean where a triple junction developed during the separation of the continents of South America and Africa in the late Jurassic (Whiteman, 1982). Throughout its history, the delta has been fed by the Niger, Benue and Cross rivers, which between them drain more than 106 km² of continental lowland savannah. Its present morphology is that of a wave-dominated delta, with a smoothly seaward-convex coastline traversed by distributary channels. Subsidence of the African continental margin and cooling of the newly created oceanic lithosphere followed this separation in early Cretaceous times. Marine sedimentation took place in the Benue Trough and the Anambra Basin from mid-Cretaceous onwards. The Niger Delta started to evolve in early Tertiary times when clastic river input increased (Doust and Omatsola, 1989). Generally, the delta prograded over a subsiding transition zone termed the continental-oceanic lithosphere and spread onto oceanic crust of the Gulf of Guinea during the Oligocene era (Adesida *et al.*, 1997). The weathered flanks of out-cropping continental basement sourced the sediments through the Benue-Niger drainage basin. The delta has since Paleocene era prograded a distance of more than 250 km from the Benin and Calabar flanks to the present delta front (Evamy *et al.*, 1978). The Delta structure and stratigraphy are intimately related, with the development of each being dependent on the interplay between sediment supply and subsidence rates. The dominant subsurface structures are syn- and post- sedimentary normal faults which

affect the main delta sequence. They die out upwards into the alluvial sands at depth near the top of the marine claystones. Major growth-fault trends cross the delta from northwest to southeast, dividing it into a number of structural and stratigraphic belts, called depobelts (figure 1.12), which become younger towards the south. The deltaic sequence in each of these depobelts is distinct in age, so that they actually represent successive phases in the delta's history.

Hydrocarbons have been located in all of the depobelts of the Niger Delta, in good quality sandstone reservoirs belonging to the main deltaic sequence (the 'paralic sequence' of common usage). Most of the larger accumulations occur in roll-over anticlines in the hanging-walls of growth faults, where they may be trapped in either dip or fault closures. In the 30 or 50 years since the first discoveries were made, approximately 25 MMMbbl of oil and an unestablished, but very substantial quantity of associated and non-associated gas have been discovered. Most fields are small, ranging up to 315 MMbbl, though several giant oil fields contain recoverable reserves in excess of 500 MMbbl. The hydrocarbons are found in multiple pay sands with relatively short columns, and adjacent fault blocks usually have independent accumulations.

The delta sequence comprises an upward-coarsening regressive association of Tertiary clastic up to 40,000 feet (12 km) thick covering a total area of about 35×10^6 acre (140,000 km²). It is informally divided into three gross geologic formations: (i) basal marine claystones and shales (Akata Formation); (ii) alternations of sandstones, silstones and claystones, in which the sand percentage increases upwards (Agbada Formation); (iii) alluvial sands, at the top (Benin Formation). Various genetic reservoir units are present within the various formations as presented in the following subsection.

2.2 Genetic Reservoir Units within the Niger Delta Province

Genetic reservoir units (simply lithofacies associations) are the result of a practical subdivision of a reservoir into components which have a consistent range of reservoir properties, a consistent external geometry, and a set of log responses (electrofacies) by which they can be consistently recognized. This up-scaling step from lithofacies to genetic reservoir unit (micro to meso-scale) is a key stage in the reservoir geological modelling process. The genetic units present in a cored reservoir interval are usually specified in the routine geological description of cores. Genetic units can also be described interactively from well logs (gamma ray, density and neutron); and petrophysical log responses (Porosity-Permeability relationships). It provides the link which ensures that the petrophysical properties measured from core is properly incorporated into the volume cells (voxels) used in reservoir modelling. Electrofacies refers to groups of rocks which have similar physical properties as measured by petrophysical logging tools.

The deltaic deposits of the Tertiary Niger Delta are a heterogeneous succession comprising major sandstone bodies alternating with claystones, siltstones and thinly interbedded sandstones. Core and well logs electrofacies analysis resulted in the identification of eight (8) main genetic units within the Niger Delta as:

2.2.1 Channel Sandstone

This is subdivided into Fluvial Channel and Tidal Channel Sandstone. This genetic unit comprises erosive-based, blocky shaped, sandstone bodies characterized by coarse – medium grained cross-bedded sandstones. Sandstone bodies may be single-storey or multi-storey and display a wide range in thickness from 5 – 350 feet. Multi-storey units commonly contain relatively thin intervals of Channel Heterolithic units which separate

the storeys. Storey (a strata or set of strata comprising a single level or multilevel structure) stacking patterns are reflected in weak coarsening and fining-upward trend within the blocky units.

Channel sandstone units are characterized by little or no separation between the neutron porosity and density in a depth plot. The gamma ray has a blocky shape and sharp base. The neutron and density response of these channels is similar to that of Upper Shoreface Sandstone units. However, the channels display lower apparent neutron porosities and higher density than nearby shoreface intervals. This characteristic occurs despite the fact that core porosities measured from these intervals are often similar to those from Channel and Upper Shoreface sandstones (ϕ -k cross plots). This behavior has been observed in several studies in the Niger Delta, and is due to the difference in sorting between the well-sorted shoreface and more poorly-sorted channel sediments. Channel Sandstone units normally have significantly higher core permeabilities than Upper Shoreface elements (ϕ -k cross plots). Channel sandstone units can also be distinguished from Upper Shoreface elements by their rapid lateral changes in thickness and the down-cutting of the channel base into deeper stratigraphic levels.

The differentiation of Channel and Upper Shoreface sands in reservoir units is considered necessary as the significantly higher permeability of the former is expected to result in non-uniform rates of drainage. Grain size, grain sorting, reservoir properties, and degrees in shift of the neutron and density porosity logs allow the differentiation of two types of channel unit, namely Fluvial Channel and Tidal Channel Sandstone. Fluvial Channel Sandstone are characterized by poorly sorted, gravelly coarse grained cross-bedded sandstone units with core porosities of 20-30% and high core permeabilities of

5,000 - 25,000 mD. In contrast Tidal Channel Sandstones comprise well – very well sorted, medium – fine grained cross-bedded sandstones with slightly higher core porosities of 20-35% and lower core permeabilities of 1,000-10,000 mD. The contrast in grain size, sorting and reservoir quality between the channel types varies between studied reservoirs. In many wells they show a marked difference in core porosity and permeability values. It should be noted that the practicality of differentiating these channel sub-units must be decided on an individual reservoir/field basis.

2.2.2 Channel Heterolithic

Two types of Channel Heterolithic unit have been recognized on the basis of log profiles, reservoir quality, and level of bioturbation, namely Stratified Channel Heterolithics (Type 1) and Bioturbated Channel Heterolithics (Type 2). These genetic units consist of interbedded sandstones, siltstones and claystones which display distinctive fining-upward profiles 2 – 35 feet thick.

They are closely associated with Channel Sandstone genetic units which they gradationally overlie.

On logs they have fining-upward and bell-shaped GR log profiles. In comparison to Channel Sandstone units the GR displays an increase of some 30 – 50 API, whilst the neutron-density logs show a progressive vertical change from little or no separation to separation of +10 to +15 porosity units. Core porosities and permeabilities display a similar comparative decrease (average porosity decrease of 5 –10%, permeability decrease of 25 – 75%). The overall fining-upward is the result of an upward increase in clay content interpreted to be the product of the deposition by lateral accreting fine-grained point bars in the upper part of fluvial or tidal channels. The small scale alternation of sandstone and shale records fluctuations in discharge.

The GR and neutron-density response of these units is similar to that of both the Lower Shoreface and Coastal Plain Heterolithic, particularly the former with respect to petrophysical characteristics/wireline log responses. The Channel Heterolithic units can be differentiated by i) log profile and stratigraphic position - their fining upward profile and development above Channel units is characteristic (although care has to be taken as fining-upward Lower Shoreface units occasionally overlie Channel units); ii) core porosity-permeability cross plots - they have higher core permeabilities associated with their coarser grained sandstone strata. They can also be distinguished from Lower Shoreface elements by their rapid lateral changes in thickness. Channel Heterolithic units may be erosionally overlain by Channel units or gradationally by Coastal Plain Shales and Heterolithics. They may also be overlain by Lower Shoreface units which they are separated from by a flooding surface (often cemented).

2.2.3 Upper Shoreface Sandstone

Upper shoreface units are coarsening-upward, shale-free, sandstone successions which range in thickness up to 35 feet. The basal parts of the units are characterized by very well sorted hummocky or swaley cross-stratified fine-grained sands. Wave rippled sands are developed locally. In complete successions the upper parts comprise well sorted, medium-lower coarse grained, trough cross-stratified. Cross-bedding may be unidirectional, bi-directional or multi-directional. Poorly-sorted gravelly sands with abundant carbonaceous plant-debris were rarely observed. Carbonate-cemented, fossiliferous sandstones less than 1 meter thick may cap units. These are transgressive lags formed during shoreface flooding events, cementation being initiated during transgression and continuing during burial (Blendinger 1992). The units were deposited

in the upper part of a prograding wave-dominated shoreface. The sedimentary structures and absence of shale deposits indicate deposition between fair weather wave base and the beach.

Upper Shoreface unit develop above Lower Shoreface unit with which they have a gradational basal contact. Their upper contact is typically erosional in the form of the scoured base of a Fluvial or Tidal Channel unit or a marine flooding surface, with a thin transgressive lag, and overlain by a retro-gradational Lower Shoreface deposits. The petrophysical characters of the units are characterized by little or no separation between the neutron-density porosities in a depth plot, and by low GR values which indicate the occurrence of clean sand. Although these characteristics are shared by the channel units, upper shoreface elements can be distinguished from channels by their coarsening-upward log profiles (bell-shaped neutron-density separation), gradational contact with underlying lower shoreface units and their gradational lateral change in thickness and continuity. They also display slightly lower density and higher neutron porosity values. Carbonate-cemented sandstones are recognized as sharp, isolated peaks on the sonic, density and resistivity logs. Upper shoreface sands commonly display high levels of radioactivity with GR values comparable to those of marine shales. These petrophysical characteristics/well log responses are clearly identified on RhoB – GR cross plots. The reservoir properties of these units are characterized by good reservoir quality with core porosities ranging from 25-35% and core permeabilities from 1,000-10,000 mD. Thin carbonate-cemented sandstones are commonly tight with permeabilities of 0.1-100 mD. These units display comparable core porosities but significantly lower core permeabilities than Channel Sandstone units (ϕ – K Crossplots).

2.2.4 Lower Shoreface Heterolithic

They are divided into the Proximal and Distal Lower Shoreface Heterolithic. Lower Shoreface units are typically coarsening-upward successions or a stacked series of successions varying up to 70 feet in total thickness. Individual successions (parasequences) are of the order 15-50 feet thick. Internally, sediments coarsen upward from thin ripple-bedded fine sandstones, siltstones and claystones into medium bedded (decimeter scale) fine sandstones and siltstones. The units are characterized by wave structures (wave ripples and hummocky cross-strata) and interpreted to be deposits of wave-dominated shoreface systems. Current-dominated successions interpreted as mouth-bar deposits are rarely developed. The units may gradationally coarsen-upward into Upper Shoreface units, or more typically, are erosively capped by Fluvial or Tidal Channel sand bodies.

Lower shoreface units are characterized by a gradual coarsening-upward clearly reflected in a bell-shaped profile to the neutron-density separation and funnel-shape of the GR and deep resistivity logs. This is the result of an upward decrease in clay content. The logs have a serrate character reflecting the heterolithic nature of the deposits. Neutron porosity–density log differences vary from approximately +25 to approximately -5 porosity units. Because there is little contrast between the levels of radioactivity exhibited by marine shales and lower shoreface elements, the GR log should really only be used to differentiate clean sands from lower shoreface/marine shales. Caution must also be exhibited for radioactive Upper Shoreface sands. The contact between Lower and Upper Shoreface units is normally gradational. Lower Shoreface deposits may also be overlain by Marine Shales, the contact often being

marked by a thin (less than 1 meter) carbonate-cemented, sandstone or heterolithic horizons. These are interpreted to be cemented marine flooding surfaces.

These units have a wide range in reservoir qualities with core porosities from 10-35% and core permeabilities from 0.1-3,000 mD. The large range in values reflects the interbedding of silty shales (non-reservoir), thin rippled sands (poor quality reservoir 10-100's mD) and decimeter thick sheet sands (good quality reservoir of 100's-1,000's mD). Lower Shoreface units can be subdivided on the basis of their stratal thickness, log responses and reservoir quality into two variants. Distal Lower Shoreface sub-units comprise thinly interbedded (centimeter scale) rippled sandstones and shales. The sandstones are typically wave rippled. Proximal Lower Shoreface sub-units are sandstone-dominated with medium scale sandstone strata (decimeter-meter thick) interbedded with thinner (centimeter-decimeter) heterolithic intervals. Sandstones are typically hummocky cross-stratified.

Thin bedded shoreface reservoirs commonly make poor oil reservoirs with low recovery efficiencies though the thicker proximal sands may be prolific. The reservoirs may be strongly compartmentalized by shales and cemented flooding surfaces. Significant volumes of hydrocarbons may be accessed through these units if they pass down-structural-dip into high quality Upper Shoreface sands.

2.2.5 Marine Shale

Marine Shale units comprise successions of silty shales in which siderite cements (nodules and sheets) may be common. The shales may contain thin streaks and lenses of very fine sand and coarse silt. Micropalaeontological and palynological analysis indicates that the marine clays were deposited in inner to middle neritic zones (Weber 1971).

The petrophysical character of inter-reservoir marine shales normally vary between 15 and 180 feet in thickness and can be distinguished by their large degree of positive separation on the neutron-density logs (+30 to +50 porosity units). Although these shales display high GR values (approximately 110 API units or greater), it should be noted that in some cases there is little contrast with the levels of radioactivity of Lower Shoreface units (particularly the shale-dominated Distal Lower Shoreface).

Consequently, in those wells which do not have both neutron and density logs, marine shale elements are more accurately identified by using the deep resistivity tool readings. Maximum flooding surfaces within marine shale can also be recognized by locating the point of maximum separation between neutron porosity and density logs. This corresponds to the lowest shale resistivity value.

2.2.6 Coastal Plain Sandstone

These units comprise coarsening-upward successions, up to 15 feet thick, of very well to poorly sorted, fine-medium grained sandstone. The unit possesses gradational bases and occurs above Coastal Plain Heterolithics units. The sandstone contains an association of interbedded planar beds and trough cross-bedded sands, the latter often becoming dominant vertically. Ripple cross-lamination occurs locally. Cross-strata may have basal lags and foreset streaks of gravelly-coarse sand. In some units the uppermost part comprises very well sorted, planar bedded sands. The uppermost parts of successions (1-7 feet) may be rooted. Units are either capped gradationally by coastal plain shales (in some wells a thin coal) or erosively overlain by channelized sandstones (both fluvial and tidal). These units are interpreted to be the proximal parts of bay-fill or (less commonly) floodplain successions. The coarser-grained units are probably the deposits of crevasse splay lobes or minor distributary mouth bars,

preserved structures indicating sedimentation by sheet floods containing small dunes. Units capped by very well sorted sands may be the product of washover fans or flood tidal deltas in which the sand sorting reflects wave and tidal current reworking.

The petrophysical character of these units is depicted by a smooth funnel-shape with a gradational base on the GR and neutron-density logs. The sands are characterized by little or no separation between the neutron and density logs in a depth plot. The petrophysical signature is similar to upper shoreface units but they generally form smaller scale sequences and are expected to pass laterally into channel or coastal plain heterolithic units.

The reservoir properties of these units are characterized by good reservoir quality with core porosities ranging from 25-35% and core permeabilities from 1,000-10,000 mD. They typically display a trend of vertically increasing reservoir quality.

2.2.7 Coastal Plain Heterolithic

These units are characterized by small coarsening-upward heterolithic successions of thinly interbedded sandstones, siltstones and claystones which range from 5 – 20 feet thick. They typically overlie Coastal Plain Shale with a gradational contact (dominantly bay shale), rarely developing above Coastal Plain floodplain shale.

Wave-rippled heterolithics are usually dominant at the base of the succession, pass gradationally or abruptly into decimeter scale planar bedded graded sandstones and siltstones with occasional cross-strata. Carbonaceous plant debris is common, and granule streaks and stringers occur rarely in sandstone strata. Syn-sedimentary micro-faulting has been occasionally observed.

These successions are capped by coarsening upward Coastal Plain Sandstone or blocky to fining-upward Channel Sandstone units. They are interpreted as distal bay-fill successions produced by the progradation of small mouth bars, crevasse splay lobes, flood tidal deltas or washover fans. Wave action reworked the sands in the distal part of the bay while currents issuing from distributary, tidal channels or washover processes were more dominant towards the bay margins. These units may also form small-scale (5-15 feet) fining-upward successions above Coastal Plain shales.

The petrophysical attribute of these units are characterized by coarsening-upward log shapes reflected in a bell-shaped neutron-density log separation. Neutron-density difference decreases from approximately +20 to +5 units, the result of an upward-decrease in clay content.

The reservoir properties are characterized by a poor to moderate reservoir quality with a wide range in core porosities (10 - 30%) and core permeabilities (1-1,000 mD) reflecting the heterolithic character of the unit. Reservoir quality typically increases vertically.

2.2.8 Coastal Plain Shale

These shale-dominated units are characterized by an association of carbonaceous, rooted and bioturbated shales and thin coals which were deposited in shallow bays and flood basins on the coastal plain. This unit range in thickness from 5 – 20 feet. They commonly display an internal organization with the gradational vertical passage from grey rooted floodplain shales into black organic rich mudstones with/without thin coal seams. These grade upward into bioturbated bay shales or return to an interval of rooted floodplain shales. Erosive flooding surfaces with thin transgressive sandstone lags containing clay and coal clasts may develop at the base of the bay shales.

Coastal Plain Shales are characterized by their large degree of separation on the neutron-density logs (+20 to +40 porosity units) and high GR values (typically 80 API units or greater). Bay shales display the highest GR values (approximately 100 API units) and neutron-density separation and rooted floodplain shales (often silty) the lowest. Carbonaceous shales are marked by a relatively low density compared to bay shales and where developed, coals are easily recognized by their extremely low density and high neutron porosity values (commonly off scale) and slow sonic transit times. The coals display a 20-40 API unit GR reduction relative to shales.

There is little contrast between the levels of radioactivity, resistivity and neutron-density separation exhibited by Marine and Coastal Plain Shale units (particularly the bay shale intervals). On logs, marine shales can be differentiated on the basis of their size, lateral extent and stratigraphic context having a larger thickness, greater lateral extent and being overlain by large shoreface units. Coastal Plain Shales alternate and pass laterally into Channel units and small scale Coastal Plain Heterolithic-Sandstone successions and may contain coals. They can form laterally extensive reservoir seals or discontinuous local baffles.

Chapter 3

Theory of Capillary Pressure Modelling (CPM)

3.1 Capillary Curves Measurement Techniques

The term "capillary curve" is used to refer to a capillary pressure versus fluid saturation plot determined on a rock sample. Most capillary pressure measurement yield drainage curves where the non-wetting fluid displaces the wetting fluid. Sample selection is critical to obtaining usable and reliable capillary curves. The total sample dataset must be chosen such that it covers the various genetic units/facies, as well as porosity and permeability ranges. In some techniques, the actual formation fluids can be employed. However, since the measurements are not performed at reservoir conditions of temperature and pressure, live fluid with dissolved gas cannot be used. A variety of techniques exist, some of which can also be used in imbibition mode, where the wetting fluid displaces the non-wetting fluid. This permits the determination of hysteresis in the capillary curves. The maximum attainable pressure varies depending on the applied techniques. High pressure allows the investigation of smaller pore sizes and secondary porosity. Laboratory capillary curves can be measured using several fluids that often differ from the reservoir fluids.

Table 3.1 gives a comparison of drainage capillary pressure measurement methods.

The various laboratory techniques employed in measuring capillary pressures include:

- Pressure equilibrium Method
- Mercury Injection Capillary Pressure (MICP)
- Centrifuge
- Porous Plate
- Continuous Injection
- Scanning Electron Microscopy (SEM)

Table 3. 1: Comparison of techniques for measuring drainage capillary curves

	Equilibrium Technique	Mercury Injection Method	Conventional Centrifuge
Typical Timing	Slow (5 weeks)	Fast (1 day)	Fast (3days/run)
Height above FWL	100 feet gas; 200 feet oil	22,000 feet gas; 45,000 feet oil	250 feet gas; 2,500feet oil
Confining stress	Yes	No	No
Destructive test	No	Yes	weak samples
Unconsolidated samples	Yes	No	Yes, in principle
Equilibrium conditions	Yes	Yes	Yes (nearly)
Affected by clay	Yes	No	Yes
Cost	Expensive	Cheap	Medium
Clay-bound water (CBW) correction required	No	Yes	No

Generally, because of the uncertainty in the conversion factor, the unknown influence of clay on the wetting properties of a rock, and effect of clay bound water; it is advisable to measure capillary curves with actual reservoir fluids. The fast mercury/air technique is adequate for cases where the effect of clay is negligible. Measured capillary pressures have to be converted to reservoir conditions using the differences in density, the interfacial tension (σ) and contact angle (θ) between the rock and the reservoir and laboratory fluids (table 3.2).

Table 3. 2: Typical values for interfacial tension (σ) and contact angle (θ) in laboratory system

Wetting Phase	Non-Wetting Phase	Conditions T, P	Contact Angle, θ	IFT, σ (dynes/cm)
Brine	Oil	Reservoir T, P	30	30
Brine	Kerosene	Laboratory T, P	30	48
Brine	Air	Laboratory T, P	0	72
Brine	Gas	Reservoir T, P	0	50
Oil	Air	Reservoir T, P	0	4
Air	Mercury	Laboratory T, P	140	480

In practice, capillary pressure is taken to be proportional to the interfacial tension and the cosine of the contact angle, resulting in the following transform:

$$P_{c,res} = \frac{(\sigma \cos \theta)_{res}}{(\sigma \cos \theta)_{lab}} P_{c,lab} \quad [3.1]$$

3.2 Capillary Pressure Petrophysical Models

The Capillary Pressure Model is a reservoir model in which a theoretical water saturation profile, based on capillary pressure data, is compared with a routine petrophysical saturation profile. Comparisons yield a wide variety of reservoir interpretations including: identification of hydraulic units in pressure communication and controlled by a single hydrocarbon/water contact, heights and locations of transition zones, highlights rock type differences, and distinguishes potential water sands in a gross hydrocarbon-bearing interval. The technique can be applied to wells that have no measured capillary pressure, so long as the same genetic unit is represented on which the model is based. If the well has different genetic unit, not previously encountered, the model will not correlate.

Since the capillary pressure curves are characterized by a shape factor, there is information available concerning pore size distribution. Using the Laplace-Washburn equation (1921), it is possible to calculate the size of a cylindrical pore-throat ('throat') intruded by a non-wetting fluid applied at a pressure, P relative to the evacuated void space within a sample:

$$P_c = \frac{-2\gamma \cos \theta}{r} \quad [3.2]$$

For instance, mercury intrusion measures the volume, V of mercury intruded at a pressure, P corresponding to a throat radius, r . Mercury typically has a mercury/solid/air contact angle, θ : 140° and interfacial tension, γ of 480 dynes/cm (Van Brakel *et al.*, 1981); and P_c = capillary pressure (dynes/cm²).

Thus,

$$r (\mu m) = \frac{107.6}{P_c} \quad [3.3]$$

Van Brakel *et al.* (1981) discussed some of the problems of mercury porosimetry. One source of error in measuring rock porosity is that the pores are not necessarily cylindrical. Purcell (1949) was instrumental in developing mercury injection techniques, and equation 2 has been the basis of further work by many authors. Capillary pressure versus mercury saturation commonly is plotted on arithmetic or semi-log plots (figure 3.1), although the saturation scale sometimes is reversed so that it increases from right to left. This is usually replaced by water saturation as the wetting phase (figure 1.11 and 1.12).

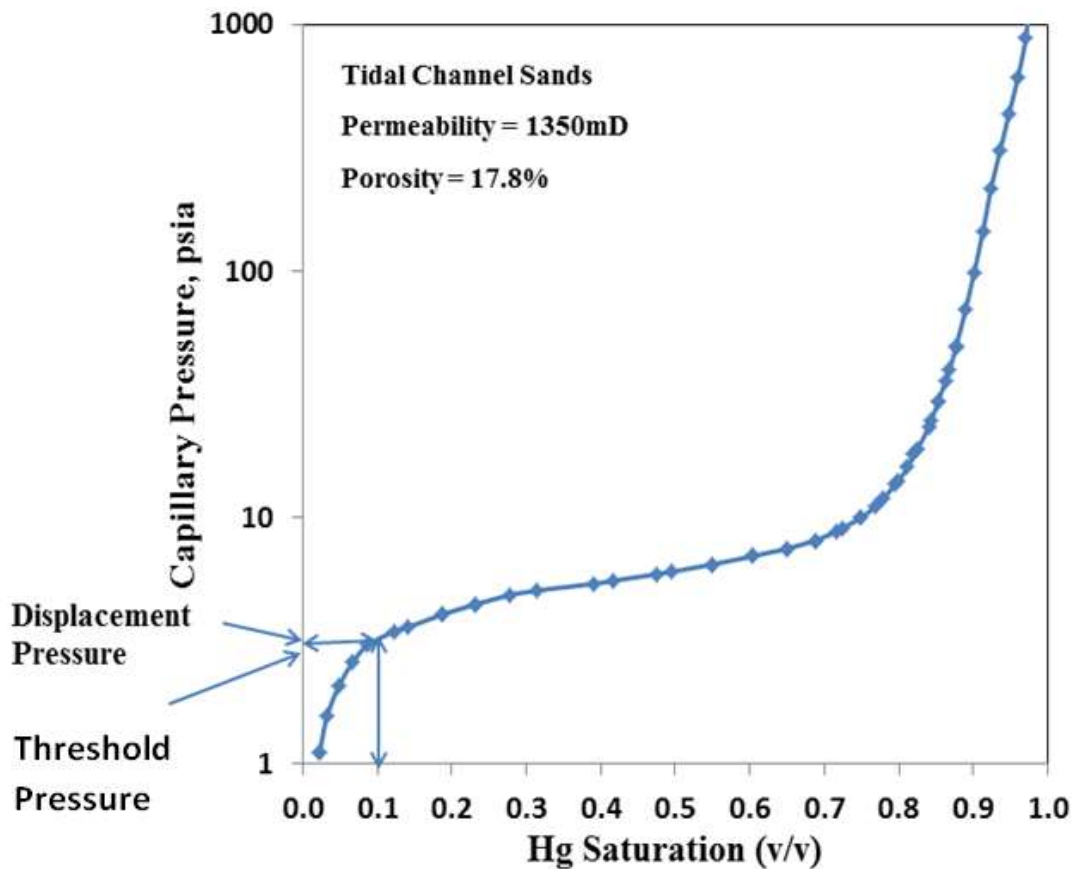


Figure 3. 1: Semilog plot of mercury injection-capillary pressure data. Katz and Thompson (1987), defined the threshold pressure graphically as the inflection point at which the curve becomes convex upward. The displacement pressure (P_d) was defined by Schowalter (1979) as the pressure at a mercury saturation of 10%.

The entry pressure on a mercury injection-capillary pressure plot is the point on the curve where the mercury first enters the pores of the rock. This point is indicative of the largest pore aperture size (Robinson, 1966). This parameter often is vague and difficult to determine because the sample size and surface irregularities of the rock relative to pore geometry creates a boundary condition that affects the low-mercury saturation part of the curve.

Schowalter (1979) recognized this problem and pointed out that the important aspect for evaluating seals for traps is to determine the pressure required to form a connecting

filament of non-wetting fluid through the largest connected pore apertures of the rock. He measured this pressure by making electrical conductivity readings during mercury injection and found the mercury saturation ranged from 5 – 17%. He wanted a pragmatic approach to use on existing mercury injection data where electrical conductivity measurements were not available. Therefore, he defined the term displacement pressure as the pressure at 10% mercury saturation (figure 3.1), for use in evaluation of hydrocarbon entrapment. Katz and Thompson (1986, 1987) defined threshold pressure as the pressure at which mercury forms a connected pathway across the sample. They indicated that the measured threshold pressure corresponded graphically to the inflection point on a mercury injection plot.

For each capillary pressure curve, the following parameters are recorded: porosity, permeability, pore entry pressure, irreducible water saturation, and shape of the capillary pressure curve. These factors are combined with petrophysical calculations of the reservoir relating porosity to irreducible water saturation. A series of algorithms, which are specific to the reservoir examined, allow calculations to be made showing changes with depth of theoretical water saturation, specific to the particular porosity profile, values of irreducible water saturation, again specific to the particular porosity profile, and the amount of potential mobile water at each level. The level of zero capillarity (or free water level), that determines the theoretical saturation profile is the user's choice, and can be fixed by trial and error. The theoretical saturation profile is compared with log-calculated water saturation. If there is divergence between the two curves, it is most often due to: an incorrect choice of the level of zero capillarity. However, any divergence might also be due to the incorrect log-calculated saturations (incorrect values of R_w , m , n , etc.), changing rock type (changing bound water volumes).

3.3 Applications of Capillary Pressure Model to Reservoir Understanding

Capillary pressure measurements and derived saturation-height functions can be used in a number of different ways. The most important is in volumetric determinations. The use of saturation-height functions for formation evaluation purposes is also very important. The correspondence between theoretical and log-calculated saturation profiles can be used in a variety of ways as highlighted below:

- To identify, with precision, the level of free water and the hydrocarbon/water contact, even if the well has not penetrated this level.
- Height of the hydrocarbon/water transition zone, and, at any level, the potential bulk volume of the rock occupied by mobile water.
- Vertical intervals within the well that are in hydraulic continuity, with respect to any hydrocarbon/water system.
- Levels in the hydrocarbon column that might have been affected, at the time the well was logged, by offset production.
- Multiple free water levels in the same well, indicating multiple stacked accumulations.
- Changing rock types and reservoirs in isolation from their neighbors.

The applications of capillary pressure modelling to reservoir management are as follows:

3.3.1 Exploration and Geological Applications

Geologists have a number of different requirements for petrophysical data. From capillary pressure measurements and saturation-height functions, geologist may require FWL estimates, spill points, sealing capacities and estimates of a potential reservoir. However, their most important requirement is for saturation-height functions for

volumetric estimation exercises. For an exploration well that has an isolated accumulation, and/or the suggestions of a transition zone on the flanks of an accumulation the following data are available:

- Location of oil/water or gas/water contacts to help in estimates of volumetric reservoir content. These data can be compared with geological definitions of reservoir geometries having multiple wells.
- Structural elevation that has to be achieved so that porosity development is above the top of the transition zone. This would help in locating offset exploratory and/or step-out wells.
- Levels of the reservoir in hydraulic continuity. Any shales within each accumulation are likely to be laterally discontinuous; whereas, the shales (and/or other barriers) which separate accumulations are likely to be laterally continuous, at least over the area of the specific accumulation.

3.3.2 Reservoir Engineering

Like geologist, reservoir engineers seek to determine the initial saturation distribution in a reservoir from capillary pressures. In addition, capillary pressures are vital in describing gas-oil and water-oil displacement processes.

For water displacement processes, the water imbibition curve gotten after the first drainage cycle is the appropriate measurement. Measurements of the imbibition curve as well as the second drainage curves are required for reservoir simulation. The imbibition curves also provide information on residual oil saturations. For gas, polymer, steam or other EOR displacement techniques, the appropriate imbibition curves must be measured.

The influence of capillary pressure on displacement processes is dependent on the wettability of the reservoir. When water-flooding oil-wet layered reservoirs with large permeability contrasts, water will preferentially flow into the highly permeable layers. Early water breakthrough and low vertical sweep efficiencies result. However, should the rock be water-wet; then the water will flow into the tight layers too, significantly increasing sweep efficiency.

In fractured reservoirs, water invades a fracture system that was initially oil-filled. The displacement process is controlled by gravity forces (due to fluid density differences), the pressure difference between the matrix and fracture systems and the capillary forces. The capillary connectivity is critical to the recovery processes in fractured reservoirs. If capillary contacts exist between vertically stacked blocks, the capillary curve is valid for the entire stacked vertical system. Ultimate recovery would be higher than for a reservoir where there was no capillary continuity between blocks.

Reservoir engineers often use "pseudo capillary pressure curves". The term pseudo capillary pressure curve refers to capillary pressure curves not obtained from any of the laboratory processes. They describe pressure difference between the hydrocarbon and water phases at the center of a reservoir block. These curves are used in simulators to determine saturation changes in response to pressure changes. In addition, reservoir as well as production engineers apply capillary pressure curves for:

- Definition of oil/water or gas/water contacts for fluid gradient characterization.
- An alternative to Leverett-J functions in describing saturation profiles through a single set of calculations, based only on the choice of zero capillarity depth.
- Recognition of different rock types with differing values of bound water volumes.

- Identification of intervals that, at least initially, should produce water-free hydrocarbons.
- Identification of intervals that, if completed, will produce hydrocarbons and water.
- Recognition of levels that have been affected by offset production (watered out).

3.4 Capillary Curve Corrections and Conversions

Capillary pressure is one of the key factors determining the initial distribution of fluids and the production behavior of reservoirs. Before practical use can be made of them, laboratory measurements have to be corrected and converted to capillary curves at reservoir conditions. These corrections should be applied before any smoothing of the data takes place. In some cases, a reduction in saturation 2-5% has been noted by applying stress corrections to pre-smoothed curves (Brown *et al.*, 1951). The three (3) major corrections applied to capillary pressure curves are captured below:

3.4.1 Closure Correction

Any shape at the low pressure end of a capillary curve which appears to deviate from the expected shape of the pressure/volume curve is referred to as closure or packing.

The phenomenon which affects this shape can be caused by:

- i. true closure effect
- ii. true properties of the pore network (e.g. vugs in carbonate system), or
- iii. both of these

True closure effect results from roughness of the plug sample. In a mercury/air capillary pressure measurement, if the largest pore throats are smaller in size than the voids created by surface irregularities, the latter will be filled with mercury before true entry

into the pore network occurs. On the capillary curve, this appears to be entry of a volume of mercury into the pore network. Closure effects are more severe for samples with high external surface area to volume ratios. Thus, capillary pressure measurements run on small samples are likely to have larger closure effects than those run on larger samples. Note that correcting a capillary curve for closure effects tends to be more of an art than a science.

3.4.2 Stress Correction

Under reservoir conditions, rocks suffer different stress regime than during laboratory capillary curve measurements, the latter usually being made under laboratory conditions. Such stress relief increases both porosity and permeability, and affects capillary curve derived saturations. Permeability increases in the range of 10-20% have been found as a result of in-situ stress relief in some field. The influence of confining stress is most pronounced around the entry region (low mercury saturation) and become less important at higher mercury saturation. The presence of in-situ stress moves the capillary curve to higher pressure and to lower non-wetting phase saturation (generally higher S_w). Juhasz (Juhasz 1979) proposed an empirical approach to correct for the effects of in-situ stress.

$$P_c^* = P_c \left[\frac{\phi_{res}}{\phi_{lab}} \right]^{-0.5} \quad [3.4]$$

$$S_{nw}^* = 1 - S_{nw} \left[\frac{\phi_{res}}{\phi_{lab}} \right] \quad [3.5]$$

where

P_c = measured capillary pressure

P_c^* = stress corrected capillary pressure

S_{nw} = measured non-wetting phase saturation

S_{nw}^* = stress corrected non-wetting phase saturation

ϕ_{res} = in-situ porosity, usually estimated from a laboratory-derived relation

ϕ_{lab} = laboratory measured total porosity (under atmospheric conditions)

3.4.3 Clay-Bound-Water or Shaliness Correction

Cleaning and drying disturbs the clay in the pores, influencing the micro-porosity and therefore the measured capillary curve. Clay structures tend to reduce the effective radius of any pore throat and hence increases the pressure needed to enter/invade the pore system in a typical clastic setting.

In addition, at reservoir conditions a portion of the water contained in the pores is associated with the clay mineral as bound water. This Clay-Bound Water (CBW) is removed during the cleaning and drying of the sample prior to capillary pressure measurement. The amount of CBW appears to depend on both the shale content and the salinity of the formation water.

The effect of CBW on the capillary curve depends on the wetting fluid used to obtain the curve. If the wetting phase does not interact with the clay then the capillary curve does not account for CBW and yields too low water saturation. This is the case with kerosene/air and mercury/air capillary curves. Hence, a particular point on these curves has to be corrected to both a higher pressure and higher wetting phase saturation.

Air/brine capillary curves do incorporate the effect of CBW, at least when the correct brine salinity is used. In formation evaluation, it is the contribution of cation-exchange sites to the formation electrical properties that is important. Various techniques are used to measure the cation exchange capacity (CEC) in the laboratory, such as wet

chemistry, multiple salinity, and membrane potential. Wet chemistry methods, such as conductometric titration, usually involve destruction or alteration of a portion of the core sample.

The *CEC*, meq/100g measured using the wet chemistry method as follows:

$$Q_v = \frac{(1-\phi) * \text{Dry Shale Density} * \text{CEC}}{100 * \phi} \quad [3.6]$$

dry shale density = 2.62g/cc, and $Q_v = \text{CEC}$ per total pore volume in meq/ml

A plot of Q_v versus ϕ using the Shoreface Sand dataset from the study area results:

$$Q_v = \left(0.0587 * \frac{1}{\phi}\right) - 0.2108 \quad [3.7]$$

Hill, Shirley and Klein (1979) developed an empirical relationship between the amount of *CBW* and Q_v derived from a set of samples. The technique assumes a uniform distribution of *CBW* over all pores, which may not be realistic.

$$P_{c \text{ CB_CORR}} = P_{c \text{ lab}} \sqrt{\frac{\phi_{eff}}{\phi_t}} \quad [3.8]$$

$$S_{w \text{ CB_CORR}} = 1 - (1 - S_{w \text{ lab}}) \cdot \frac{\phi_{eff}}{\phi_t} \quad [3.9]$$

$$\frac{\phi_{eff}}{\phi_t} = 1 - \left(0.22 + \frac{0.6425}{\sqrt{\text{salinity}}}\right) * Q_v \quad [3.10]$$

ϕ_t = Laboratory total porosity & ϕ_{eff} = effective porosity estimated from $\frac{\phi_{eff}}{\phi_t}$

Formation water salinity is approximately 17,000 ppm (16.98 g/LNaCl equivalent) for the study area.

3.5 Capillary Curve Fitting and Smoothing

In order to produce a continuous curve from the measured capillary pressure data, some kind of curve interpolation is necessary. If there are lots of points covering the entire range of interest then interpolation can be linear between these points. However, it is usually more appropriate to describe the curve mathematically, enabling fluid saturation to be calculated from the capillary pressure (P_c) or height (h) above the free water level (HAFWL).

It's assumed that all corrections such as closure, stress and clay bound water have been applied. In addition, it's also preferable to keep all data in laboratory units, and not transformed to reservoir conditions. This is because; it is easier to transform a derived function than a lot of individual data.

Figure 3.2 defines typical characteristics of a capillary pressure (P_c) curve. Each curve is defined by an entry pressure (P_{ce}) or height of the contact above the FWL (h_d), a value of irreducible water saturation ($S_{w,irr}$) and a shape/curve type. Note that in the curve fitting equations, " P_c " can be replaced by " h " if the data has been transformed to reservoir conditions. The term " S_{wet} " is used to refer to the wetting phase saturation and as such is meaningful to both laboratory and reservoir conditions. Other terms such as bulk volume of the non-wetting phase [$BV_{nw} = \phi \cdot (1 - S_{wet})$] may be substituted for S_{wet} when attempting to improve a curve fit.

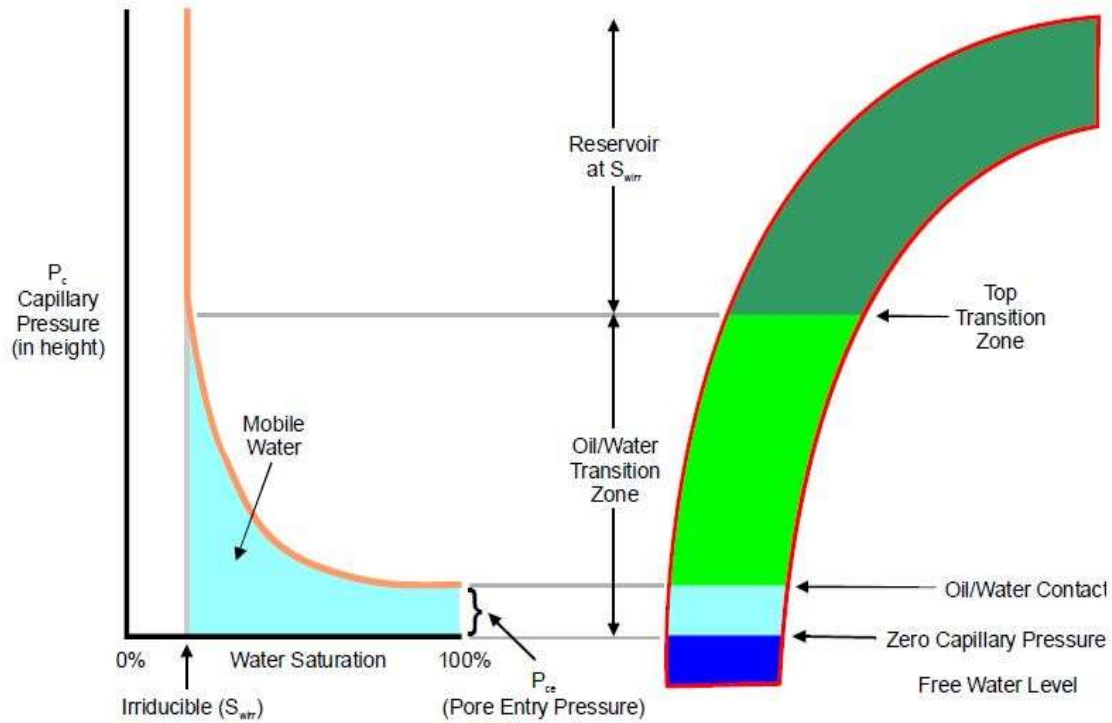


Figure 3.2: Schematic diagram of a Capillary Pressure Curve and hydrocarbon column

There are various mathematical treatments purporting to describe capillary pressure dataset in terms porosity, permeability and other rock parameters. In practice, it matters little which type of function you fit through your measured points as long as it honors the data. Here comparison of the least squares coefficient of determination "*adjusted r²*" is also used as a basis for determining how good a curve fit is.

Difference between the smoothed curve and the real data must be examined so that uncertainties can be assigned to derived capillary pressure or saturation-height functions.

3.5.1 J. Leverett Function

J. Leverett, 1941 established the first semi-empirical relationship termed the J-function.

As a dimensionless capillary correlation function, the J-function attempts to normalize capillary pressure curves by incorporating absolute permeability and porosity in form

hydraulic radius $\sqrt{\frac{k}{\phi}}$. The modified Leverett J-function which accounts for wettability is

defined as:

$$J(S_{wet}) = \frac{P_c}{\sigma \cos \theta} \sqrt{\frac{k}{\phi}} \quad [3.11]$$

k = permeability, cm^2 (1 D = $9.86923 \times 10^{-9} \text{ cm}^2$)

$J(S_w)$ = dimensionless capillary pressure-saturation function

σ = interfacial tension, dynes/cm

θ = contact angle of incidence for wetting phase, radians

ϕ = porosity, fraction of pore volume

S_w = wetting phase saturation, fraction of pore volume

p_c = capillary pressure, dynes/cm^2

$\sqrt{\frac{k}{\phi}}$ = equivalent length, cm

This function which is sometimes termed the universal J-function did not produce a single correlation for the different types of formations. Brown (1951), correlating data for a large number of carbonate cores, concluded that the J-correlation should be used for cores from a single formation and that improvement is obtained if the correlation is restricted to specific facies from the same formation. Rose and Bruce (1949) also presented correlations for eight (8) different formations showing separate distinguishable curves for the different formations.

3.5.2 Thomeer Function

Thomeer, 1960 & 1983 noted that when P_c and BV_{nw} are plotted on a log/log plot, the best fit curve approximates a hyperbola. By assuming that they are true hyperbolas, then they can be expressed mathematically as:

$$BV_{nw} = BV_{nw\infty} \cdot e\left(\frac{-G}{\log_{10}(P_c/P_d)}\right)$$

$$\text{or } (1 - S_{wet}) = \frac{BV_{nw\infty}}{\phi} \cdot e\left(\frac{-G}{\log_{10}(P_c/P_d)}\right) \quad [3.12]$$

$$S_{wet} = S_{wirr} + (1 - S_{wirr}) \left\{ 1 - e\left(\frac{G}{\ln\left(\frac{P_e}{P_c}\right)}\right) \right\} \quad [3.13]$$

BV_{nw} = bulk volume occupied by the non-wetting phase at pressure, P_c

$BV_{nw\infty}$ = bulk volume occupied by the non-wetting phase at infinite pressure

(approximately equal to interconnected pore volume)

P_d = entry pressure; G = geometric factor

In theory, the procedure involves first plotting the measured capillary pressure data versus the bulk volume of the non-wetting phase on a log/log plot. The plotted points are then matched with one of the "family" of "G" curves generated using the Thomeer equation. Once a matched curve has been found, the "G" value for your capillary curve is known. $BV_{nw\infty}$ and P_d values are found by intersections of the asymptotes with the x and y axes respectively. In practice the fitting technique can be semi-automated using a spreadsheet with interactive graphics, making the overlaying of plots redundant. By

estimating one of the variable first, linear regression can be used. Iteration to maximize the correlation coefficient enables a rapid fit of the Thomeer parameters to be made.

3.5.3 Trigonometric Tangent Function

In practice, it has been proven impossible to match many capillary curves adequately using the Thomeer parameters (Thomeer, 1983). An investigation using some carbonate capillary curves resulted in the following equation:

$$P_c = a \cdot \tan \left[\frac{\pi}{2} ((1 - S_{wet}) + (1 - S_{nw\infty})) \right] + b \quad [3.14]$$

"a" is the constant defining the shape of the capillary curve and "b" governs the entry pressure of the curve. $S_{nw\infty}$ is the extrapolated maximum non-wetting phase saturation at infinite pressure.

If the Thomeer function is unable to provide a suitable fit for longer transition capillary curves, then the Trigonometric-Tangent function may be appropriate.

A variation on the Trigonometric-Tangent has been used for very low permeability samples term the Trigonometric-Secant function as described below:

$$P_c = c \cdot \left\{ \frac{1}{\sin \frac{\pi}{2} ((1 - S_{wet}) + (1 - S_{nw\infty}))} - 1 \right\} + d \quad [3.15]$$

"c" is the factor determining the shape of the curve and "d" a constant approximating the entry pressure.

3.5.4 Brook's Corey Function

This is the most applicable capillary pressure model in the petroleum and soil physics industry. The model was developed based on evaluation of several drainage capillary pressure curves for consolidated porous media.

Brook & Corey, 1964 observed that all drainage capillary pressure curves can be represented by linear functions:

$$\ln S_{wet}^* = -\lambda \ln P_c + \lambda \ln P_e \quad [3.16]$$

$$\ln P_c = -\frac{1}{\lambda} \ln S_{wet}^* + \ln P_e \quad [3.17]$$

S_{wet}^* = reduced wetting phase saturation

$$S_{wet}^* = \frac{S_{wet} - S_{wirr}}{1 - S_{wirr}} \quad [3.18]$$

P_e = entry pressure = pressure on the straight line @ $S_{wet}^* = 1$, ie $S_{wet} = 1$.

λ = Pore size distribution index obtained from slope of the straight line.

A porous media with uniform pore size implies λ tends to infinity. For capillary curves with wide pore size distribution, λ is small, and vice versa. Resolving equation above yields the Brook's Corey drainage capillary pressure model:

$$S_{wet} = S_{wirr} + (1 - S_{wirr}) \left(\frac{P_e}{P_c} \right)^\lambda \quad [3.19]$$

3.5.5 Lambda Function

The lambda (λ) function was specially developed to describe capillary pressure curves. It represents both long and short transition zones well. The lambda function can be represented in the following form:

$$S_{wet} = a.Pc^{-\lambda} + b \quad [3.20]$$

a , b and λ are all regression constants. Although this formula does not apparently contain a porosity-dependent variable, λ can usually be correlated with porosity. Excellent fit are achievable with the lambda function compared to other functions.

3.5.6 Entry Height Functions

There are three commonly used non-linear functions which are very similar. They are used to handle low porosity/permeability reservoirs with long transition zones.

3.5.6.1 Function 1

The simplest non-linear function has asymptotes at 0 and infinite pressure:

$$S_{wet} = \frac{1}{(a+Pc^b).\phi^d} \quad [3.21]$$

" a ", " b " and " d " are fitting constants.

3.5.6.2 Function 2

The logarithmic function has a similar shape in the transition zone to function 1. It can be unpredictably close to zero pressure and high up in the hydrocarbon leg.

$$S_{wet} = \frac{a+b.\log(Pc)+d.\log(Pc)^2+f.\log(Pc)^3}{\phi^g} \quad [3.22]$$

The coefficients a , b , d and f primarily influence different parts of the curve. At low pressures, ' a ' predominates, while ' f ' does at high pressures. The ϕ^g term is only used

when averaging a set of capillary curves measured on samples of differing porosities. There exist more degrees of freedom than with Entry Height function 1, resulting in a better fit.

3.5.6.3 Function 3

This function is very similar to function 1, differing only in a pressure multiplier.

$$S_{wet} = \frac{1}{(a+b.P_c^d).\phi^e} \quad [3.23]$$

Note: When fitting the data from capillary pressure measurements on a single plug, then Entry Height function 3 is equivalent to Entry Height function 1. The ϕ^e term is only used when averaging a set of capillary curves measured on samples of differing porosities.

3.5.7 Exponential Function

An exponential can also be used for capillary pressure curve fitting. The exponential function follows the form:

$$S_{wet} = a.e^{b.P_c} + d \quad [3.24]$$

a, b and d are fitting constants.

Curve fits using exponential are best for low permeability samples or samples away from sharp transition zones.

3.5.8 Hyperbola Function

A rectangular hyperbolic function can also be fitted through capillary pressure data. The hyperbolic function follows the form:

$$(P_c - a) * (S_{wet} - b) = k \quad [3.25]$$

a, b and k are constants determined during the regression process.

With the hyperbolic function, it is difficult to get a good fit to sharp transition zones when fast changes in saturation occur over small pressure intervals. However, an excellent fit is usually possible above the transition zone.

3.5.9 Polynomial Function

A third order polynomial function can be used to approximate capillary pressure curves. Sharp transition zones are difficult to match, but the fit for low porosity/permeability formations can be reasonable.

$$\log(S_{wet} - k) = a + b.Pc + d.Pc^2 + e.Pc^3 \quad [3.26]$$

a, b, d, e and k are all constants defining the capillary curve.

The value of "k" will be close to $S_{wet,irr}$. Taking $\log(S_{wet})$ instead of S_{wet} provides much better curve correlations. A polynomial function can be unstable in shape. The number and position of the points used for the regression can have a strong influence on the curve shape.

3.5.10 Sigmoidal Function

The sigmoidal function was originally developed by British Petroleum (B.P.) for use in the good quality sandstone of the Forties Field. It usually gives a reasonable fit in medium to high porosity formations with short hydrocarbon columns. The sigmoidal function cannot handle capillary curves with significant entry pressures very well, and also unable to match the sharper transition zones. The function may also approach too quickly to the irreducible wetting-phase saturation.

$$S_{wet} = \frac{1}{1 + e^{-y}} \quad [3.27]$$

$$\text{where: } y = a + b.x + d.x^2 + f.x^3 + g.e^{h.P_c} + j.x.e^{k.P_c}$$

$$x = \phi - m.$$

The constant defining the curve are a, b, d, f, g, h, j, k and m. If fitting individual curves, then only the "a" and "g" terms are significant, thereby reducing the equation to:

$$y = a + b.e^{d.P_c}$$

3.6 Permeability Modelling from Capillary Pressures/Saturation Curves

Numerous models have been reported in the literature utilizing various parameters derived from many sources (e.g., well logging, core analysis, pressure transient testing, and history matching). With the latest advances in formation evaluation and characterization of complex reservoir systems, new workflows have been proposed for consistent and accurate reservoir description and modelling of multi-modal pore systems where mercury injection capillary pressures are used mainly to determine grid cell properties. Researchers have reported that permeability modelling from mercury injection capillary pressure dataset can be categorized into two main categories (Comisky et al., 2007). The first category is permeability models derived based on the application of the percolation theory where fluid flow behavior through porous media is modelled using probabilistic principles (Kesten, 2006). The other category covers permeability models derived based on the combination of Poiseuilles and Darcy flow equations where the porous media are considered as a bundle of parallel capillary tubes. For a given dataset containing porosity, permeability and capillary curves for different plug samples, a multi-variate regression can be used to obtain an equation linking all the parameters. For the core-derived relationship to remain valid, a constant

petrophysical calibration to various genetic reservoir units must be established.

However, it is a good practice to still measure permeability and porosity on the same sample used for capillary curve measurements.

Moreover, it should be noted that permeability is a tensor, which implies it is not the same in all directions. For instance, horizontal permeability is usually higher than vertical permeability. Consequently, all that can be achieved from capillary curves is the order of magnitude of some "average permeability".

Highlighted below are the various approaches to estimating permeabilities from capillary curves:

3.6.1 Integrating the Area under the Capillary Curve (Kozeny Methodology)

Kozeny generalized the Darcy's equation by assuming a statistically homogeneous and isotropic distribution of pore voids. He proposed a method for estimating permeability by integrating under the pressure versus saturation curve.

He introduced a term "A" for the surface area per unit volume.

$$K = \frac{\phi^3}{Z \cdot A^2} \quad [3.28]$$

Z is the Kozeny constant which accounts for departures from the idealized model.

A value of Z generally used is 5.

The value of A can be estimated from the capillary curve, although a correction for the effective surface area is required. Not all fluid filling a porous body participates in the flow. A fraction held immobile is assumed approximately equal to the irreducible wetting phase saturation, $S_{wet,irr}$.

Hence the effective surface area per unit volume is given as:

$$A_e = \frac{\phi}{\sigma} \cdot \int_{S_{wet,irr}}^1 P_c dS_{wet} \quad [3.29]$$

A correction to the porosity term in the permeability equation must then be added i.e. ϕ is replaced by $\phi \cdot (1 - S_{wet,irr})$. The equation for permeability can then be restated as:

$$K = \frac{\phi \cdot \sigma^2}{5} \cdot (1 - S_{wet,irr})^3 \cdot \left[\int_{S_{wet,irr}}^1 P_c dS_{wet} \right]^{-2} \quad [3.30]$$

If a lambda function has been fitted through the capillary pressure data, then the required integral can be determined analytically. From the lambda function, if S_{wet} is given by:

$$S_{wet} = a \cdot P_c^{-\lambda} + b \quad [3.31]$$

Then P_c can be described by:

$$P_c = \left(\frac{S_{wet} - b}{a} \right)^{-\frac{1}{\lambda}} \quad [3.32]$$

Hence:

$$\int_{S_{wet,irr}}^1 P_c dS_{wet} = \frac{a \cdot \lambda}{\lambda - 1} \cdot \left[\left(\frac{S_{wet} - b}{a} \right)^{1 - \frac{1}{\lambda}} \right]_{S_{wet,irr}}^1 \quad [3.33]$$

By substitution, the equation for estimating permeability is derived as:

$$k = \frac{\phi \cdot \sigma^2}{5} \cdot (1 - S_{wet,irr})^3 \cdot \left(\frac{a \cdot \lambda}{\lambda - 1} \right)^{-2} \left\{ \left(\frac{1 - b}{a} \right)^{1 - \frac{1}{\lambda}} - \left(\frac{S_{wet} - b}{a} \right)^{1 - \frac{1}{\lambda}} \right\}^{-2} \quad [3.34]$$

The method is extremely sensitive to the value of $S_{wet,irr}$ used. This value can be very difficult to determine from mercury/air capillary pressure curves owing to air compression at higher pressures.

3.6.2 Purcell Parameter

Purcell (1949) introduced for the first time a method to determine capillary pressure curves by forcing mercury into a core sample that is being held under vacuum pressure. He also proposed a method to calculate permeability values by considering the porous media as a bundle of disconnected capillary tubes having similar lengths but different radii. To account for heterogeneity in reservoir systems, he introduced the dimensionless lithology factor; F . Purcell used a total of 27 rock samples with permeability in the range from 0.1 mD to 1,459 mD from the clastic system. He reported a value of 0.216 for the lithology factor that best replicated the air permeability measurement in his dataset.

3.6.3 Thomeer Parameter

Thomeer (1960 and 1983) developed a mathematical description of capillary pressure and mercury saturation, and first plotted mercury injection data as a log-log plot. This plot yields a curve that approximates a hyperbola (Figure 3.3).

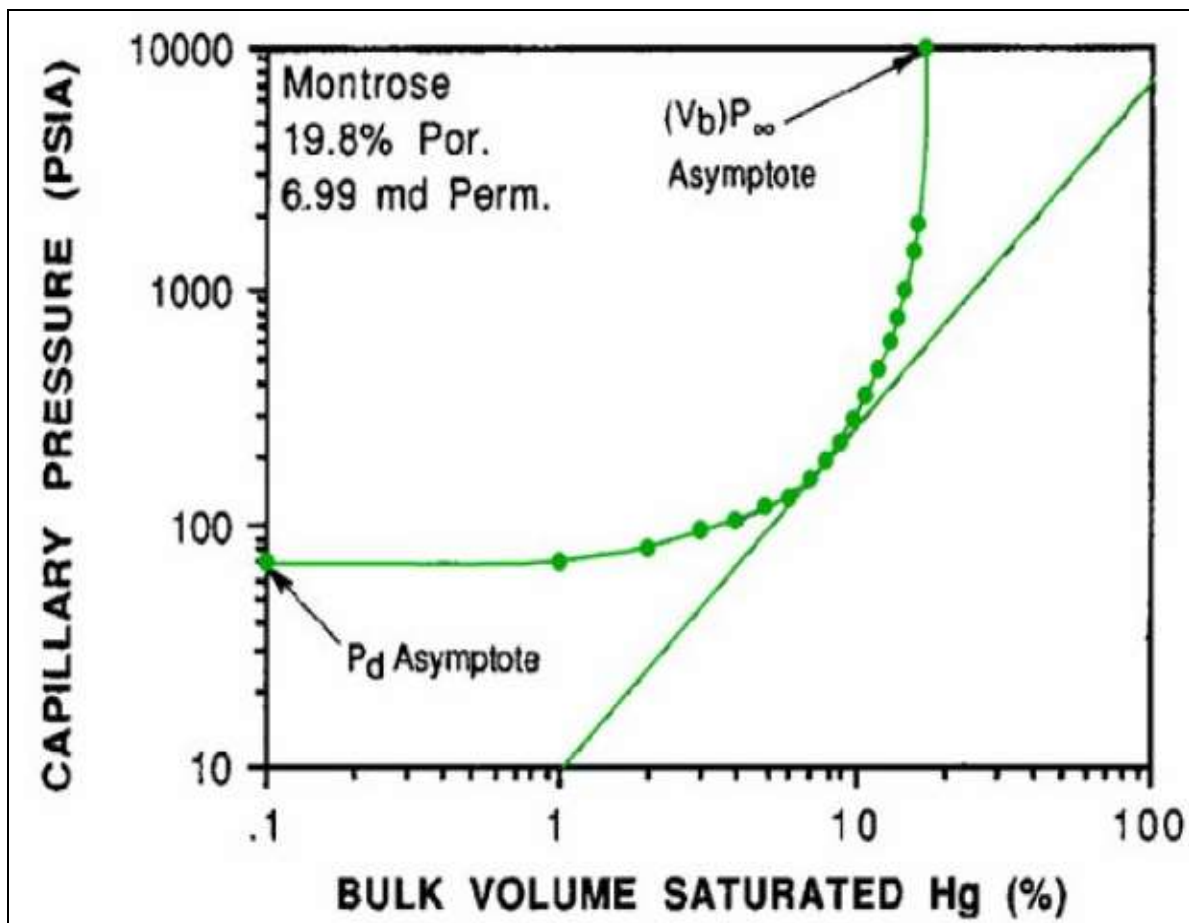


Figure 3.3: A log-log hyperbolic plot of mercury injection data [after Thomeer (1960) and Swanson (1981)]. Thomeer used the values of the asymptotes in his mathematical description. The 45°-line is tangent to the hyperbola at the apex

The location of the hyperbola with respect to the x and y axes is defined by the position of the two asymptotes. Thomeer called these the extrapolated displacement pressure (P_d on the y axis) and the bulk volume occupied by mercury at infinite pressure ($BV_{nw\infty}$ on the x axis). The shape of the hyperbola is related to pore geometry, which leads to Thomeer's pore geometrical factor (G). G is based on the possibility of a family of hyperbolic curves having G values from zero to 10, with low values constituting larger

and better-sorted pore apertures and hence indicating better reservoir characteristics. Not all curves, however, are hyperbolic and suitable for assignment of G values. Thomeer showed graphically that a relationship exists among air permeability, $BV_{nw\infty} / P_d$, and G; and that pore geometry affects permeability and mercury injection. Thomeer used the values of the asymptotes in his mathematical description. The 45°-line is tangent to the hyperbola at the apex. Some mercury curves have no apex.

A major aim of his work was to determine permeability from capillary curve derived parameters only. Results published 1960 showed that for individual values of G, a strong relationship exist between permeability and the ratio $BV_{nw\infty} / P_d$. In other words, G adjusts the basic permeability to $BV_{nw\infty} / P_d$ relation for differences in pore geometry between rock samples. The original relationship was refined in 1983 with larger datasets, yielding a meaningful analysis. The following relationship resulted:

$$K_a = 3.8068 G^{-1.3334} (BV_{nw\infty} / P_d)^2 \quad [3.35]$$

P_d in psi, BV in % pore volume and K_a mD.

The graphical relationship was based on 144 samples, with no geological description of the data. In 1983, a modified version of the first model was presented, where Thomeer introduced the pore geometrical factor, F_g , into the mathematical model and updated the model constants. In the latter model, Thomeer used 279 rock samples in which 165 were from the clastic system and the remaining 114 from the carbonates. The dataset ranged between 0.1 mD to 2,000 mD.

3.6.4 Swanson's Methodology for Correlation with Capillary Curve Data

Swanson, B.F. (1981) established the position on the mercury injection curve that represents a continuous, well-interconnected pore system through the rock using 319 rock samples representing 203 from the clastic rocks and 116 from the carbonate system. He used a porosimeter with a heating coil and molten Wood's metal to illustrate visually the distribution of the non-wetting phase at various pressures. After having been injected at a low pressure, the cooled and crystallized Wood's metal had a spotty distribution in the rock. With increasing injection pressure, the non-wetting phase entered smaller pore apertures and the volume of the Wood's metal increased. Eventually, an injection pressure was reached whereby the Wood's metal occupied pore sizes that effectively interconnected the major pore system that dominates fluid flow. He noted that at this point, "the mercury saturation expressed as percent of bulk volume is indicative of that portion of the space effectively contributing to fluid flow." He determined that on a mercury injection curve, this point corresponded to the apex of the hyperbola of a log-log plot.

Swanson proposed a technique that utilizes a correlation with the maximum value of BV_{nw}/P_d to estimate permeability. A graphical technique is normally used to determine the maximum value of BV_{nw}/P_d . The capillary pressure data points are plotted on a log-log scale as P_c versus BV_{nw} . For a plot with same scale value, a line drawn at angle of 45° slanted to the left can be shifted to find the tangent to the capillary curve. The intersection of the tangent line with the capillary curve is the point of maximum BV_{nw}/P_d .

Swanson (1981) developed the following relationship based on 319 clean sandstone and carbonate samples:

$$K_{air} = 339 * \left[\left(\frac{S_{HG}}{P_c} \right)_{apex} \right]^{1.691} \quad [3.36]$$

K_{air} is air permeability (mD), S_{HG} is the bulk volume mercury saturation (%), and P_c is capillary pressure (psi) corresponding to the apex of a hyperbolic log-log mercury injection plot. Swanson also showed a similar relationship for brine permeability (mD) at 1000 psi effective stress. This relationship was based on 56 clean sandstone and carbonate samples: The permeability relation derived by regression analysis on a large dataset of both sandstone and carbonate samples is given below:

$$K_w = 355. \left[\left(\frac{BV_{nw}}{P_c} \right)_{max} \right]^{2.005} \quad [3.37]$$

K_w is the estimated brine permeability.

The brine permeabilities used to derive the relation were measured at stressed conditions (1000 psi), so the K_w estimates are also at these conditions, which had an improved standard deviation. The advantage of using stressed liquid permeability is that overburden pressure and the gas slippage effect are taken into account. The correlation is best at medium to high permeabilities. Juhasz (1979) established a relationship between K_w and air permeabilities (K_a) as follows:

$$K_w = 0.292 * (K_a)^{1.186} \quad [3.38]$$

Swanson (1981) also developed a nomograph based on equation 37, which uses the apex of the hyperbola of a log-log plot such as Figure 3.3. This nomograph permits direct estimation of brine permeability from mercury injection data. He showed that the

apex was the same for core plug data and simulated drill cuttings (i.e., crushed rock from sample adjacent to the plug). This suggests that useful mercury injection data might be obtained from drill cuttings. Other work also has expressed the opinion that useful mercury injection tests could be run on drill cuttings (Purcell, 1949).

Katz and Thompson (1986, 1987) reported the following relationship:

$$K = \frac{1}{226} I_c^2 \cdot \left(\frac{\sigma}{\sigma_o} \right) \quad [3.39]$$

K = air permeability (md),

I_c = characteristic pore size (i.e., the calculated pore size { μm } for threshold pressure at which mercury forms a connected pathway through the sample), and $\left(\frac{\sigma}{\sigma_o} \right)$ = ratio of rock conductivity to conductivity of formation water.

Seeburger and Nur (1984) showed that the pore spaces of many reservoir rocks have a random, broad distribution of pore sizes, which suggests that transport through pores must be understood in terms of a broad distribution of local conductance (Katz and Thompson, 1987). Equation 39 is applicable to sandstones and carbonates and appears to provide a good estimate of permeability (Thompson et al., 1987). This approach, however, requires a rock sample, laboratory measurement of threshold pressure, and measurement of rock and formation water conductivity.

3.6.5 Windland's Empirical Relationship for Permeability Modelling

H. D. Winland developed an empirical relationship among porosity, air permeability, and the pore aperture corresponding to a mercury saturation of 35% (r_{35}) for a mixed suite of

sandstones and carbonates. Winland ran regressions for other percentiles (30, 40, and 50), but the best correlation (highest R^2) was the 35th percentile. No explanation was given for why the 35th percentile gave the best correlation. His data set included 82 samples (56 sandstones and 26 carbonates) with low permeabilities that were corrected for gas slippage and 240 other samples with uncorrected permeabilities. The Winland equation was used and published by Kolodize (1980):

$$\text{Log } r_{35} = 0.732 + 0.588 \text{ Log } K_{air} - 0.864 \text{ Log } \phi \quad [3.40]$$

where: r_{35} is the pore aperture radius corresponding to the 35th percentile,

K_{air} is uncorrected air permeability (mD), and ϕ is porosity (%).

3.6.6 Pittman's Methodology for Correlation with Capillary Curve Data

Pittman (1989 and 1992), developed multiple correlations to determine pore aperture radii at different mercury saturation percentiles from porosity and permeability values using some of the same cored wells as Winland. He showed that the net feet of sandstone having an r_{35} greater than 0.5 μm was useful for delineating the trap. Updip dry holes have no net sandstone with an $r_{35} < 0.5 \mu\text{m}$; whereas, a good well in the field has 39 ft (11.9 m) of net sandstone with an $r_{35} > 0.5 \mu\text{m}$. Pittman (Pittman, 1992) investigated the relationship between a single parameter derived from capillary pressure data and permeability. They sought the best correlation between these parameters. Their investigation was limited to sample with unimodal pore throat size distributions. Both authors verified the volume of the pore system needed to be saturated in order to produce an interconnected filament of that phase through a sample. The pore throat corresponding to such a saturation threshold would logically correlate to permeability.

For sandstone samples, the pore throat radius that matches to a saturation of 35% gave the best correlation - the r_{35} parameter (Pittman, 1992). He established that uncorrected air permeability is best estimated at the apex shown on the plot of the ratio of mercury saturation over capillary pressure against mercury saturation. 202 rock samples from the clastic system and out of which 103 samples were from Winland suits were used to calibrate his model. The uncorrected air permeability measurement in Pittman's dataset ranged from 0.05 mD to 998 mD while the porosity ranged from 3.3% to 28%.

3.6.7 Permeability Correlations for the Niger Delta Reservoirs

One of the most accepted and frequently quoted relations between permeability and the properties of the porous medium was introduced by Kozeny (1927) and later modified by Carman (1937, 1956).

The resulting equation is largely known as the Kozeny-Carman (KC) equation.

$$k = \frac{\phi r^2}{8\tau} \quad [3.41]$$

r = radius of a cylindrical capillary tube, and τ = tortuosity factor

Tiab *et al.*, and Amaefule *et al.* (1997) modified the Kozeny-Carman equation using the reservoir quality index (RQI) and Flow Zone Indicator Concept. Amaefule *et al.* recognized that the hydraulic quality of a reservoir is controlled by the pore geometry and pore throat size distribution and not strictly on porosity and irreducible saturation alone as expressed by Timur (1968) & Coates (1981). These attributes are functions of mineralogy (i.e. type, abundance, morphology and location relative to pore throats) and

texture (i.e. grain size, grain shape, sorting and packing). It was also observed that various permutations of the geological attributes indicate that there are distinct rock units with similar pore throat attributes. Amaefule *et al.* then postulated that the ratio of permeability to effective porosity was a unique index of the hydraulic quality of a reservoir rock with respect to the pore throat size distribution (which is the key determinant of hydraulic behavior). Thus, by modifying the Kozeny-Carman equation the reservoir quality index (RQI) was defined by the given expression:

$$RQI = 0.0314 \cdot \sqrt{\frac{K}{\phi}} \quad [3.42]$$

Equivalently,

$$RQI = 0.0314 \cdot \frac{1}{\sqrt{F_s \tau S_{gv}}} \left(\frac{\phi}{1-\phi} \right) \quad [3.43]$$

Amaefule *et al.* also defined the term flow zone indicator (*FZI*) by:

$$FZI = \frac{0.0314}{\sqrt{F_s \tau S_{gv}}} \quad [3.44]$$

The *FZI* can be rearranged in terms of the measurable *RQI* as given below:

$$FZI = \frac{RQI}{\phi_z}; \quad [3.45]$$

$$\phi_z = \frac{\phi}{(1-\phi)} \quad [3.46]$$

where: ϕ_z is the pore volume to grain volume ratio.

This FZI is intrinsic to a reservoir and is such that rocks or associations of rocks with identical FZI values are expected to have identical hydraulic behaviors. According to Amaefule *et al.*, the FZI is a unique parameter that incorporates the attributes of texture and mineralogy in the discrimination of distinct pore geometries and genetic reservoir units.

In terms of the FZI, the permeability can be written as:

$$K = 1014(FZI)^2 \frac{\phi^3}{(1-\phi)^2} \quad [3.47]$$

Thus, knowledge of the FZI serves as a basis for the proper estimation of the permeability in reservoir interval. The Facies' or Genetic unit averages of FZI values based approach is adopted for the Niger Delta fields, onshore Nigeria (Uguru *et al.*, 2005). For offshore fields within the Niger Delta, facies based porosity - permeability transform are typically used for permeability prediction based on core data from wells (figure 10) encompassing the six (6) depositional belts and major genetic reservoir units within the Niger Delta silici-clastic system (Chapter 2). Extension of the facies based Niger Delta permeability model has also been validated with the challenging offshore units: The Channel Storey Axis (CSA), Channel Lag (LAG), The Channel Storey Margin (CSM), Inter Channel Thin Beds (ICTB), and Mud Rich Thin Beds (MRTB).

CHAPTER 4

Theory of Nuclear Magnetic Resonance (NMR)

4.1 Theoretical Background

NMR logging was first introduced during the 1960s when NML (Nuclear Magnetic Logging) tools were used to make crude free-precession measurements in the Earth's magnetic field. The NML tools were retired from service in the late 1980s. Modern pulsed-NMR tools were introduced in the early 1990s, and this technology has had a major effect on formation evaluation. A wide variety of wireline and LWD tools and services is available. Nuclear Magnetic Resonance (NMR) has found many applications in the Oil and Gas industry (e.g. Kleinberg *et al.* 1996, Kenyon 1997, Altunbay *et al.* 2001, Haruna *et al.*, 2014)). NMR instrument (logging tool or laboratory unit) measures the strength and decay with respect to time of the signal induced by magnetization of hydrogen nuclear spins. The strength of the signal is proportional to the amount of hydrogen atoms in the fluid (water or hydrocarbon) in the measurement volume and thus to the porosity of a rock. The decay in magnetization represents a sum of exponentially decaying contributions originating from hydrogen spins experiencing different local surroundings, which are responsible for the relaxation of the nuclear magnetization.

The NMR measurement comprises two steps. The first step is to create a net magnetization of the reservoir fluids (Freedman *et al.*, 2004). As the logging tool moves through the borehole, the magnetic-field vector, B_0 , of the magnet polarizes the hydrogen nuclei in the reservoir fluids creating a net magnetization. The magnetization is along the direction of B_0 , which is called the longitudinal direction. The magnitude of B_0 typically is a few hundred gauss in the near-wellbore region (within a few inches of

the borehole wall). The magnitude of B_0 decreases with the radial distance from the magnet, which causes a magnetic-field gradient or distribution of gradients over the measurement volume. As discussed below, the magnetic-field gradient is used to identify and characterize the fluids in the reservoir.

Before exposure to B_0 , the magnetic moments of the hydrogen nuclei are randomly oriented so that the fluids have zero net magnetization. During the polarization time, T_p , the magnetization grows exponentially toward its equilibrium value, M_0 . The time constant that characterizes the exponential build-up of the magnetization is the longitudinal relaxation time, which is referred to as T_1 . The T_1 build-up of the magnetization during the polarization time is shown in Figure 4.1a.

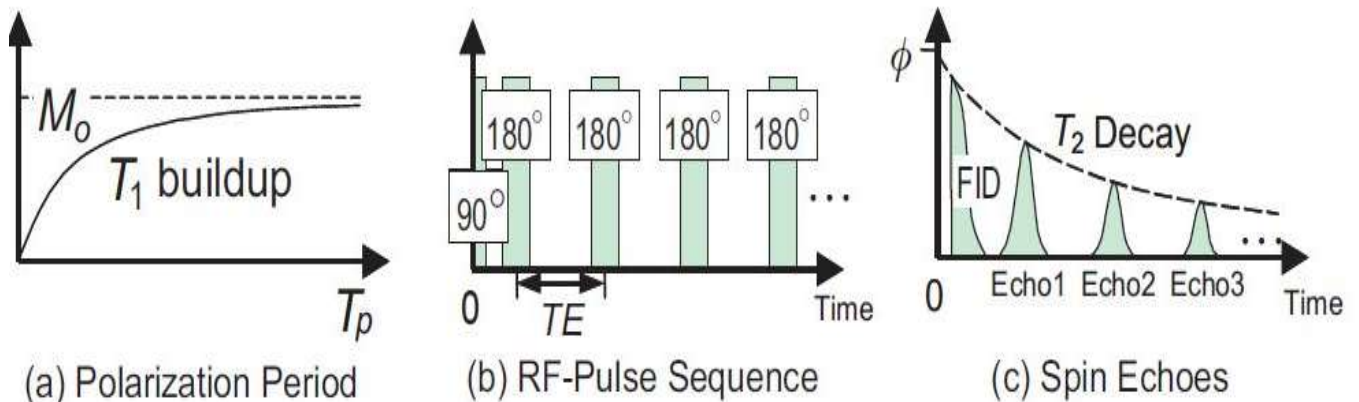


Figure 4. 1: The NMR-measurement process (after Freedman 2006).

The first step (a) is the polarization/wait period during which the reservoir fluids are magnetized. The second step (b) is the application of RF pulse sequence to the formation, which creates the spin-echo signals (c).

In reservoir rocks, a distribution of T_1 values is needed to describe the magnetization process. The T_1 distribution reflects the complex compositions of hydrocarbons and the distribution of pore sizes in sedimentary rocks. A polarization time equal to at least three times the longest T_1 is used to ensure that adequate magnetization is achieved. If a polarization time is too short, NMR-derived porosities underestimate true formation porosities. Immediately following the polarization time, a train of RF pulses is applied to the formation. The first RF pulse is called a 90° pulse because it rotates the magnetization vector, which initially is parallel to B_0 , into the transverse plane perpendicular to B_0 . Once the magnetization is in the transverse plane, it rotates around B_0 , producing a time-varying signal in the same antenna used to create the pulses. An NMR free-induction-decay (FID) signal first occurs immediately after the 90° pulse but decays too fast to be detected. The 90° pulse is followed by a series of evenly spaced 180° pulses that are used to refocus the magnetic moments of the hydrogen nuclei to form coherent spin-echo signals. The spin echoes are recorded between each pair of 180° pulses. The RF pulses and spin-echo signals are shown schematically in figures 4.1b and 4.1c, respectively. The signals are called echoes because they reach maximum amplitude at the midpoint between each pair of 180° pulses and then decay rapidly to zero before the following pulse, which refocuses the magnetic moments to produce the next echo.

The RF pulses and associated spin echoes in figures 4.1b and 4.1c are known as the Carr-Purcell-Meiboom-Gill (CPMG) sequence. It is the most widely used NMR logging sequence. The envelope of the spin-echo signal decays exponentially with a characteristic time constant, T_2 , known as the transverse or spin-spin relaxation (i.e., decay) time. The amplitude of the spin-echo decay curve extrapolated back to zero time

(immediately following the 90° pulse) is equal to the NMR-derived total porosity, assuming that the hydrogen index of the fluid is equal to 1. An important specification for an NMR logging tool is its minimum echo spacing. The minimum echo spacing plays an important role, together with the S/N ratio, in determining the T_2 sensitivity limit—the shortest T_2 value that can be measured by the tool. Short minimum echo spacing is essential for accurate and repeatable measurements of NMR total porosity in formations containing clay bound and small-pore waters (i.e., for measuring T_2 values shorter than approximately 3 milliseconds).

The number of echoes and the echo spacing, TE , in a CPMG sequence are programmable acquisition parameters. Both are selected on the basis of logging objectives and expected formation and fluid properties. In a typical NMR measurement, thousands of echoes are acquired over a period of approximately 1 second. The number of echoes depends on the expected formation T_2 relaxation times. Formations with long T_2 relaxation times (e.g., formations with light oils or rocks with large pores and/or vugs), more echoes are needed to measure the long T_2 values accurately in the T_2 distribution. In practice, the diffusion of molecules in the tool's magnetic-field gradient causes an additional T_2 diffusion-decay mechanism that places an upper limit on the longest T_2 that can be measured. Longitudinal relaxation times, T_1 , are not affected by diffusion.

For fluids in rock pores, three independent relaxation mechanisms are involved - Bulk relaxation, Surface relaxation and Diffusion-induced relaxation.

The transverse relaxation time T_2 of the pore fluid is given by the equation:

$$\frac{1}{T_2} = \frac{1}{T_{2bulk}} + \frac{1}{T_{2surface}} + \frac{1}{T_{2diffusion}} \quad [4.1]$$

T_2 is transverse relaxation time of the pore fluid

T_{2bulk} is T_2 relaxation time of the pore fluid as it would be measured in a container so large that container effects would be negligible

$T_{2surface}$ is T_2 relaxation time of the pore fluid resulting from surface relaxation

$T_{2diffusion}$ is T_2 relaxation time of the pore fluid as induced by diffusion in the magnetic field gradient

For a hydrogen nucleus in a water molecule, in a water-wet rock, the T_2 is given by:

$$\frac{1}{T_2} = \frac{1}{T_{2bulk}} + \rho \frac{S}{V} \quad [4.2]$$

$$\frac{1}{T_{2surface}} = \rho \frac{S}{V} \quad [4.3]$$

The proportionality constant ρ , between T_2^{-1} and Surface-to-Volume ratio of the pore, $\frac{S}{V}$ (which is inversely proportional to the radius of the pore bodies, $R_{porebody}$.) is called the surface relaxivity.

The bulk relaxation rate, $T_{2,bulk}^{-1}$ is normally negligibly small and the relaxation rate $\left(\frac{1}{T_2}\right)$ is dominated by the surface relaxation rate $\left(\frac{1}{T_{2surface}}\right)$. Hence, for a fully water-filled pore, $T_2 \sim \frac{V}{S} \sim R_{pore}$, i.e. T_2 is proportional to the size of a pore. The magnitude of signal decaying with each T_2 directly gives the pore volume corresponding to a certain R_{pore} .

The whole set of amplitudes obtained from the decay inversion procedure is thus proportional to the pore size distribution of a rock. Therefore, for a fully water-filled pore:

$$T_2 = \frac{1}{\rho} * \frac{V}{S} = \frac{a}{\rho} * R_{porebody} \quad [4.4]$$

The generally applied interpretation method of NMR data is to split the signal into a fast relaxing part and a slow relaxing part. The first is interpreted as bound water (BVI), and the later as free fluid (FFI), i.e. mobile water and/or hydrocarbons. The split between these two parts is made by applying a cut-off in T_2 , typically at 33 ms in sandstone (figure 4.2).

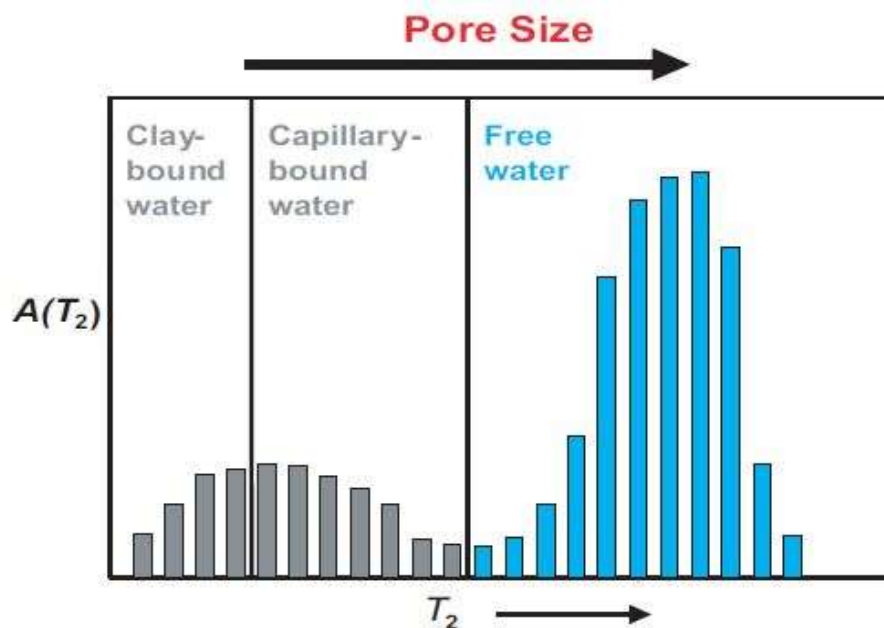


Figure 4.2: NMR T_2 distribution of typical water-saturated sandstone (after Freedman 2006)

While this has proven to be very powerful, a key shortcoming with this simple approach is that bound water is not an absolute quantity, but related to capillary pressure.

Applying a single cut-off is equivalent to choosing a single pressure. Hence, the logical improvement would be to convert NMR relaxation time distributions directly to capillary pressure curves. The main advantage would be that capillary pressure data can be acquired continuously and with sampling equal to that of the wireline logs.

4.2 Genetic Units Averages of Kappa for Capillary Pressure Estimation from NMR measurements

The methodology (after Coates *et al.*, 1999) described here is based on the inverse dependency between capillary pressure and pore throat radius, on one hand; and the rate of NMR transversal (cross-sectional) relaxation and pore radius on the other hand. Typical NMR experiment involves exciting the hydrogen nuclei from their energy state of equilibrium by means of radio frequency pulses.

The initial magnitude of the magnetization decay is proportional to the amount of hydrogen nuclei in resonance with the external magnetic field. Mathematically, the relaxation process can be described as the sum of exponential functions, where each of them represents a pore size for the water-wet, water saturated sample. The underlying equation is the following:

$$M(t) = \sum_{i=1}^n M_i e^{-\left(\frac{t}{T_{2i}}\right)} \quad [4.5]$$

where $M(t)$ is the time dependent total magnetization, M_i represents the magnetization of the hydrogen nuclei in resonance in the i -pore size family and T_{2i} is its characteristic transversal relaxation time.

The Laplace inversion of the magnetization decay function (equation 4.5) yields a distribution of the transversal relaxation times that can be interpreted as a pore size distribution, being the area under the distribution directly proportional to the porosity. The rate in which the nuclei go back to the equilibrium state is defined as the inverse of the transversal relaxation time (T_2).

In general, the hydrogen nuclei will interact with the pore surface faster in smaller pores than in larger ones, resulting in low T_2 values associated within the smaller pores and vice versa (figure 4.3).

Therefore, $1/T_{2S}$ is a function of the pore size as well as the capability of the pore surface to influence the relaxation (figure 4.3).

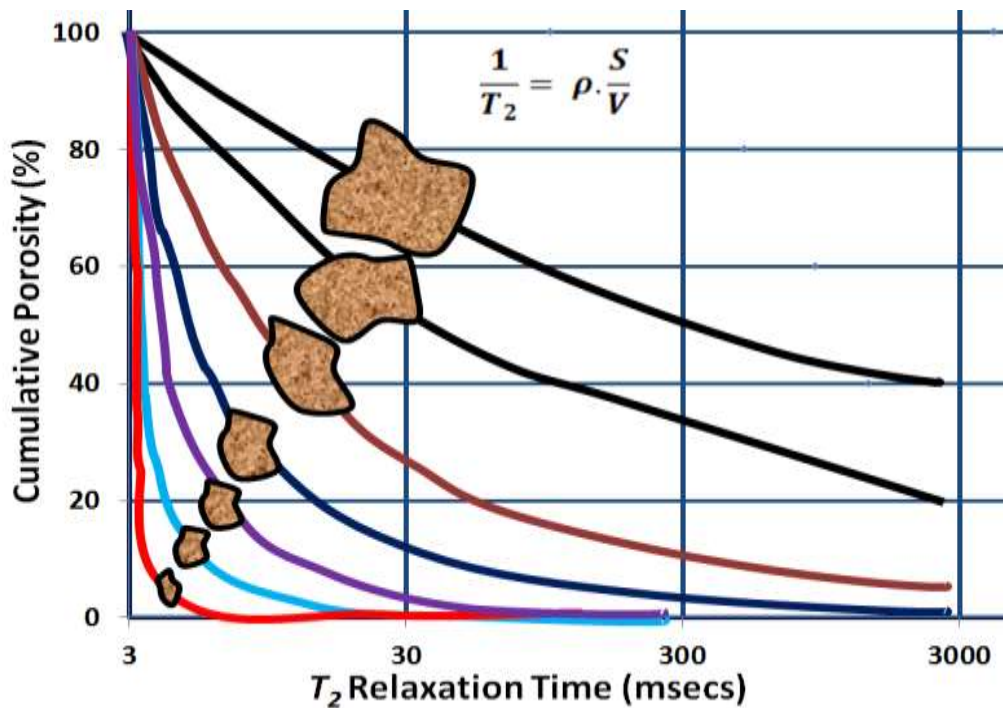


Figure 4.3: Magnetization decay as a function of the pore size, indicating the relationship between T_2 values and pore bodies. Low T_2 values are associated with the smaller pores and vice versa. This serve as the basis for assuming that only small pores (with shorter T_2 's) contribute to the irreducible water saturation

The equation describing the total relaxation rate is the following:

$$\frac{1}{T_2} = \frac{1}{T_{2S}} + \frac{1}{T_{2B}} + \frac{1}{T_{2D}} \quad [4.6]$$

where $1/T_{2S}$ is the surface to volume ratio relaxation decay, $1/T_{2B}$ is the bulk relaxation rate and $1/T_{2D}$ is the diffusivity relaxation rate.

During hydrogen nuclei interaction with the pore surface in a water-wet, water saturated pores, the contribution of the surface relaxation (T_{2S}) is faster than the bulk (T_{2B}) relaxation rate (Coates et al., 1999).

And as such, NMR transverse relaxation time (T_2) is mainly sensitive to pore-body size. In a fully water wet sample measured under constant magnetic field, the bulk relaxation and diffusion coupling are negligible, and as such, T_2 is related to pore-body size by:

$$\frac{1}{T_2} \equiv \frac{1}{T_{2S}} = \rho \cdot \frac{S}{V} \quad [4.7]$$

where ρ is the proportionality constant termed the surface relaxivity ($\mu\text{m/s}$), and $\frac{S}{V}$ is the surface to pore volume ratio (μm^{-1}) which quantifies the pore-body dimension.

It is important to note that equation 4.7 is only valid when the pore is completely filled with the wetting phase with no diffusive coupling. A high relaxivity implies rapid decay in magnetization and vice versa.

Table 4.1 presents the surface to volume ratio of some simple pore-body geometries.

In this work, spherical pore geometry is assumed to correlate NMR and mercury injection measurements.

Table 4. 1: Surface to volume ratio of simple pore-body geometries (modified after Chicheng et al., 2013)

Pore Geometry	Surface	Volume	Surface/Volume (S/V)
Sphere (radius = R_b)	$4\pi R_b^2$	$\frac{4}{3}\pi R_b^3$	$3/R_b$
Cube (length = a)	$6a^2$	a^3	$6/a$
Open-ended Cylinder (radius = R_b ; height = h)	$2\pi R_b h$	$\pi R_b^2 h$	$2/R_b$

The table depicts that S/V is inversely proportional to the pore body radius (R_b); and substituting for S/V in equation 6 for a spherical pore body, T_2 is expressed as:

$$T_2 = \frac{R_b}{3\rho} \quad [4.8]$$

In practice, the T_2 values are predetermined and the amplitudes are calculated from a least-square algorithm following the Laplace inversion scheme.

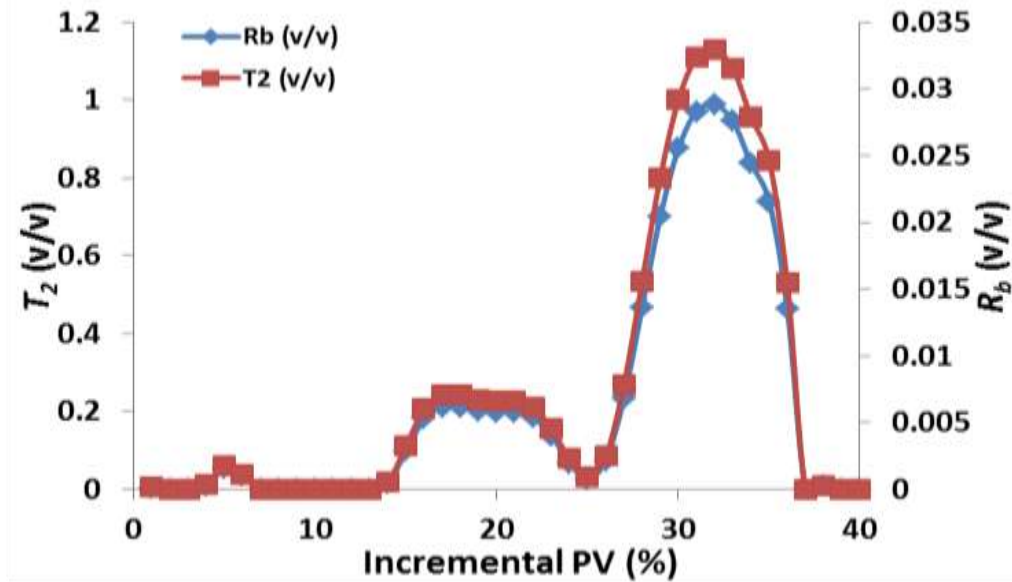


Figure 4.4: NMR T_2 conversion to pore-body size distribution assuming spherical pore bodies using dataset from the Channel Storey Margin unit. The rock surface relaxivity, $\rho = 10 \mu\text{m/s}$ was obtained from the Sørland *et al.* (2007) relationship

Figure 4.4 demonstrates the existence of a relationship between the NMR T_2 distribution and pore-body distribution based on equation 4.8. This formed the basis for my assertion. The subsequent sections present the methodology employed for characterizing complex reservoir lithologies based on genetic units' averages of kappa for improved capillary pressure modelling.

4.3 NMR-Log Interpretation

T_2 Distributions provide much useful information about reservoir-rock and fluid properties and constitute the basic outputs displayed on an NMR log. T_2 distributions computed from NMR echo data are used to compute NMR total, bound-fluid, and free-fluid porosities, and also are used for permeability and reservoir-quality estimation. T_2

distributions are computed by fitting spin-echo signals to a sum of approximately 30 single-exponential functions, each with amplitude, $A(T_2)$, and associated decay time, T_2 . The fitting procedure is achieved by a mathematical technique known as inversion. The outputs of the inversion are the amplitudes, $A(T_2)$, in porosity units corresponding to each T_2 value.

A semi-log plot of $A(T_2)$ versus T_2 is known as a T_2 distribution (figure 4.2). This partitions the distribution curve into two (2) sections: bound water (BVI) and free water (FFI) by use of empirically determined cutoffs.

The area under the T_2 distribution equals NMR total porosity. Figure 4.2 shows a T_2 distribution for typical water-saturated shaly sandstone. In water-saturated rocks, T_2 distributions are qualitatively related to pore-size distributions. The T_2 values typically span several decades from less than 1 millisecond to several seconds.

The wide range of T_2 values observed in sedimentary rocks is caused by the broad distributions of pore sizes. As a first-order approximation, each T_2 in the T_2 distribution is proportional to a pore-size diameter. Thus, the short T_2 values in a T_2 distribution are associated with signals from water in small pores, whereas the longer T_2 values correspond to signals from water in larger pores. T_2 distributions are used to predict total porosity, bound-fluid porosity, free-fluid porosity, permeability, and pore-size distribution.

Comparisons frequently are made between the pore-size information contained in T_2 distributions and mercury-injection capillary pressure curves. It is important to note that capillary pressure curves provide information on pore-throat sizes, whereas T_2 distributions are related to pore-body sizes. T_2 distributions have been found to provide information that complements capillary pressure curves in many types of sandstone that have pore-body and pore-throat sizes that are well correlated.

4.4 Lithology Independent NMR Total Porosity

One of the most significant recent advances in formation evaluation is lithology-independent NMR total porosity. Freedman (2004), established that the measurement of lithology-independent total porosity is unique to NMR tools because porosities derived from density, neutron, and sonic measurements depend on knowing rock-matrix properties. In heterogeneous formations having mixed or unknown lithology, the use of NMR logs for accurate porosity prediction is highly recommended.

The NMR-log porosities are insensitive to the lithology changes and read correctly over the entire interval. NMR total porosity equals actual formation porosity in most hydrocarbon-bearing and wet rocks, including shale. However, exceptions can occur in heavy-oil reservoirs with oil viscosities on the order of 10,000 cp or greater (Freedman, 2004). Such oils can have T_2 distributions with significant amplitudes below the T_2 sensitivity limits of NMR tools. NMR-derived porosities in these heavy-oil reservoirs underestimate true formation porosities. The deficit of NMR-derived porosities compared with density-log porosities can be used to infer the presence of heavy oil and, with some assumptions, to place bounds on the oil viscosity and oil saturation.

4.5 Construction of Capillary curves (P_c) from NMR T_2 distribution

The migration of a non-wetting fluid into a rock is described by a drainage capillary pressure curve. The capillary resistance encountered by the non-wetting fluid phase as it attempts to enter the pores of the rock is dependent on wettability, the surface tension of the fluid interface and the pore-throat radius and is expressed as:

$$P_c = \frac{2\sigma\cos\theta}{r_{porethroat}} \quad [4.9]$$

where: σ is surface tension

θ is contact angle between the fluid interface and pore wall, and is a measure of wettability.

Therefore, a drainage capillary pressure curve can be related to a pore throat distribution via:

$$\frac{1}{r_{porethroat}} = b * P_c \quad [4.10]$$

Volokitin *et al.* (1999) established that capillary pressures, P_c , and NMR T_2 measurements represent two different distributions in pore systems: the pore throat size distribution and the pore body size distribution.

Intuitively, one can reason that there should be a relationship between pore-body radius and pore-throat radius, based on the assumption that the radius of grains for sandstones (and some carbonates) determines the size of the pore-body as well as the size of the pore-throat. The conversion of NMR T_2 distributions to synthetic-capillary pressure curves as applied in this work is based on the assumption that the above relationship exists and can be represented through a simple geometric parameter.

Therefore, if $R_{porebody}$ is proportional to $r_{porethroat}$, it means that one can be derived from the other, once the proportionality constant (or function, as this may be a parameter that changes with the pore system and/or rock fabric) is known. To estimate capillary pressure curves from the NMR T_2 distribution, a proportionality constant κ (Kappa), must therefore be established between the two measurements (Volokitin *et al.*, 1999).

This constant can be expressed (directly) as:

$$\kappa = \frac{P_c}{T_2^{-1}} = \frac{2\sigma \cos \theta * a * R_{porebody}}{\rho r_{porethroat}} = \text{constant} * \frac{R_{porebody}}{r_{porethroat}} \quad [4.11]$$

$$P_c = \frac{2\sigma \cos \theta}{r_{porethroat}} \quad \text{and} \quad T_2 = \frac{a * R_{porebody}}{\rho}$$

For hydrocarbon bearing reservoirs, NMR signal has a relaxation time that also depends on the fluid viscosity instead of purely on pore size, and this could lead to erroneous results if a direct T_2 - P_c conversion is applied.

Therefore, prior to construction of capillary pressure curves from NMR acquired in an oil bearing reservoir, a hydrocarbon correction should be applied. This technique is based on the fact that hydrocarbons enter the larger pores only.

For sand-shale sequences, like the Deep Water Turbidite field, the choice is a single Kappa, κ . The main contrasts between saturation height functions in different facies most likely originate from differences in pore-size distribution, which will be properly replicated by NMR spectra converted with the same κ . For this reason, a single $\kappa = 10$ has been established for the canyon reservoirs (Olubunmi *et al.*, 2011).

The NMR to P_c conversion was optimized by establishing the value that provides the best match between saturation from T_2 derived capillary pressure curves and the saturation from MICP.

The Capillary pressure curves (MICP) measured from core plugs taken at different depths was compared with capillary pressure curves constructed from the T_2 distribution at similar depths. Comparison shows that the MICP is relatively well

reproduced and the conversion from NMR to P_c using a single κ is sufficient. The average error in saturation is 6.5 saturation units.

4.6 Estimating NMR-Derived Permeability in Sandstones

Two (2) empirical permeability equations are used widely in the industry-the Schlumberger-Doll Research (SDR) and the Timur-Coates equation. The NMR permeability equations provide estimates of brine permeabilities in water-saturated sandstones as follows:

Timur/Coates NMR permeability equation:

$$K_{Coates} = A. (10. \phi)^B. \left(\frac{FFI}{BWT}\right)^C \quad [4.12]$$

A = Coates pre-factor, formation-dependent coefficient = 1

B = Coates porosity exponent= 4

C = $\left(\frac{FFI}{BWT}\right)$ exponent = 2

FFI = Free Fluid Index

BWT min (v/v) = minimum value for total bound water = 0.01

SDR NMR permeability equation:

$$K_{SDR} = A. (\phi)^B. (T_2)^C \quad [4.13]$$

A = SDR pre-factor, formation-dependent coefficient = 4

B = SDR porosity exponent = 4

C = T_2 mean exponent = 2

A good correlation between pore-body and pore-throat sizes exists for sandstone, which is the underlying basis for NMR-derived permeability. Both permeability estimators contain model parameters (e.g., exponents and proportionality constants). The default parameter values used by service companies usually provide NMR permeability logs that are qualitatively accurate (i.e., they can be used to predict that one zone is more permeable than another zone). Although this information is valuable, the estimated permeabilities can deviate significantly from those of the formation.

To estimate quantitatively accurate log permeabilities for a specific type of rock, it is recommended that measurements on core samples be analyzed to determine optimal permeability-equation parameters. Estimates of SDR and Timur-Coates permeability both are affected by hydrocarbons, and more research is needed to develop equations to predict relative permeabilities to hydrocarbons and water. The SDR and Timur-Coates permeability equations are based on assumptions that are not valid for carbonates because pore-body sizes measured by NMR and pore-throat sizes are not well correlated in carbonates. Carbonates also can have NMR signals from fluids in isolated vugs, which contribute to NMR porosity but not to permeability.

CHAPTER 5

Material and Methodology

Well logs and core analysis samples & reports were collected from various depositional environments within the Niger Delta system. Independent analysis and interpretation was undertaken to ensure data quality assurance and reduce uncertainties. Sample selection and evaluation as well as methodology developed to enable me meet the aforementioned objectives are described in the following sections below. In addition, the workflow adopted for the study is also presented in figure 5.1.

5.1 Sample Selection and Data Analysis

The dataset for this work stems from three distinct geological environments of deposition that have been found in the deltaic deposits of the Cenozoic Niger Delta ranging in age from Middle to Late Miocene. These are the Continental, Tidal and the Coastal depositional environments. They encompasses the six (6) depobelts within the Niger Delta Petroleum systems as highlighted in section 1 above, and from five (5) genetic reservoir units identified based on available core data, log responses, and depositional environments for the Tertiary Niger Delta system:

- i. Channel Heterolithics,
- ii. Lower shoreface Sands,
- iii. Upper shoreface Sands,
- iv. Tidal Channel Sands, and
- v. Fluvial Channel Sands.

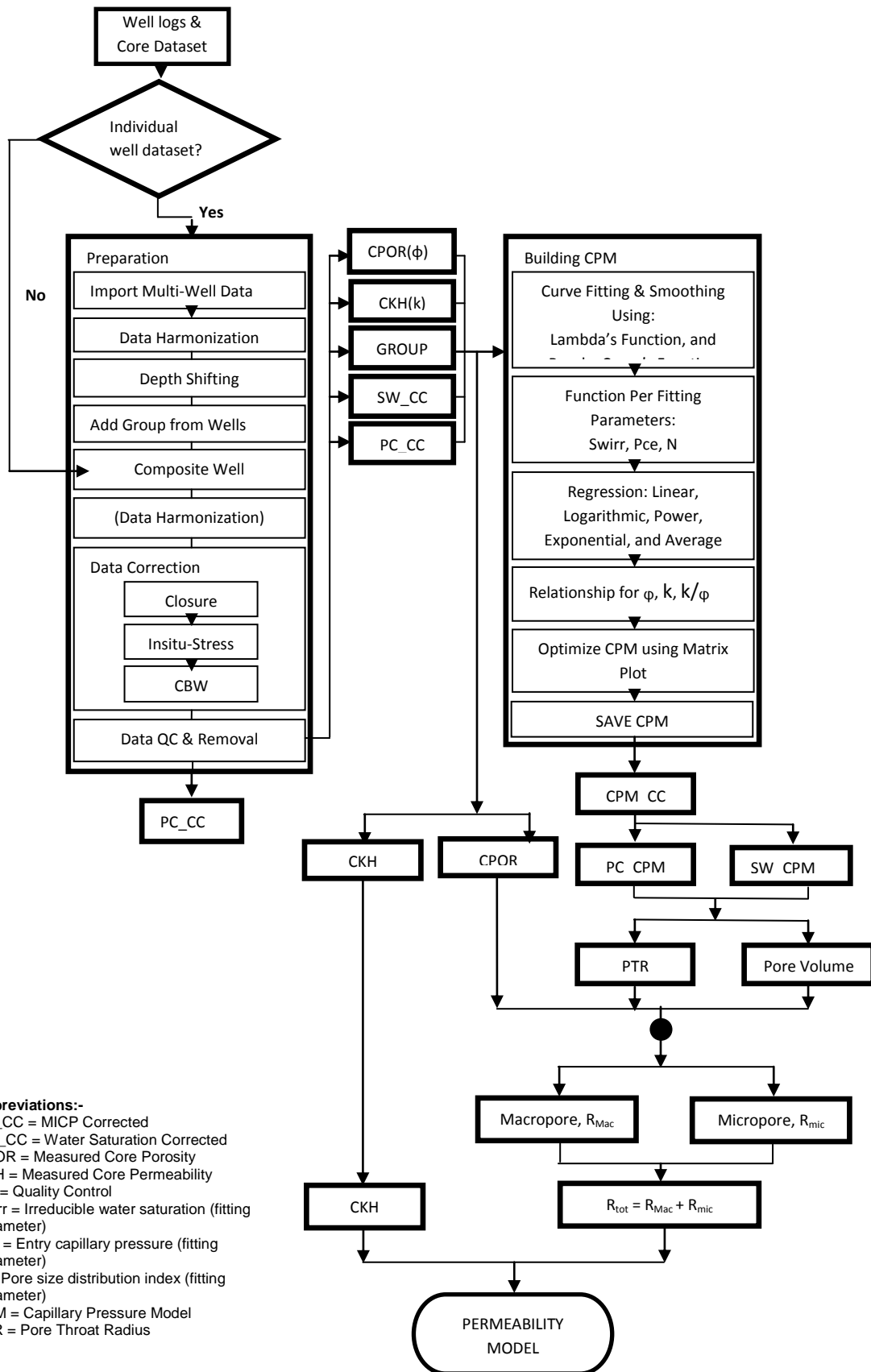


Figure 5. 1: Workflow adopted for the study.

Highlighted below is an inventory of dataset employed for the study:

- Geologic data
 - Petrographic & X-ray Diffraction (XRD) analysis, core descriptions/images
- Routine and Special Core Analysis data
 - Mercury Injection Capillary Pressures (MICP)
 - Air Brine Capillary Pressures
 - Air Permeability (k) and Porosity (ϕ)
- Well Logs
 - Gamma Ray (GR), Spontaneous Potential (SP), Caliper, Density (RhoB), Neutron, Resistivity and Nuclear Magnetic Resonance (NMR).
- Static and dynamic reservoir dataset from Field “AX”
 - Table 5.1 below highlights the geologic, geophysical and engineering dataset from nine (9) wells employed for reservoir characterization.

Table 5. 1: Data Inventory for Reservoir Modelling

S/N	DATA TYPE	A1	A2	A2S	A3	A4	A5	A6	A7	A8	A9
1	3D PRE & POST STACK Seismic Volume	✓	✓	✓	✓	✓	✓	✓	✓	✓	✓
2	TWT-Depth Checkshot Data	✓	✓	X	X	✓	✓	X	X	X	X
3	Deviation data: Gyroscopic multi-shot survey with TVDSS (using minimum curvature method)	✓	✓	✓	✓	✓	✓	✓	✓	✓	✓
4	Well Log data: Comprehensive suite of logs (GR, Cal RhoB, CNL, Sonic, LL9S and LL9D)	✓	✓	✓	✓	✓	✓	✓	✓	✓	✓
5	RFT pressure data were recorded for fluid contact and PVT analysis	X	✓	X	X	✓	✓	X	X	X	X
6	Side wall samples: For detailed lithological description and fluorescence test for fluid typing	X	✓	X	✓	✓	✓	✓	X	✓	✓
7	Core Data: A comprehensive analysis for both conventional RCA and advanced SCAL	X	X	X	X	X	X	X	X	✓	✓
8	Production and Event histories	X	✓	✓	✓	✓	✓	✓	✓	✓	✓

The wide range of dataset covering the six (6) depobelts within the study area was chosen to honor the depositional fabric and diagenetic overprint of the area, as well as validate the generality and applicability of the proposed model for the petroleum system. The representativeness of the each genetics unit classification was analyzed by carefully ensuring that the sample covers the full range of pore network characteristics; and bears approximately same flow units.

Figures 5.2, 5.3, 5.4 and 5.5 demonstrate a color coded illustration of the various genetic reservoir units, indicative of a strong correlation between the units.

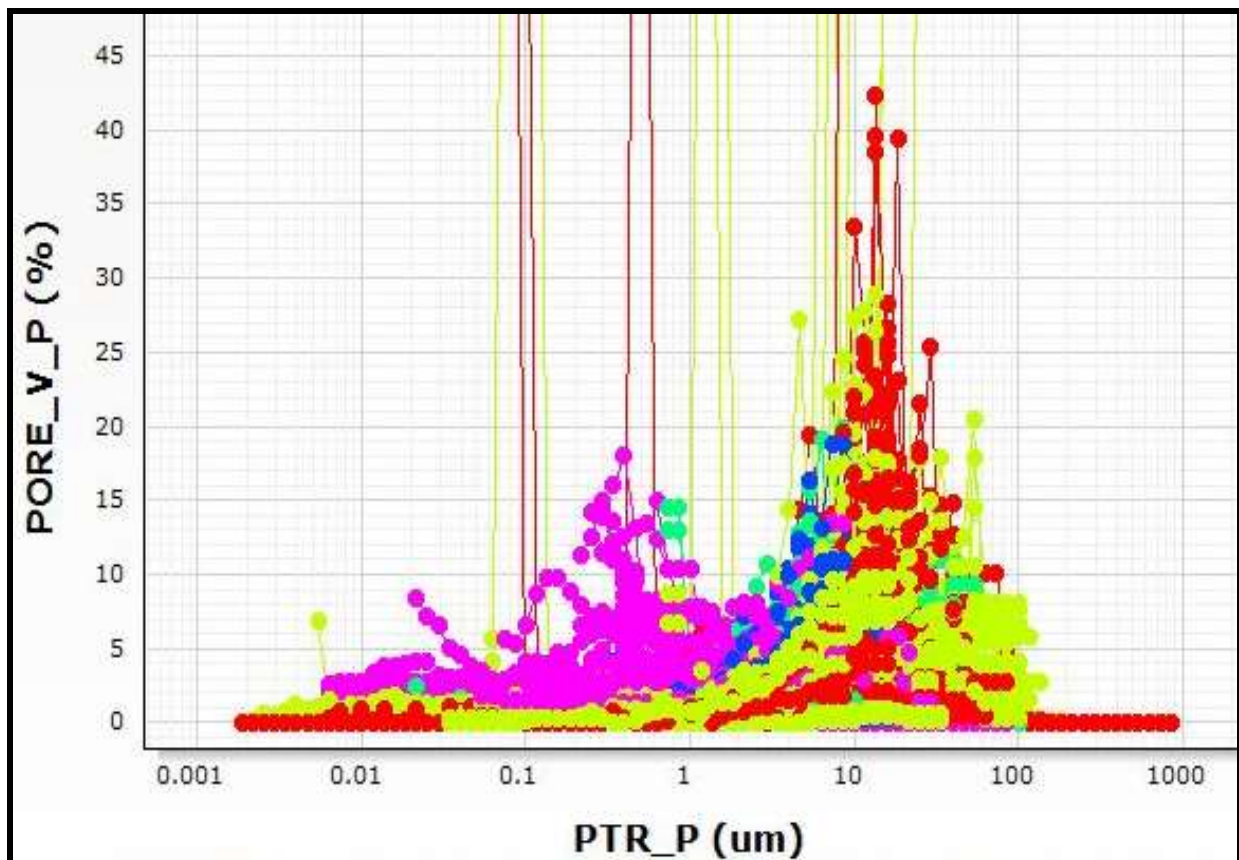


Figure 5. 2: Uncorrected pore throat size distribution demonstrating a relationship between the rock units and capillary parameters. Petrophysical and geologic rock quality increases from the purple (Heterolithic units) to the red (Fluvial Channel units)

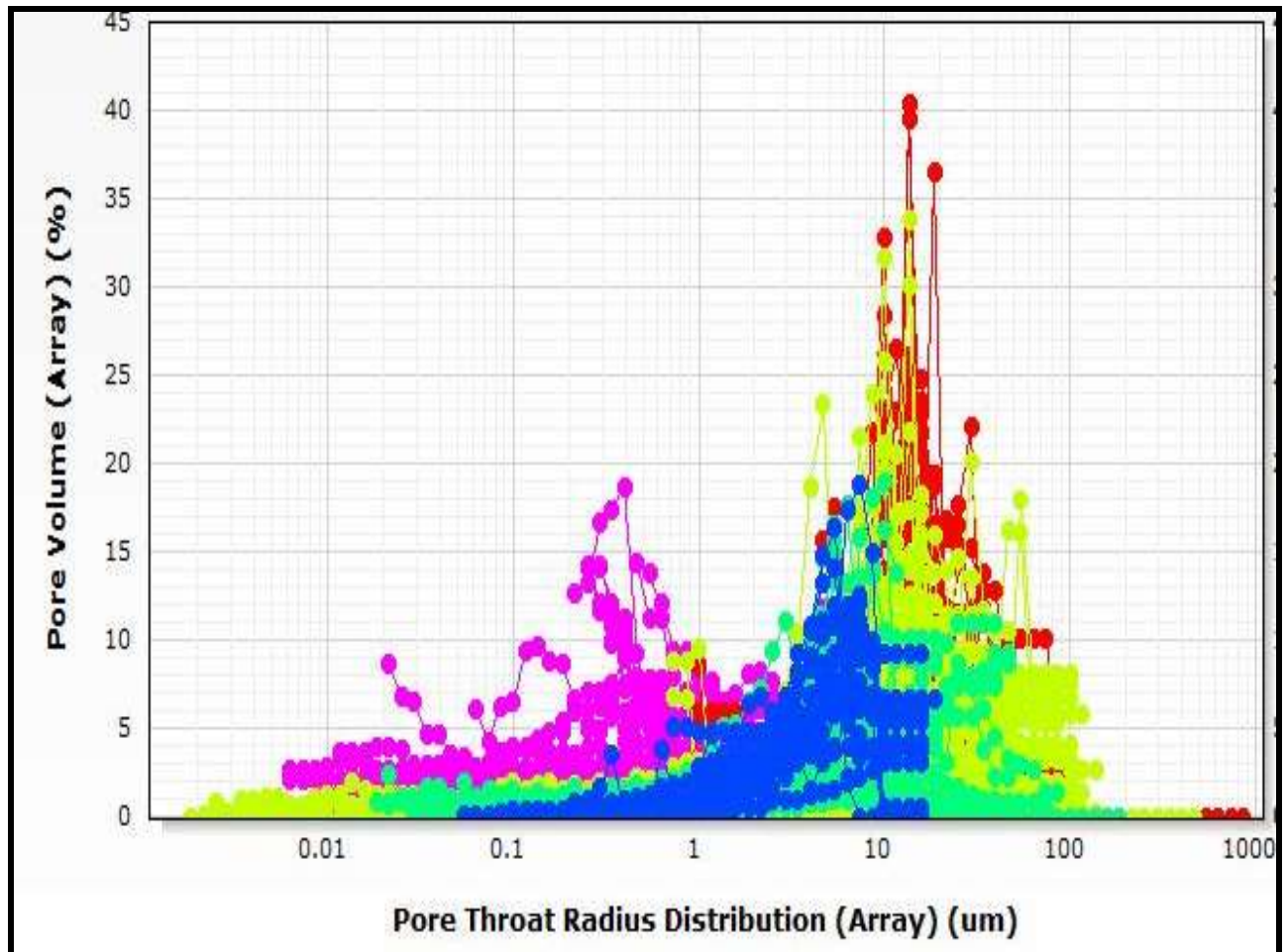


Figure 5.3: Corrected pore throat size distribution demonstrating a relationship between the rock units and capillary parameters. Petrophysical and geologic rock quality increases from the purple (Heterolithic units) to the red (Fluvial Channel units)

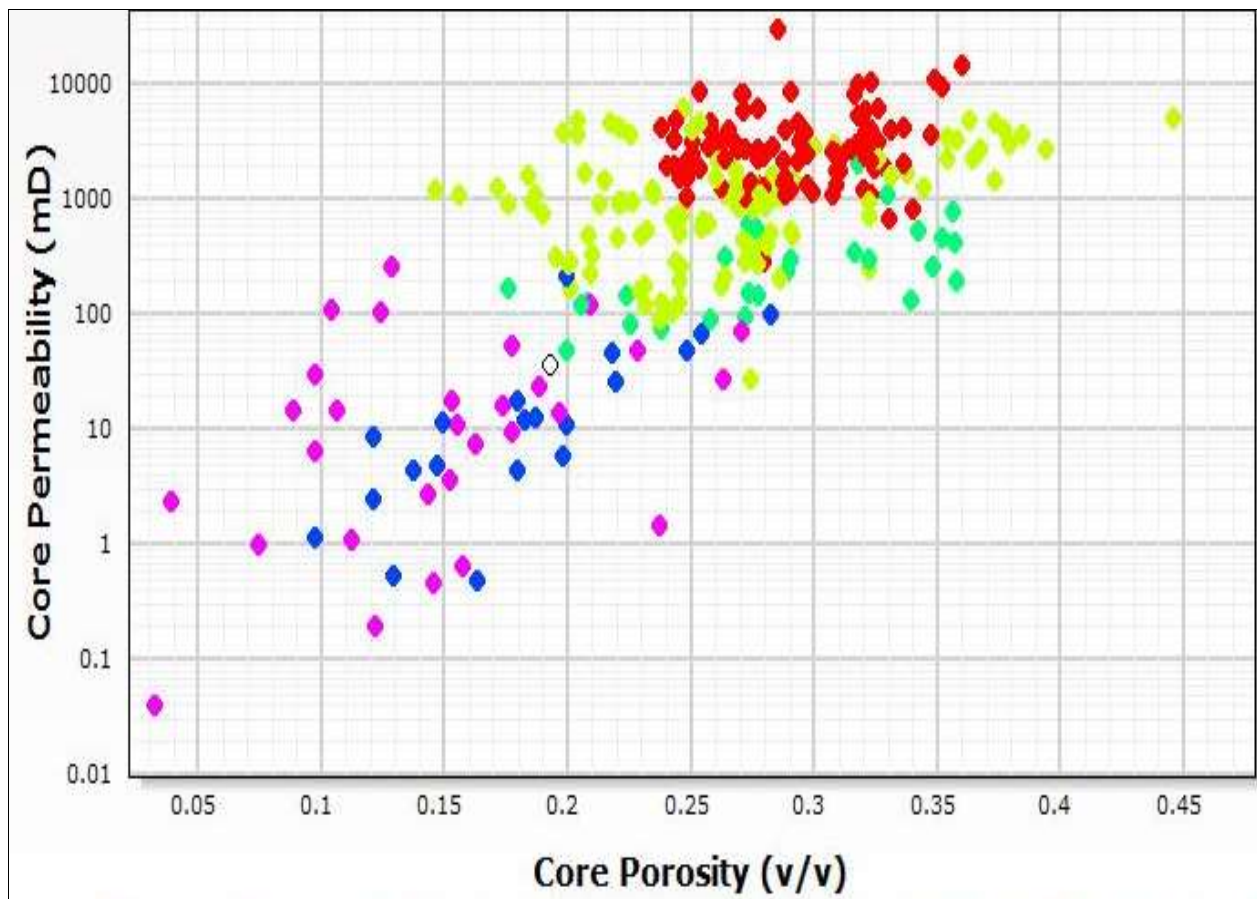


Figure 5. 4: Core permeability versus porosity for the different genetic reservoir units demonstrating a relationship between the various rock units and petrophysical attributes. Reservoir quality increases from the purple (Heterolithic units) to the red (Fluvial Channel units)

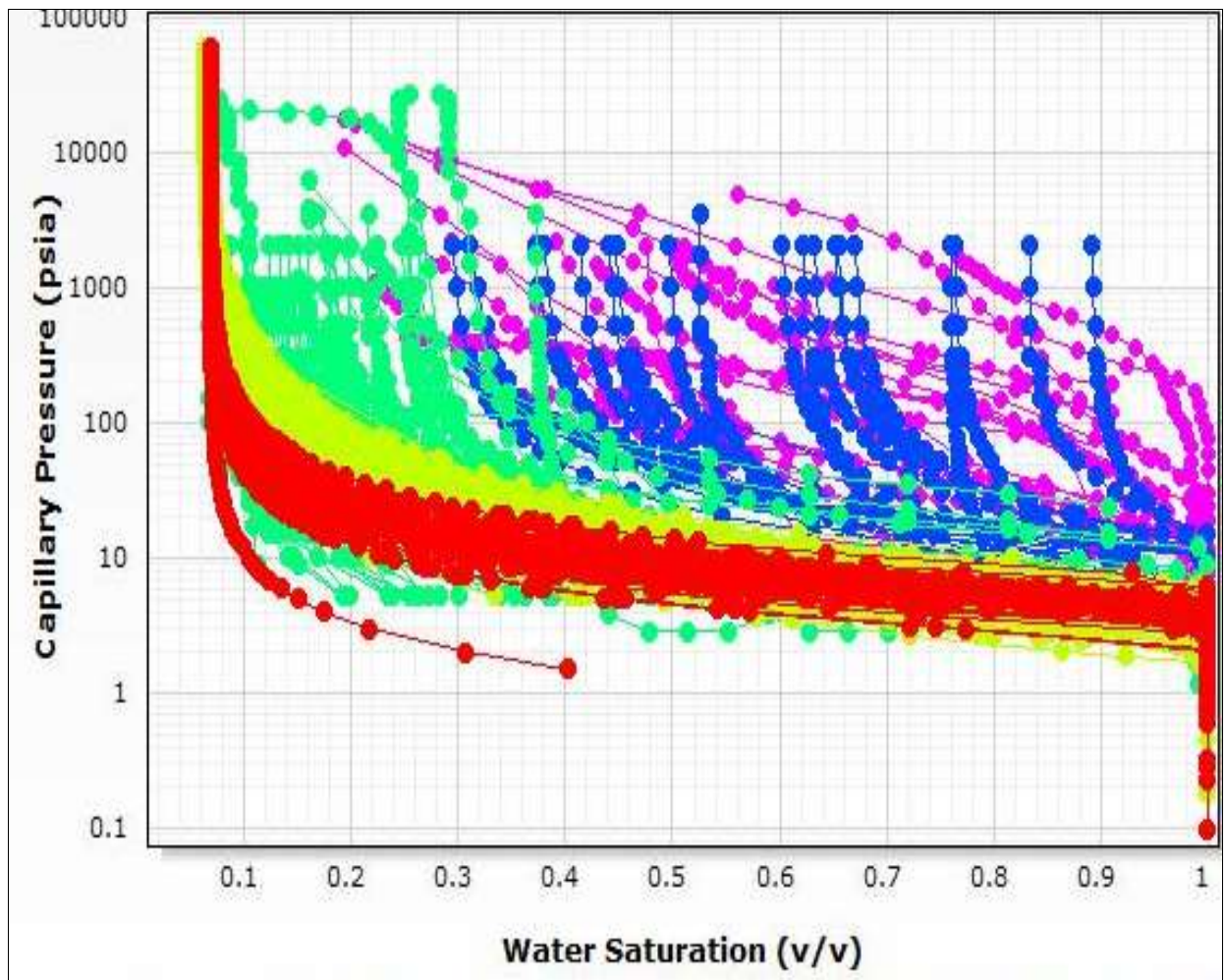


Figure 5.5: Corrected capillary pressure curves demonstrating a relationship between the various rock units and capillary parameters. Petrophysical and geologic rock quality increases from the purple (Heterolithic units) to the red (Fluvial Channel units)

I reviewed approximately 320 MICP datasets but used only 289 in this work. The data not used in this study were set aside for a variety of reasons, including, erroneous capillary behavior such as poor calibration and poor characters. Note that only mercury-air (MICP) capillary pressure data was used and – so, air-oil, air-brine and oil-water data were all converted to MICP datasets. In addition, I also ensured the 289 datasets were corrected for closure, stress and clay bound water effect. About 9% of the total dataset were affected by closure error which was probably due to true closure effect. This reflects the surface roughness of the plug sample used for the analysis.

If the largest pore throats are smaller in size than the voids created by surface irregularities, the voids will be filled with mercury before true entry into the pore network occurs. Correcting the capillary curves for closure effects was more of an art than a science.

The varying distribution of clay and variable formation salinity within the shaly sandstone and turbidite sands as depicted from XRD and petrographic analysis, calls for a careful analysis for the effect of clay bound water (CBW) and its subsequent effect on the effective pore throat radius. Figure 5.6 shows a decrease in the non-expansive clay group from 70% at 6,890ftah to 17% at 12,170 ft MD and a corresponding increase in the expansive group from 21 - 83% along the same depth interval.

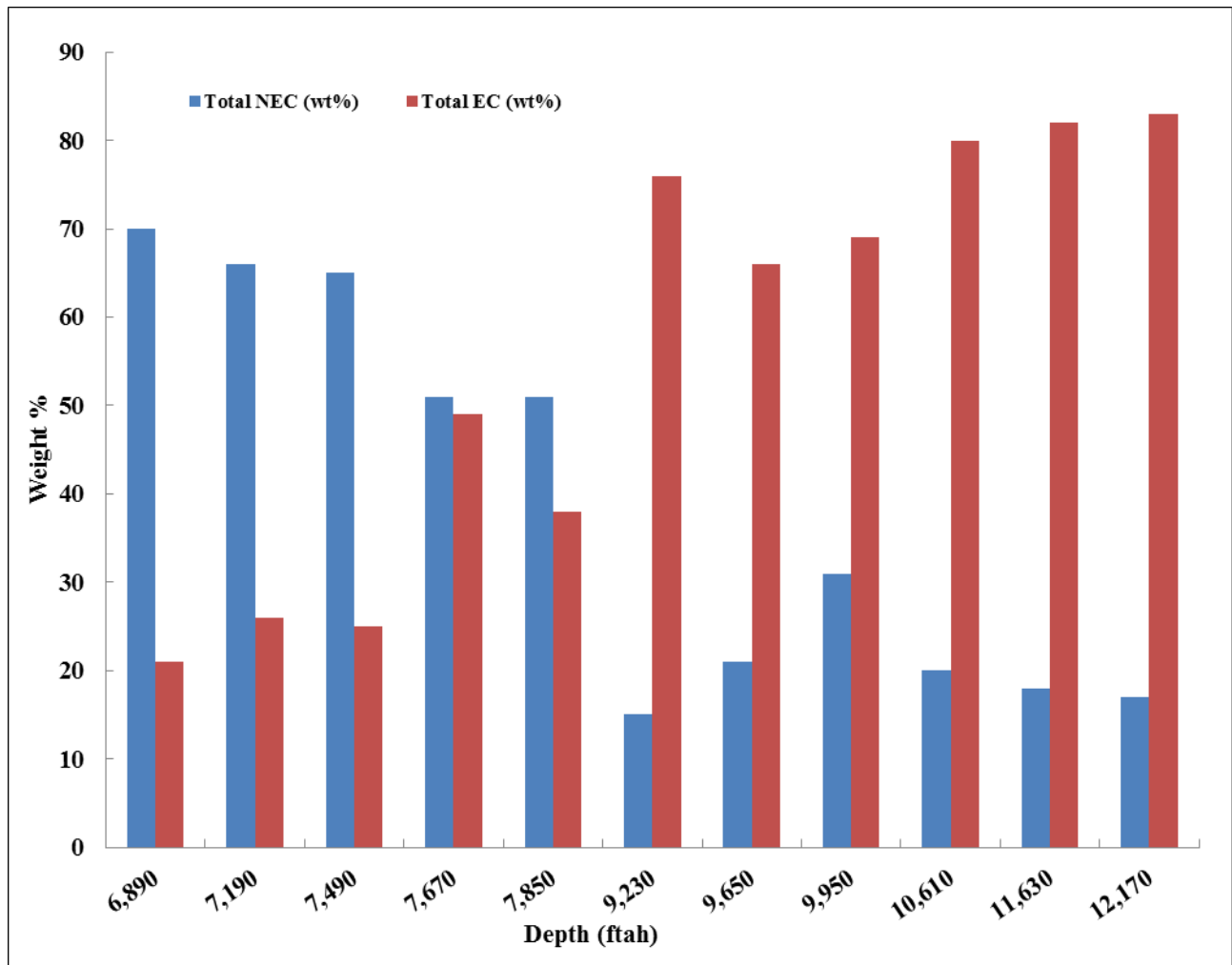


Figure 5.6: Regional distribution of Expansive Clay (EC) and Non Expansive Clay (NEC) minerals in the Niger Delta (obtained from table 1.1); indicating the strong dominance of expansive clay group with depth

At 9,950 ftah, the kaolinite group disappears while the sepiolite-palygorskite and illite/illite-smectite montmorillonite group increases significantly (figure 5.7).

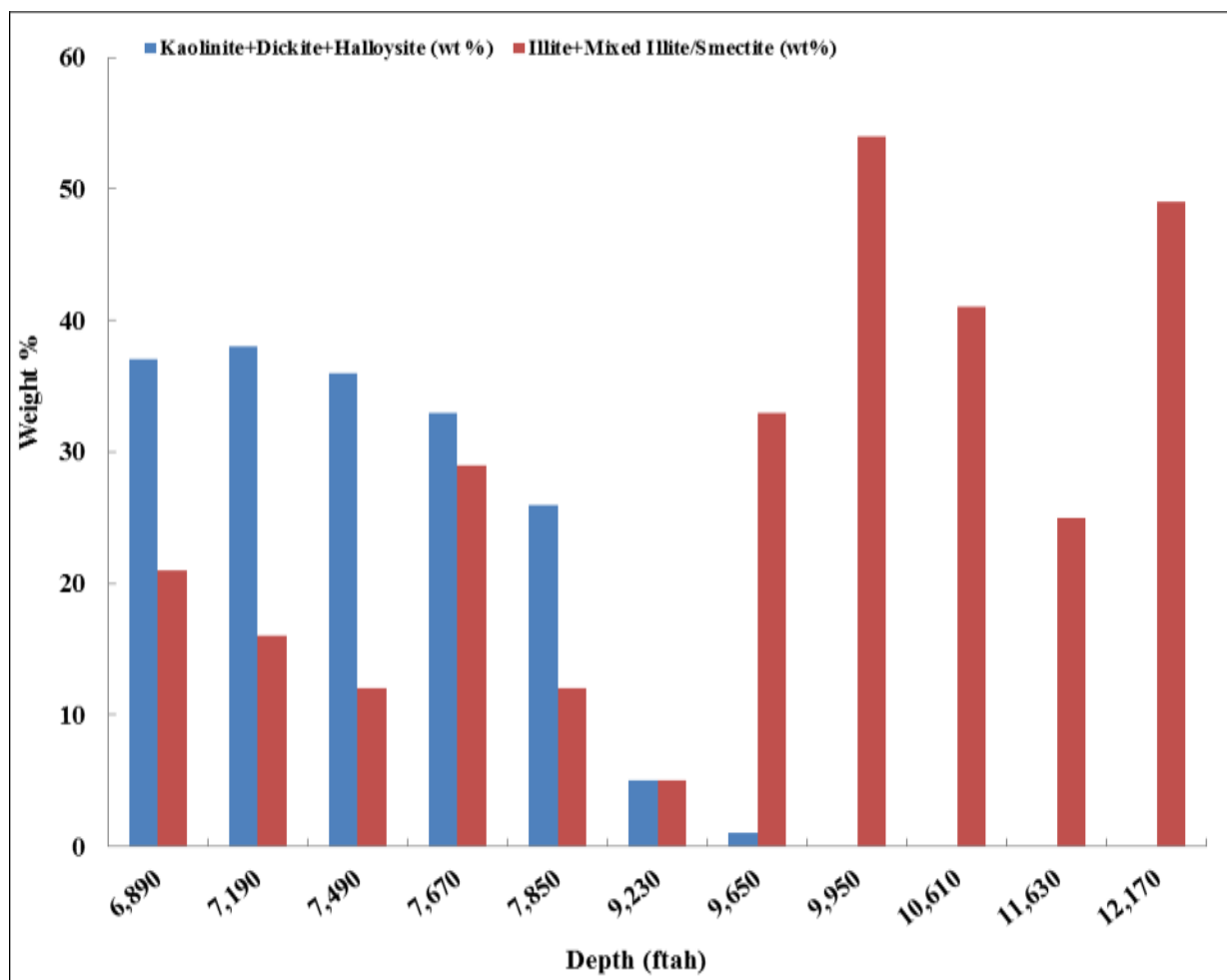


Figure 5.7: Niger Delta Regional Distribution of Kaolinite and Illite/Smectite Clay Minerals, indicating increasing dominance of the expansive illite and mixed illite/smectite group as a function of depth (obtained from table 1.1)

CBW correction as described by Hill, Shirley and Klein (1979), was not applicable due to variation of expansive clay minerals indicative of non-uniform distribution of CBW within the pore spaces.

Since mercury as the wetting fluid does not interact with the clay within the plug samples, the derived MICP curves does not account for CBW effect and hence yields too low water saturations (see figures 5.8 and 5.9). Air/brine capillary curves do incorporate the effect of CBW, when the right brine salinity is employed.

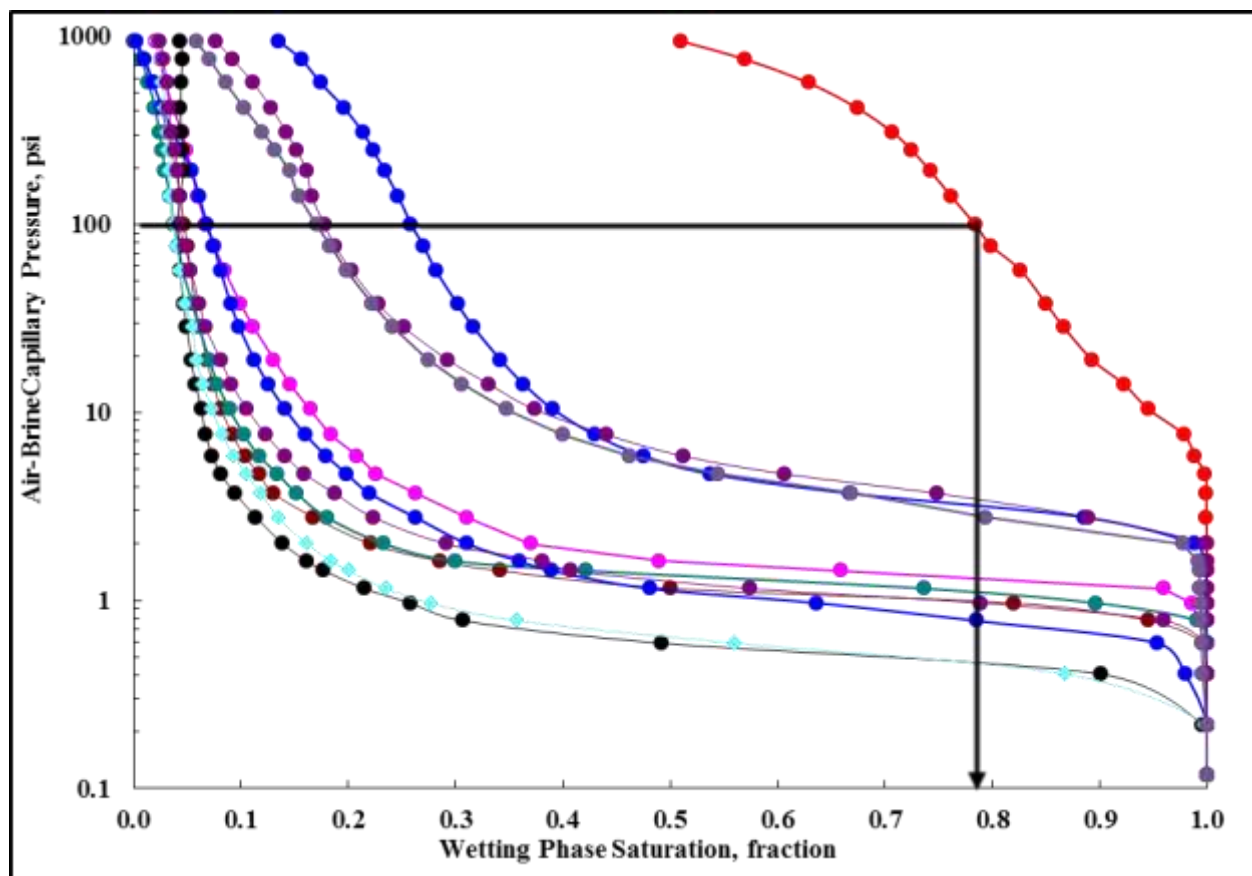


Figure 5.8: Air/Brine Capillary Pressure curves for Sand 'X', obtained from Field 'Y', Deep Water – Niger Delta. This presents typical reference sample used for CBW correction

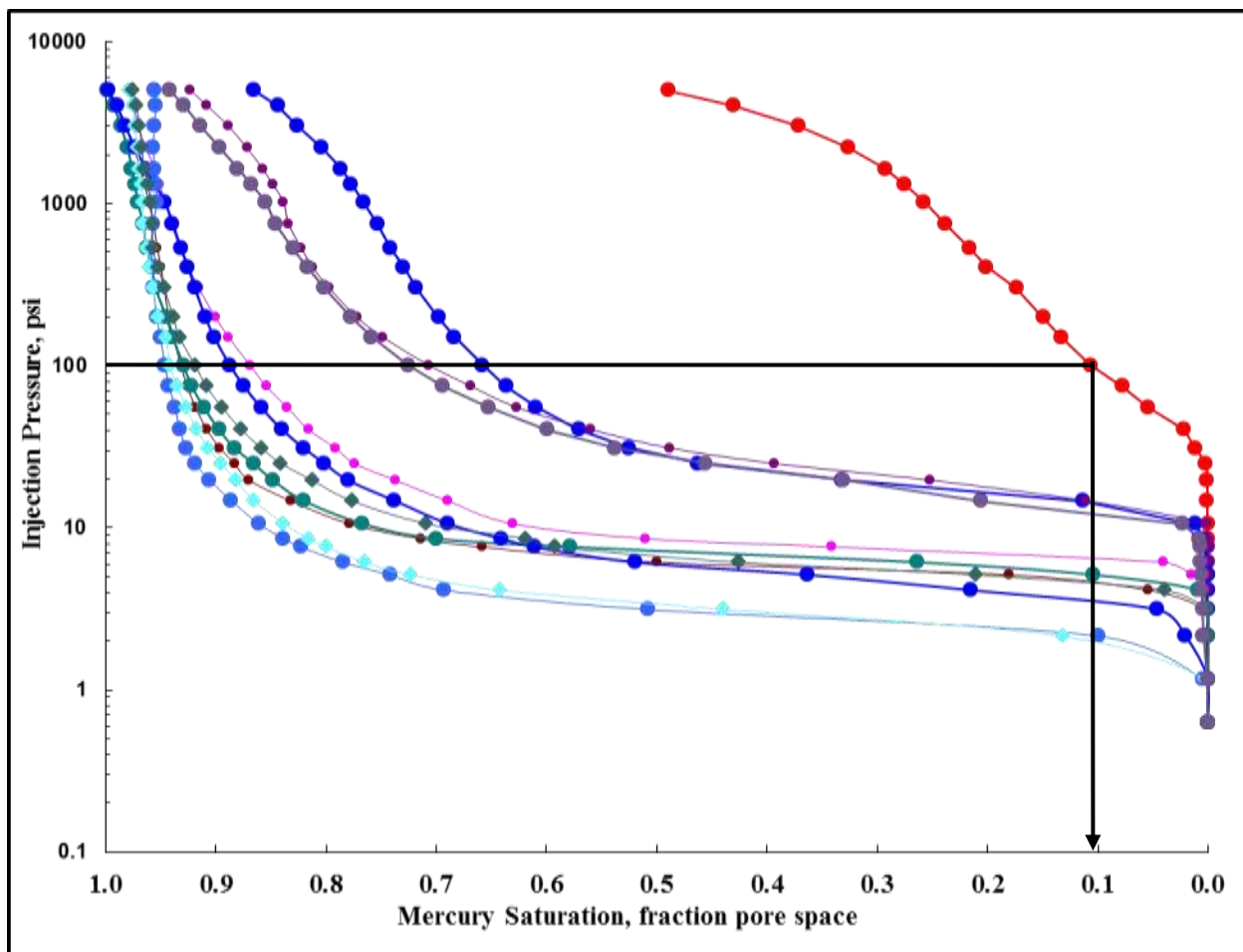


Figure 5.9: Mercury Injection Capillary Pressure curves for Sand 'X', obtained from Field 'Y', Deep Water – Niger Delta. Capillary curves were corrected for CBW effects using the air/brine data (figure 5.8)

In this study, two approaches to account for the effect of CBW was employed- direct and indirect. The direct approach was achieved by comparing air/brine and MICP curves for each dataset in the respective unit; and indirectly by reconciling the MICP curve derived saturations with log-derived saturations. For the direct approach, the difference in saturation between the two curves at a specific pressure is considered a measure for the amount of CBW. Figure 5.7 and 5.8 illustrates this concept.

At a reference pressure of 100 psi, sample 1 (red color) indicate an air/brine wetting phase saturation of 21% (figure 5.8), while MICP yielded 10.1% (figure 5.9). A difference of 10.9% at 100 psi gives a measure for the amount of CBW.

Hence, the particular point on the MICP curve was corrected to both a higher pressure and higher wetting phase saturation (figure 5.10).

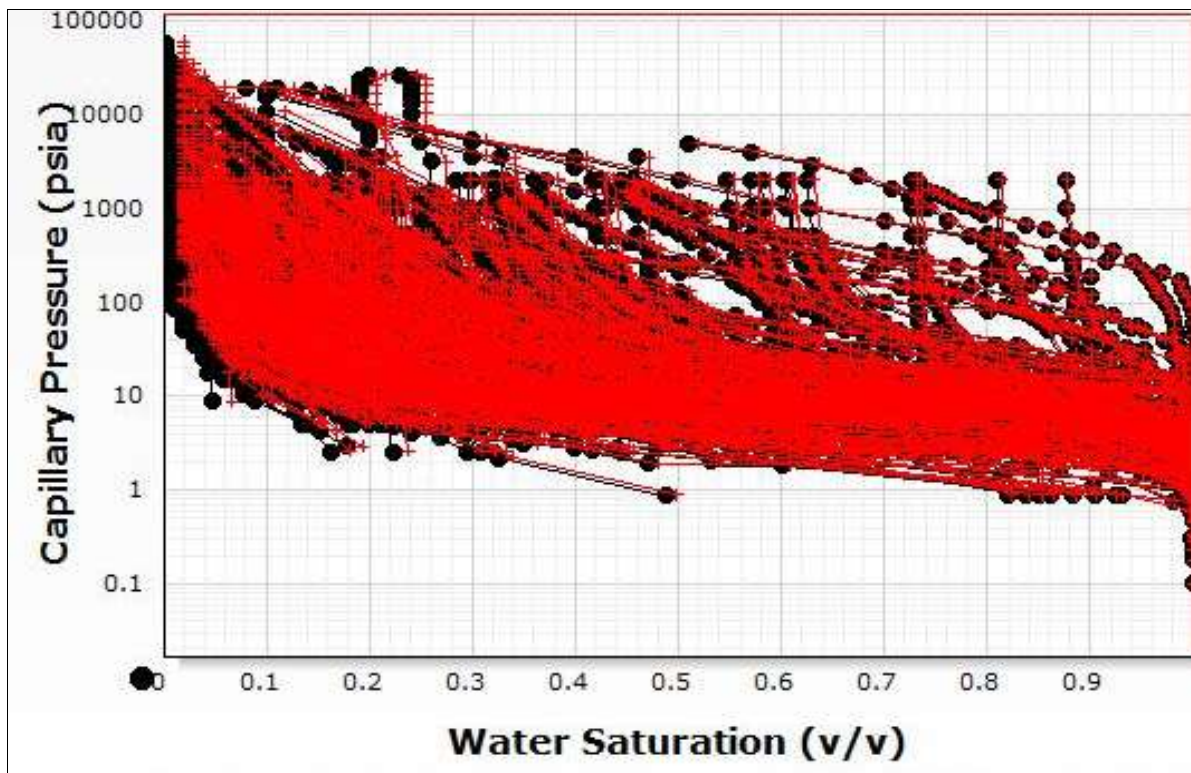


Figure 5.10: Capillary pressure curves exhibiting the effect of CBW correction on MICP dataset. Reduction in wetting phase saturation (red curves) indicate the effect of CBW since mercury as the wetting fluid does not interact with the clay within the plug samples

This was applied to all dataset used for the study. The indirect approach was employed to dataset lacking corresponding air/brine capillary pressures at same depth. The procedure requires porosity, water saturation, true vertical depth subsea (TVDSS) to correct for hole deviation, and depth to free water level (FWL). The core and log derived saturation were depth matched covering the formation of interest. The data was sorted into various porosity classes and data for each class was plotted separately on a depth versus saturation plot. Data points were curve fitted using the lambda function in each class to obtain a synthetic capillary curve.

The effect of insitu-stress was accounted for using the empirical pseudo-stress correction technique proposed by Juhasz (1979). This is demonstrated in figure 5.10.

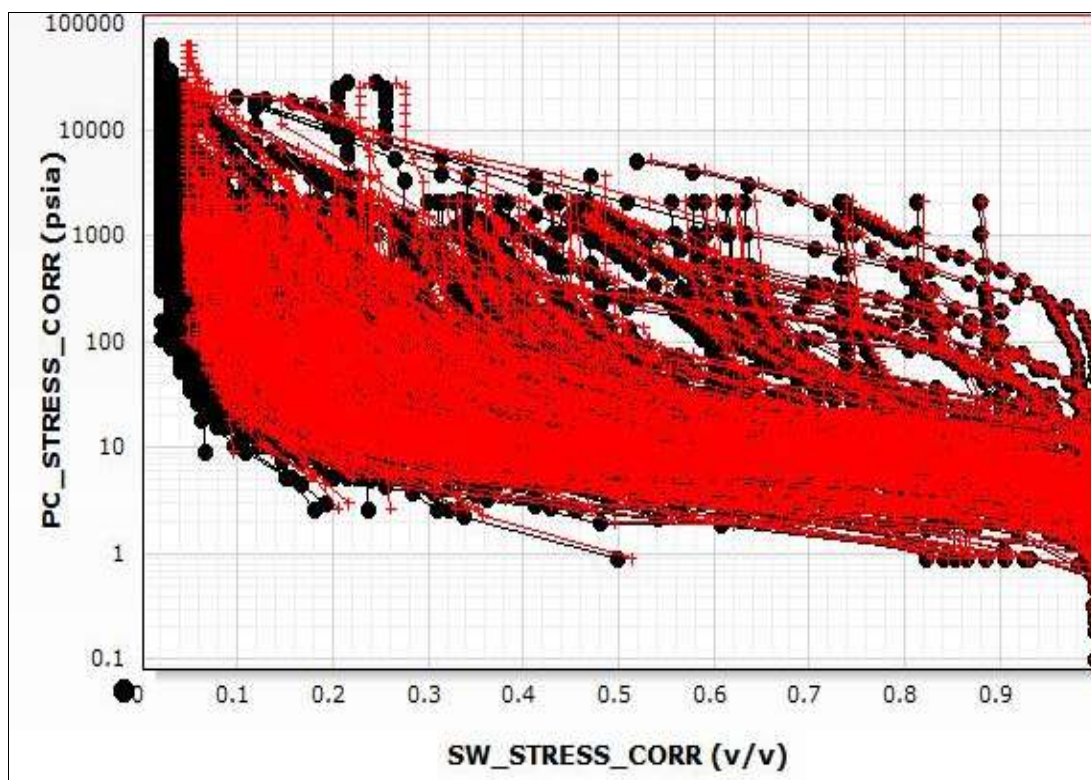


Figure 5.11: Capillary pressure curves exhibiting the effect of insitu stress correction on MICP dataset. Reduction in wetting phase saturation (red curves) indicate the effect of relieved insitu stress at reservoir conditions.

For each MICP sample, complementary datasets comprising core photos, petrographic description, routine core analysis (stress corrected porosity, air permeability and grain density) were available. I ensured that the permeability and porosity were measured on the same core sample used for capillary curve measurements. Thus, the analysis conducted was to check if the genetic units possess predictably distinct properties characterizing reservoir quality indicators as depicted by figures 5.2, 5.3, 5.4, and 5.5.

In addition, 40 MICP datasets from three (3) distinct Fields within the Niger-Delta Province not included in the model building phase was secluded for purposes of validating the model.

5.2 Genetic Reservoir Units Definition: Sedimentologic Characterization and Rock Type Definition

Detailed genetic reservoir unit (lithofacies associations) characterization of the total dataset (adopted from Shell Petroleum Development Company (SPDC)-geologic integration team documentation, 2009), was achievable by carefully observing the various lithofacies description specified in the routine geological core description and analysis (figures 1.1 & 1.2), petrographic analysis (figures 1.6, 1.7 and 1.8), XRD analysis (table 1.1) and electrofacies – reservoir quality imprints (figure 5.12) analysis with strict adherence to petrophysical log responses for the various depobelts.

Ultimately, Rock Type definition employed for this study is an iterative process, taking into account geological and petrophysical considerations and at the same time views the wider reservoir engineering considerations of what matters most for fluid flow and recovery. In my analysis, I always compare MICP data points with the geological data available from core description and petrographic analysis and with routine porosity and permeability data. In this way I aim to understand the spatial organization of rock property variability across a range of scales. This resulted in a detailed sedimentologic characterization of the various genetic units applicable to the study.

Figures 5.2 – 5.5 shows typical plots used for petrophysical characterization. It's observed that multiple samples from same genetic unit exhibit some commonality. The red and green color codes indicative of Fluvial Channels with mean porosity - 20.5%, mean permeability – 4,526 mD; and Tidal Channels having a mean porosity - 19.7 %, and mean permeability – 1,014 mD). The blue and purple color codes-Lower shoreface Sands on the figure depicts wide range in reservoir qualities with core porosities from 10-35% and core permeabilities from 0.1-3,000 mD. The large range in values reflects the inter-bedding of silty shales (non-reservoir), thin rippled sands (poor quality reservoir 10-100's mD) and decimeter thick sheet sands (good quality of 100's-1000's mD).

5.3 Pore Throat Size Histogram Analysis

The capillary curve reflects the distribution of pore throat radii and their associated pore volumes. Knowledge of this size distribution in a reservoir is essential for understanding the saturation and permeability profiles. Histogram analysis provides a more statistically robust analysis for a group of samples of same genetic reservoir unit.

Equation [3.2] expresses a relationship between capillary pressure and pore system via a pore throat size radius and capillary pressure (Laplace-Washburn, 1992):

$$\text{Pore throat radius } (\mu m), R_p = \frac{2\sigma \cos\theta}{P_c} = \frac{107.6}{P_c}$$

The relationship basically provides the order of magnitude of the pore throat size distribution. The correlation is basically an approximation developed from straight capillary tube bundle model, and in essence only gives an insight to pore throat sizes. Direct application may result to under-estimating both the large and small pore throat sizes (Romson 1992).

Therefore, to capture the distribution of pore throat sizes and associated pore volumes, I determined the average pore throat radius for each of the genetic units using the equation. Figure 5.12 illustrates the distribution for the channel heterolithic unit.

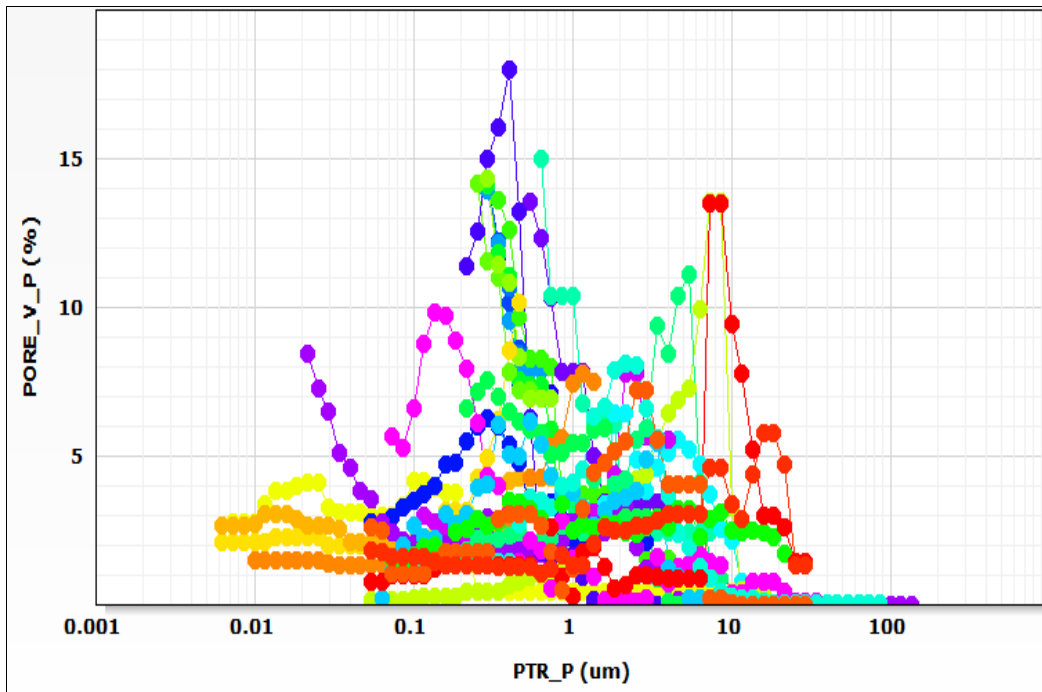


Figure 5.13: Pore throat size distribution for individual sample within the Channel Heterolithics unit. This demonstrates a heterogeneous unit with dominant micropores

Cumulative histogram analysis was then performed on each unit and the total dataset to examine their modality. Histogram analysis provides a more statistically robust analysis for a group of samples of the same genetic reservoir unit. The analysis as portrayed in figures 5.14, for the channel heterolithic unit, indicates a bimodal system.

This gives a notion of the curve fitting process for each genetic unit. Simple pore system with unimodal distribution will be fitted with a single function. Genetic units with two (2) modes (bimodal system, figure 5.13) will require two (2) sets of equation to fit the data.

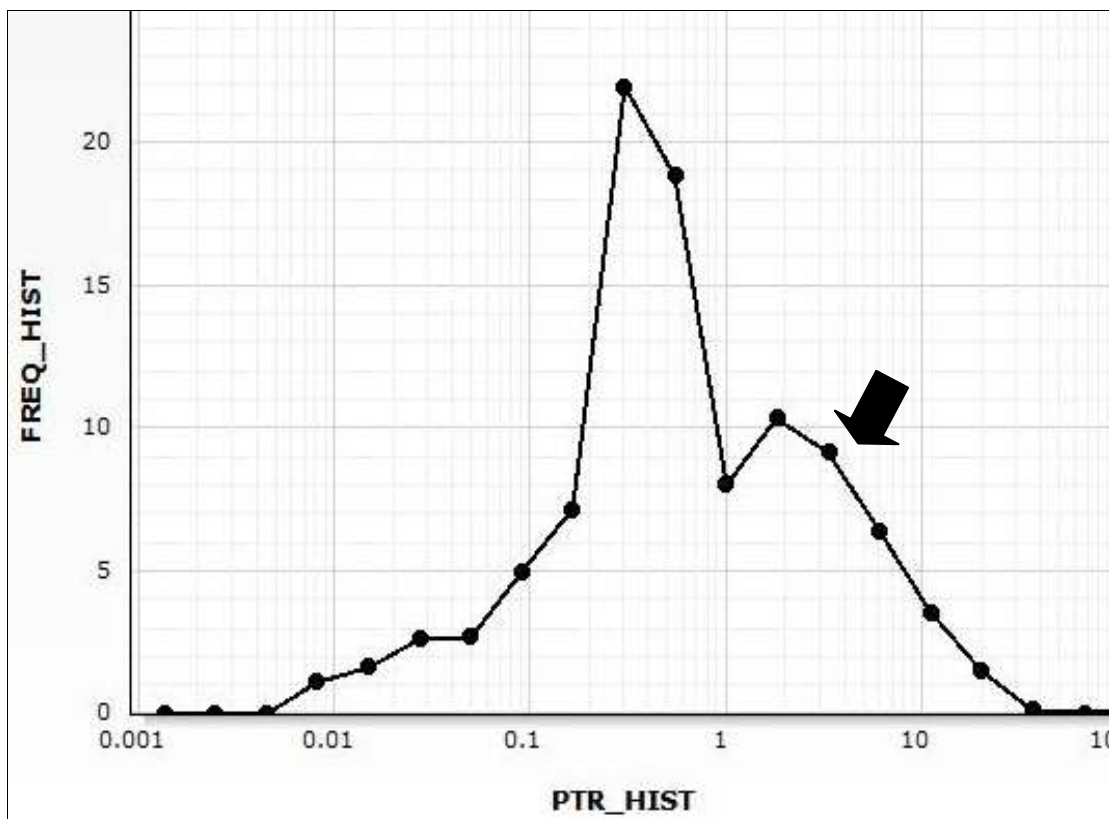


Figure 5.14: Plot of cumulative pore throat distribution for Channel Heterolithics rock unit demonstrating a bimodal distribution and dominant micropores population

5.4 Pressure Range Setting and Curve Fitting

Amongst the various mathematical treatments purporting to describe capillary pressure datasets in terms of porosity, permeability and other rock parameters; the Lambda and Brooks-Corey functions with three fitting parameters: irreducible water saturation (S_{wirr}), entry capillary pressure (P_{ce}) and pore size distribution index (λ, N), tends to honor the data more. Comparison of the least squares coefficient of determination ' R^2 ' is used as a basis for determining the curve fit.

For each capillary pressure curve, a best fit is calculated as a function of water saturation. The difference between the smoothed curve and the real data was examined so that uncertainties can be assigned to derived capillary pressures.

The ensemble of the three fitting parameters is plotted versus the petrophysical rock quality indicators: ϕ , k , $\sqrt{\frac{k}{\phi}}$, respectively. This implies establishing a relationship between the function parameters which defines capillary pressures and the petrophysical properties as quality controlled using matrix plot. Several regression analyses are made in order to fit these fitting parameters to the core petrophysical properties. The different regressions include: linear, logarithmic, power, exponential and average regressions.

The Lambda (λ) can be represented in the following form:

$$S_{wet} = a.P_c^{-\lambda} + b \quad [5.1]$$

where a , b and λ are all regression constants.

Although this formula does not apparently contain a porosity-dependent variable, λ can usually be correlated with porosity.

The Brook's Corey drainage capillary pressure model is:

$$S_{wet} = S_{wirr} + (1 - S_{wirr}) \left\{ \frac{P_e}{P_c} \right\}^{\frac{1}{N}} \quad [5.2]$$

S_{wet} = wetting phase saturation, S_{wirr} = irreducible water saturation,

P_e = entry pressure = pressure on the straight line at $S_{wet} = 1$, and

$\{N \text{ and } \lambda\}$ = Pore size distribution index, which controls P_c versus S_{wet} steepness, obtained from slope of the line.

For each function parameter, the regression with the highest correlation coefficient (R^2) is shown. Fixing the fitting parameters to a specific regression, results in re-calculating the parameters, and at this step the parameters are becoming functions of the cores petrophysical properties. This step creates the capillary pressure model (CPM).

For each capillary pressure curve, a new fit is created using core porosity, permeability and recalculated values of fitting functions termed the capillary pressure model (CPM).

For a given dataset containing: porosity, permeability, capillary pressure curves and saturation for different plug samples, a multi-variate regression can be used to obtain an equation linking all the parameters.

5.5 Permeability Modelling from Capillary Pressure

For MICP analysis, a 2 microns pore throat radius definition criteria for microporosity was also applicable to the study area (see figure 5.14). The histogram of the pore throat size distribution shows positively skewed distribution with a strong peak (global maxima) at 0.3 microns pore throat radius indicative of the dominant micropore population for the channel heterolithic unit. Therefore, microporosity and macroporosity is usefully separated by using a 2 microns radius cut-off.

The porosity-permeability cross plot for the Channel Heterolithic unit (figure 5.15), shows a large spread in measured permeability covering several orders of magnitude for a given porosity value.

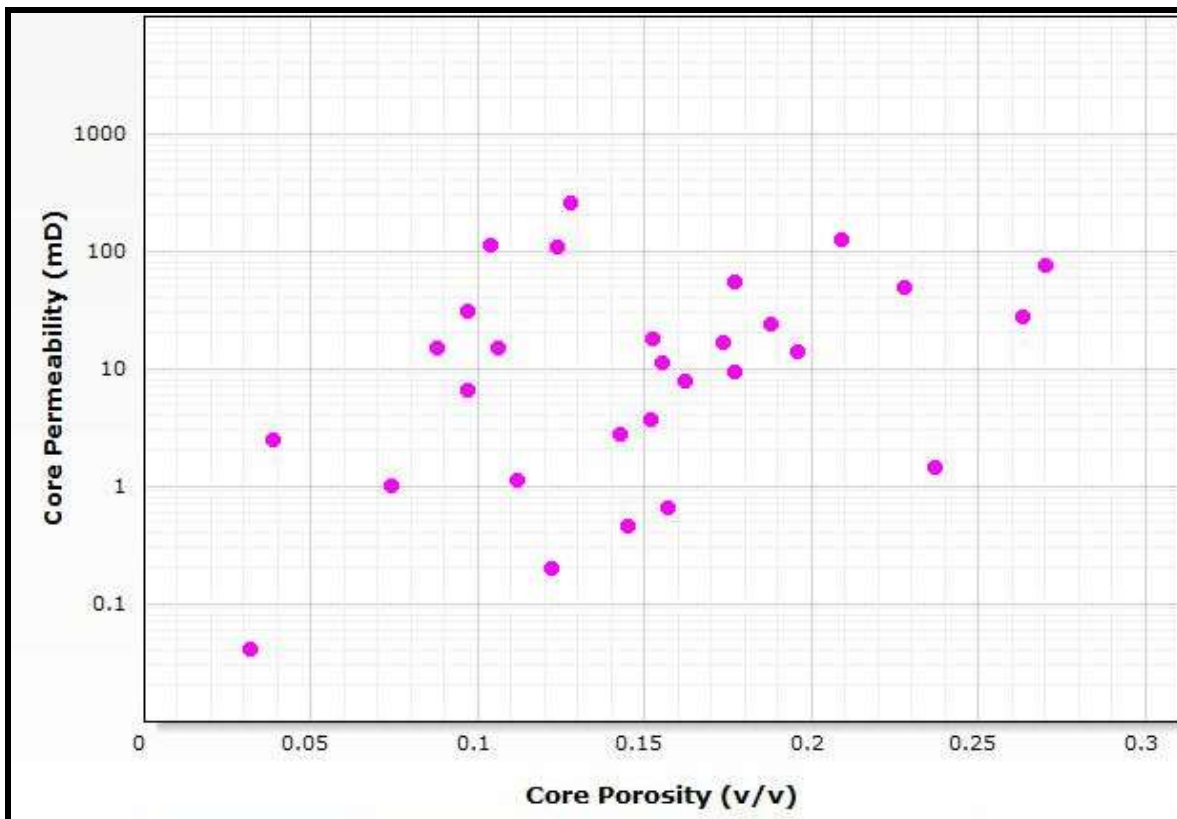


Figure 5.15: Plot of permeability versus porosity for the Channel Heterolithics rock unit demonstrating poor rock properties with average permeability of 10 mD

Uncertainty might be reduced, if only the large pores are considered in the analysis separate from the small pores for each genetic unit. A plot of corrected core permeability against macropore pore volume (partial porosity) as presented in figure 5.16 indicate a trend with a correlation coefficient (R^2) factor of 0.315 and a Root Mean Square Error (RMSE) value of 1.8911.

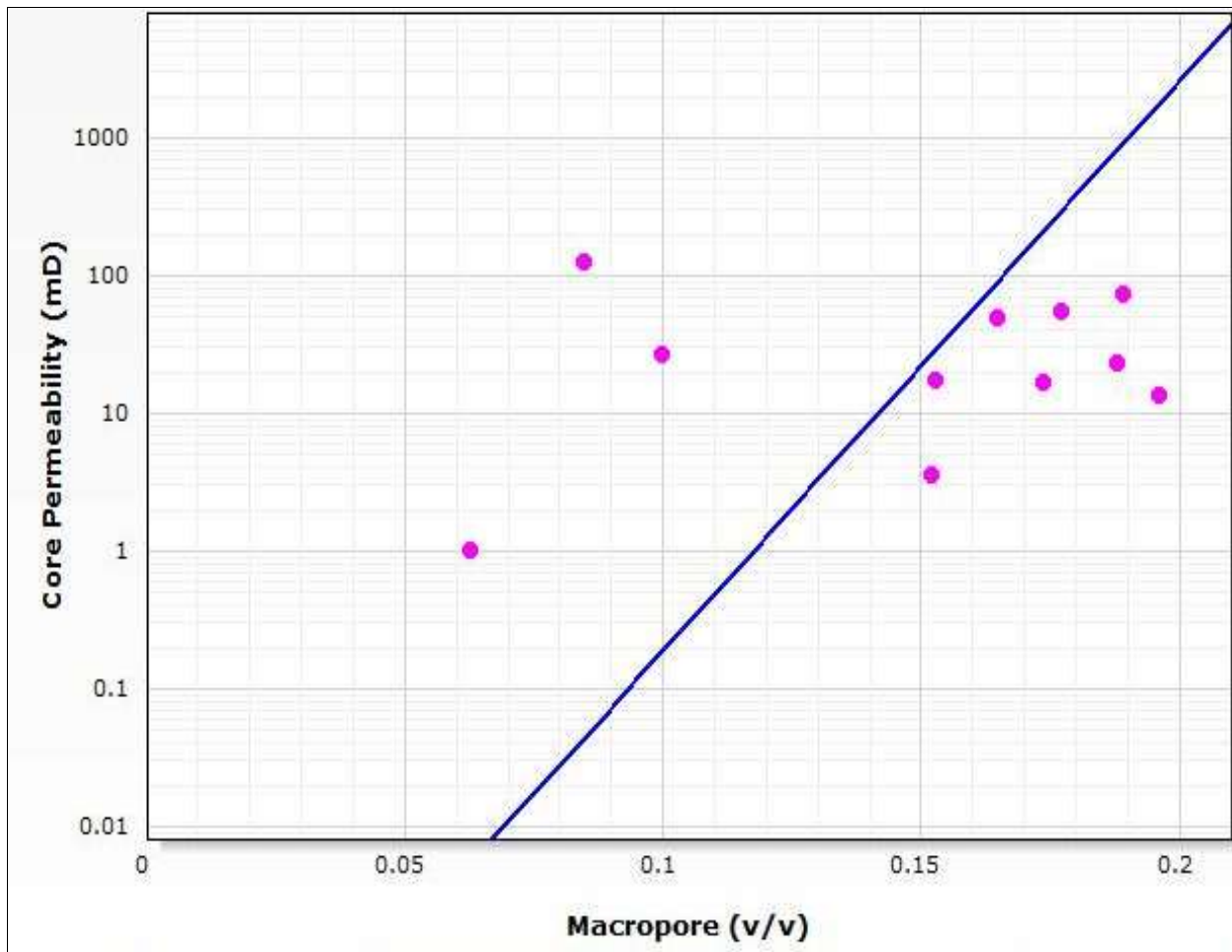


Figure 5.16: Plot of permeability versus macroporosity ($\phi_i \sum_i S_{wi}$) for Channel Heterolithic rock unit demonstrating improved correlation compared to typical porosity/permeability plots, due to influence incremental wetting phase saturation (S_{wi}) at every capillary pressure step

“It’s expected that the population of the larger pores (visible in the P_c) will have a strong effect on the measured permeability. It is expected that there exist a visible difference in the cross plot, if the permeability is not only dependent on the pore volume of macropore but also on the pore throat sizes within the macropore fraction” (Hulea *et al.*, 2011). Figure 5.17 clarifies the above argument, resulting to a better R^2 factor of 0.835 and a reduce RMSE of 0.384, for same genetic reservoir unit.

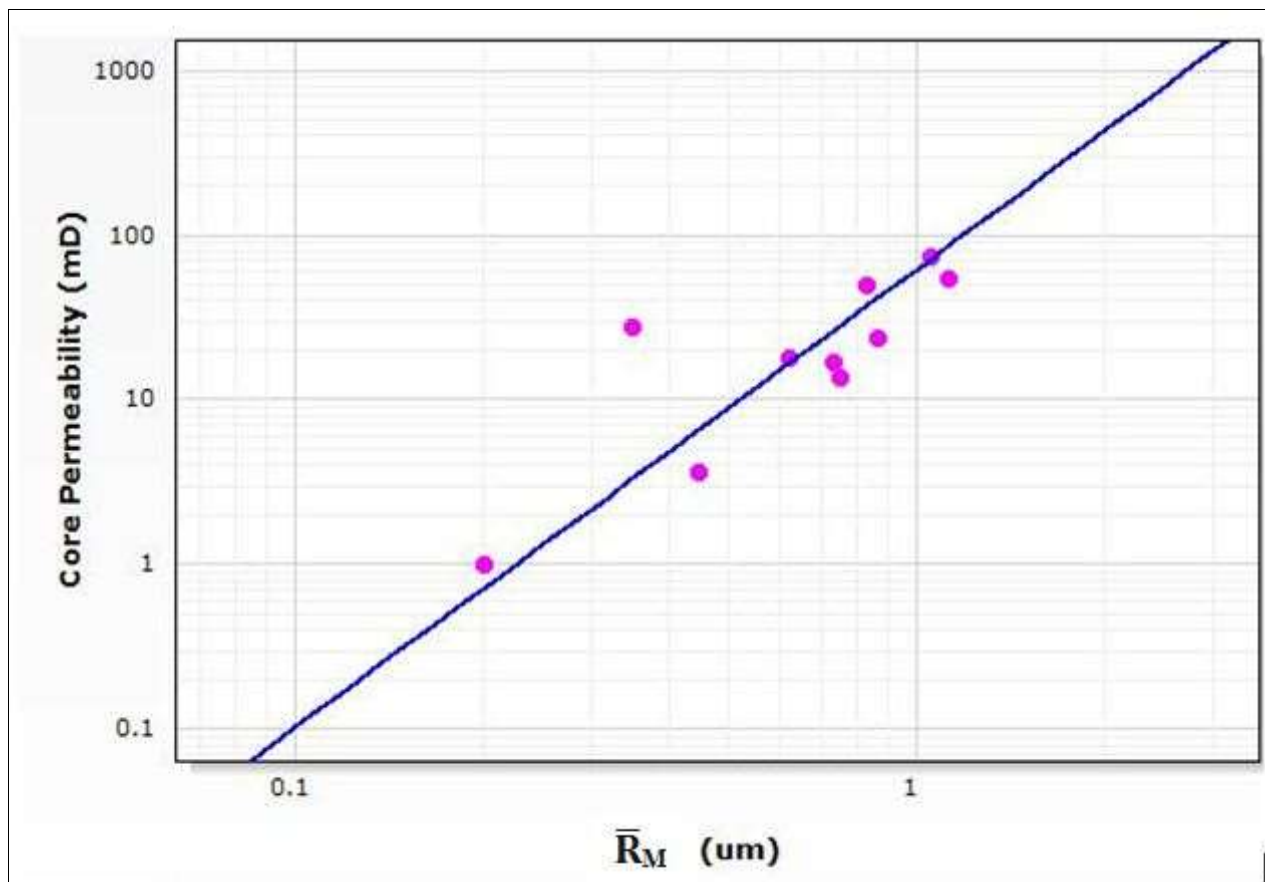


Figure 5.17: Plot of permeability versus macropore normalized pore throat radius $[\phi_i \sum_i S_{wi}(R_{pi})_{Mac}]$ for the Channel Heterolithic genetic reservoir unit, indicating higher correlation coefficient due to influence of pore throat radius (R_{pi}) at every capillary pressure step

The matrix cross-plot shows the ensemble of the three (3) parameters plotted against ϕ , k , $\sqrt{\frac{k}{\phi}}$, resulting in nine (9) cross plots (figure 5.18).

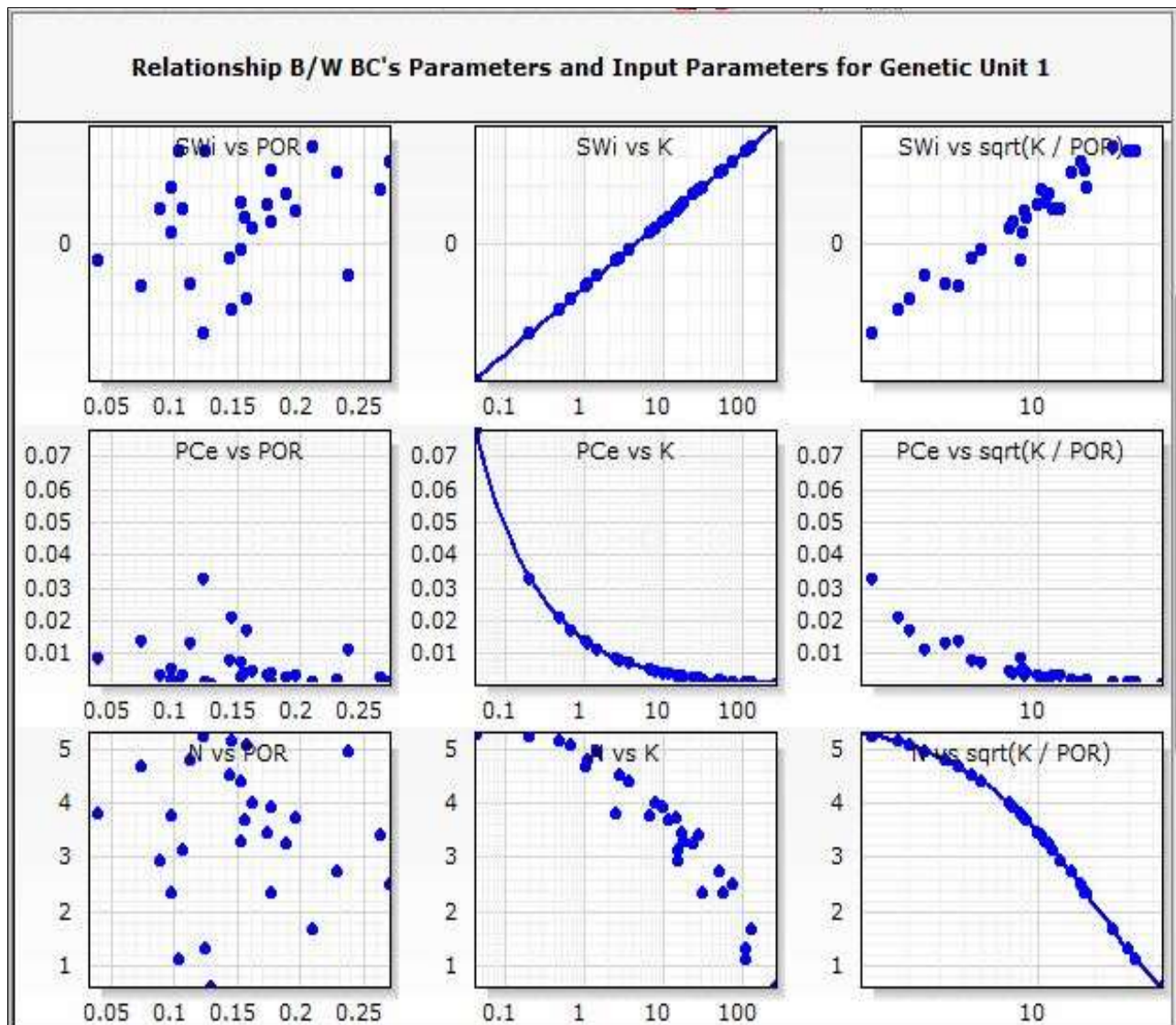


Figure 5.18: Matrix Plot of Input Parameters (ϕ and k) demonstrating relationship with capillary pressure parameters (SW_{irr} , P_e and N) for the Channel Heterolithic genetic unit

Figures 5.19, 5.20 and 5.21 using the Fluvial Channel Sands also demonstrates same scenario as elucidated above using the Channel Heterolithic reservoir unit. This is done for all genetic unit classification applicable to this study (table 5.2). The curve fitting methodology achieves appreciable match as demonstrated in figure 5.19, which invariably modifies the input parameters (core permeability and porosity).

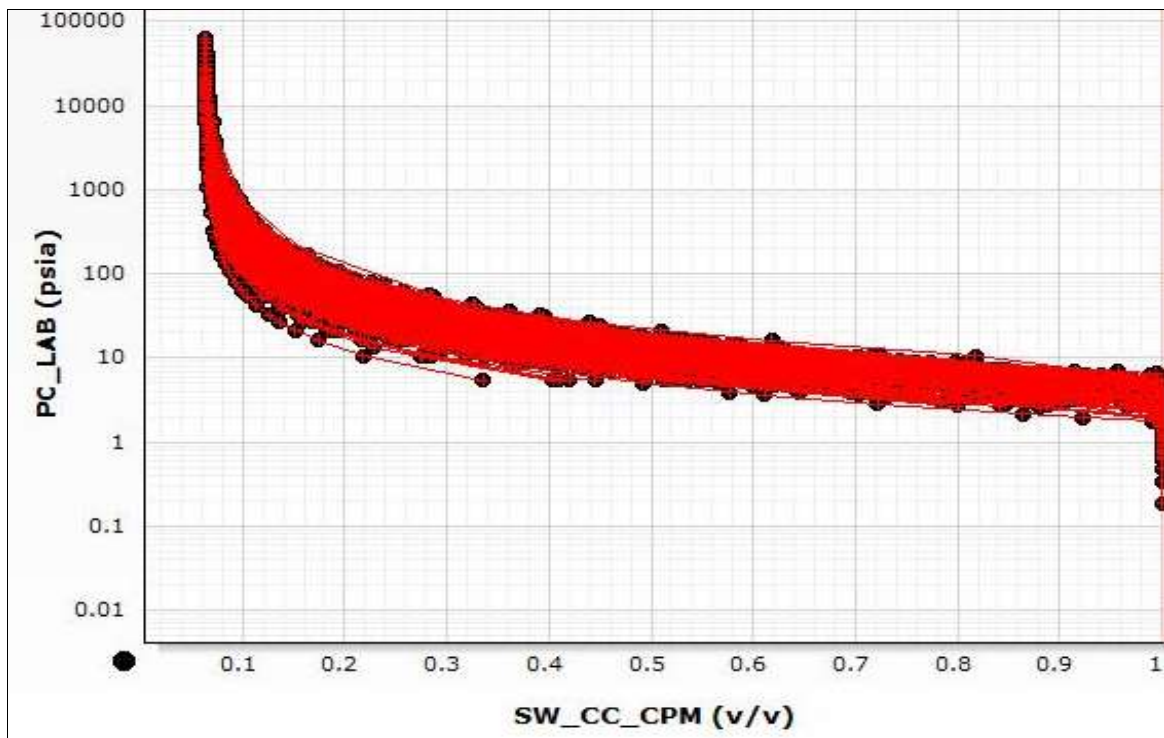
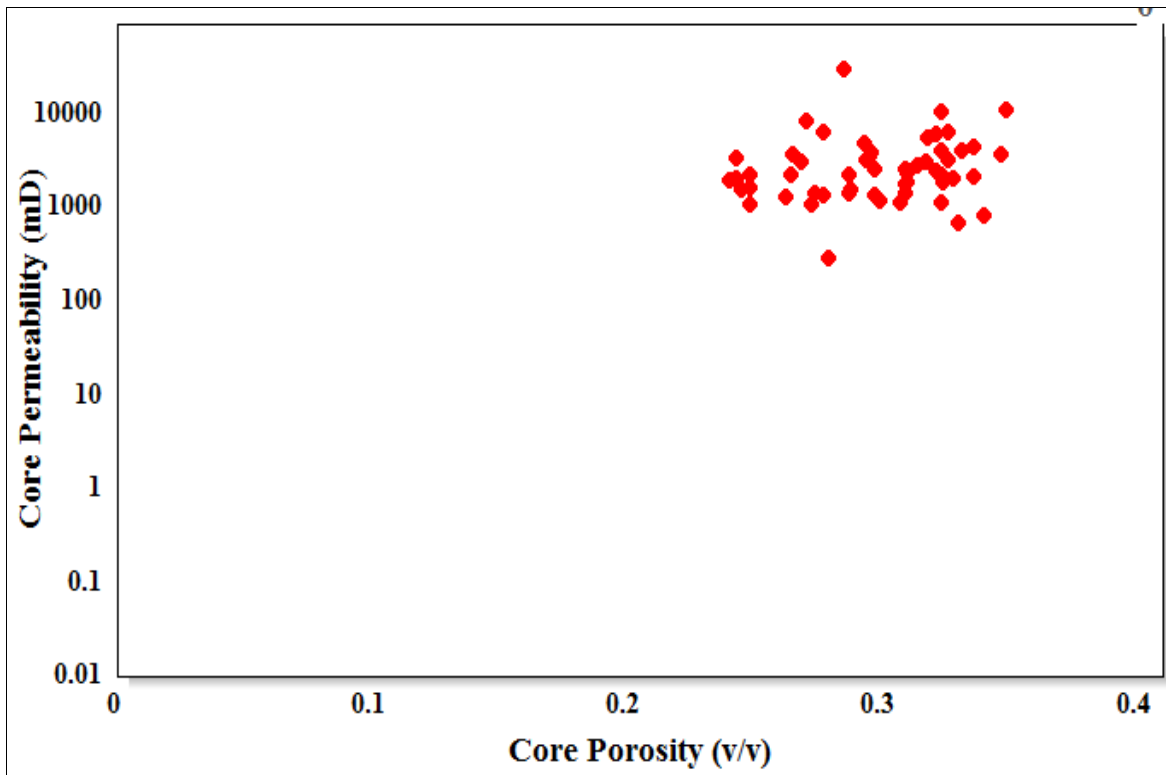


Figure 5.19: Capillary pressure versus water saturation curve fit for the Fluvial Channel sand unit indicating appreciable match between measured and calculated capillary curves



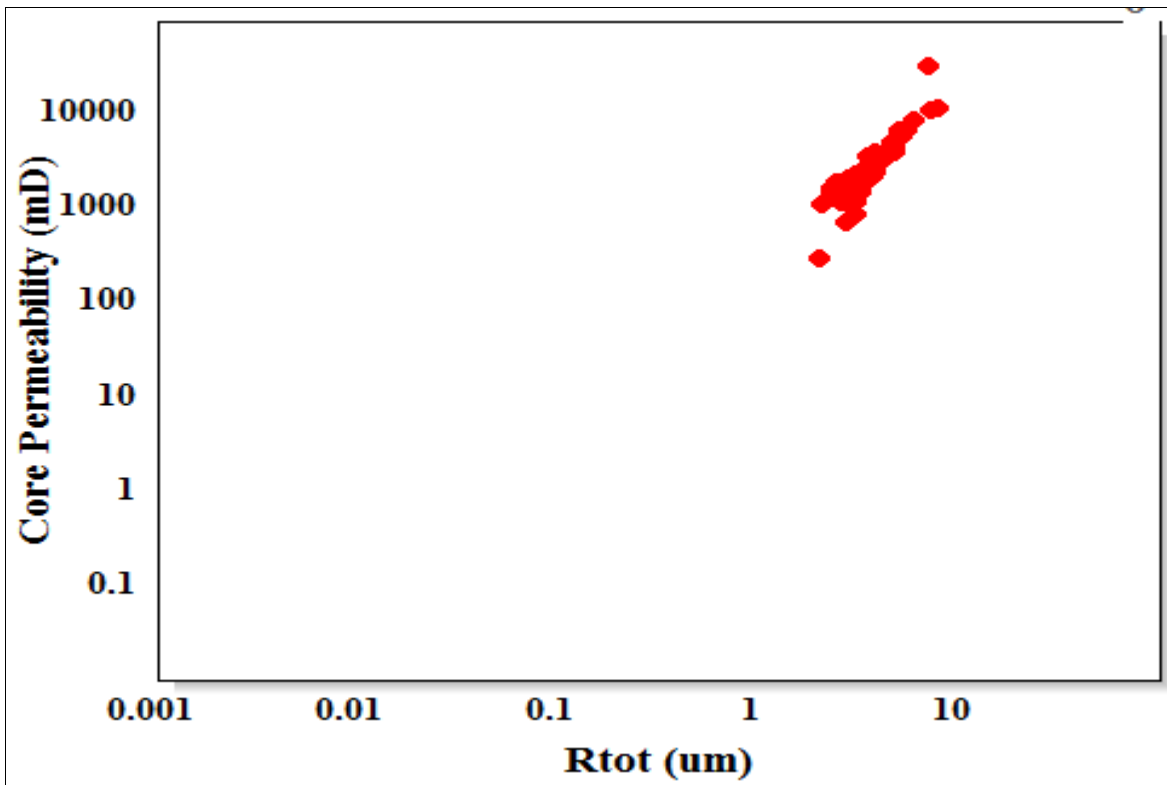


Figure 5.21: Plot of core permeability versus total normalized pore throat radius

$\left[\phi_i \sum_i S_{wi} (R_{pi})_{Mac} \right]$ for Fluvial Channel sands showing very good reservoir properties

associated with the unit. Observable improvement in correlation coefficient is attributed to influence of pore throat radius (R_{pi}) at every capillary pressure step.

Table 5.2: Relationship between Brooks Corey & Petrophysical Properties for the Genetic Units

Genetic Reservoir Unit Based Capillary Pressure Model Using Brooks Corey Function	
(unit system: Sw [v/v], Pc[bar], K [mD], POR [v/v])	
RT_1_Channel Heterolithics	$Sw = \text{MIN}(1, \text{MAX}(0, (-0.139775 + 0.224929 * \text{LOG}_{10}(K)) + (1 - (-0.139775 + 0.224929 * \text{LOG}_{10}(K))) * ((0.0138413 * \text{POWER}(K, -0.53815)) / Pc) ^ (1 / \text{POWER}(10, 0.750142 - 0.0212616 * \text{SQRT}(K / \text{POR}))))))$
RT_2_Lower Shoreface Sands	$Sw = \text{MIN}(1, \text{MAX}(0, 0.374862 + (1 - 0.374862) * (0.00147221 / Pc) ^ (1 / (22.1743 * \text{POWER}(\text{SQRT}(K / \text{POR}), -1.04828))))))$
RT_3_Upper Shoreface Sands	$Sw = \text{MIN}(1, \text{MAX}(0, 0.066 + (1 - 0.066) * ((0.0321596 * \text{POWER}(\text{SQRT}(K / \text{POR}), -0.960882)) / Pc) ^ (1 / (3.07309 + 2.52473 * \text{LOG}_{10}(\text{POR}))))))$
RT_4_Tidal Shoreface Sands	$Sw = \text{MIN}(1, \text{MAX}(0, 0.0625 + (1 - 0.0625) * ((0.00250621 - 0.000989623 * \text{LOG}_{10}(\text{SQRT}(K / \text{POR}))) / Pc) ^ (1 / (0.95132 * \text{POWER}(\text{POR}, -0.253711))))))$
RT_5_Fluvial Channel Sands	$Sw = \text{MIN}(1, \text{MAX}(0, 0.058 + (1 - 0.058) * ((0.0033641 - 0.00129079 * \text{LOG}_{10}(\text{SQRT}(K / \text{POR}))) / Pc) ^ (1 / 0.851109)))$

Therefore, it's convenient to define normalized macropore porosity or a macropore normalized pore throat radius as:

$$\overline{R_{Mac}}(\mu m) = \phi_i \sum_i S_{wi} (R_{pi})_{Mac} = \phi_i \cdot 10^{\sum_i \Delta S_{wi} \log_{10}(R_{pi})_{Mac}} \quad [5.3]$$

$$\overline{R_{Mic}}(\mu m) = \phi_i \sum_i S_{wi} (R_{pi})_{Mic} = \phi_i \cdot 10^{\sum_i \Delta S_{wi} \log_{10}(R_{pi})_{Mic}} \quad [5.4]$$

Hence for a given genetic unit, the total normalized pore throat radius is calculated as:

$$\overline{R_{Tot}} = \overline{R_{Mac}} + \overline{R_{mic}} \quad [5.5]$$

This captures the relative contribution of a pore system as a complex interplay of porosity, pore connectivity, grain packing, and grain size rather than porosity alone. This correction now includes the total porosity as the sum of segregated pore volumes; where:

ϕ_i (v/v) = contribution of the total porosity accessible at the *i*-th pressure step

S_{wi} (v/v) = incremental pore volume at the *i*-th pressure step

$\overline{R_{Mac}}$ (μm) = pore throat radius greater than 2 μm at the *i*-th pressure step

$\overline{R_{mic}}$ (μm) = pore throat radius less than/equal to 2 μm at the *i*-th pressure step

Figure 5.22 depicts a plot of corrected measured permeability (*CKH*) as a function of the total normalized porosity ($\overline{R_{Tot}}$) shows an alignment on the same trend for all genetic units analyzed in this study. A correlation coefficient factor (R^2) of 0.88, and an adjusted value of 0.76 is obtained for the normalized pore throat radius, ($\overline{R_{Tot}}$) compared to R^2 of 0.56 for the porosity versus permeability plot (figure 5.4).

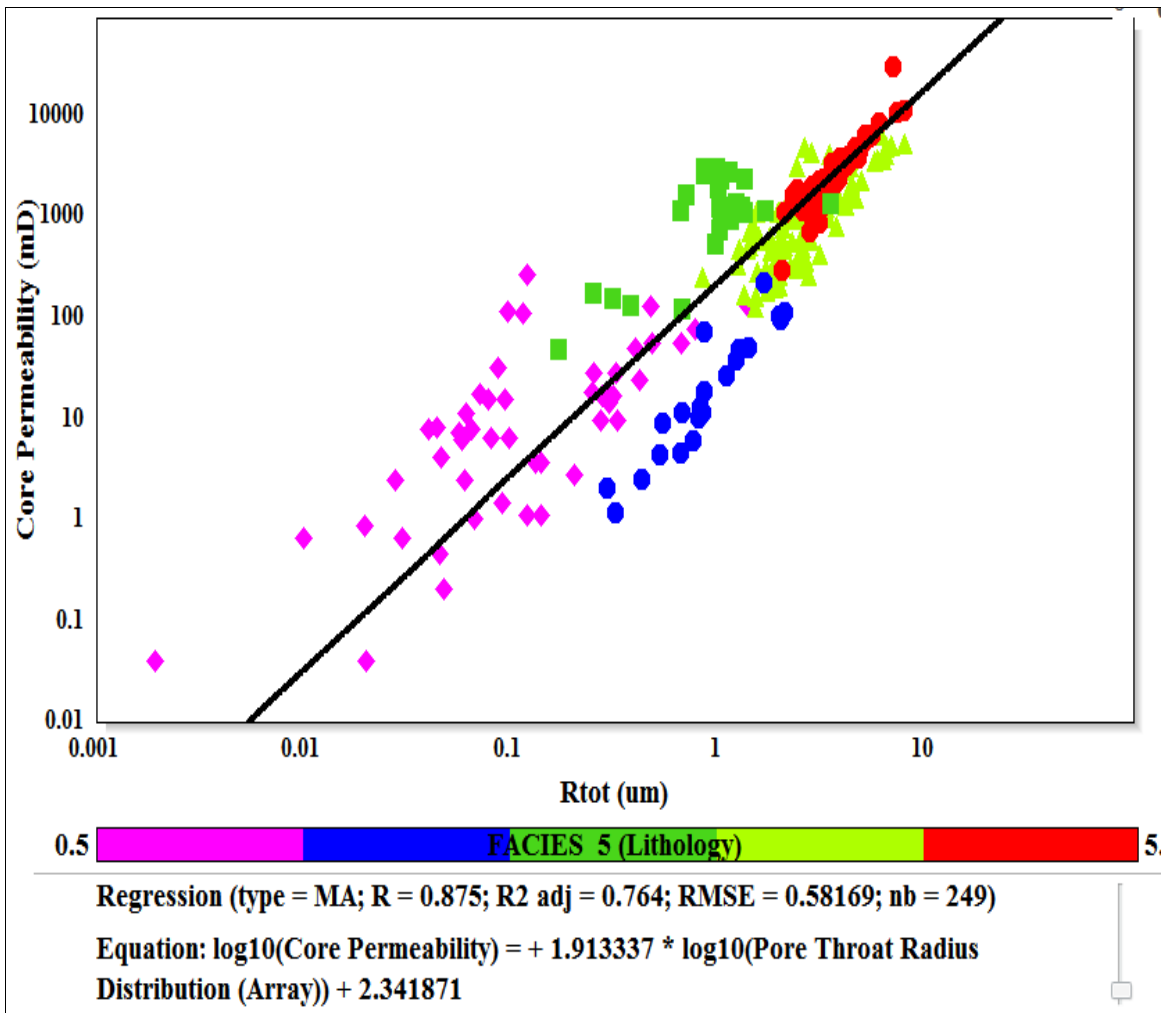


Figure 5.22: Plot of core permeability versus total normalized pore throat radius ($\overline{R_{tot}}$) for all the genetic units classified in the study, indicating the proposed model and improved correlation

This effectively reduces the uncertainty in the permeability to about one order of magnitude. Note that the dataset employed for this model is plug scale, and thus requires upscaling before the correlation can be applied at larger scales.

CHAPTER 6

Data Analysis, Results, and Discussions

6.1 Introduction

The model for permeability prediction can be simplified to a single term with the following mathematical expression:

$$\log_{10} K = a \log_{10} \overline{R_{tot}} + b \quad [6.1]$$

The single constant “a” characterizes the normalized pore throat radius for the clastic system analyzed, with the coefficients: a = 1.913 and b = 2.342.

$$\overline{R_{tot}} = \phi_i \sum_i S_{wi} R_{pi} = \phi \cdot 10^{\sum_i \Delta S_{wi} \cdot \log_{10}(R_{pi})} \quad [6.2]$$

It is worth mentioning that the coefficients in equation (6.1) are unique to the genetic reservoir units observed, with different coefficients characterizing the pore throat sizes within the study area as tabulated below:

Table 6. 1: Proposed Model Coefficients for Various Genetic Units

S/N	Genetic Reservoir Units	a	b
1	Channel Heterolithics	1.91	2.69
2	Lower shoreface Sands	2.39	1.34
3	Upper shoreface Sands	2.42	3.14
4	Tidal Channel Sands	2.61	1.87
5	Fluvial Channel Sands	2.67	1.90

6.2 Statistical Significance of Model Coefficients for the Proposed Genetic Unit Based Permeability Model

The different coefficients characterizing the proposed model as depicted by the genetic reservoir units (table 6.1) is attributed to the sedimentologic and petrophysical character of the units as discussed earlier in chapter 2. This is observed in their varying grain size, grain sorting and reservoir properties. The coefficients represent separate normalized pore throat sizes versus permeability relationships, which characterize the reservoir quality of the units. As anticipated, the Fluvial Channel sand (with the highest coefficient of 2.67) is characterized by high core porosities (20 – 30%) and permeabilities (5,000 – 25,000 mD). The gradation in value of these coefficients to a least value of 1.97 (muddy-dominated Channel Heterolithics) is attributable to the geologic and petrophysical character of the various units.

The fit of the regression model was analyzed by checking the residual plots. Table 6.2 presents model constants, coefficients, t-values and p-values obtained from the output of the linear regression analysis for various genetic units. α -level of 0.05 was chosen to verify the statistical significance of the coefficients in the proposed relationship between the response variable (core permeability) and the predictor variable ($\overline{R_{tot}}$). The p-values were strictly below the α -levels, and hence the sample statistic of the proposed model proves to be too unlikely to have occurred by chance. The lower standard errors of the coefficients and appreciable adjusted least squares correlation coefficient of all the units analyzed within the clastic reservoir system are indicative of a strong relationship between the predictor and response variables.

It suffices to say that the sample is statistically significant and therefore the test's null hypothesis is rejected.

Table 6.2: Statistical Significance of Coefficients for the Proposed Permeability Models

Genetic Reservoir Units	Predictor	Model Coefficients	Correlation Coefficient, R ²	Correlation Coefficient, R ² Adj.	Standard Error of Coefficients	P-value $\alpha=0.05$
Channel Heterolithics	Constant	2.69	0.738	0.535	0.21	0.188
	Rtot	1.91			0.19	0.003
Lower Shoreface Sands	Constant	1.32	0.937	0.872	0.03	0.025
	Rtot	2.39			0.13	0.000
Upper Shoreface Sands	Constant	3.14	0.711	0.583	0.08	0.004
	Rtot	2.42			0.32	0.027
Tidal Channel Sands	Constant	1.87	0.773	0.594	0.08	0.000
	Rtot	2.61			0.17	0.000
Fluvial Channel Sands	Constant	1.90	0.909	0.823	0.08	0.000
	Rtot	2.67			0.15	0.000

The efficacy of the proposed model was validated using dataset from three (3) fields within the Niger Delta that were not involved in the modelling phase. SCAL and RCA were performed on the plug samples and datasets were used as input into the proposed model and validated as follows: 28 plug samples were obtained from six (6) wells the Onshore Coastal Swamp, Central Swamp and Deep Water depobelt of the Delta. A plot of corrected core permeabilities versus the predicted permeability from the proposed normalized pore throat model gave a correlation coefficient of 0.987 and RMSE of 0.092 as seen in figure 6.1.

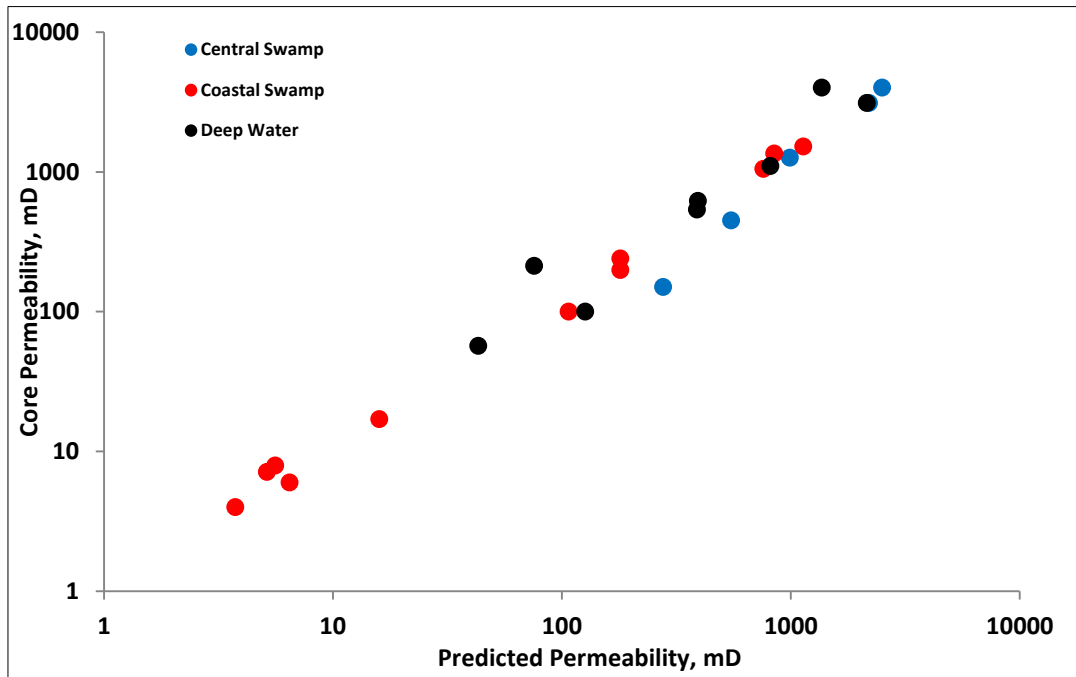


Figure 6.1: Plot of measured permeability versus $\overline{R_{tot}}$ predicted permeability based on SCAL dataset from three (3) depobelts, indicating good correlation.

A major input parameter for the proposed normalized pore throat methodology for improved reservoir characterization is the pore throat radius at every pressure step (R_{pi}) (equation [6.2 and 6.2]). This is an intrinsic component of capillary pressures obtained from MICP special core analysis dataset. The proposed model is hampered due to unavailability of core dataset from uncored reservoir intervals to generate the R_{pi} component. A critical review of subsurface geophysical parameters from well logs depicts the existence of a strong relationship between pore body and pore throat radius for estimating R_{pi} 's in uncored reservoir intervals.

Presented in subsequent subsections are two methodologies for estimating the pseudo averages of R_{pi} from the NMR distribution of transversal (cross-sectional) relaxation T_2 time and conventional geophysical logs in the absence of the NMR T_2 data.

6.3 Proposed Model Calibration using NMR T_2 transversal relaxation time

6.3.1 Capillary Pressures and Pore Throat Distribution from NMR measurement

An alternative approach aimed at deriving primary drainage capillary pressure from NMR core and the distribution of transversal (cross-sectional) relaxation T_2 times from well data was developed by Volokitin *et al.* (1999) as elucidated earlier in Chapter 4.

The approach relies on an underlying assumption that a relationship exist between pore-body radius (as represented by the NMR T_2 distribution) and pore-throat radius (which drives capillary behavior). The hypothesis is the resulting relationship (between the NMR T_2 distribution and pore-throat distribution) embedded within a single universal proportionality parameter termed kappa, κ ; where:

$$P_c = \kappa \left(\frac{1}{T_2} \right) \quad [6.3]$$

$$kappa, \kappa = \frac{P_c}{T_2^{-1}} ; \text{ and } P_c = \frac{2\sigma \cos\theta}{r_{neck}} ;$$

where: σ = interfacial tension; θ = contact angle between the fluid interface, and the pore wall, and r_{neck} = pore-throat radius.

They concluded that the universal scaling factor, $\kappa = 3$ psi Hg.sec seems to work for all clastic reservoirs, and as such making their technique very valuable in exploration wells. Olubunmi and Nwosu (2011) tested the Volokitin *et al.* hypothesis in one of the Deep Water turbidite reservoirs in Niger Delta, composed of four genetic reservoir units: CSA, CSM, ICTB and MRTB units. They proposed a scaling factor, $\kappa = 10$ psi Hg.sec as suitable for estimating realistic capillary pressures from T_2 distribution against earlier works by Volokitin *et al.* which postulated a universal scaling factor, $\kappa = 3$ psi Hg.sec.

In an effort to estimate pore throat radius as input to the proposed normalized pore throat radius permeability model, and using same Deep Water dataset from earlier works for the clastic turbidite sequence, I evaluated various kappa scaling factors within acceptable minimum and maximum limits.

Figure 6.2 present dataset obtained from laboratory special core analysis (at a net confining stress of 1,850-1,950 psi) and routine core analysis from 11 core samples at depths between 9,000 – 10,000 feet, from the Deep Water Canyon reservoirs within the Tertiary Niger Delta Province.

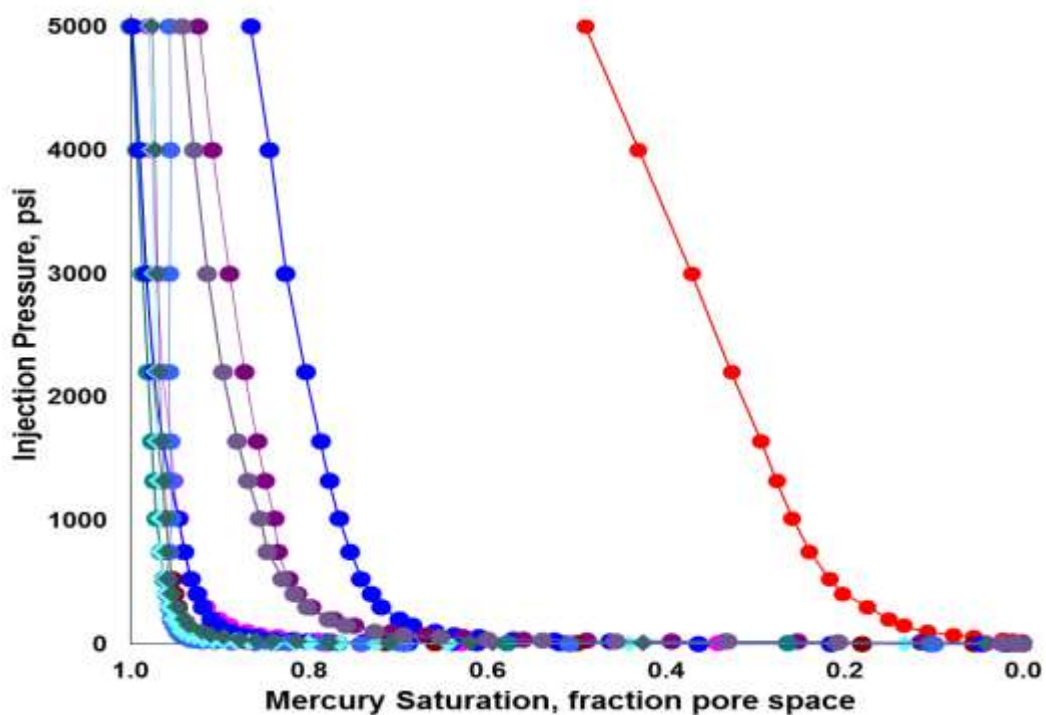


Figure 6.2: Mercury Injection Capillary pressure curves obtained at a confining stress (1,850-1,950 psi), indicating 11 special core analysis samples from various genetic reservoir units from the Deep Water turbidite environment

Pore throat distribution were computed using kappa values within acceptable limits to demonstrate their relationship with laboratory mercury injection capillary pressure (MICP) data from a full-bore core. Figure 6.3 presents the pore throat distribution obtained from laboratory special core analysis employed as reference to the kappa predicted capillary pressure curves expressing the sample unimodality and rock fabric. This indicates a maximum of 24% pore volume accessible to the Channel Storey Axis unit.

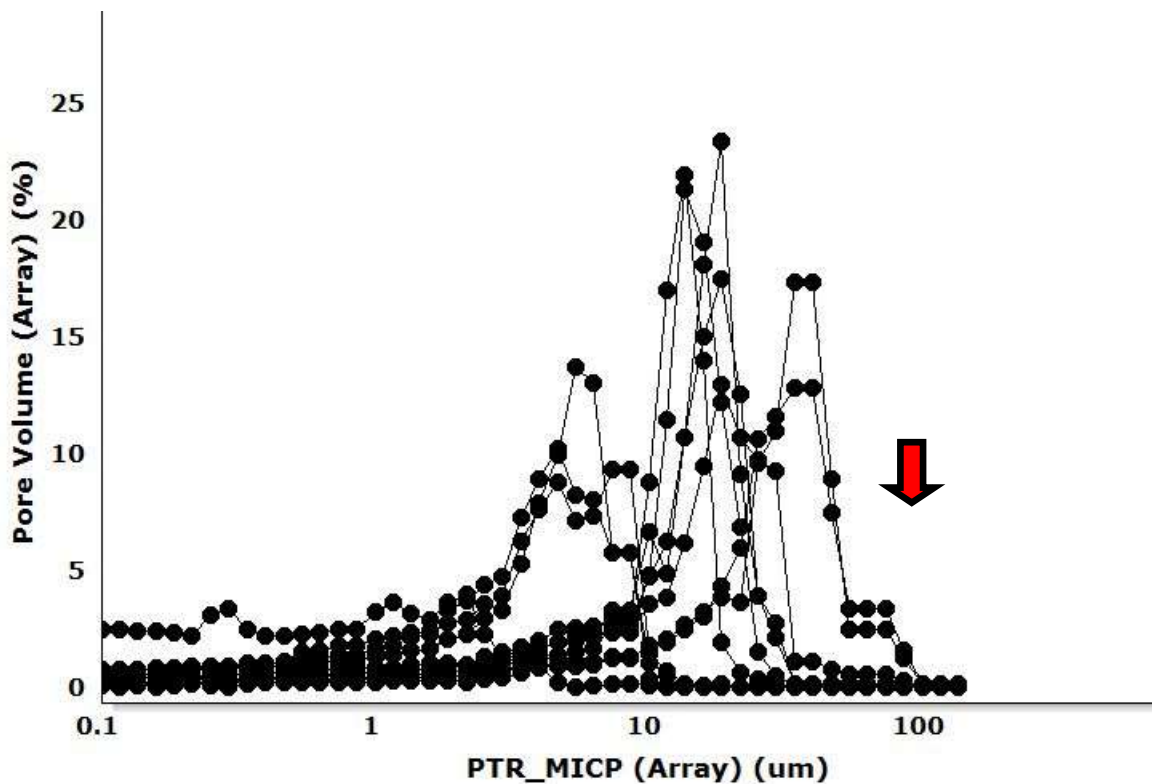


Figure 6.3: Pore throat size distribution obtained from mercury injection capillary pressure dataset with the red arrow indicating macropores greater than 100 microns for the Deep Water turbidites dataset (offshore Niger Delta)

Figure 6.4 through figure 6.6 present pore throat distribution plots obtained from kappa derived NMR capillary pressures using dataset from same well with mercury injection capillary pressures from the Deep Water canyon reservoir. The analysis incorporated the Volokitin *et al's* algorithm using a multiple regression analysis for kappa values of 2, 3, 5, 7 and 10 psi Hg.sec.

A scaling factor of 2 psi Hg.sec (see the bottom plot of figure 5) indicates appreciable correlation with the measured pore throat radius from MICP dataset compared to existing works for pore body/pore throat definition.

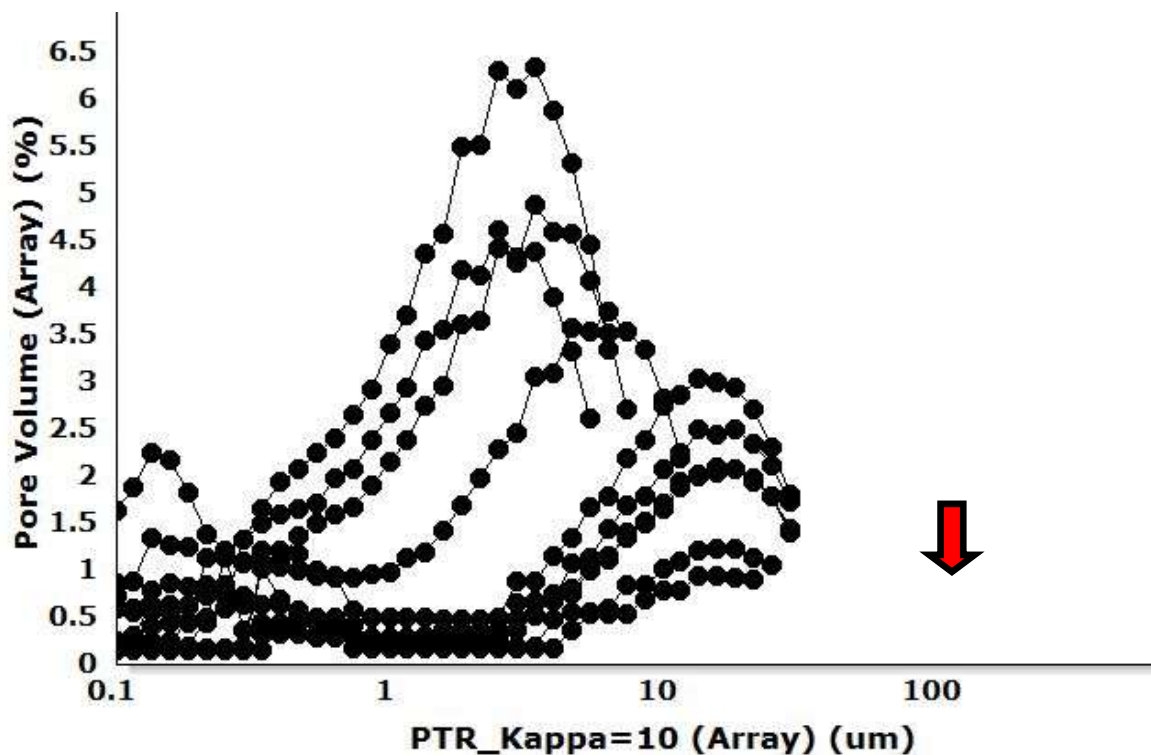


Figure 6.4: Plot of Pore Throat Size Distribution predicted from NMR capillary pressure for $kappa = 10$ (Olubunmi and Nwosu; 2011.). Red arrow indicates the deficiency of the model in modelling macropores with reference to laboratory measured MICP data (figure 6.3).

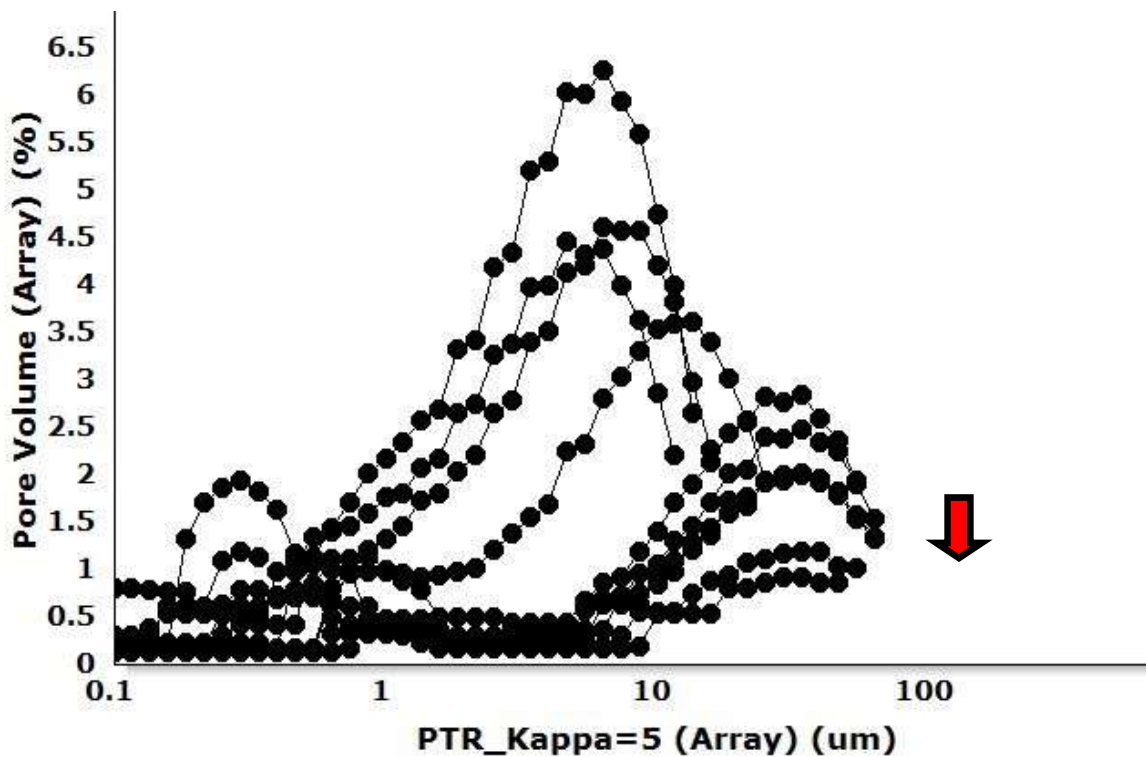
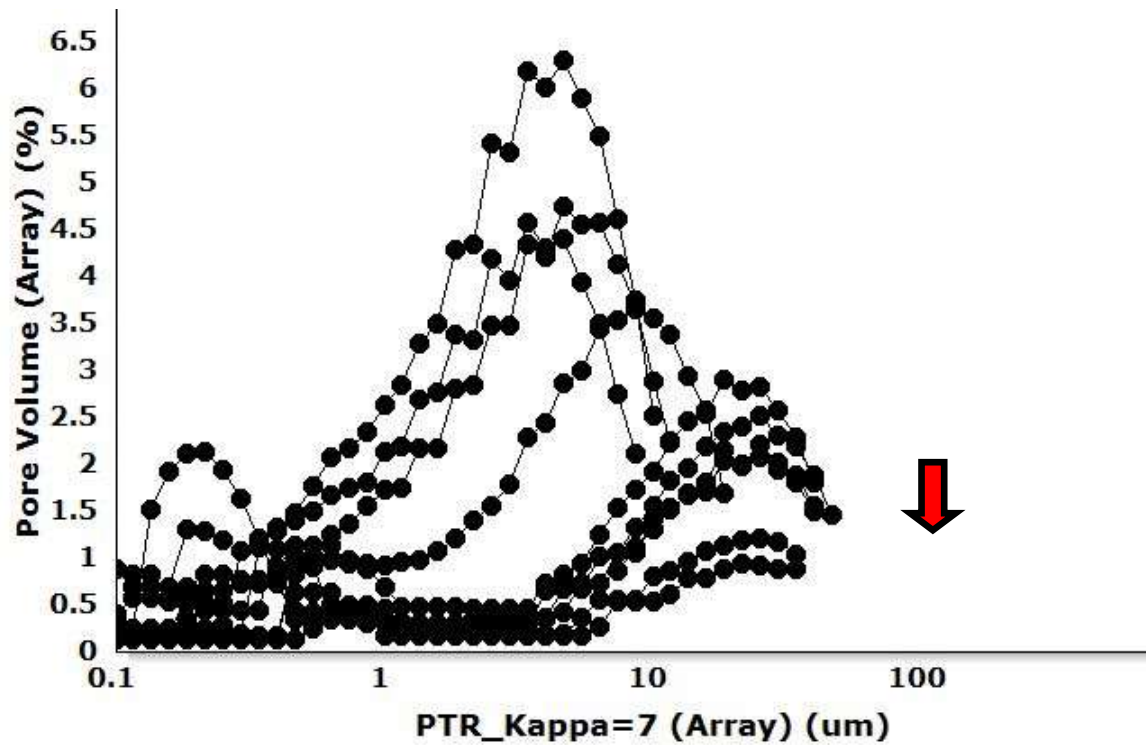


Figure 6.5: Pore Throat Size Distribution predicted from NMR capillary pressures for $\kappa = 7$ and 5. Red arrow indicates the deficiency of the model in modelling macropores with reference to laboratory measured MICP data (Figure 6.3).

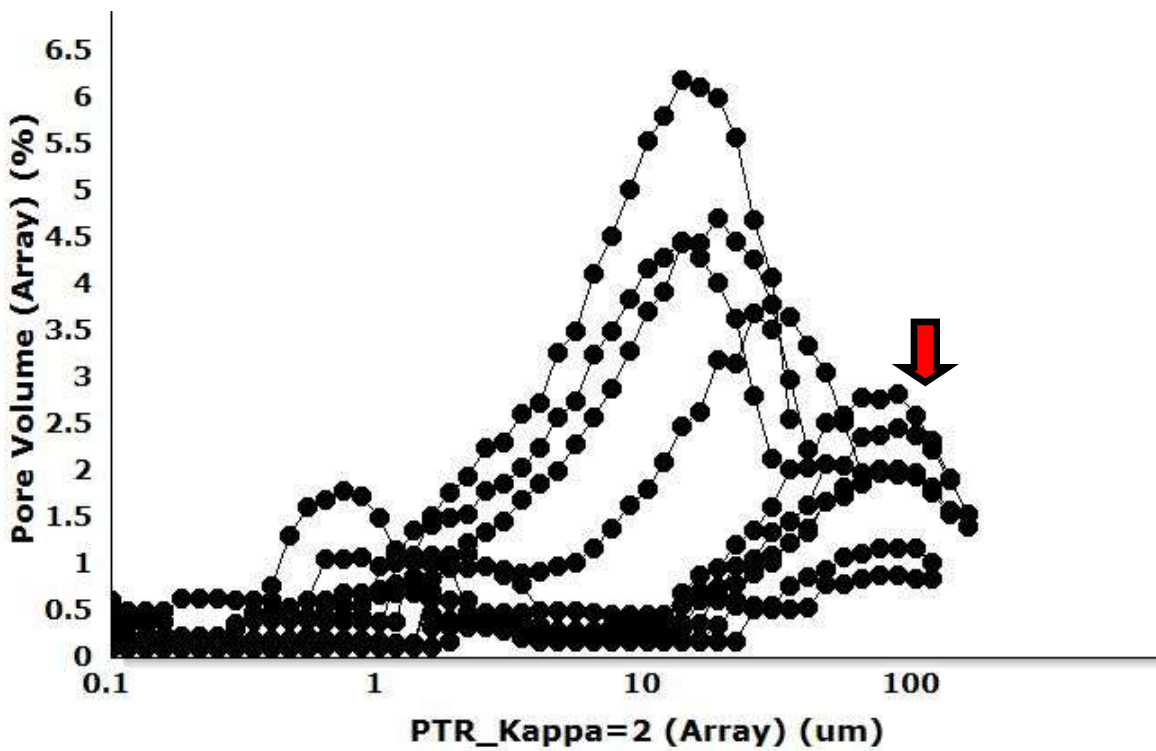
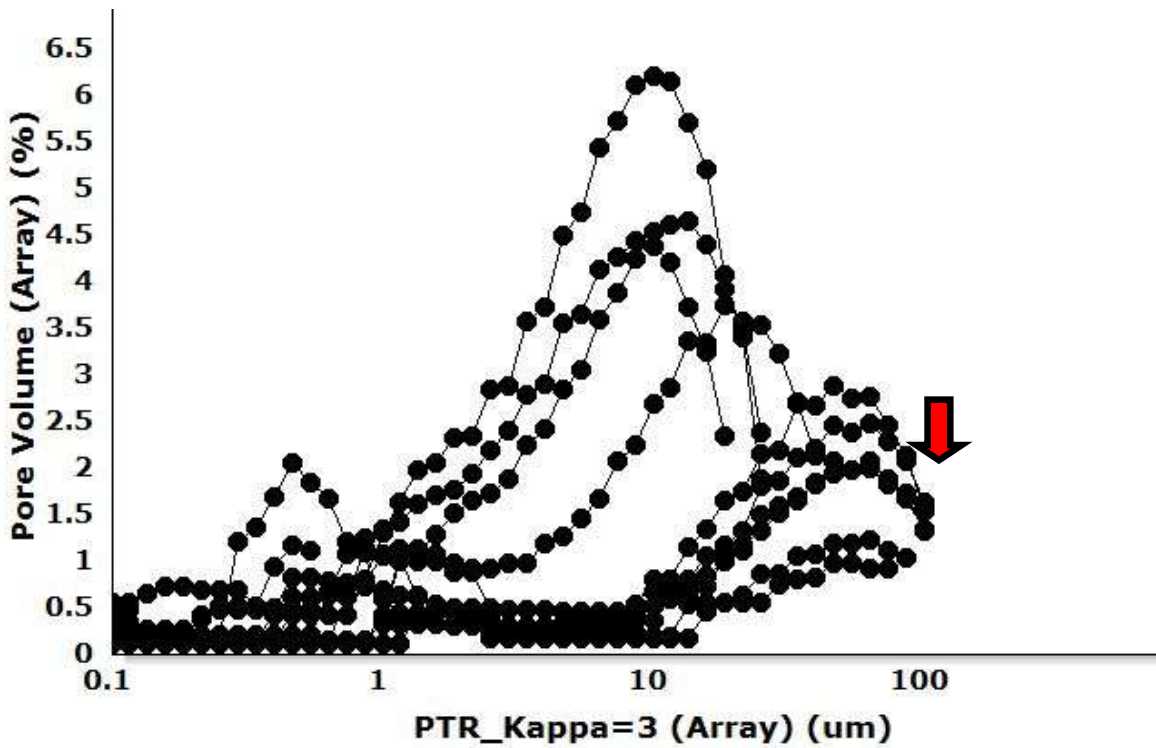


Figure 6.6: Pore throat size distribution derived from NMR Capillary Pressures for $\kappa = 3$ and 2 (current study). Red arrow indicates the capability of the proposed model in modelling pore distribution with reference to laboratory measured MICP data (Figure 6.3).

Varying the kappa scaling factor demonstrates the inadequacies of using a single proportionality constant in modelling pore throat distribution greater than 10 microns, and thereby questions the proposed existence of a linear relationship between the NMR T_2 distributions and measured capillary pressures. As such a single kappa factor is insufficient in characterizing pore throat distribution for reservoir with complex lithologies.

In addition, the existing kappa based algorithm for transforming NMR T_2 distribution to capillary pressures under-predicts the pore volume accessible to pore throat distribution for all Kappa values tested.

For all cases of kappa tested as presented in figure 6.4 through figure 6.6, a maximum of 6.4% pore volume is accessible to the pore throat distribution for same reservoir unit. This denotes a 73% reduction in accessible pore volume compared to the laboratory measured dataset.

In this present work, the laboratory measured capillary pressures are compared with NMR derived ones for calibration with emphasis on various genetic units. Preliminary analysis aimed at validating the existence of the proposed relationship (equation 6.3) between measured capillary pressures and inverse NMR T_2 distribution after Volokitin *et al.* indicate a nonlinear relationship as demonstrated in figure 6.7.

If Volokitin assumption as shown in equation 6.3 is valid, the plot in figure 6.7 should have yielded a straight line.

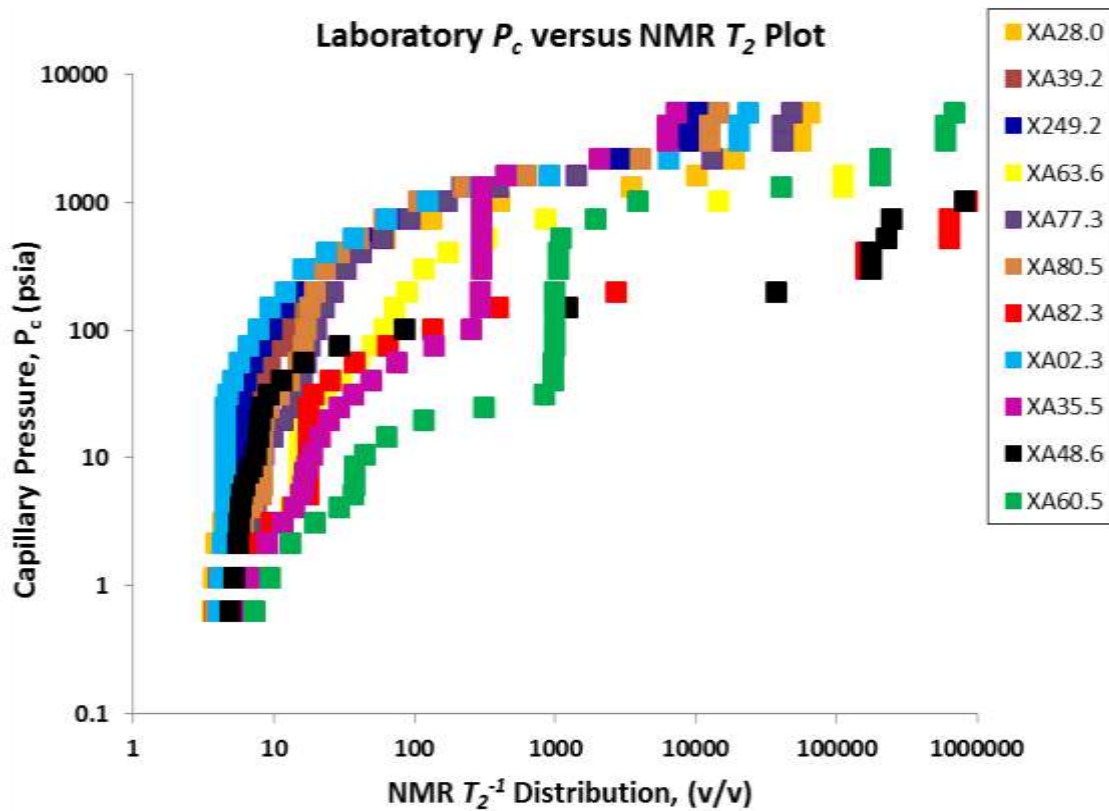


Figure 6.7: Mercury Injection Capillary pressure curves versus inverse NMR T_2 distribution for sample dataset indicating nonlinearity in relationship.

A possible averaging for the kappa proportionality constant for the range of capillary pressures as described above for all dataset shows a negative exponential relationship between measured capillary pressures and inverse of NMR T_2 distribution (figure 6.7).

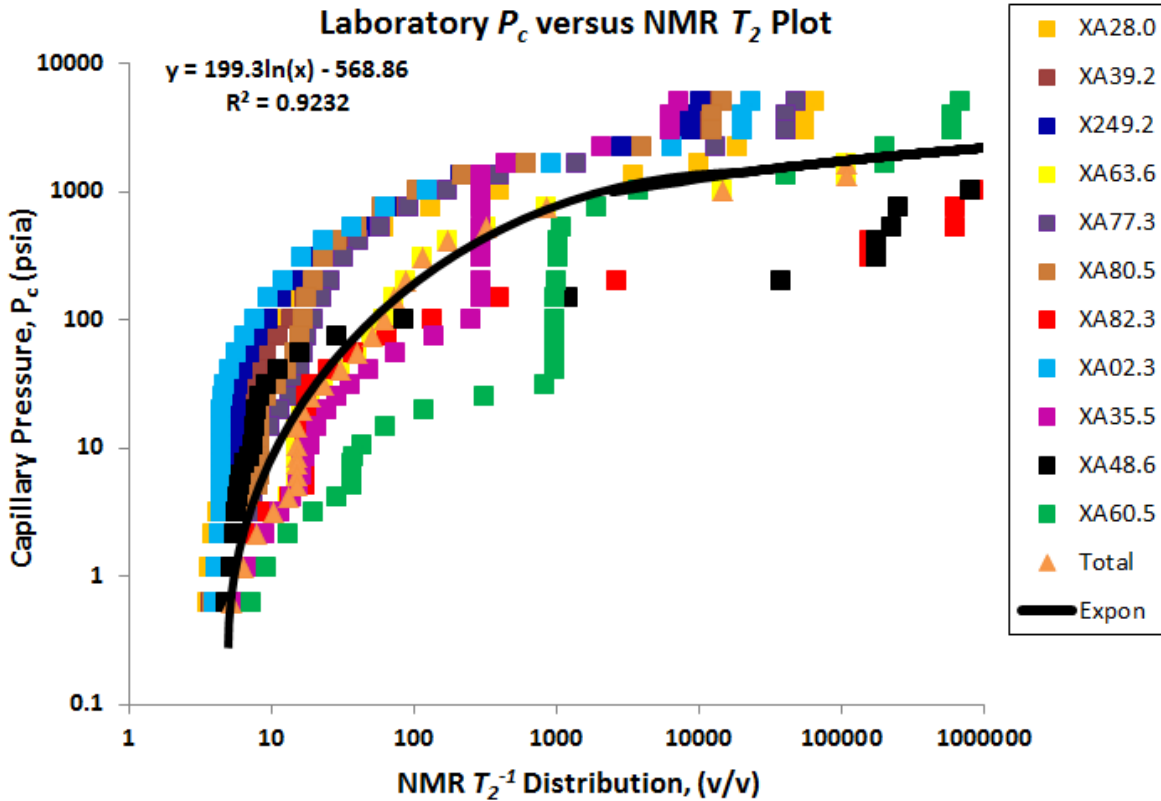


Figure 6.8: Mercury Injection Capillary pressure curves versus inverse NMR T_2 distribution for sample dataset indicating nonlinearity in relationship.

The least squares best fit exponential model to the data as shown using figure 6.7 is then:

$$P_c = \ln\left(\frac{1}{T_2}\right) \kappa \quad [6.4]$$

where kappa, κ is the shift factor for modelling the individual sample dataset.

Analysis indicate that the linear relationship as embedded within the kappa scaling factor as defined by equation 1, only exist beyond certain pressure threshold values.

Application of capillary pressure cutoff delineating the entry pressures for all samples as presented in figure 6.8 demonstrates the aforementioned assertion (equation 6.5).

$$\log[(P_c)_i - (P_c)_{cutoff}] = \log T_{2i}^{-1} \pm \log k \quad [6.5]$$

This implies that Volokitin *et al.* proposal is not valid for $(P_c)_{cutoff}$ equals zero or negligible; typical in homogeneous and well sorted formations. This is one of the motivations for the current study.

A quick look analysis of figure 6.8 also indicates the possible presence of four (4) reservoir zones within the system.

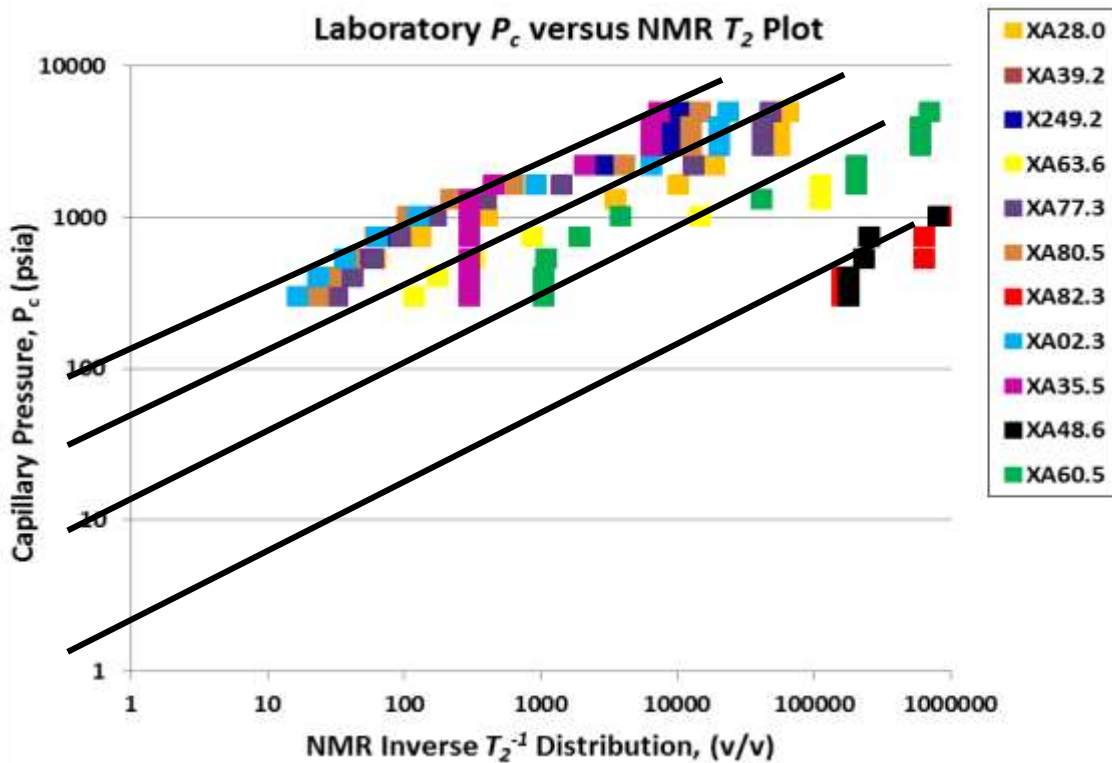


Figure 6.9: Mercury Injection Capillary pressure curves versus inverse NMR T_2 distribution for samples dataset from indicating nonlinearity in relationship.

The various values of kappa from figure 6.8 at NMR T_2 inverse of 1 are 110, 60, 15 and 3 corresponding to the CSA, CSM, ICTB and MRTB genetic reservoir units respectively. NMR capillary pressures were estimated from the relationship in equation 6.5 above and compared with laboratory measured dataset.

Figure 6.9 presents a plot of mercury injection capillary pressures versus NMR predicted pressures using the relationship in equation 6.5. This indicates a good correlation between both parameters at pressures beyond the imposed cut off pressures.

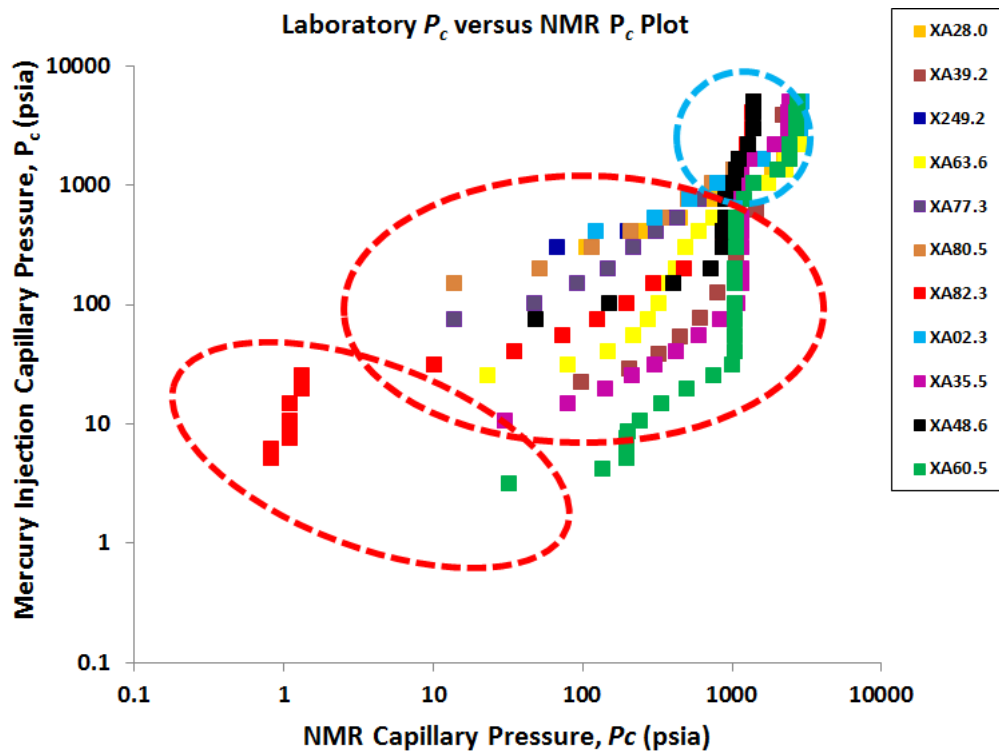


Figure 6.10: Mercury Injection Capillary pressure curves versus NMR predicted capillary pressures for the dataset indicating poor correlation at pressures below the imposed cut offs for the entry pressures and transition zone.

The results demonstrate the weaknesses of existing methodology in relating pore-body radius (as represented by the NMR T_2 distribution) to pore-throat radius (which drives capillary behavior). It suffices then to conclude that there exist no direct linear

relationship between the NMR T_2 distribution as proposed by Volokitin *et al.*, In addition, a constant scaling factor for kappa is insufficient in modelling subsurface capillary pressures/pore throat distribution from NMR T_2 logs; and as such, a more accurate prediction can be obtained through local calibration, possibly allowing the scaling factor to vary as a function of rock types (pore size/grain sorting) and influence of clay diagenesis within the clastic system.

The following sub-section presents an analytical methodology for improved capillary pressures and pore throat radius estimation from NMR measurements based on genetic reservoir units' averages of Kappa for the Niger Delta clastic reservoir as case study.

6.3.2 Flow Unit Based Analytical Methodology for NMR-Pc Calibration

The following steps were adopted for calibrating capillary pressures obtained from mercury injection pressures (P_c) to NMR T_2 values:

1. Reservoir characterization aimed at integrating the distribution of depositional facies defined by geologic study with the vertical sequence of rock types determined from reservoir quality studies. In principle, the focus is to delineate zones composed of similar rock types that are in hydrodynamic communication. Each flow unit possesses stratigraphic continuity with a strong relationship to pore geometries and capillary characteristics (entry pressures and irreducible water saturation).
2. Invert the NMR T_2 -distribution in porosity units (v/v)/time-domain CPMG echo decay provided by logging service companies to a standard T_2 -parameter-domain distribution (msecs). This presents the processed T_2 distribution with T_2 -bins ranging on a logarithmic scale depending on the NMR tool type.

3. Generate the cumulative T_2 distribution (sum of amplitudes) curve.

Songhua *et al.* (1998) demonstrated the relationship between core NMR measurements and NMR log data as presented in figure 6.10.

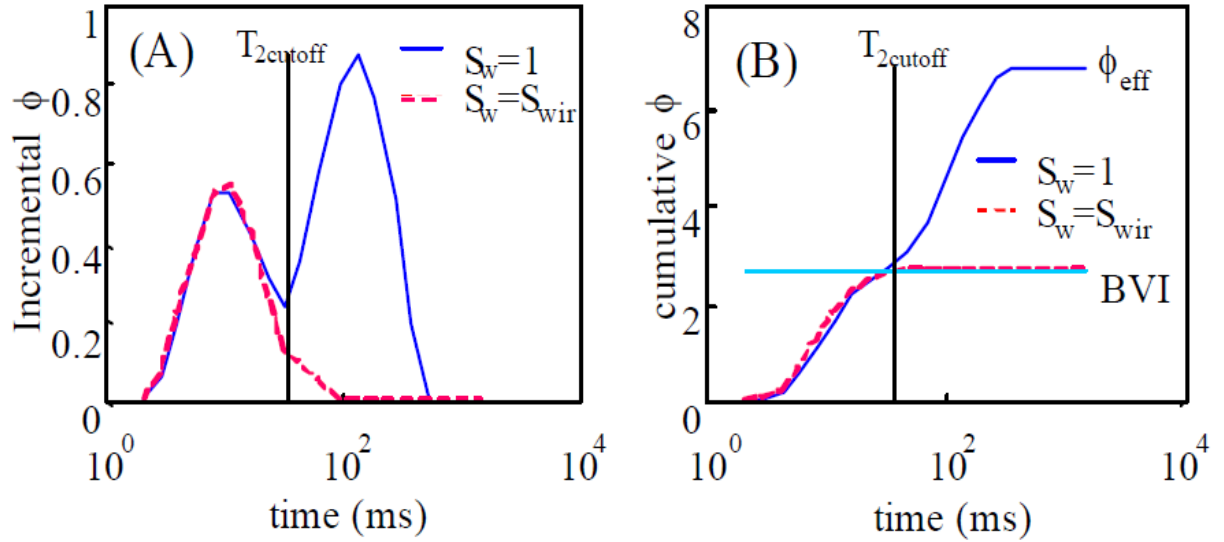


Figure 6.11: Illustration of T_2 cutoff estimation process with NMR core measurements.

(A) is the incremental distribution and (B) is the cumulative distribution (after Songhua *et al.*, 1998).

The cumulative porosity distribution plot above is used for estimating T_2 cutoff and bulk volume irreducible (BVI). As illustrated, this corresponds to the maximum cumulative porosity where irreducible water saturation from the core NMR measurement intercepts the NMR T_2 log.

4. Calibrating NMR T_2 distribution to laboratory measured MICP dataset.

$$P_c = P_{nw} - P_w = \frac{2 \cdot \sigma \cdot \cos \theta}{r} \quad [6.6]$$

Equation 6.6 indicates an inverse proportionality between capillary pressures and pore throat radius r , and recall that the T_2 distribution is directly proportional to pore body radius, R_b . It suffices to infer that T_2 distribution and capillary pressures are associated with the pore geometry. Because the grain size determines both the pore body and the pore throat radius, a relationship between R_b and r can be expected.

Combining equations 6.4 and 6.6, we obtain:

$$P_c = \frac{2.\sigma.\cos\theta}{T_2.3.\rho.\beta} \quad [6.7]$$

where β relates the pore-throat radius to the pore body radius.

The expression in equation 6.7 can also be summarized as:

$$P_c = \left(\frac{1}{T_2}\right)\kappa \quad [6.8]$$

where κ is defined as:

$$\kappa = \frac{2.\sigma.\cos\theta}{3.\rho.\beta} \quad [6.9]$$

The terms ρ and β vary with the mineral composition of the rock, and in a brine-wet rock, T_2 in smaller pores will be less than T_2 in large pores; consequently, identical pore water in different rocks can have a wide range of relaxation times because of variations in ρ .

Sørland *et al.* (2007) proposed the average surface relaxivity ($\bar{\rho}$) based on laboratory CPMG measurement for transforming the T_2 to pore body distribution.

The $\bar{\rho}$ is expressed as:

$$\bar{\rho} \equiv \sum_{i=1}^n \varepsilon_i \left(\frac{1}{T_{2i}}\right) * \left(\frac{S}{V}\right)^{-1} \quad [6.10]$$

with ε_i being the volume fraction of pores with $(S/V)_i$, and n is the number of bins for the NMR measurement.

Based on classification from the various units, average Kappa values were estimated using the proposed relationships shown in equations 6.9 & 6.10 above. The calibrated kappa functions were further used to generate capillary pressures from the NMR T_2 distribution.

Guodong J. *et al.*, (2012) proposed a methodology for computing the wetting-phase saturation (S_w) corresponding to the NMR derived capillary pressures from the NMR T_2 distribution as:

$$S_w(T_2) = \frac{1}{\varphi_T} \int_{T_{2min}}^{T_2} \varphi(T'_2) dT'_2 \quad [6.11]$$

where φ_T is the total porosity; $\varphi(T_2)$ is the T_2 distribution in porosity units, and T_{2min} is the minimum T_2 of the distribution.

Applying NMR T_2 cutoff to delineate the bulk volume irreducible (BVI) from the Bulk Volume Moveable (BVM) presents an improved calibration of NMR derived saturation to measured data, over existing works by Guodong J. *et al.*, (2012). This approach is based on the assumption that the smaller pore spaces are occupied by the wetting phase alone, and the irreducible water (S_{wirr}) saturates the pores with T_2 less than a threshold relaxation time ($T_{2cutoff}$), whereas the fluids in pores with $T_2 > T_{2cutoff}$ are movable.

Hence, the saturation of water at a height above FWL can be given by:

$$S_w(T_2) = \underbrace{\frac{1}{\varphi_T} \sum_{T_{2min}}^{T_{2cutoff}} \varphi(T_2) \kappa}_{\text{BVI}} + \underbrace{\frac{1}{\varphi_T} \sum_{T_{2cutoff}}^{T_{2max}} \varphi(T_2) \kappa \alpha}_{\text{FFI}} \quad [6.12]$$

where: $\alpha = \frac{2\sigma \cos \theta}{3\rho T_2 h(\rho_w - \rho_{HC})g}$; and κ = genetic units averages of kappa.

5. NMR derived capillary pressure curve does not necessarily match the measured curve. The results differ in the entry capillary pressures and irreducible water saturation. This is due to the fact that the capillary pressure curves goes down to the irreducible water saturation (S_{wirr}) on the abscissa while the NMR derived curve goes almost to zero water saturation. The S_{wirr} contains up to the BVI fluid volume. To achieve a match between the NMR derived versus the laboratory measured capillary pressure curve, it is necessary to rescale the NMR saturation. As a measure of the fit quality for a given value of kappa, we introduced the average saturation error between the constructed NMR capillary pressure curve and the corresponding MICP. This saturation is the root mean square (RMS) average of saturation differences: $S_w(P_c) - S_w(Kappa.T_2^{-1})$. A plot of the measured water saturation (S_w') versus NMR saturation (S_{w-NMR}) demonstrates a possible linear relationship between the response and predictor variable with a constant shifting parameter for the various genetic reservoir units. The shift parameters were calibrated for specific reservoir units, resulting in a master equation or averaged curve. Therefore the calibrated NMR saturation (S_w') can be expressed in form of a linear relationship as follows:

$$S_w' = A + B(S_{w-NMR} + C) \quad [6.13]$$

Where:

“A” and “B” are constants, while “C” is a genetic unit based shifting scaling parameter.

However, the modification of S_{wi} results in altered initial T_2 cut-off, and hence S_w' increases beyond 100%, which requires further recalibration to measured saturation.

6.3.3 NMR-Pc Calibration: Application to Reservoir Characterization Using the Niger Delta Deepwater Turbidites as Case Study

6.3.3.1 Data Gathering and Reservoir Quality Characterization

Figure 6.2 and Figure 6.12 & 13 presents dataset and associated analysis obtained from laboratory special core analysis (at a net confining stress of 1,850-1,950 psi) and routine core analysis from 11 core samples at depths between 9,000 – 10,000 feet, from the Deep Water Canyon reservoirs within the Tertiary Niger Delta Province. Detailed laboratory core analysis and description for lithofacies definition, understanding the environment of deposition, and petrographic studies were made possible with assistance from Shell Nigeria. Conventional as well as NMR T_2 spectrum logs were also obtained from same cored interval.

In this present work, the laboratory measured capillary curves are compared with NMR derived ones for calibration with emphasis on various genetic units.

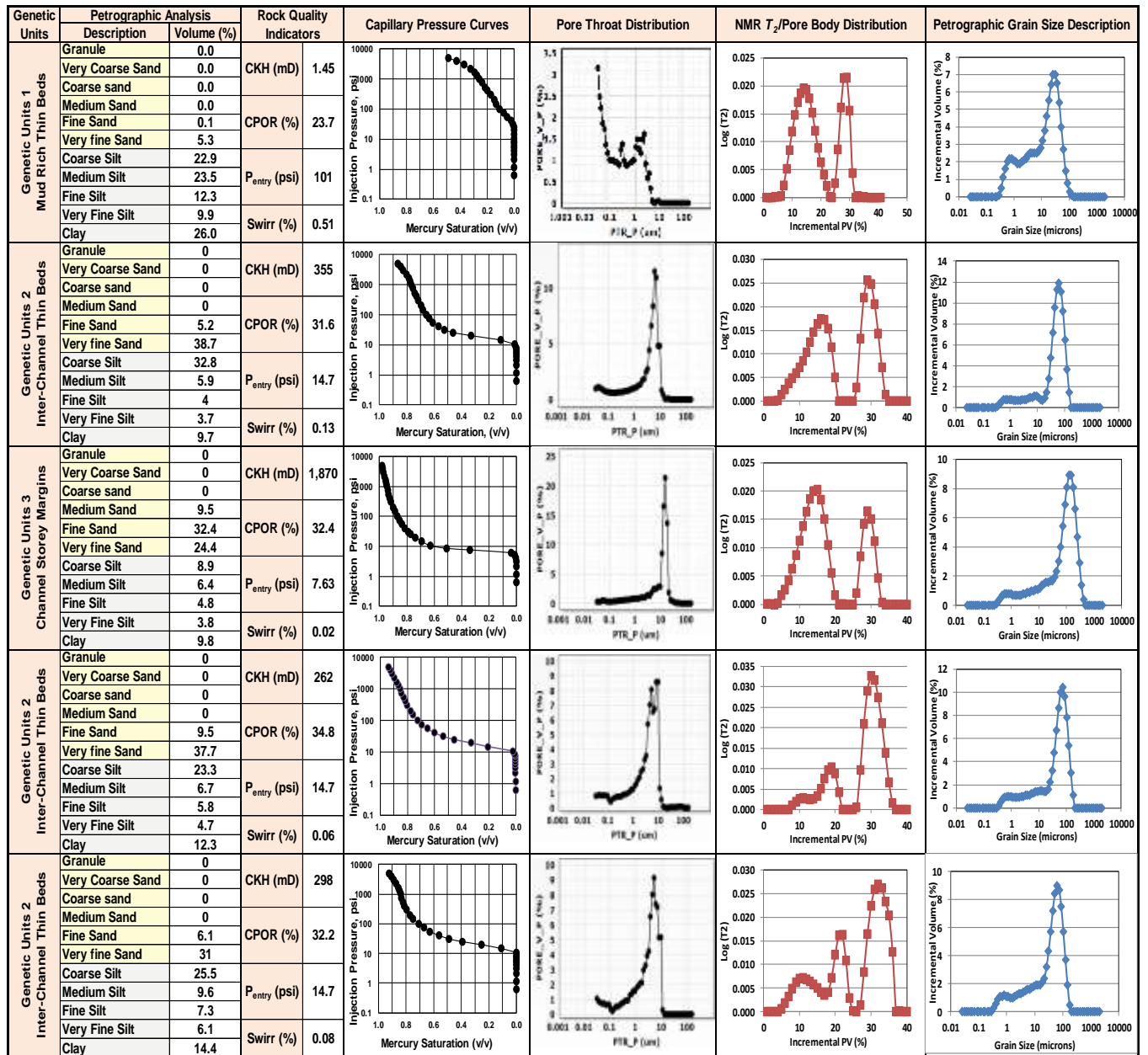


Figure 6.12: Sample 1 – 5 employed for the study. This present petrographic grain analysis, NMR T_2 distribution and MICP distribution demonstrating various rock quality indicators; relationship between pore bodies and pore throats for various genetic reservoir units, within the Deep Water Niger Delta.

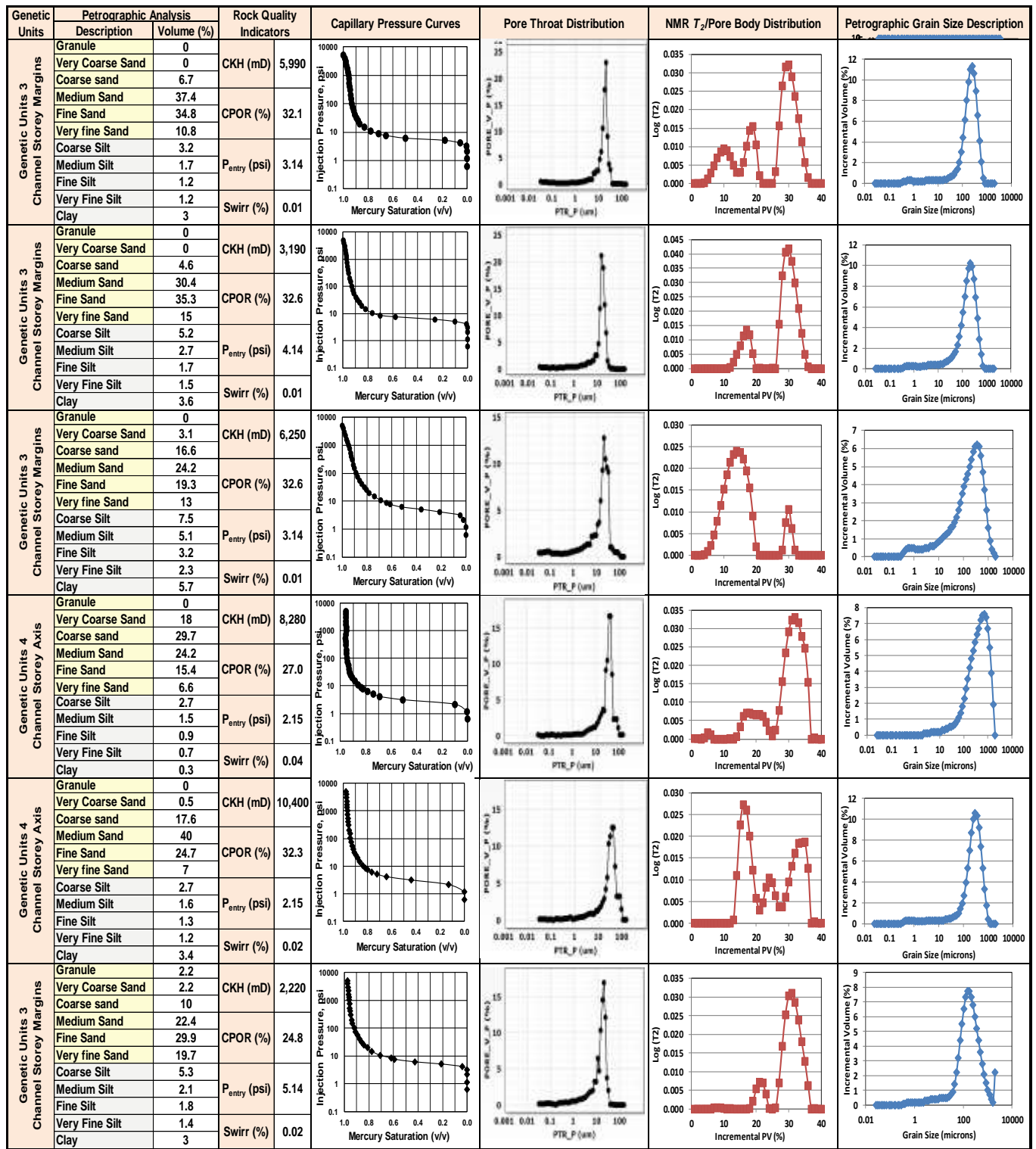


Figure 6.13: Sample 6 – 11 employed for the study. This present petrographic grain analysis, NMR T_2 distribution and MICP distribution demonstrating various rock quality indicators; relationship between pore bodies and pore throats for various genetic reservoir units, within the Deep Water Niger Delta.

Petrographic data gives focus to pore bodies – their size, shape and relationship to rock fabric. MICP data on the other hand provides data on pore throats. The two data types are complementary and comparisons between the data types give extra insights into the pore system. A comparison of petrographic analysis, T_2 distribution and MICP data together provides answers to following questions: (i) which pore type(s) provides the main pore connectivity and hence mostly impacts permeability? (ii) What is typical about pore throat size signatures for a particular genetic reservoir? (iii) What is the spatial architecture of the pore systems in various distributions? and (iv) How can we quantify the porosity composition per pore system? Table 6.3 presents the rock quality/petrofacies classification based on pore throat ranges identified from petrographic and sieve analysis as well as pore throat radius distribution from mercury injection capillary pressures. The $2 \mu\text{m}$ cutoff criteria (Onuh *et al.*, 2015) for delineating micropores from macropores for the clastic system is also applicable to the dataset. This serves as a basis for preliminary definition of rock fabric and genetic units for all samples; and for classification of the dataset into groups of different porosity ranges.

Table 6.3: Pore throat ranges of petrofacies.

Pore Throat Types	Size Range (microns)
Megapores (petrofacies 1)	> 10
Macropores (petrofacies 2)	5 - 10
Mesopores (petrofacies 3)	2 - 5
Micropores (petrofacies 4)	0.1 - 2
Nanopores (petrofacies 5)	< 0.1

Figure 12 & 13 demonstrates that a given T_2 value can be interpreted as a pore-body (Equation 7). For grain size of a certain distribution, the pore-size will follow a closely linked distribution. This in turn implies that NMR relaxation times will follow a distribution controlled by grain size distribution as demonstrated in Figure 12 & 13. This presents the relationship between pore bodies as defined by the NMR T_2 distribution, petrographic grain size distribution and pore throat embedded in capillary pressures from mercury injection.

Multiple pore types will have their individual size distribution and each distribution will translate into individual T_2 distributions controlled by the pore sizes and their surface to volume ratio. Under this hypothesis, the observed T_2 distribution will be the sum of multiple distributions, each corresponding to the size distributions of individual pore types. Identifying these individual distributions reveals information on pore types.

Detailed core analysis for lithofacies association from the available dataset depicts the four (4) prevailing genetic reservoir units within the deep water asset. Table 6.4 below presents the classification adopted for this study.

Table 6.4: Genetic Units Classification for the Turbidite/Deep Water Environment developed for the study.

Units	Generalized Classification	Genetic Reservoir Units
1	Amalgamated Channel Fill Sandstone	Channel Lag
2		Channel Storey Axis (CSA)
3	Isolated & Sinuous Channel Complexes	Channel Storey Margin (CSM)
4		Inter-Channel Thin Beds (ICTB)
	Levee/Overbank/Mudstone	Mud-Rich Thin Beds (MRTB)
		Levees/Overbank
		Marine Mudstone

It is critical to understand that flow units may or may not correspond exactly with the depositional facies/genetic reservoir units defined in the geologic study. Figure 6.14 presents a plot of the normalized cumulative reservoir quality index (RQI_{nc}) versus depth employed for delineating the reservoir into several zones by observing changes in the slope. Consistent zones are characterized by straight lines with the slope of the line indicating the overall reservoir quality within a particular depth interval. A lower slope indicates a higher reservoir quality and vice versa. Hydraulic units delineation based on the normalized reservoir quality index shows a strong correlation with the genetic reservoir units' classification and geologic core description.

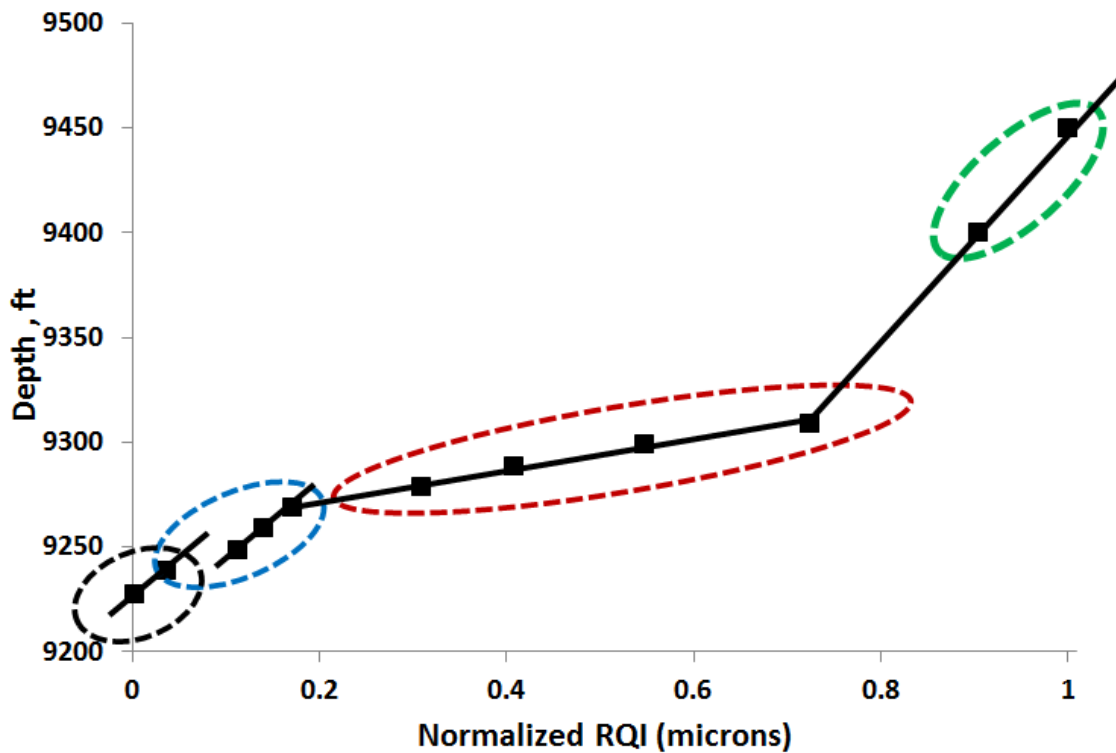


Figure 6.14: Normalized cumulative reservoir quality index (RQI_{nc}) versus depth indicating four (4) possible zones.

The total dataset was subdivided into four flow units. The integration of reservoir quality information, engineering data, and field performance history into the detailed geologic description of the reservoir is essential for any successful reservoir characterization study. Figure 6.15 presents a plot of mercury injection capillary curves delineating the various reservoir units. This shows a strong correlation between the genetic units association, rock quality and capillary parameters. This is evident of clay mineral diagenesis and its influence on grain size distribution/sorting. As such a relationship between pore bodies and pore throats will bear practical significance and relevance when constrained to the various genetic reservoir units.

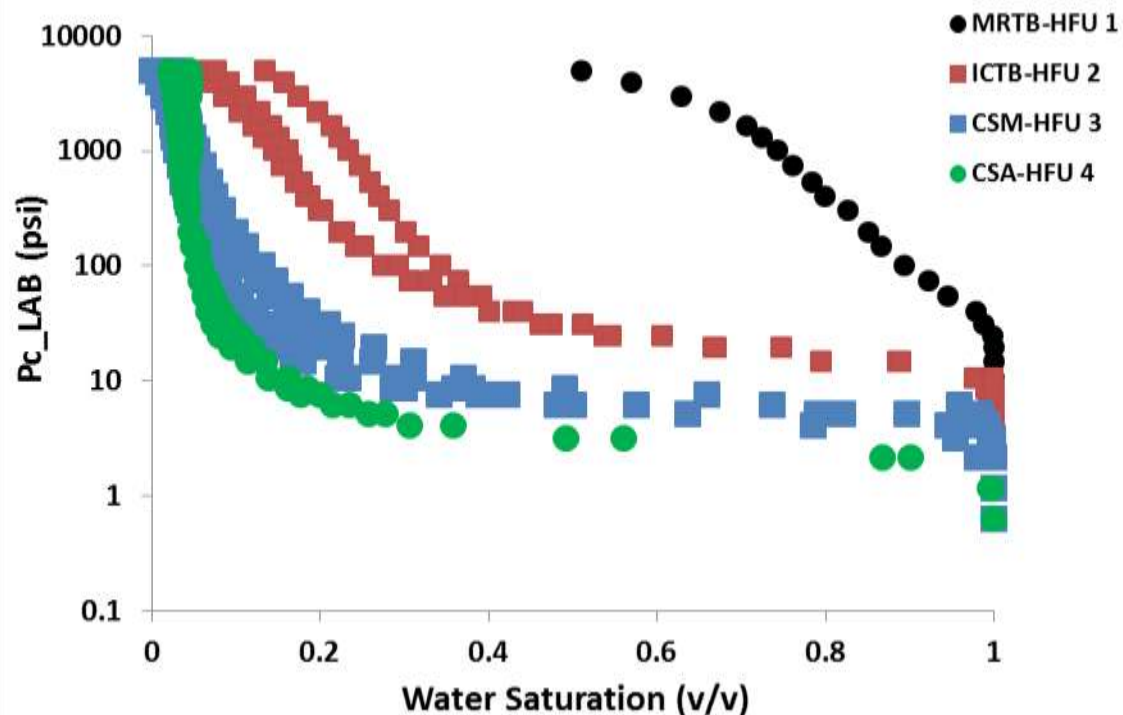


Figure 6.15: Laboratory capillary pressure curves indicating a relationship between the various hydraulic flow units/genetic rock units and capillary parameters. Reservoir quality properties increase from the black curve (HFU 1 – Mud Rich Thin Bed units) with high irreducible water saturation and entry pressures to the green curve (HFU 4 – Channel Storey Axis units) with low S_{wirr} and P_{entry} .

6.3.3.2 Calibrating NMR T_2 distribution to MICP dataset

Equation 6.8 depicts a relationship between measured capillary pressures and the NMR T_2 distribution. A semilog plot of laboratory measured capillary pressure data and the inverse NMR T_2 array data as presented in figure 6.16 for the Channel Storey Axis reservoir unit, demonstrates an existing relationship with need for recalibration. Key emphasis is the relationship between end point capillary parameters (entry pressures and irreducible water saturation).

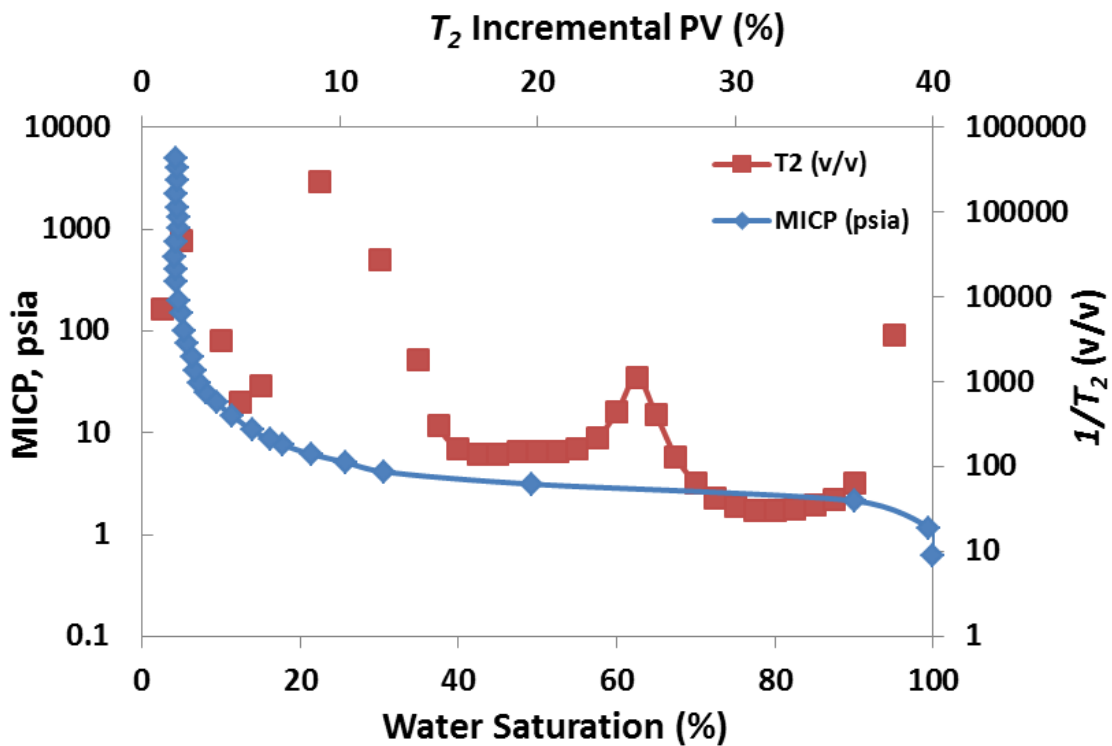


Figure 6.16: Plot of mercury injection capillary pressure and inverse NMR T_2 relaxation for the Channel Storey Axis unit for a fully saturated sample. This indicates a fair relationship between capillary parameters that requires a recalibration for improved fit.

In an attempt to calibrate the NMR T_2 log to measured capillary dataset, cumulative T_2 distribution curves were generated for individual dataset belonging to the four (4) reservoir units.

The emphasis is to establish key parameters relating capillary pressures to T_2 distribution, and the cut offs for estimating the FFI, BVI, corresponding S_{wirr} and total porosity. Figure 6.17 presents plots of NMR T_2 distribution indicating cumulative and incremental porosity using dataset from HFU 4. The figure estimates the bulk volume irreducible (BVI) for S_{wirr} modelling and total porosity available to the free and bound fluid volumes. The figure depicts a BVI and total porosity of 0.06 and 31% respectively for the unit.

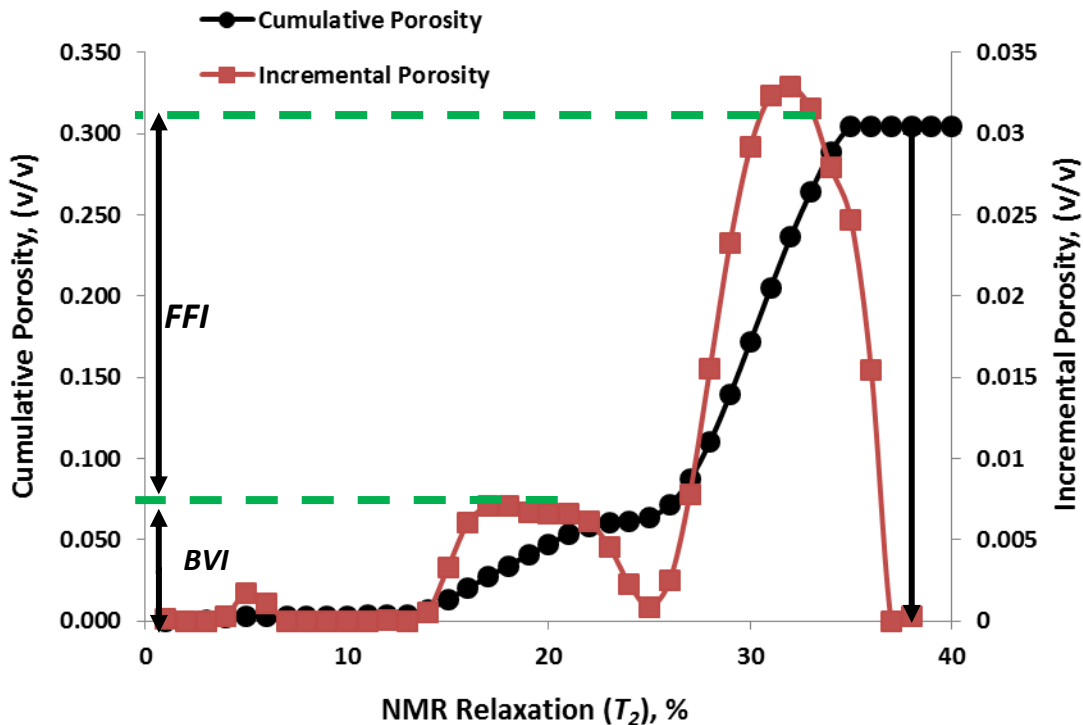


Figure 6.17: NMR T_2 relaxation plot for the Channel Storey Axis unit for a fully saturated sample. The green dash lines indicates the cut offs for estimating the FFI, BVI, corresponding S_{wirr} and total porosity determined from the cumulative porosity (sum of amplitudes) spectrum.

This confirms a good correlation between the NMR derived S_{wirr} and total porosity with the laboratory measured parameters. This was applicable to all dataset available for the study.

Based on classification from the various HFUs, average kappa values were estimated using the proposed relationships shown in equations 6.9 & 6.10 above. Nonlinear regression analysis for confidence interval and limits for kappa applicability for the various genetic reservoir units were performed. Table 6.5 presents averages of kappa values for the various genetic reservoir units defined for the deep water turbidite system. The calibrated kappa functions were used as input to generate capillary pressures from the NMR T_2 distribution.

Table 6.5: Averages of Genetic Unit based Kappa Values for NMR Capillary Pressure Modelling for the Turbidites/Deep Water Environment.

Genetic Reservoir Units	Minimum	Mean	Maximum
	Kappa κ , (psi Hg.secs)	Kappa κ , (psi Hg.secs)	Kappa κ , (psi Hg.secs)
Channel Lag	1.50	1.90	2.10
Channel Storey Axis	1.80	2.10	2.30
Channel Storey Margin	2.00	2.20	2.50
Inter-Channel Thin Beds (ICTB)	2.70	3.90	4.20
Mud-Rich Thin Beds (MRTB)	4.53	5.00	5.40
Levees/Overbank	6.40	7.50	8.20
Marine Mudstone	8.00	8.40	9.20

The modified relationship (equation 6.12) after Guodong J. *et al.*, (2012) was used to compute the wetting-phase saturation (S_w) corresponding to the NMR derived capillary pressures. Figure 6.18 through Figure 6.21 display plots of capillary pressures from NMR T_2 distribution and MICP.

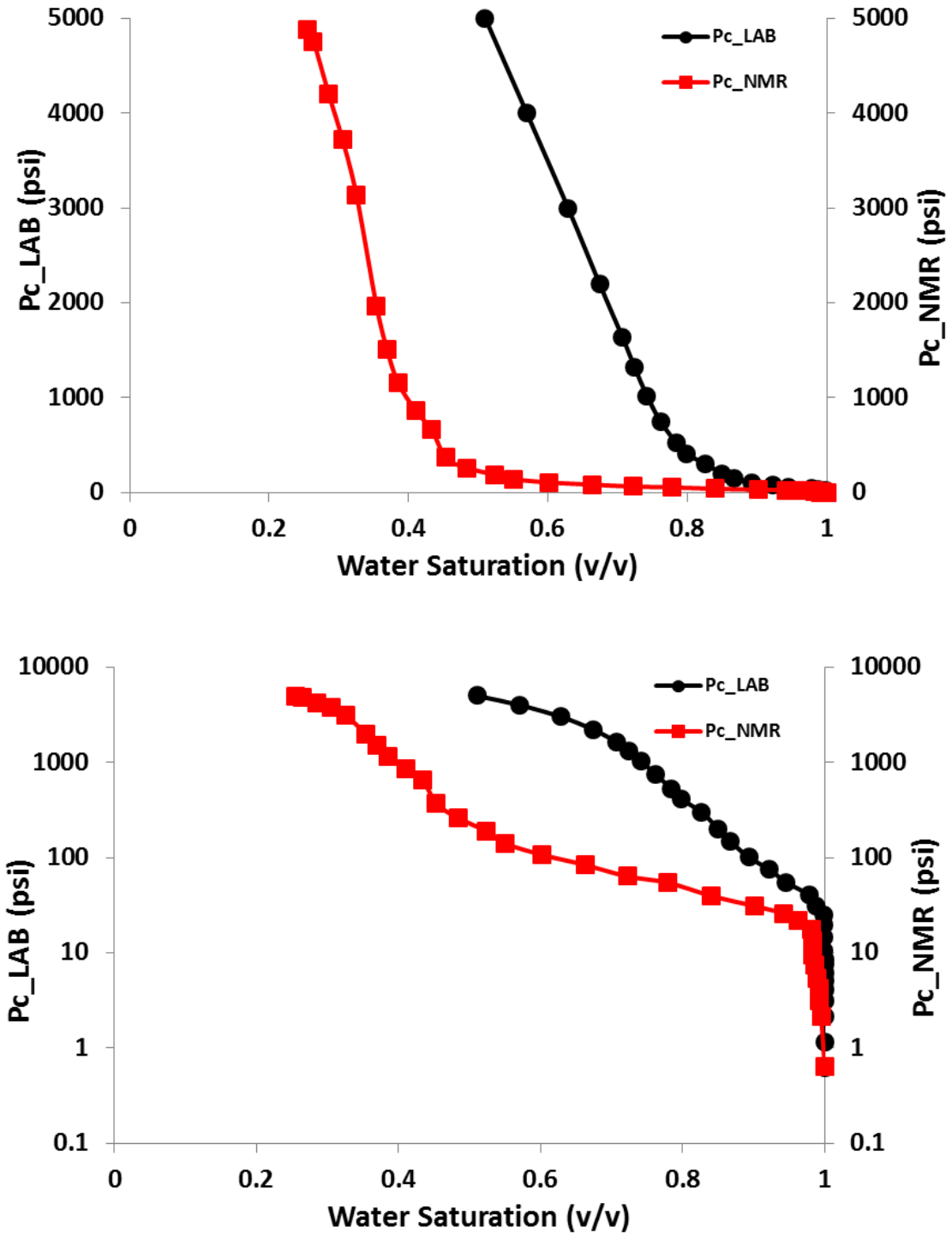


Figure 6.18: Measured capillary pressure (black) and NMR capillary pressure (red) for the Mud Rich Thin Bed Unit indicating a closer match between the entry pressures with much discrepancy with saturation (S_{wirr}). The semi-log plot (below) scales the plot for better estimates of entry/displacement pressures.

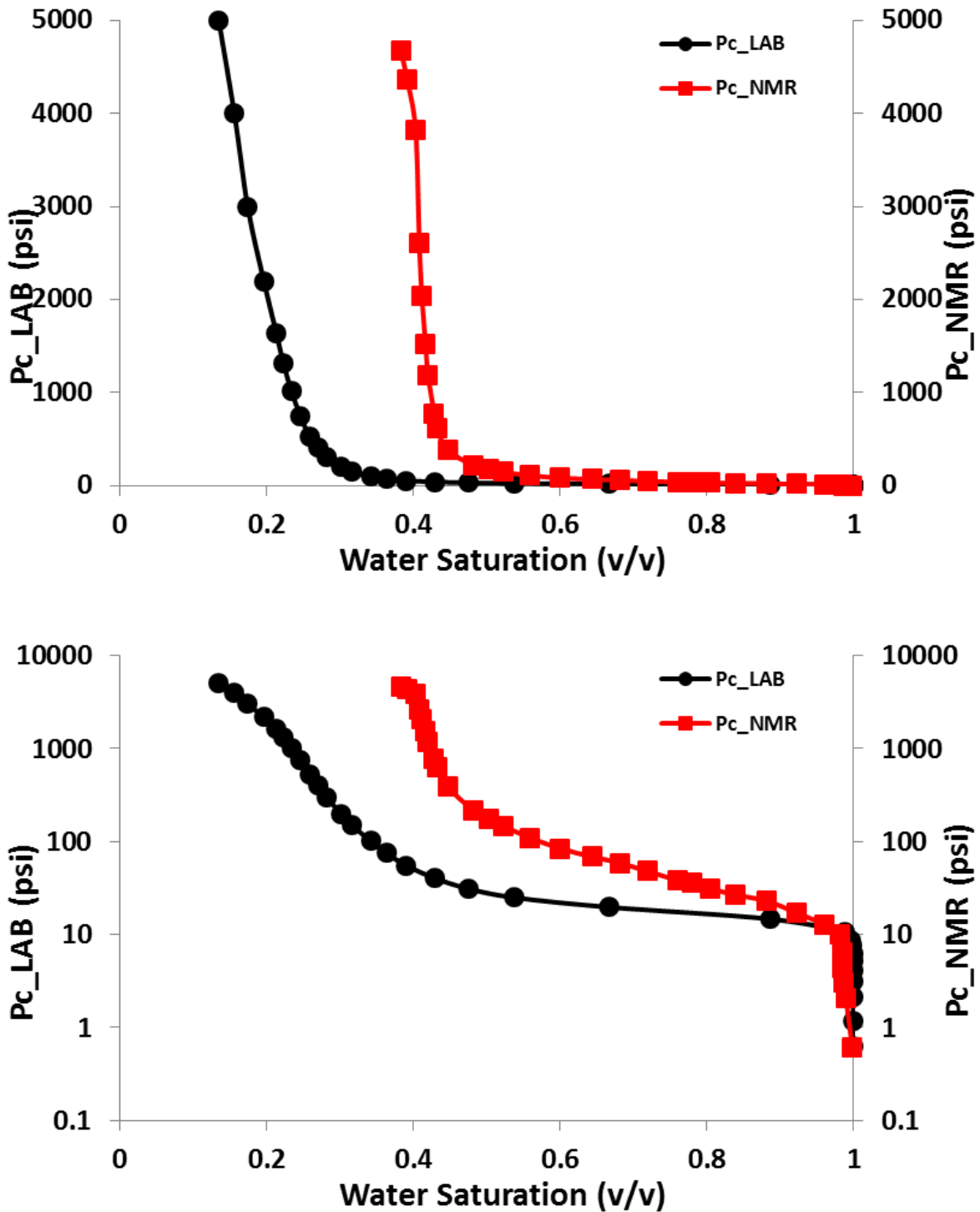


Figure 6.19: Measured capillary pressure (black) and NMR capillary pressure (red) for the Inter-Channel Thin Bed Unit indicating a closer match between the entry pressures with much discrepancy with saturation (S_{wirr}). The semi-log plot (below) scales the plot for better estimates of entry/displacement pressures.

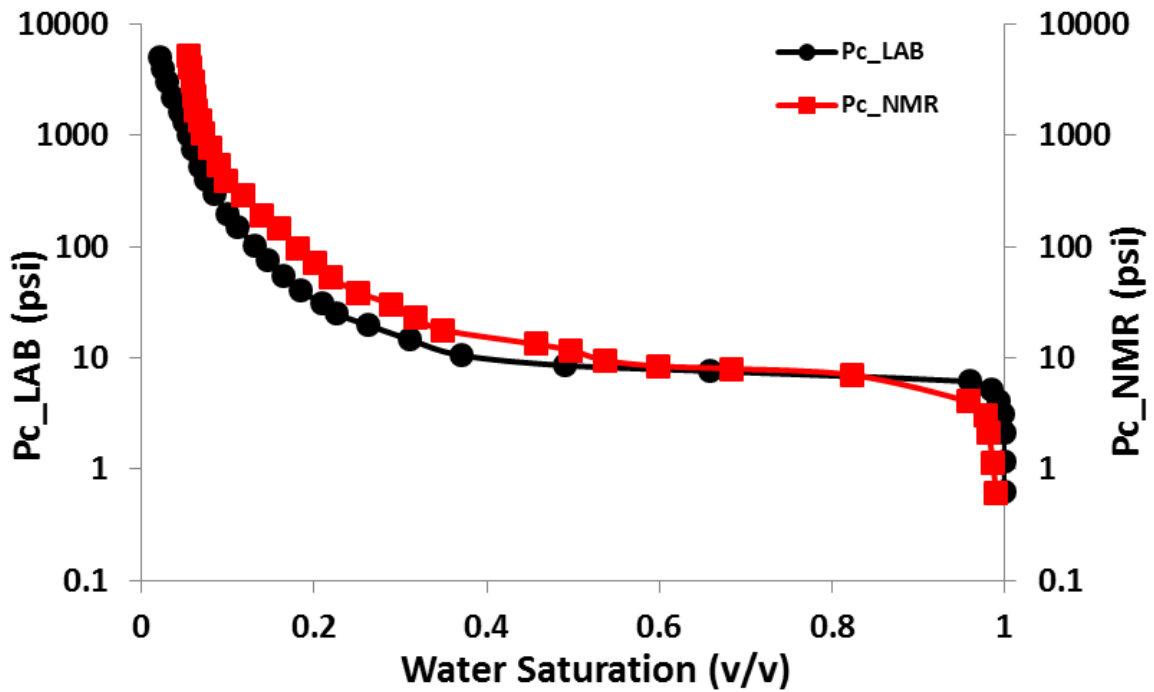
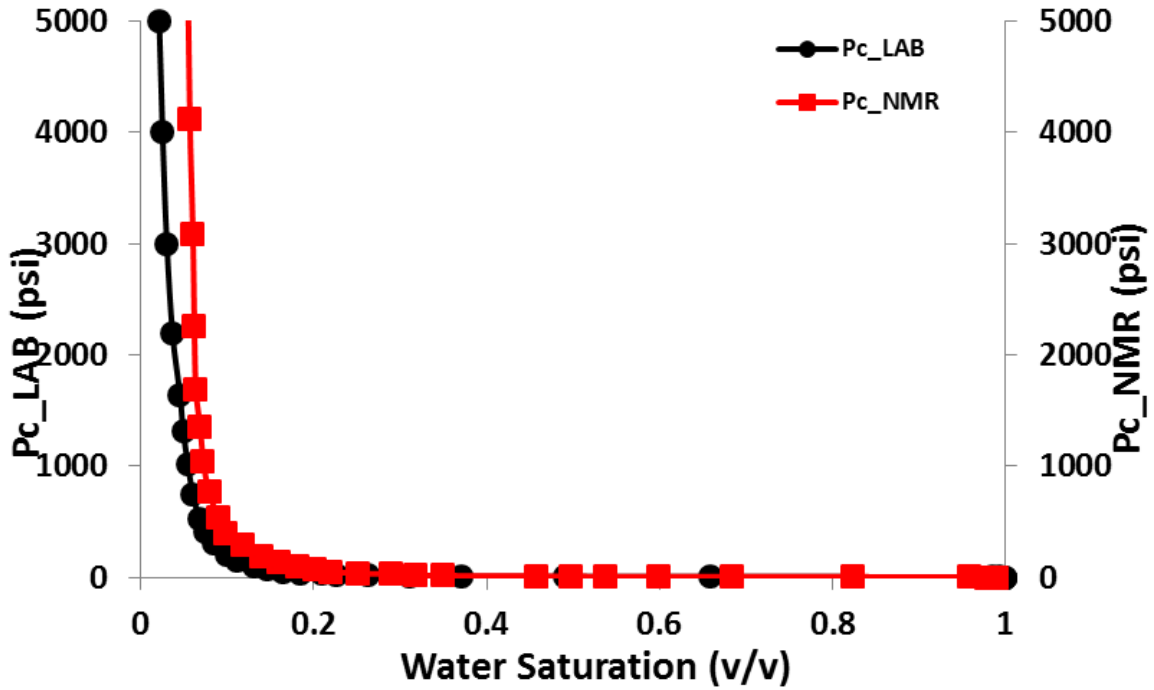


Figure 6.20: Measured capillary pressure (black) and NMR capillary pressure (red) for the Channel Storey Margin Unit indicating a closer match between the entry pressures with much discrepancy with saturation (S_{wirr}). The semi-log plot (below) scales the plot for better estimates of entry/displacement pressures.

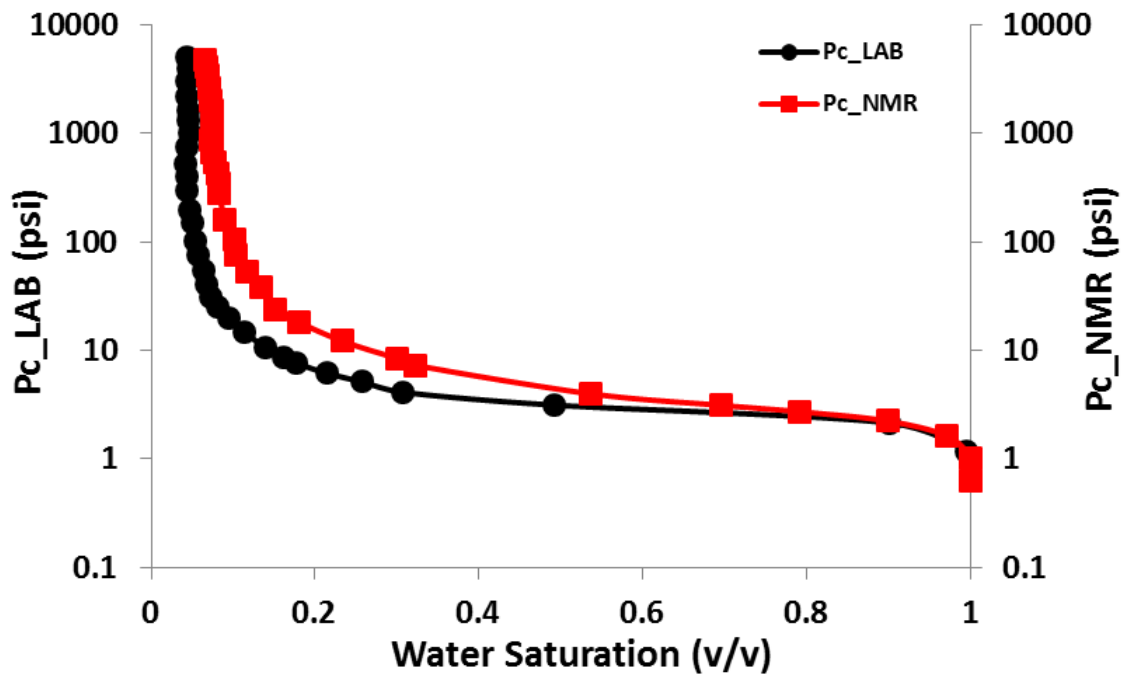
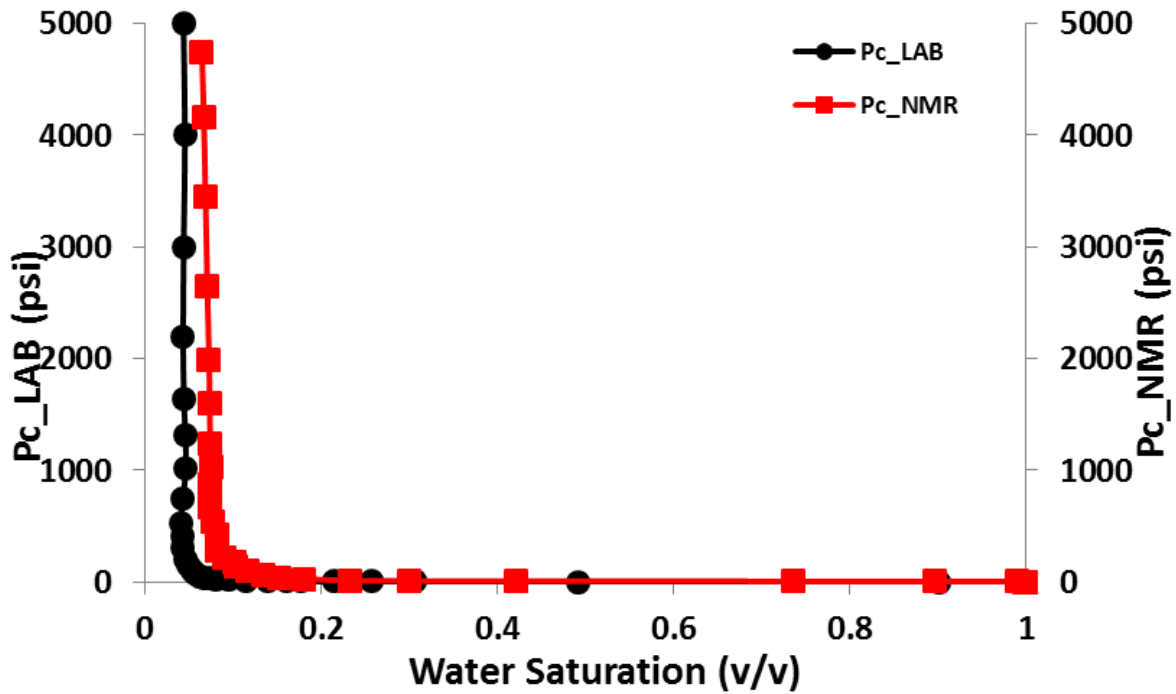


Figure 6.21: Measured capillary pressure (black) and NMR capillary pressure (red) for the Channel Storey Axis Unit indicating a closer match between the entry pressures with much discrepancy with saturation (S_{wirr}). The semi-log plot (below) scales the plot for better estimates of entry/displacement pressures.

As demonstrated for all dataset; NMR derived capillary pressure curve does not necessarily match the measured curve. The results differ in the initial entry capillary pressures and irreducible water saturation. This is due to the fact that the capillary pressure curves goes down to the irreducible water saturation (S_{wirr}) on the abscissa while the NMR derived curve goes almost to zero water saturation. The S_{wirr} contains up to the BVI fluid volume.

To achieve a match between the NMR derived capillary pressure curve and the laboratory measured curve, it is necessary to rescale the NMR saturation. This involves correction for root mean square (RMS) average of saturation differences between the NMR derived and laboratory measured saturation. As a measure of the fit quality for a given value of kappa, we introduced the average saturation error between the constructed NMR capillary pressure curve and the corresponding MICP.

This saturation is the root mean square (RMS) average of saturation differences:

$$S_w(P_c) - S_w(Kappa.T_2^{-1}).$$

Figure 6.22 present a plot of the measured water saturation (S_w') versus NMR saturation (S_{w-NMR}) for the inter-channel thin bed reservoir unit demonstrating a possible linear relationship between the response and predictor variable with a constant shifting parameter for the various genetic reservoir units.

The shift parameters for the predictor variable were calibrated for the specific genetic reservoir units within the Deep Water turbiditic environment. For this reason, the procedure is applied to several samples from which an average value for each coefficient can be obtained as shown in Figure 6.23 for S_w' versus S_{w-NMR} plot. This is equivalent to delivering a master equation or averaged curve.

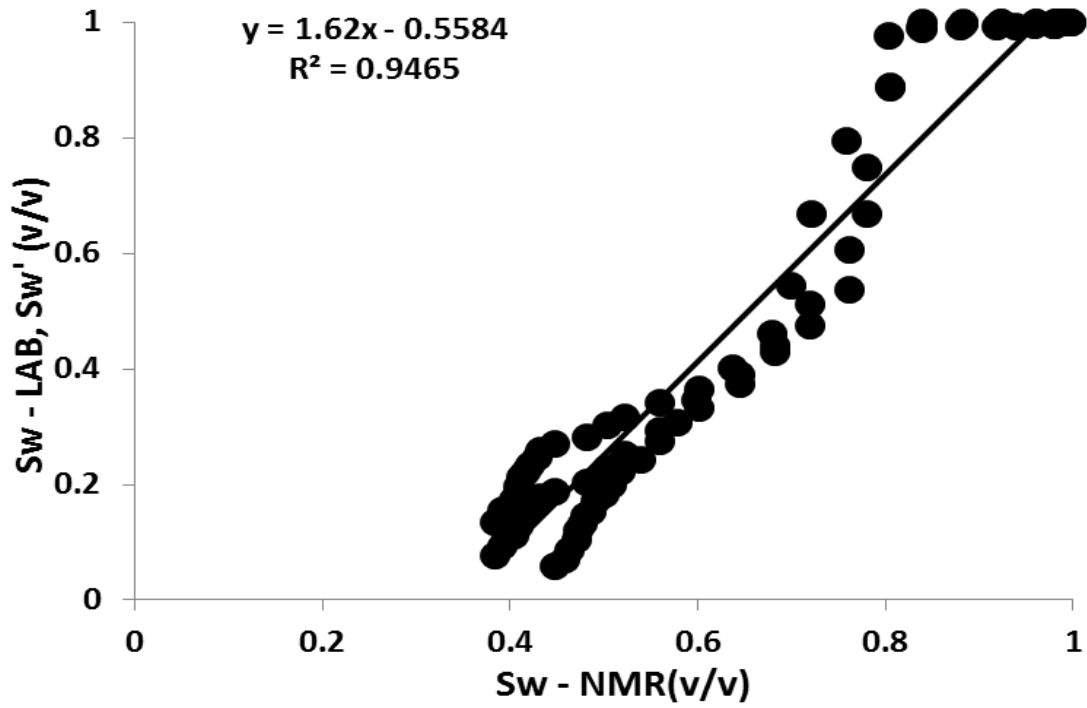


Figure 6.22: S_{w-LAB} versus S_{w-NMR} for all samples within the Channel Storey Margin unit.

The black thick line represents the average curve.

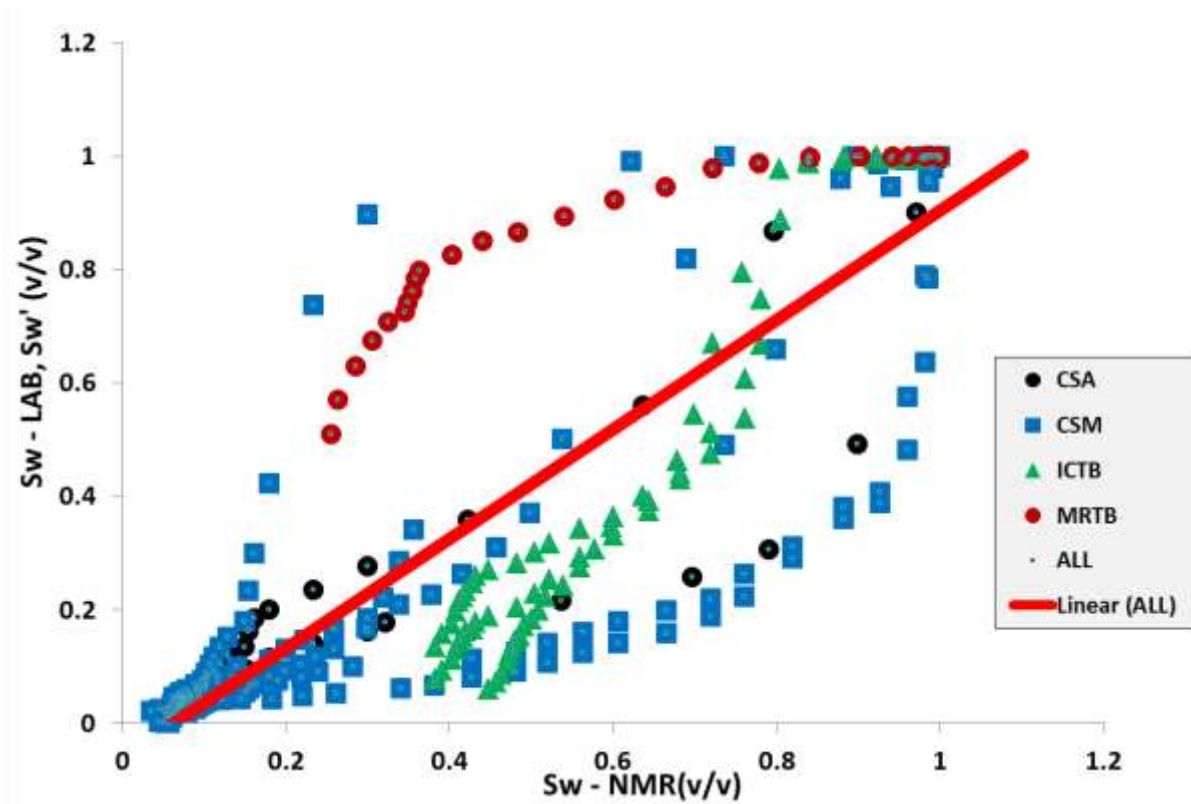


Figure 6.23: Plot of S_{w-LAB} versus S_{w-NMR} for all samples within the various genetic reservoir units. The red thick line indicates a possible averaging with various scaling factors for each unit.

Therefore the calibrated NMR saturation (S_w') can be expressed in form of a linear relationship as follows:

$$S_w' = A + B(S_{w-NMR} + C) \quad [6.14]$$

Where:

$$A = -0.2023,$$

$$B = 0.9893, \text{ and;}$$

$$C = \text{genetic unit based shifting scaling parameter (see table 6.6)}$$

Table 6.6: shows the results for the estimated coefficients

Genetic Reservoir Units	C
Inter-Channel Thin Beds (ICTB)	0.05
Channel Storey Axis (CSA)	0.29
Channel Storey Margin (CSM)	0.30
Mud-Rich Thin Beds (MRTB)	0.40

Figure 6.24 through figure 6.25 present plots of predicted capillary pressures and measured MICP. This demonstrates appreciable match with the measured core analysis dataset for all genetic reservoir units analyzed within the depositional environment. This was applicable to all dataset available for the study.

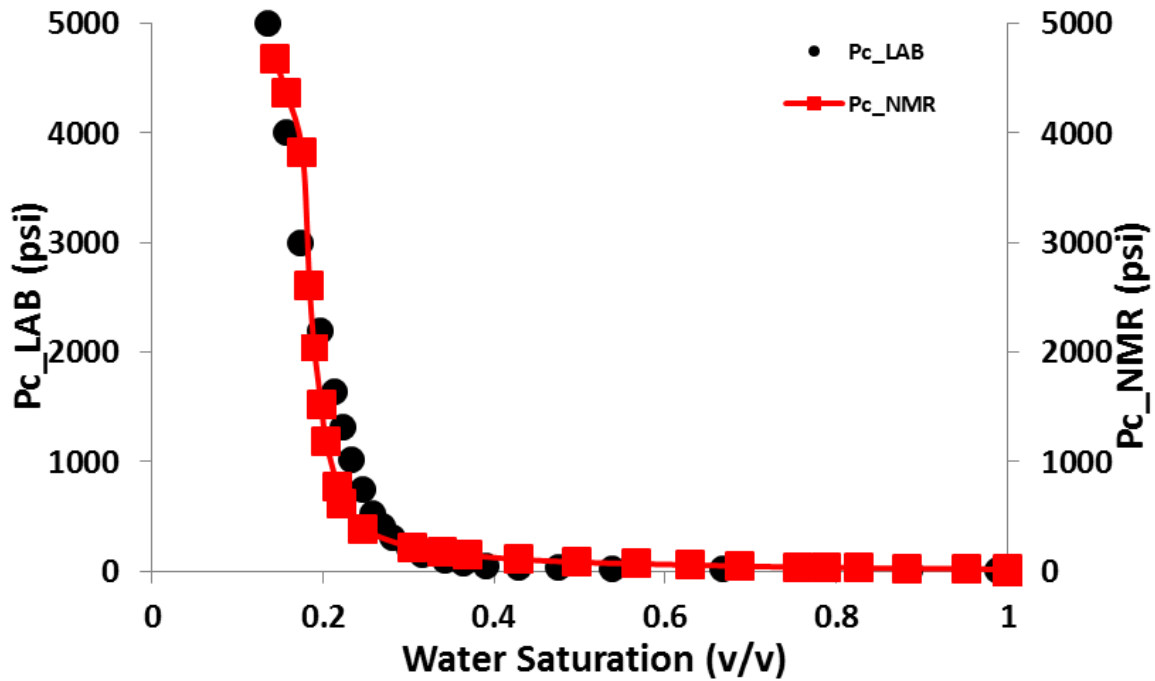
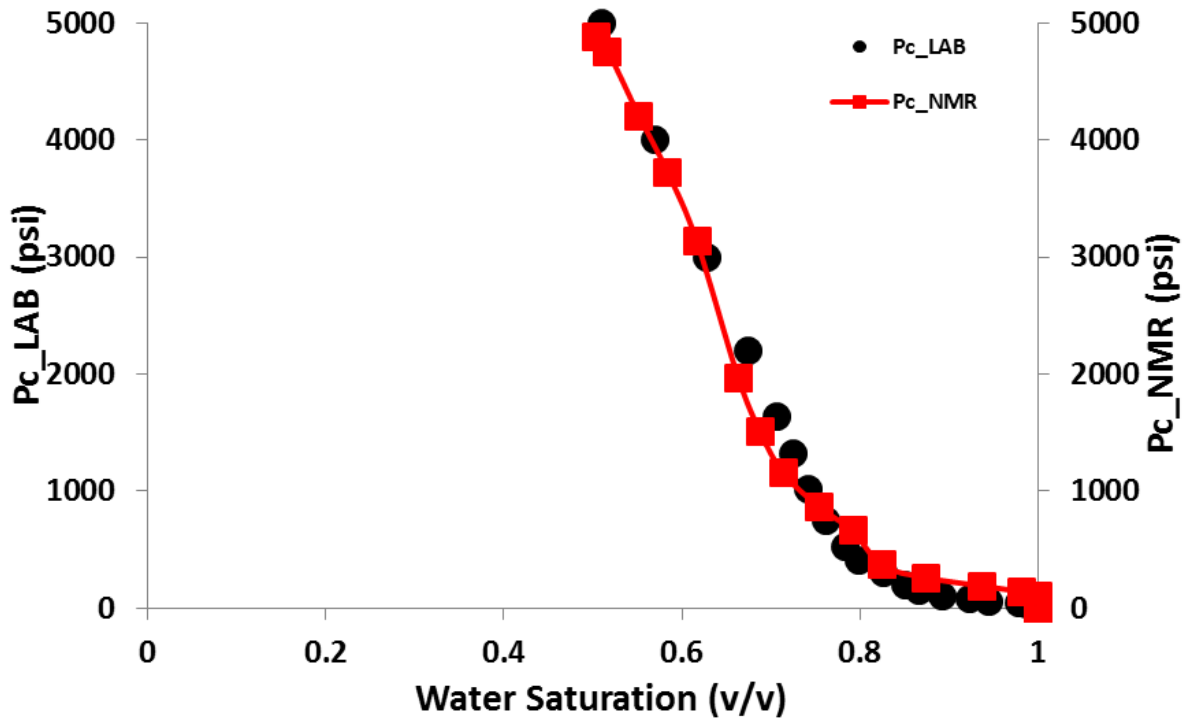


Figure 6.24: Calibrated Pc-NMR and Pc-LAB for the Mud Rich Thin Bed (Top) and Inter-Channel Thin Beds (Bottom) units indicating a good match in capillary attributes (entry pressures and irreducible water saturation).

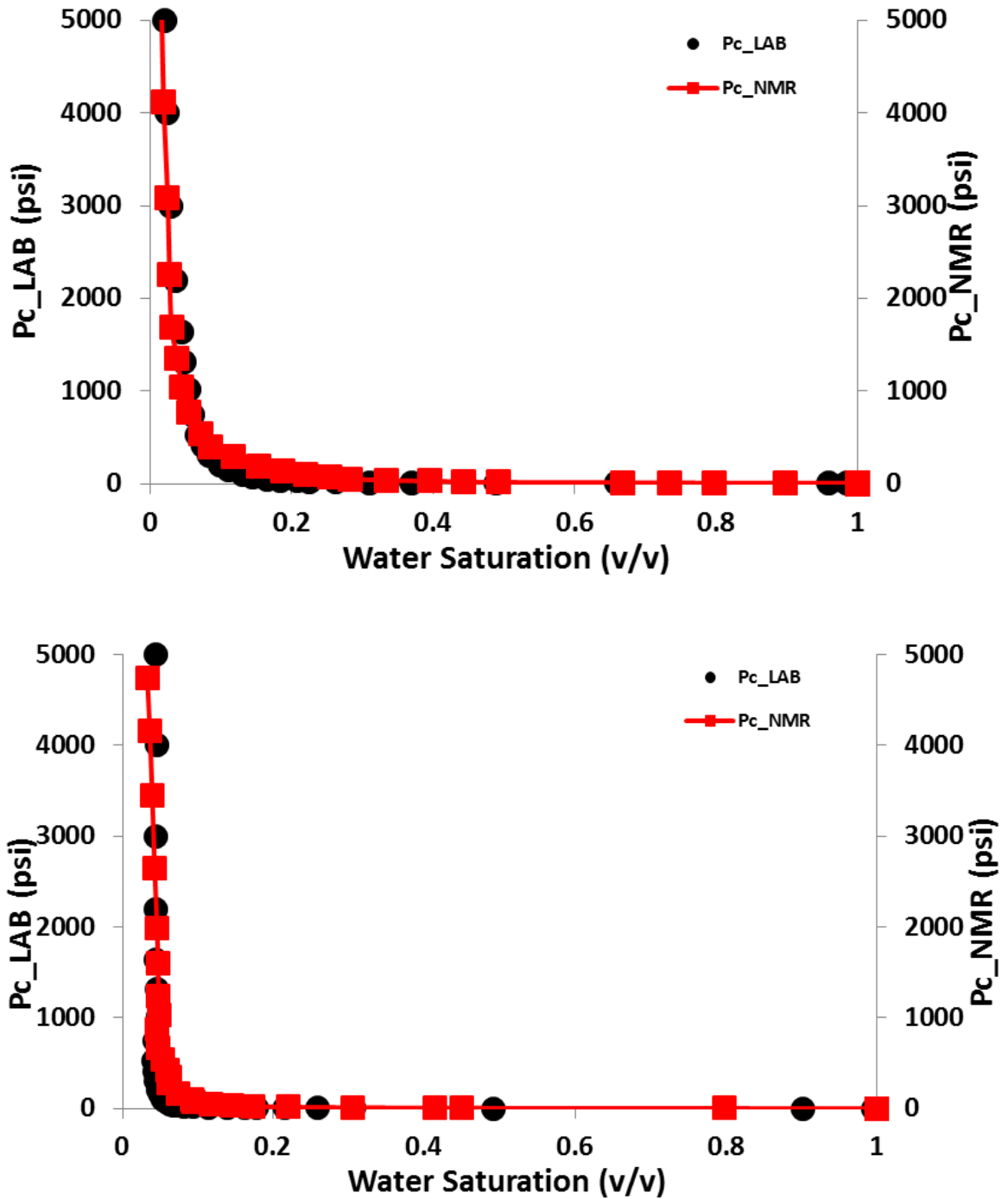


Figure 6.25: Calibrated Pc-NMR and Pc-LAB for the Channel Storey Margin (Top) and the Channel Storey Axis (Bottom) units indicating a good match in capillary attributes (entry pressures and irreducible water saturation)

Non-linear multiple regressions were performed using the proposed genetic units based kappa averages as input into the normalized pore throat permeability model. Figure 6.26 presents a petrophysical data log view of results of permeability estimates using the proposed genetic units based *kappa* averages, and compared to existing NMR based permeability predictors modelled after Coates and SDR. Permeability estimates were referenced to 75 measured core permeabilities from the Deep Water Canyon reservoir.

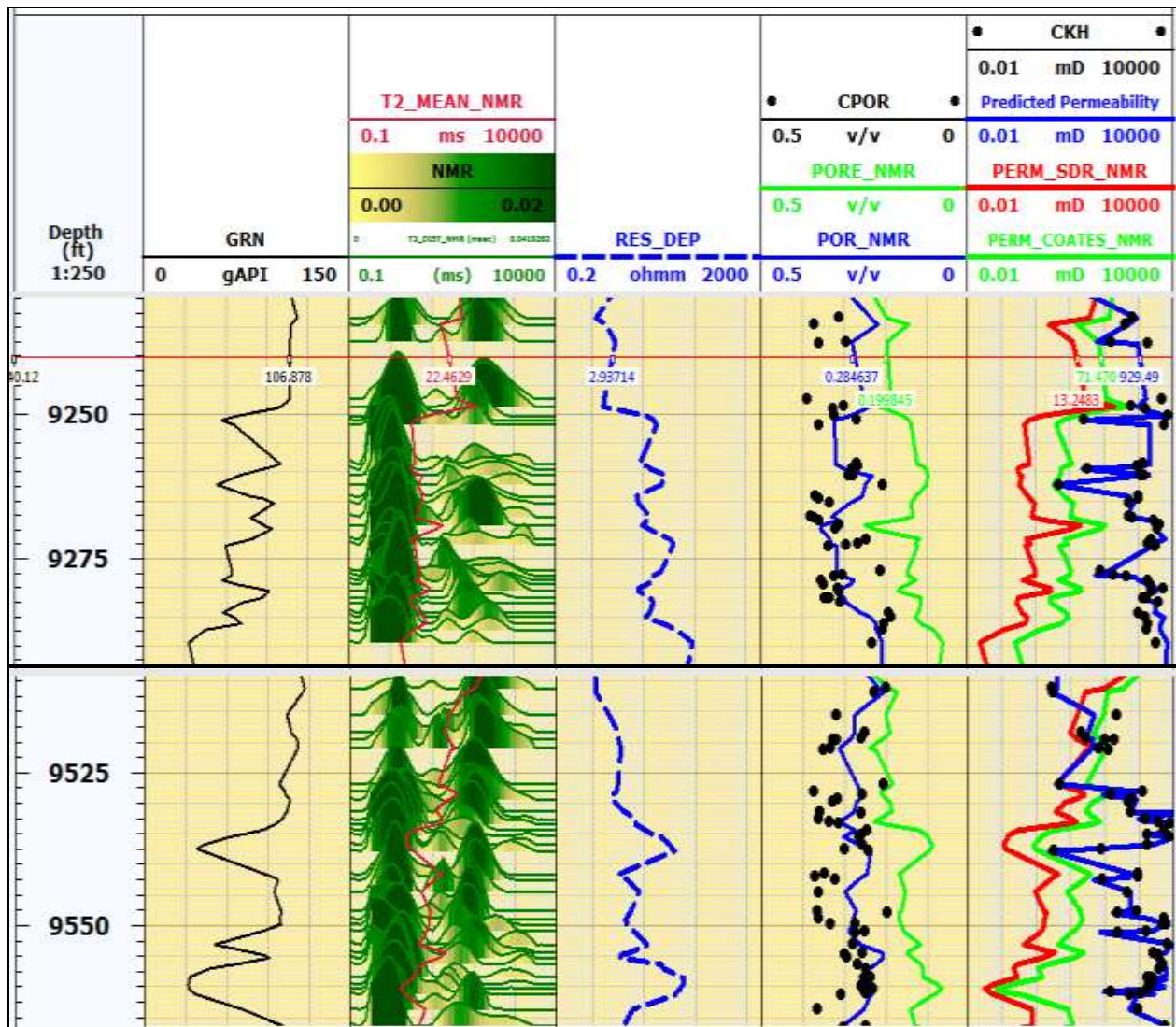


Figure 6.26: Petrophysical data view of two prolific hydrocarbon bearing zones within the low contrast and low resistive thin bedded turbidites. Track 5 presents a comparison of various permeability models indicating a good correlation between the proposed model and core derived permeabilites using 75 samples.

Statistical analysis demonstrates that the proposed P_c -NMR calibration methodology is more accurate in characterizing subsurface reservoir properties (Table 6.7). The proposed genetic unit based approach is represented with the dotted red lines indicating lower errors.

Table 6.7: Statistical analysis for various permeability models using NMR T_2 data

Statistical Parameters	Coates_NMR	SDR_NMR	Core PoroPerm	Proposed Model
Average Deviation, AD =	0.582	0.628	1.026	0.390
Average Absolute Deviation, AAD =	0.894	0.958	1.182	0.810
Maximum Error, Emax =	175.93	309.70	463.37	148.34
Average Absolute Percentage Relative Error, AAPRE =	36.52	40.78	50.06	34.45

Figure 6.26 and table 6.7 demonstrates the efficacy of the proposed methodology for improved reservoir characterization.

6.3.4 Genetic Unit Averages of Pseudo-Normalized Pore Throats and Model Upscaling

The preceding subsection presents analytical methodology for calibrating the estimating the normalized pore throat radius in the absence of core dataset. The main advantage would be that capillary pressures as well as pore throat distribution data can be acquired continuously and with sampling equal to that of the wireline logs. NMR T_2 array logs are usually not acquired conventionally in most wells drilled during field development phases as such availability of NMR dataset for all well drilled is questionable. To address this challenge, I present an upscaling of the model from core to well log scale; for application in uncored well intervals for various depositional environments within the study area. This seeks to develop genetic unit averages of pseudo normalized pore throat radius as input parameter to the proposed model for improved permeability modelling. The proposed $\overline{R_{tot}}$ model has been validated using approximately 1,000 corrected routine core analysis and corresponding well logs dataset at same formation depth interval.

6.3.4.1 Upscaling Model Formulation

The statistical analysis and practical significance of the normalized pore throat radius ($\overline{R_{tot}}$) based model for the clastic system indicates a confidence interval:

$$0.005 \leq \overline{R_{tot}} (\mu m) \leq 10, \text{ for limit of predictions (Haruna } et al., 2013 \& 2015).$$

Based on the above premise, two approaches were considered for evaluating the pseudo normalized pore throat radius as input to the proposed permeability model:

- i. Analysis of reservoir quality in reference to limits of practical significance for the normalized pore throats indicates a strong correlation. Core permeability versus porosity cross plots for all genetic units in each of the four distinct environment of deposition were analyzed to demonstrate the ranges of pseudo normalized pore throat radius. Only dataset measured at 400 psig were used to analyze for cross plot relationships. Figure 6.27 depicts distinctly that the various genetic reservoir units within the depositional environment possess characteristic $\overline{R_{tot}}$ ranges. This emphasizes possible hydraulically connected flow units.

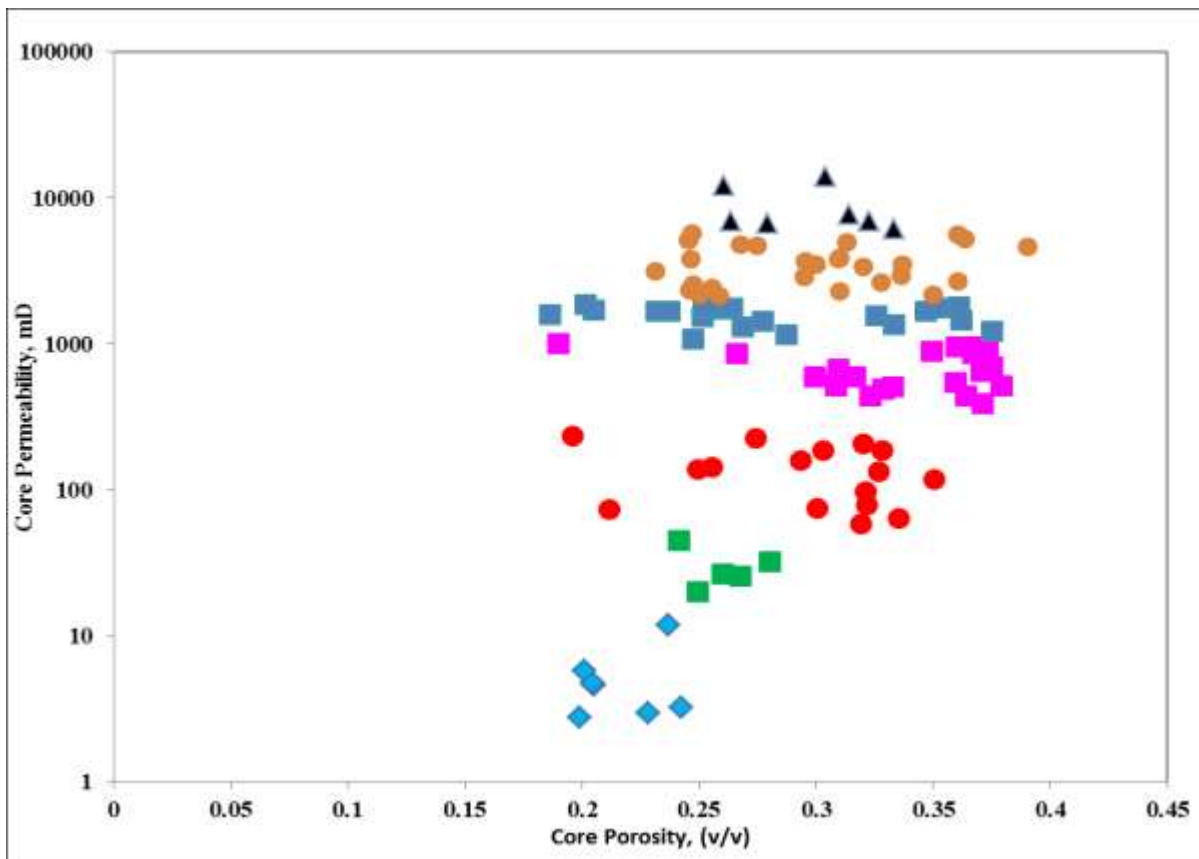


Figure 6.27: Plot of core permeability versus porosity for field X-turbiditic environment (genetic unit averages of R_{tot}). Relationship is biased to the normalized pore throat radius which demonstrates a strong correlation.

A summary of ranges of pseudo $\overline{R_{tot}}$ for the four distinct depositional environments within the deltaic Niger Delta clastic system are presented in tables 6.8, 6.9, 6.10 and 6.11.

Table 6.8: R_{tot} for the Continental/Fluvial Depositional Environment of the study area

Genetic Reservoir Units	Minimum	Mean	Maximum
	R_{tot} (microns)	R_{tot} (microns)	R_{tot} (microns)
Fluvial Channel Lag	8.34	9.00	9.61
Fluvial Channel Sandstone	5.32	6.00	7.10
Crevasse Splay Sandstone	3.70	4.00	4.40
Point Bar Sandstone	2.78	3.00	3.42
Coastal Plain Sandstone	1.80	2.00	2.43
Fluvial Channel Heterolithic	1.37	1.50	1.64
Bioturbated Channel Heterolithic	0.84	1.00	1.18
Stratified Channel Heterolithic	0.44	0.70	0.77
Point Bar Heterolithic	0.18	0.25	0.37
Coastal Plain Heterolithic	0.06	0.08	0.10
Coastal Plain Shales	0.02	0.03	0.04
Mud Shale	0.008	0.01	-

Table 6.9: R_{tot} for Turbiditic/Deep Water depositional environment of the study area

Genetic Reservoir Units	Minimum	Mean	Maximum
	R_{tot} (microns)	R_{tot} (microns)	R_{tot} (microns)
Channel Lag	8.23	9.00	9.67
Channel Storey Axis	5.40	6.00	7.30
Channel Storey Margin	3.60	4.00	4.90
Inter-Channel Thin Beds	1.80	3.00	3.35
Mud-Rich Thin Beds	0.63	0.70	0.84
Levees/Overbank	0.31	0.40	0.52
Marine Mudstone	0.01	0.10	0.23

Table 6.10: R_{tot} for Coastal/Distributary depositional environment of the study area

Genetic Reservoir Units	Minimum	Mean	Maximum
	R_{tot} (microns)	R_{tot} (microns)	R_{tot} (microns)
Foreshore	8.34	7.00	9.61
Distributary Channel Sandstone	5.32	6.00	7.10
Upper Shoreface Sandstone	3.70	5.00	4.40
Mouth Bar	2.78	4.00	3.42
Transgressive Lag	1.80	3.00	2.43
Transgressive Shoreface	1.37	2.00	1.64
Middle Shoreface	0.84	1.50	1.18
Bioturbated Channel Heterolithic	0.62	0.60	0.77
Stratified Channel Heterolithic	0.18	0.20	0.30
Proximal Lower Shoreface	0.06	0.10	0.19
Distal Lower Shoreface Heterolithic	0.02	0.04	0.06
Marine Shale	0.008	0.005	0.010

Table 6.11: R_{tot} for Tidal/Estuarine depositional environment of the study area

Genetic Reservoir Units	Minimum	Mean	Maximum
	R_{tot} (microns)	R_{tot} (microns)	R_{tot} (microns)
Estuarine Channel Lag	8.00	9.1	9.7
Estuarine Channel	5.80	6.00	8.20
Tidal Channel Bar	3.62	4.00	5.23
Tidal Channel Sandstone	2.56	3.00	3.60
Crevasse Channel	1.84	2.00	2.26
Estuarine Channel	0.80	1.00	1.37
Stratified Channel	0.28	0.50	0.73
Transgressive Sand	0.04	0.30	0.08
Tidal Flat	0.01	0.05	0.04
Marine Shale	0.008	0.01	-

- ii. Multiple non-linear regressions of genetic unit averages of pseudo $\overline{R_{tot}}$ for the distinct depositional environments demonstrates that comparing core derived permeability and $\overline{R_{tot}}$ predicted permeability, under-estimates the insitu measured permeabilities. This was applicable to the entire depositional environment. This is expected since the earlier works were based on dataset at core plug scale (equations 62 and 63). In essence, there is need for model upscaling to account for the discrepancies between the measured and predicted values. Traditionally, the Kozeny-Carman equation relates permeability to porosity and grain size:

$$K_{absolute} \approx d^2 \phi^3 \quad [6.15]$$

This form is frequently employed to mimic permeability versus porosity relationships, such as in Finney pack (Finney, 1970). The grain size “ d ” is typically kept constant during such calculations. Such approach introduces at least two errors: (a) the Kozeny-Carman equation is based on an idealized solid medium with pipe conduits, rather than a realistic granular medium and (b) even if a grain size is used, it is obvious that it varies with varying porosity.

Bearing this argument in mind, I explored how permeability can be predicted consistently within the Kozeny-Carman formalism, by varying the radii of the conduits, their number, and type for effective modelling of the subsurface reservoir. This requires additional assumptions, specifically, regarding tortuosity evolution during porosity reduction.

In the end, I arrived at a normalization of the $\overline{R_{tot}}$ using a grain to pore volume (φ_z) ratio (Haruna *et al.*, 2015):

$$\log_{10} K = a \log_{10} \overline{R_{tot}} \varphi_n + b \quad [6.16]$$

The single constant “a” characterizes the normalized pore throat radius for the clastic system analyzed, with the coefficients: a = 1.913 and b = 2.342.

The parameter, φ_n termed the normalized grain volume to pore volume ratio is given by:

$$\varphi_n = 0.3 \left(\frac{1-\varphi}{\varphi} \right) \quad [6.17]$$

This accounts for the specific surface area of the porous medium (specific pore volume) or the total area exposed within the pore space per unit of grain volume. α -level of 0.05 was chosen to verify the statistical significance of the coefficients in the proposed relationship between the response and predictor variable ($\overline{R_{tot}} \varphi_n$).

The p-values were strictly below the α -levels, and hence the sample statistic of the proposed model proves to be too unlikely to have occurred by chance.

6.3.4.2 Application of the pseudo normalized pore throat radius to Reservoir Characterization Using the Niger Delta clastic reservoirs as Case Study

The dataset for this work stems from four (4) distinct geological environments of deposition: the Continental/Fluvial, Coastal/Distributary, Tidal/Estuarine and Turbiditic/Deep water environments; within the deltaic deposits of the Cenozoic Niger Delta; ranging in age from Middle to Late Miocene. The wide range in dataset is aimed at creating a representative database to honor the depositional fabric and diagenetic

overprint of the study area. The proposed genetic unit averages of pseudo $\overline{R_{tot}}$ model was validated using dataset from the four (4) Fields within various depositional environment of the Niger Delta. In each case, the core permeability was measured using a nitrogen gas under a sleeve pressure of 400 psig permeameter and was corrected for the Klinkenberg effects. Figure 6.28 through figure 6.30 depicts the data obtained from the various depositional environment employed for this work. These include well logs: caliper, gamma ray, bulk density, neutron, resistivities and NMR; detailed geologic core description, stress corrected porosities and air permeabilities were available from routine core analysis.

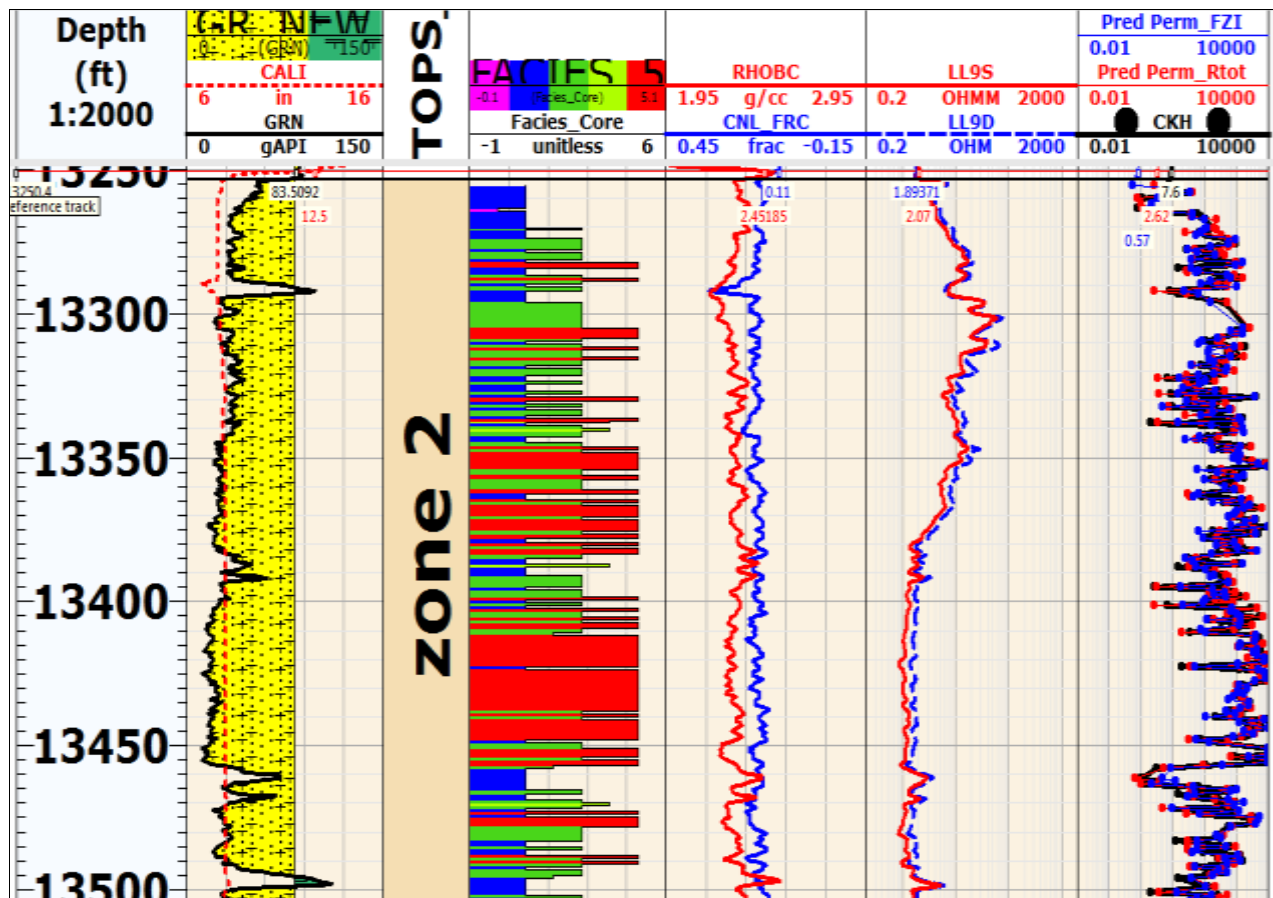


Figure 6.28: Petrophysical Data Log for Field W- Continental/Fluvial environment indicating cored intervals and varying facies association.

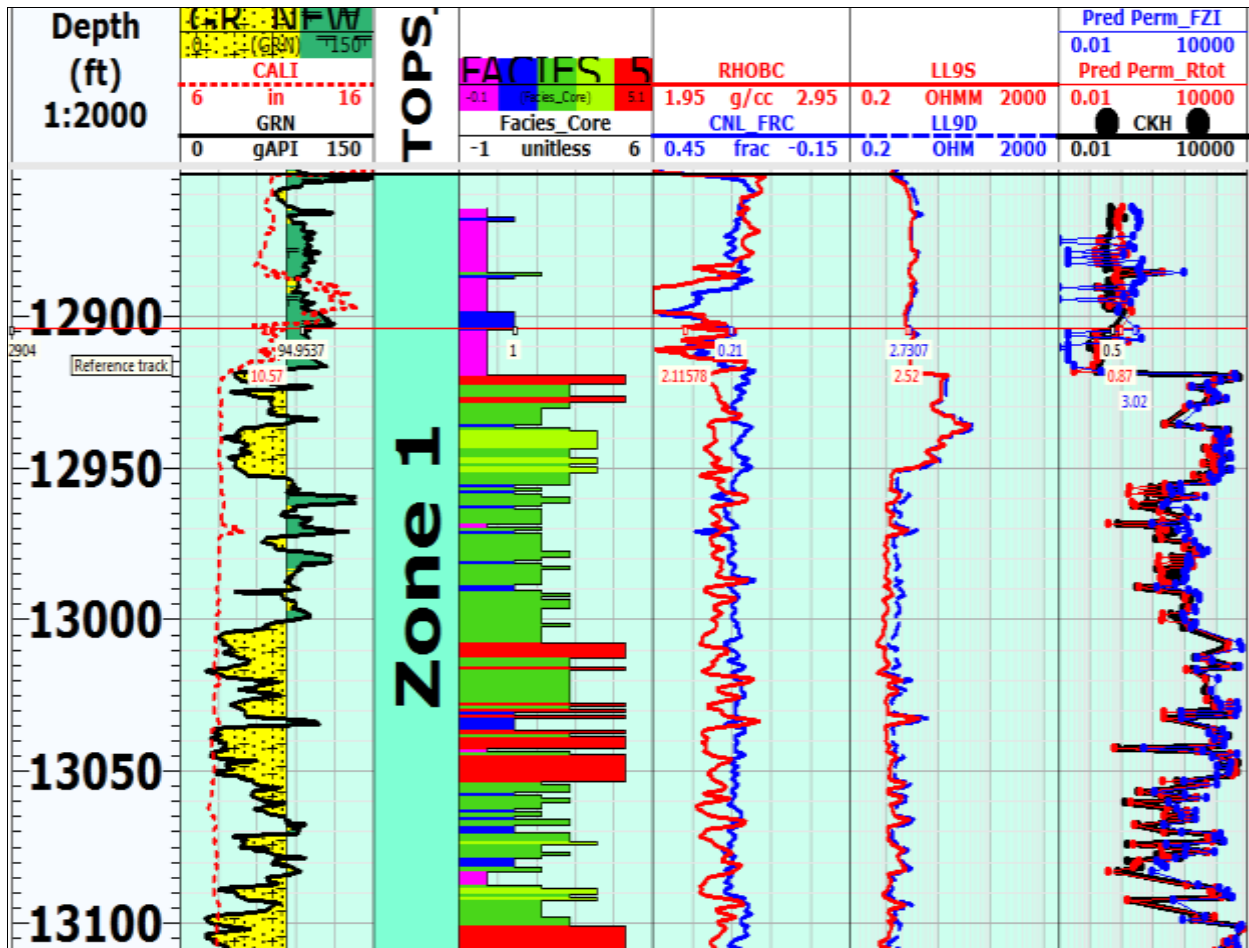


Figure 6.29: Petrophysical Data Log view for Field X- Turbiditic/Deep Water environment indicating cored interval and varying facies association.

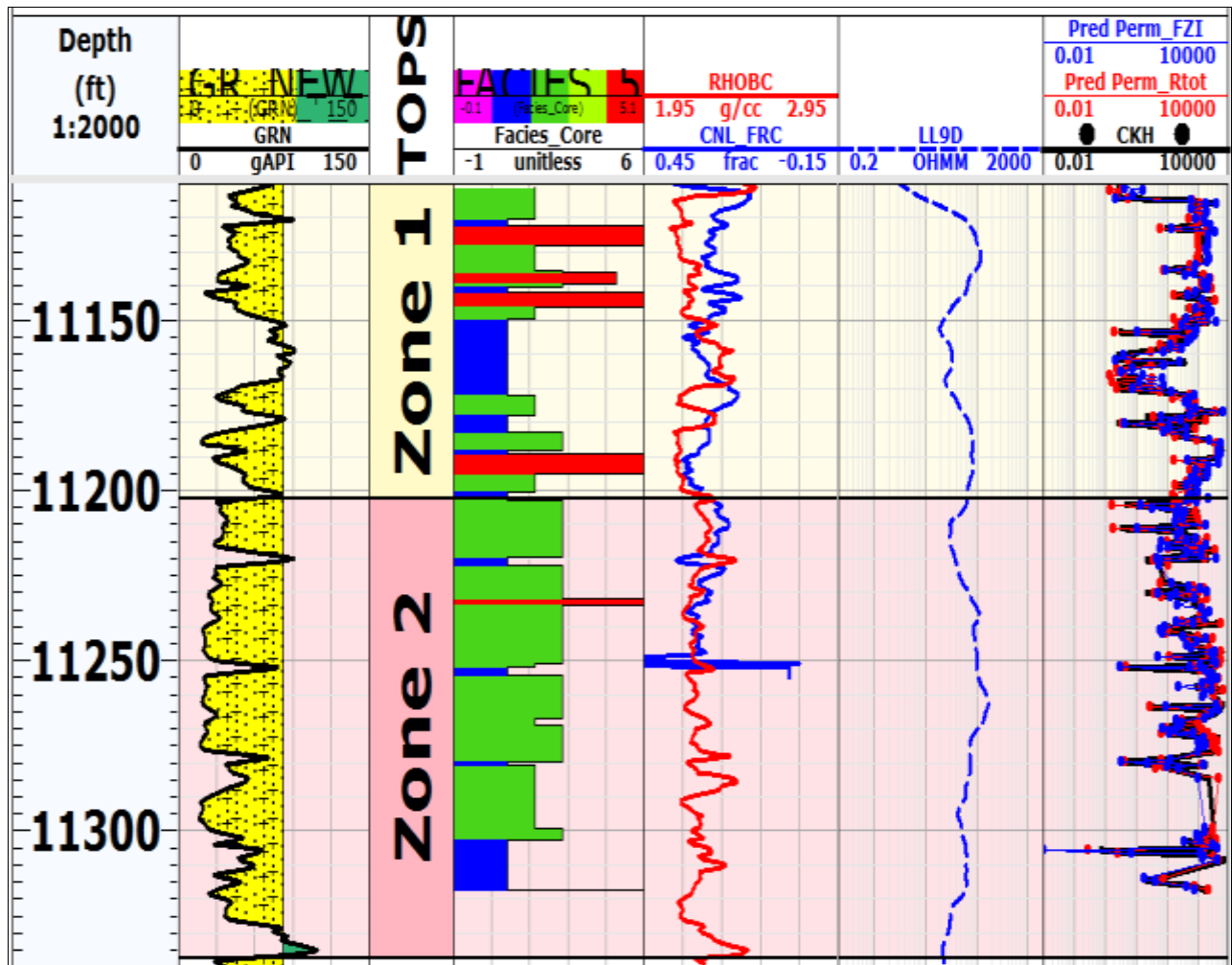


Figure 6.30: Petrophysical Data Log (PDL) view for Field Y- Coastal/Distributary environment showing cored interval and varying facies association.

A comparative evaluation of the proposed and existing permeability correlation based on Genetic Unit Averages of Flow Zone Indicators (FZI's) and Neural Networks for Niger Delta (Uguru *et al.*, 2005) was performed to evaluate the competence and applicability of the proposed model.

Track 7 of figures 6.28, 6.29 and 6.30 displays a depth plot of the proposed model; existing genetic units based FZI and cored permeabilities model indicating reasonable relationship within various depositional environments.

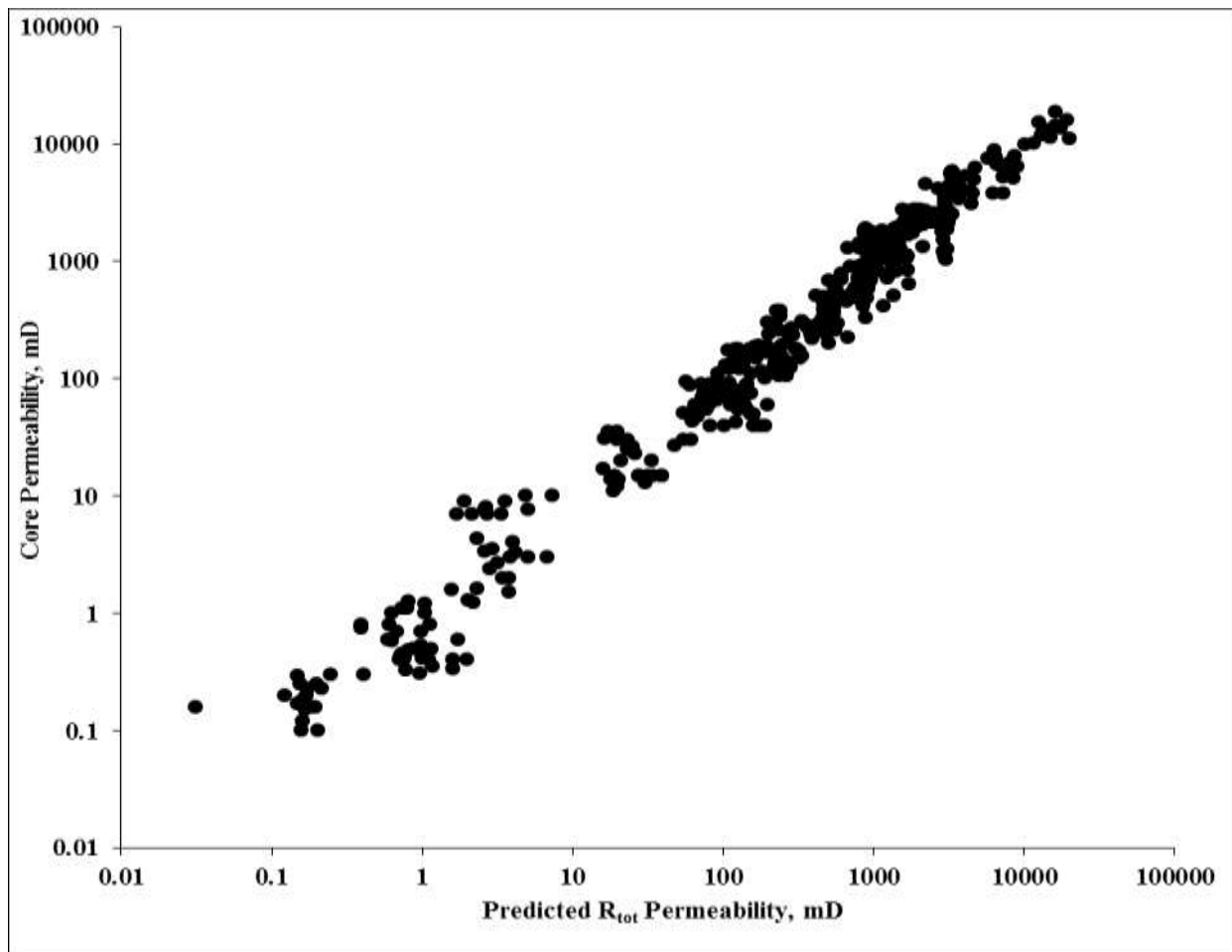


Figure 6.31: Plot of measured permeability versus $\overline{R_{tot}}$ predicted permeability for Field 'W'-Continental/Fluvial environment indicating appreciable correlation

444 measured core permeabilities were obtained from two (2) separate reservoirs from Field “W” - Continental/Fluvial Environment (figure 6.28). A plot of the measured versus predicted permeabilities (figure 6.31) results in an excellent adjusted correlation coefficient (R^2) of 0.97 and root mean square error (RMSE) of 0.01.

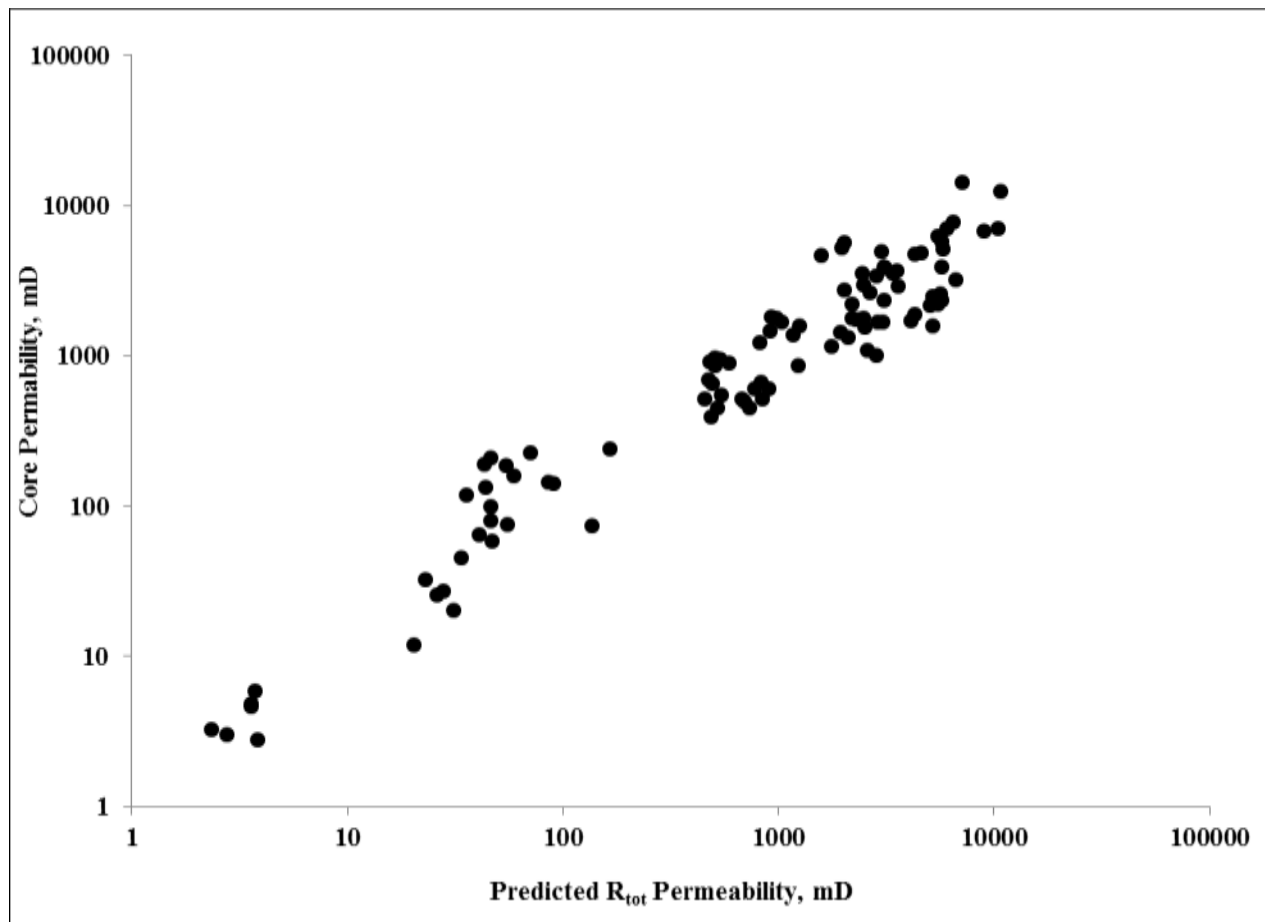


Figure 6.32: Plot of measured permeability versus $\overline{R_{tot}}$ predicted permeability for Field ‘X’- Turbiditic/Deep Water environment indicating appreciable correlation.

Field “X” located within the Turbiditic/Deep water offshore depositional environment has 103 measured core dataset covering two (2) prolific canyon reservoirs (figure 6.29). A

plot of the corrected core permeability versus predicted permeability gave an adjusted R^2 of 0.93 and RMSE value of 0.092 (figure 6.32).

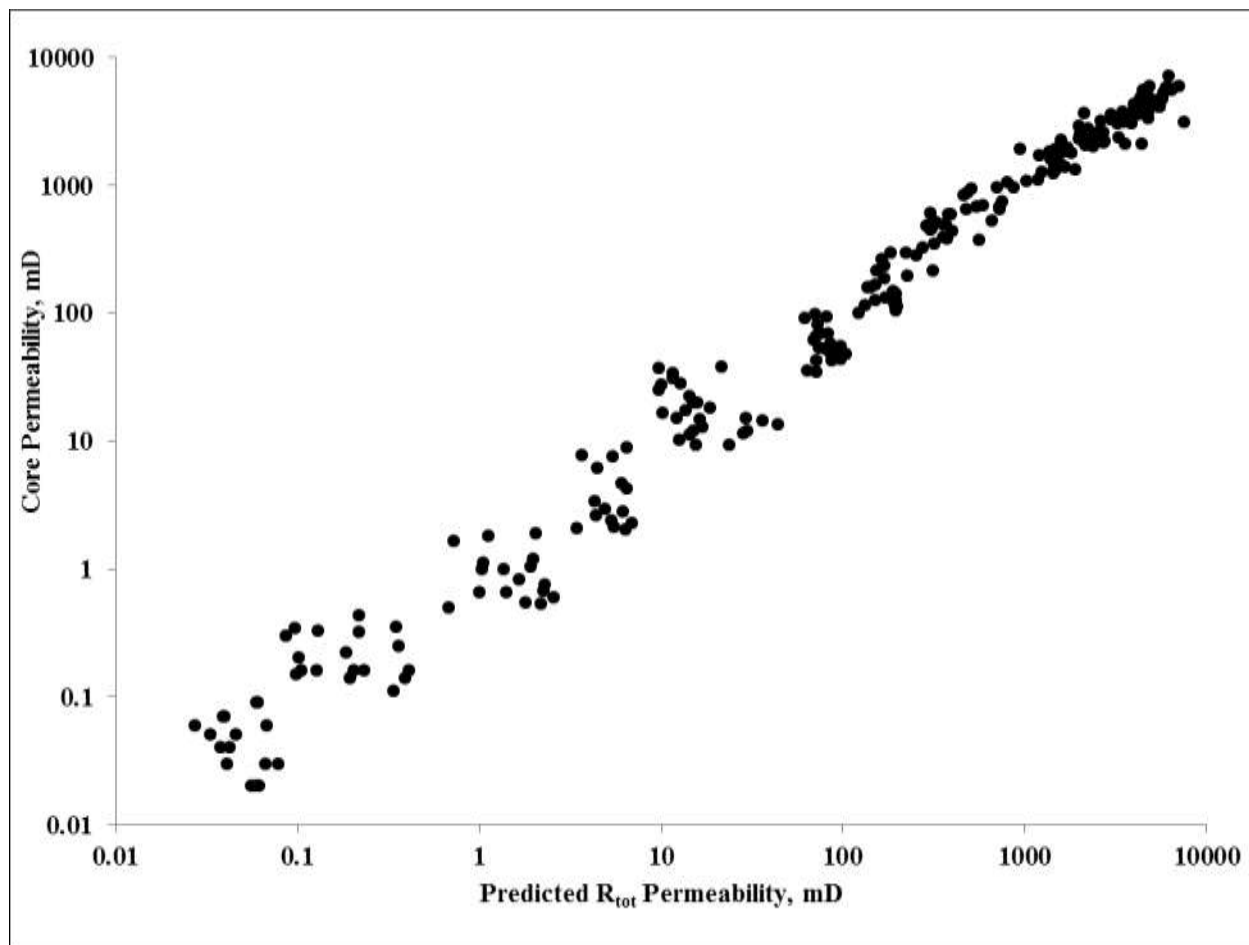


Figure 6.33: Plot of measured permeability versus $\overline{R_{tot}}$ predicted permeability for Field 'Y'- Coastal/Distributary environment indicating appreciable correlation.

205 routine core analysis dataset were also obtained from two (2) wells within the Coastal/Distributary Depositional Environment – Field “Y” (figure 6.30) at different depth intervals. Plot of the corrected core permeability versus predicted permeability gave an adjusted R^2 of 0.964 and RMSE value of 0.021 (figure 6.33).

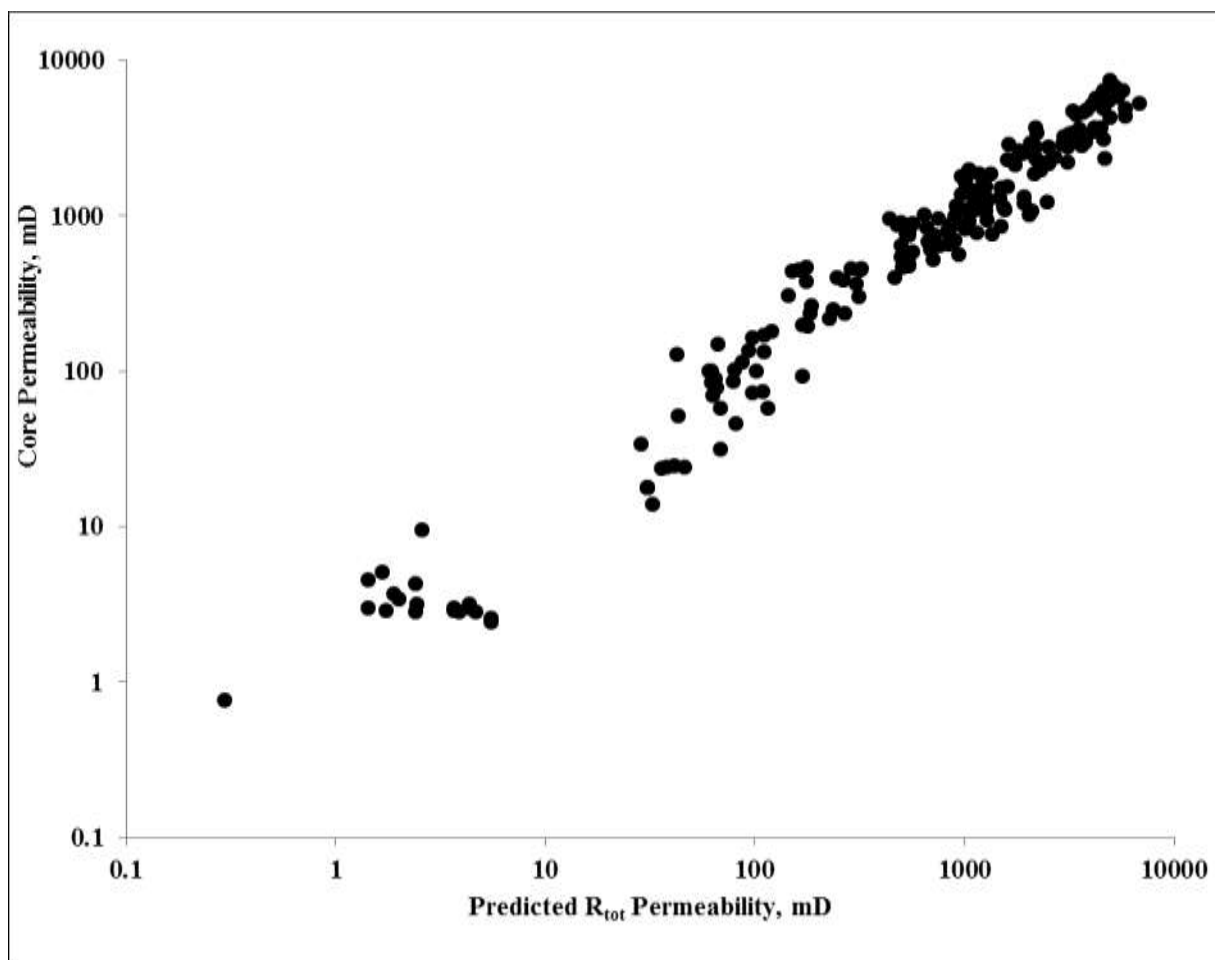


Figure 6.34: Plot of measured permeability versus $\overline{R_{tot}}$ predicted permeability for Field ‘Z’- Tidal/Estuarine environment indicating appreciable correlation.

Finally, the proposed model was applied to Field “Z” with 255 core dataset obtained from two (2) wells within the Tidal/Estuarine Environment. Figure 6.34 shows a plot of the measured versus predicted permeabilities, showing adjusted R^2 of 0.979 and RMSE of 0.010.

Furthermore, figures 6.35, 6.36 and 6.37 shows corresponding plots for corrected measured permeability versus FZI based permeability for various depositional systems applicable to this work.

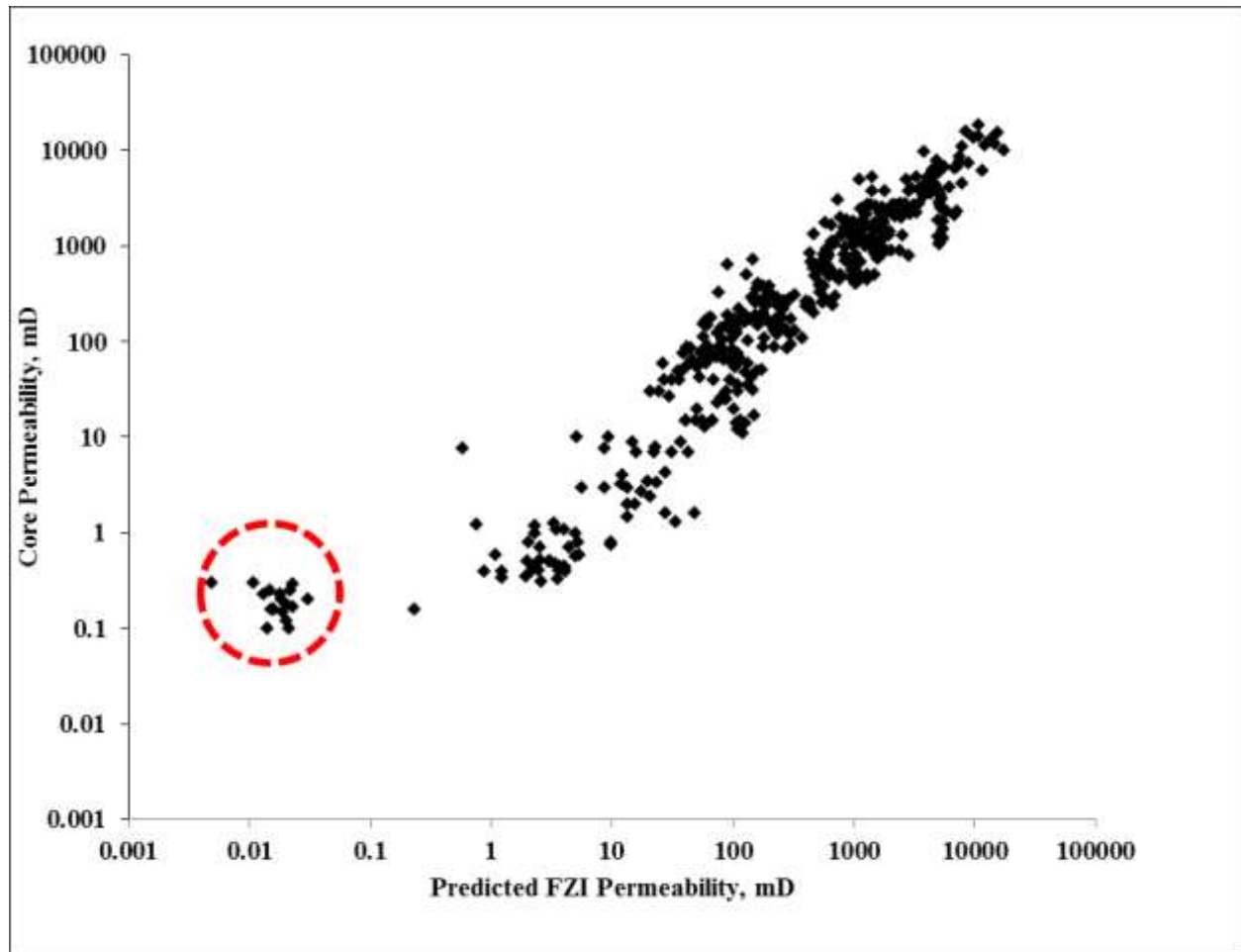


Figure 6.35: Plot of measured permeability versus FZI predicted permeability for Field 'W'- Continental/Fluvial environment. Highlighted in red indicates deviation and over-estimation of predicted permeabilities within the poorer rock facies within the unit.

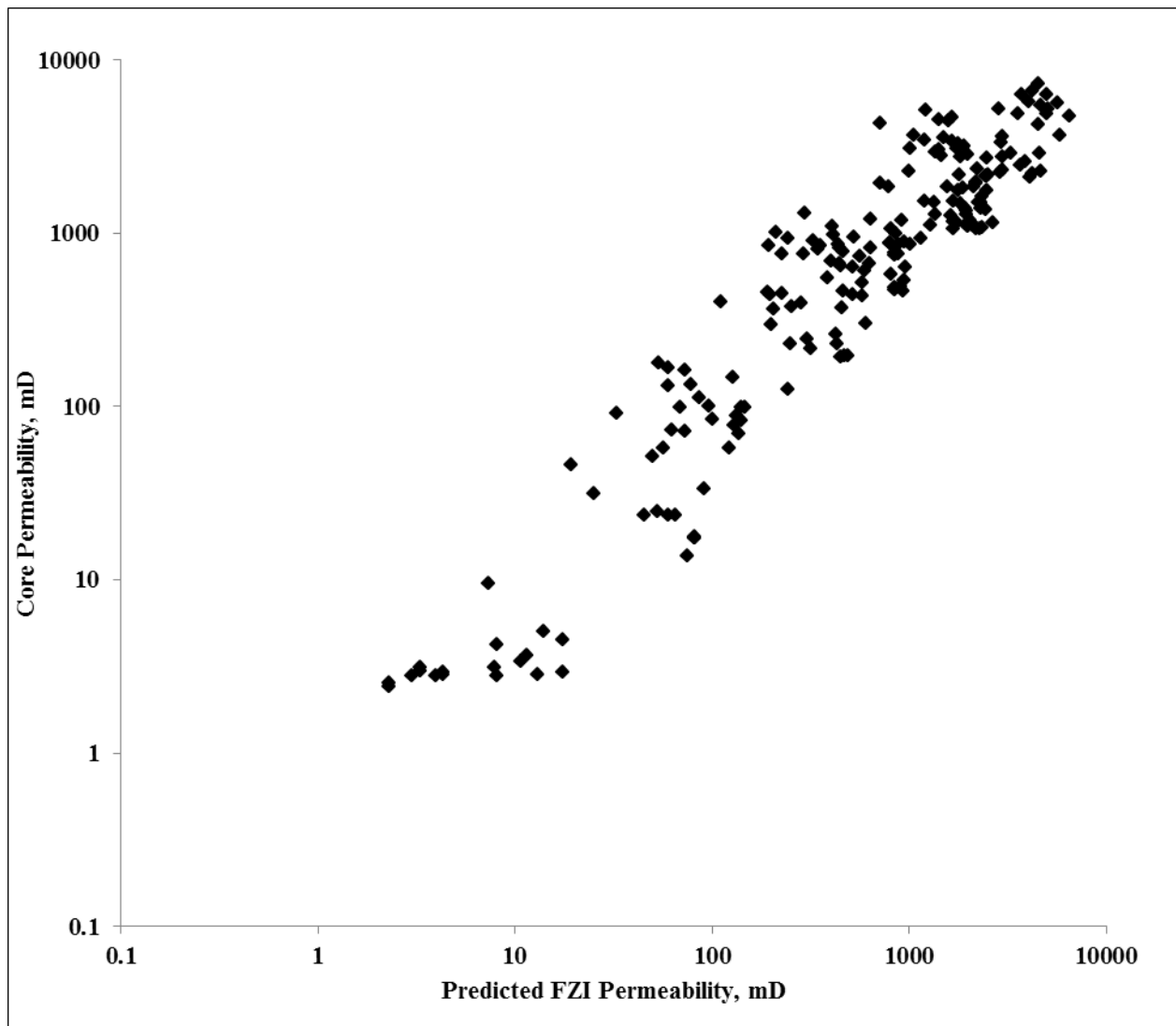


Figure 6.36: Plot of measured permeability versus FZI predicted permeability for Field 'Y'- Tidal/Estuarine environment. Large scatter indicates poorer correlation within the unit.

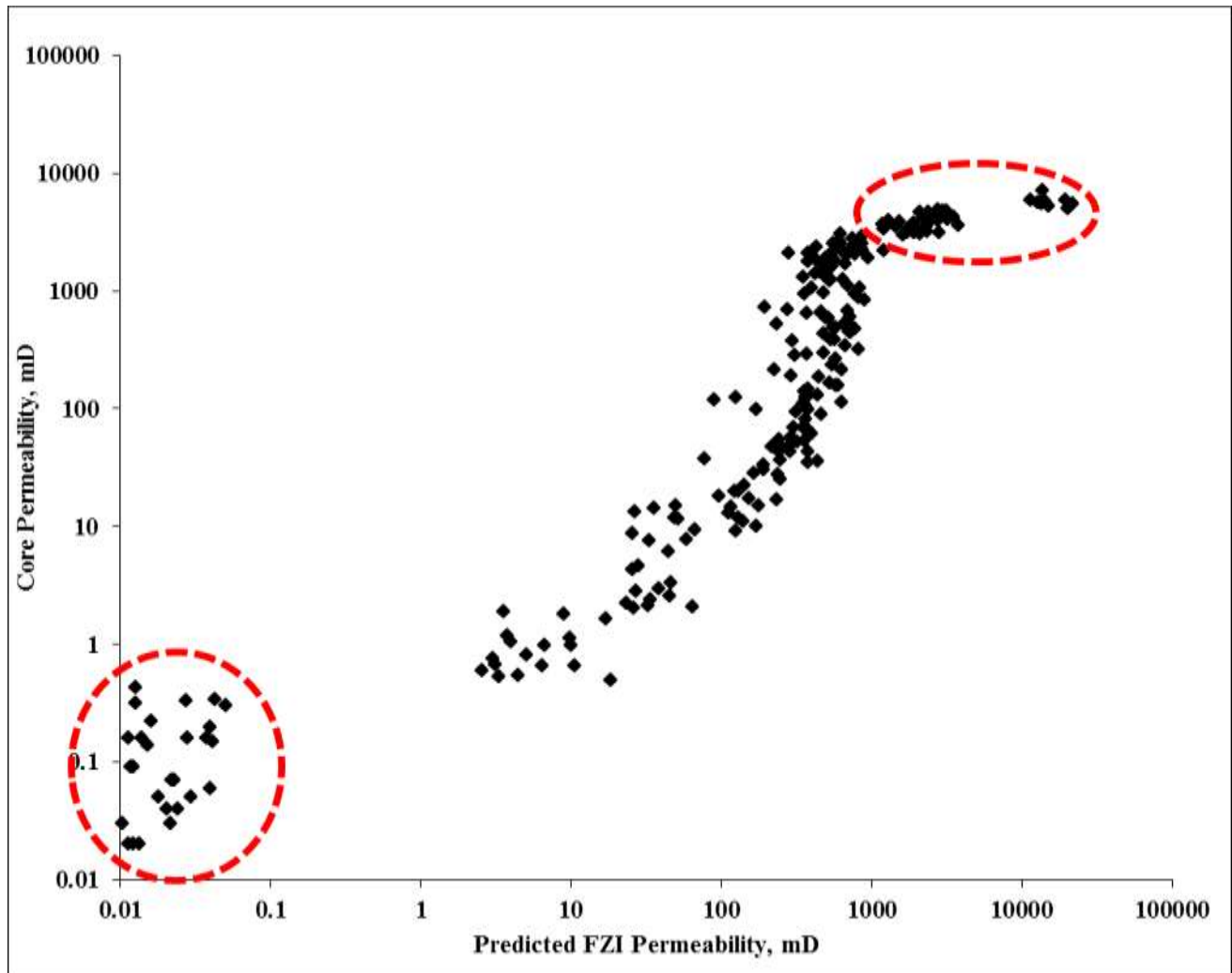


Figure 6.37: Plot of measured permeability versus FZI predicted permeability for Field 'Z'- Coastal/Distributary environment. Highlighted in red demonstrates the model deficiency in capturing extreme values of connections of permeabilities within the unit.

Table 6.12 through table 6.14 shows the summary of statistical analysis with respect to the corrected measured permeabilities at same reference depth.

Table 6.12: Statistical Error Analysis of Permeability Models in the Continental/Fluvial Depositional Environment of the study area

Statistical Parameters	Measured Permeability	Perm_R _{tot}	Perm_FZI
Number of Samples	445	445	445
Maximum	18755	19167	17426
Minimum	0.10	0.031	0.005
Mean	1352	1354	1365
Standard Deviation, SD	2501	2607	2402
Average Deviation, AD		-2	-13
Average Absolute Deviation, AAD		331	517
Maximum Error, E_{max}		400	2889
Average Absolute Percentage Relative Error, AAPRE		44	136
Correlation Coefficient, R²		0.968	0.885
Adjusted Correlation Coefficient, R²		0.968	0.883
Pearson Correlation		0.963	0.883
T-Student Distribution		-0.071	-0.235
Fisher F-Test		0.920	1.085
P value ($\alpha = 0.05$)		0.000	0.000

Table 6.13: Statistical Error Analysis of Permeability Models in Tidal/Estuarine
Depositional Environment of the study area

Statistical Parameters	Measured	Perm_R _{tot}	Perm_FZI
	Permeability		
Number of Samples	206	206	206
Maximum	7310	6901	6554
Minimum	0.76	0.294	0.008
Mean	1387	1336	1246
Standard Deviation, SD	1571	1523	1382
Average Deviation, AD		50	141
Average Absolute Deviation, AAD		325	569
Maximum Error, E _{max}		137	489
Average Absolute Percentage Relative Error, AAPRE		32	62
Correlation Coefficient, R ²		0.964	0.874
Adjusted Correlation Coefficient, R ²		0.968	0.874
Pearson Correlation		0.939	0.803
T-Student Distribution		1.337	2.140
Fisher F-Test		1.064	1.292
P value ($\alpha = 0.05$)		0.000	0.003

Table 6.14: Statistical error analysis of permeability models in Coastal/Distributary depositional environment of the study area.

Statistical Parameters	Measured	Perm_R_{tot}	Perm_FZI
	Permeability		
Number of Samples	256	256	256
Maximum	7120	7554	12326
Minimum	0.02	0.027	0.005
Mean	1235	1295	990
Standard Deviation, SD	1714	1871	1977
Average Deviation, AD		-60	245
Average Absolute Deviation, AAD		229	684
Maximum Error, E_{max}		331	3597
Average Absolute Percentage Relative Error,		48	267
Correlation Coefficient, R²		0.979	0.849
Adjusted Correlation Coefficient, R²		0.979	0.848
Pearson Correlation		0.967	0.799
T-Student Distribution		-1.971	3.276
Fisher F-Test		0.839	0.752
P value ($\alpha = 0.05$)		0.000	0.000

The lower standard errors and appreciable adjusted least squares correlation coefficient for all environments analyzed within the clastic reservoir system is indicative of a strong relationship between the predictor and response variables for the proposed model. It suffices to say that the sample statistic is statistically significant and therefore the test's null hypothesis is rejected.

6.4 Statistical Analysis and Uncertainty Modelling in Permeability

Derived from the Proposed Model

To evaluate the accuracy of the proposed model, a statistical analysis of the model was carried out by comparison to existing permeability predictor based on Genetic Unit Averages of Flow Zone Indicators (FZIs) and Neural Networks for Niger Delta reservoirs. Statistical analysis shows a lower error using the proposed model. In each case, the core permeability was measured using a nitrogen gas under a sleeve pressure of 400 psig permeameter and was corrected where necessary for the Klinkenberg and Forchheimer effects.

The statistical parameters used are as follows:

Average Deviation (AD)

$$AD = \frac{1}{N} \sum_{i=1}^N (Measured_i - Predicted_i) \quad [68]$$

Average Absolute Deviation (AAD)

$$AAD = \frac{1}{N} \sum_{i=1}^N |Measured_i - Predicted_i| \quad [69]$$

Maximum Error (E_{max})

$$E_{\max} = \max_{i=1}^N |E_i| \quad [70]$$

where $E_i = \left[\frac{K_{predicted} - K_{measured}}{K_{measured}} \right] * 100; i=1,2,3,\dots,N$

Average Absolute Percentage Relative Error (AAPRE)

$$AAPRE = \frac{1}{N} \sum_{i=1}^N |E_i| \quad [71]$$

The proposed correlation and existing correlation methods discussed earlier in chapters 2 and 4 were used to estimate the formation permeability for each dataset at different depth. Tables 6.15 shows the errors in predicting the permeability using input data ($\overline{R_{tot}}$) from SCAL, and table 6.16 shows the error in predicting permeability using input data ($\overline{R_{tot}}$) obtained from NMR T_2 spectrum.

Table 6.15: Statistical Analysis for Permeability Models

Statistical Parameters	Predicted	Predicted
	Permeability_ $\overline{R_{tot}}$	Permeability _ FZI
Average Deviation, AD =	-0.073	-0.482
Average Absolute Deviation, AAD =	0.318	0.552
Maximum Error, Emax =	86.18	140.18
Average Absolute Percentage Relative	22.70	36.19

Table 6.16: Statistical analysis for various permeability models using NMR T_2 data

	Coates_NMR	SDR_NMR	FIELD_BB	PERM_κ3	PERM Proposed
Average Deviation, AD	0.582	0.628	1.026	0.390	0.305
Average Absolute Deviation, AAD	0.894	0.958	1.182	0.824	0.810
Maximum Error, E_{max}	175.93	309.70	463.37	1178.39	148.34
Average Absolute Percentage Relative Error, AAPRE	36.52	40.78	50.06	52.12	34.45

Table 6.10 shows the errors in predicting the permeability using input data (pore throat distribution) from SCAL. The total relative error in estimating permeability in onshore fields using the proposed permeability correlation is 22.7%, which makes it more attractive than FZIs with an estimated random error of 36.2% and the modified Kozeny-Carman which has an estimated random error of at least 50%.

Table 6.15 presents a comparative analysis considering the proposed permeability models using a both $Kappa$ values of 2 and 10, and existing correlations developed by Coates and SDR for onshore dataset. This was also tested using dataset from field “BB” canyon reservoirs within the Deep Water, Niger Delta.

The Schlumberger-Doll-Research group and Coates correlations over-estimates the permeability of most of the permeable horizon in comparison with the corrected permeabilities from measured cores, resulting in a high average absolute relative error as well as maximum error compared with the proposed model.

CHAPTER 7

Improved RQI, Leverett J-function and SMLP Concept using the Normalized Pore Throat (R_{tot})

7.1 The Reservoir Quality Indicator (RQI) Concept

The Reservoir Quality Indicator (RQI) method for classifying reservoir data into distinct Hydraulic Flow Units (HFU) with specific FZI was introduced by Amaefule *et al.* (1993). They presented a reliable and robust methodology for enhanced reservoir description which also captures the pore-body/throat attributes of a given reservoir system. The methodology was based on a modified Kozeny and Carman (1927; 1937) relationship (equation 7.1). They expressed the permeability (K) in terms of effective porosity (φ_e), shape factor (F_s), tortuosity (τ) and surface area per unit grain volume (S_{gv}) as follows:

$$K = 1,014 \frac{\varphi_e^3}{(1-\varphi_e)^2} \left(\frac{1}{F_s \tau^2 S_{gv}^2} \right) \quad [7.1]$$

The parameters F_s and τ were grouped into a term called Kozeny constant. However, this term actually varies among hydraulic units, although it is constant within a given rock unit.

To address the variability of the Kozeny “constant”, Amaefule rearranged Equation 7.1 by dividing both sides by porosity and taking the square root of both sides:

$$\sqrt{\frac{K}{\varphi_e}} = \left(\frac{\varphi_e}{1-\varphi_e} \right) \left[\frac{1}{\sqrt{F_s \tau S_{gv}}} \right] \quad [7.2]$$

Then, the reservoir quality index (RQI), pore volume-to-grain ratio (φ_z) and flow zone indicator (FZI) were introduced:

$$RQI = 0.0314 \sqrt{\frac{K}{\varphi_e}} \quad [7.3]$$

$$\varphi_z = \frac{\varphi_e}{1-\varphi_e} \quad [7.4]$$

$$FZI = \frac{1}{\sqrt{F_s \tau S_{gv}}} = \frac{RQI}{\varphi_z} \quad [7.5]$$

Finally, substituting equations 7.3, 7.4 and 7.5 into 7.2 and taking logarithm of both sides results in:

$$\log RQI = \log \varphi_z + \log FZI \quad [7.6]$$

As expressed in equation 7.5, the Flow Zone Indicator FZI relates parameters as shape factor, tortuosity and surface area per unit grain volume (all controlled by mineralogy and texture of the rock) to the ratio of permeability and effective porosity. This demonstrates an improved permeability modelling as a function of porosity. Thus, poorly sorted, fine grained sands as well as rocks with high clay content, typically exhibit high surface area, high shape factor and tortuosity and hence, low FZI values. In contrast, rock samples composed of coarse grained and well sorted grains have lower surface areas, lower shape factor and tortuosity and consequently, higher FZI values.

7.1.1 Integrating the R_{tot} with the RQI Concept

The relationship for pseudo averages of normalized pore throat radius were defined as:

$$R_{tot} = \overline{R_{tot}} \varphi_n;$$

where: $\overline{R_{tot}}$ = genetic units averages of pore throat radius for the various depositional environments within the Niger Delta system; and

$$\varphi_n = 0.3 \left(\frac{1-\varphi}{\varphi} \right)$$

Substituting for R_{tot} in the RQI formulation (equation 7.3) results in:

$$RQI = 0.0314 \sqrt{\frac{K}{R_{tot}}} \quad [7.7]$$

$$\varphi_z = \frac{\varphi_e}{1-\varphi_e}$$

The plot of the logarithm of RQI versus the logarithm of φ_z rearranges the porosity-permeability relationship; and provides trends for various rock units with similar depositional/diagenetic imprints. Then, samples that lie on the same line have similar hydraulic behavior and, thereby, similar fluid-flow characteristics. These trends can be fitted with parallel straight lines with unit slope whose intercept at $\varphi_z = 1$ defines the FZI of each distinctive hydraulic unit.

7.1.2 Case Study of the Clastic Turbidite Reservoirs

The case study encompasses the Niger-Delta Deep water turbidite system composed of submarine fan models which include the: amalgamated channels, isolated channel complex, sinuous channels, channel sand complexes and levee/overbank deposits. Figures 7.1 and 7.2 presents the petrophysical data log view showing core images and routine core analysis dataset; which depicts four major genetic reservoir units classification within the system. These are the Mud-Rich Thin Beds (MRTB), Inter-Channel Thin Beds (ICTB), Channel Storey Margin (CSM) and the Channel Storey Axis (CSA). Gamma ray and deep resistivity signatures denote the environment as a low resistive and low contrast pay zone. NMR T_1 and T_2 spectrum confirms the zones as highly prolific with good reservoir and fluid properties. Special as well as routine core analysis dataset were obtained from the interval: 9,226 – 9567 ft MD.

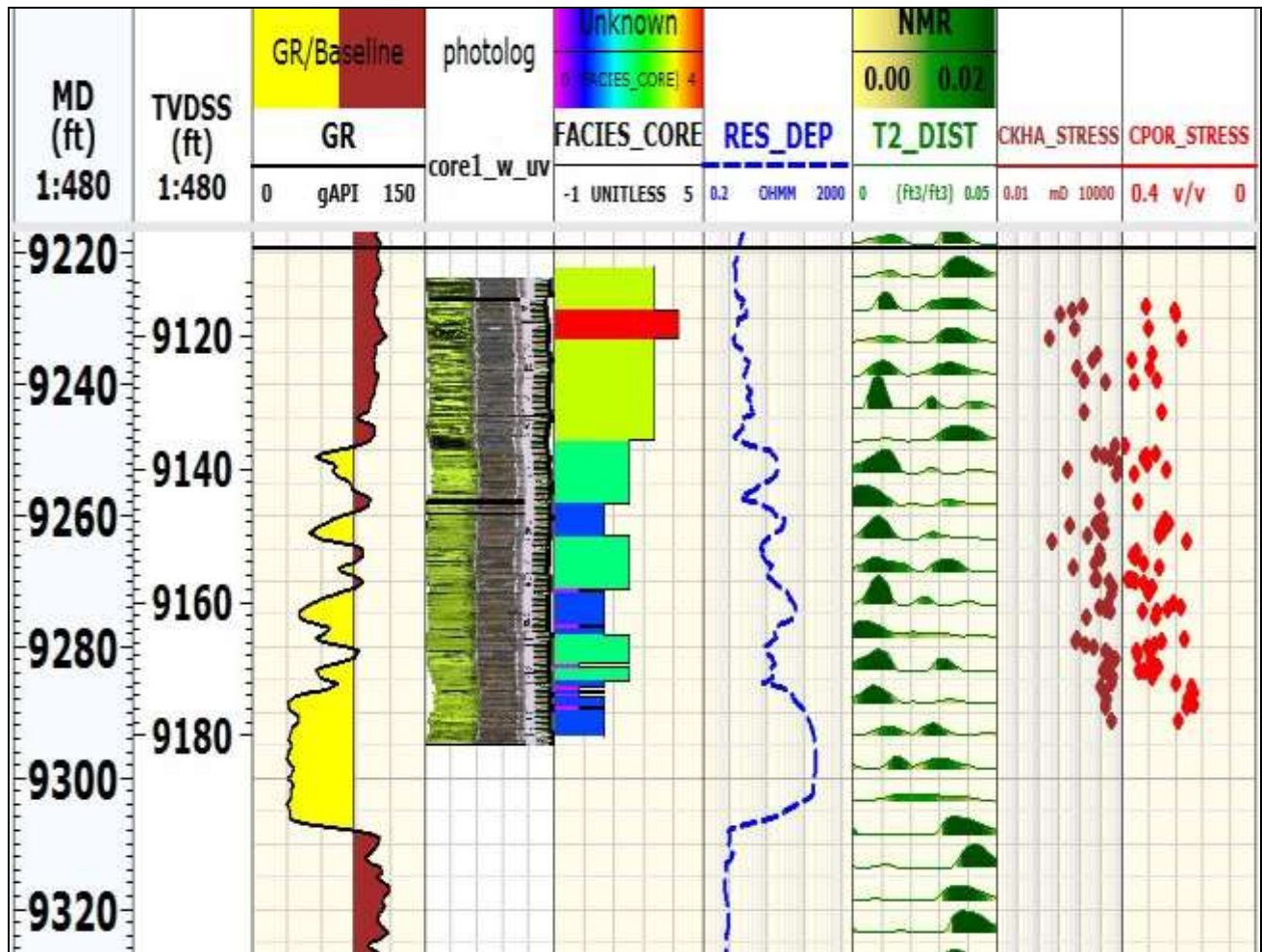


Figure 7. 1: PDL view for Zone 1 (Deep Water – Niger Delta) indicating the cored interval, complex turbiditic sequence of the submarine canyons and the four (4) facies association.

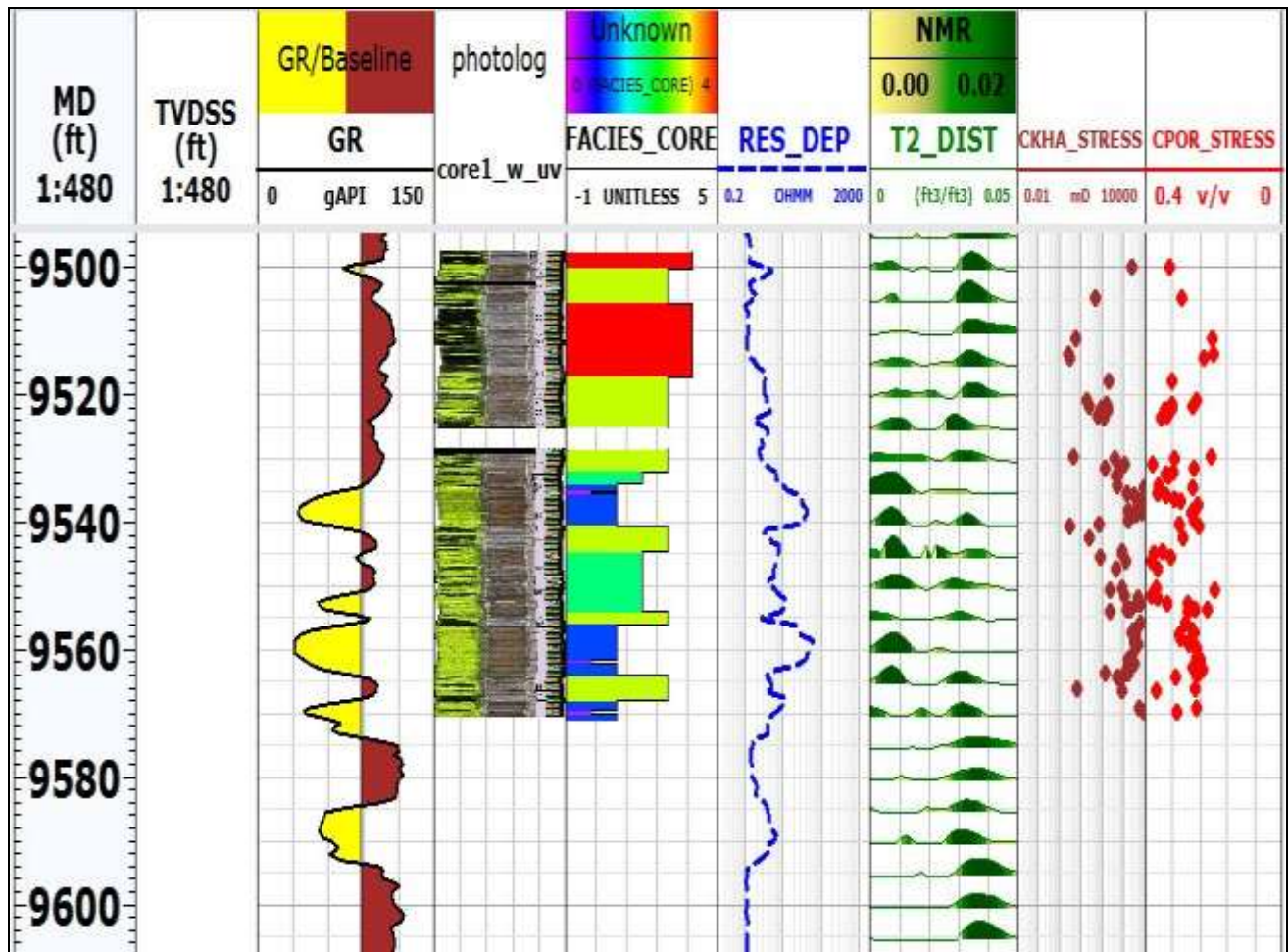


Figure 7.2: PDL view for Zone 2 (Deep Water – Niger Delta) indicating the cored interval, complex turbiditic sequence of the submarine canyons and the four (4) facies association.

Figure 7.3 demonstrates the classical porosity-permeability plot using dataset from the case study, indicating varying permeabilities at any given porosity which is typical of heterogeneous clastic reservoirs within the Tertiary Niger Delta system. Four distinct hydraulic units were established within the cored interval using both RQI methodologies.

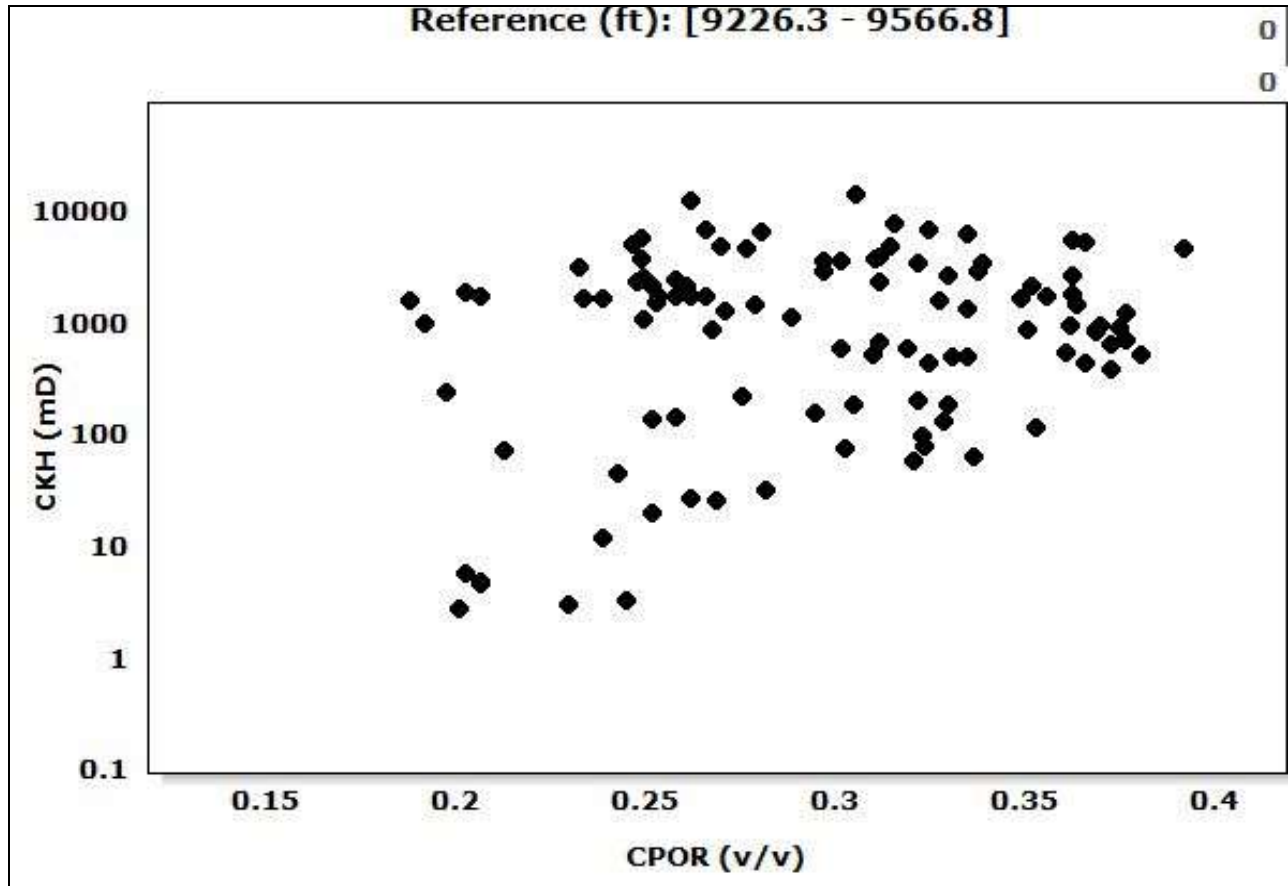


Figure 7.3: Plot of permeability versus porosity for all samples; the non-linear relationship results in very low correlation coefficient which is evident in complex shaley sandstone.

The mercury injection capillary pressure (MICP) data presented in figure 7.4 demonstrates the existence of a distinctive profile of capillary pressure versus saturation for each of the four (4) genetic reservoir units.

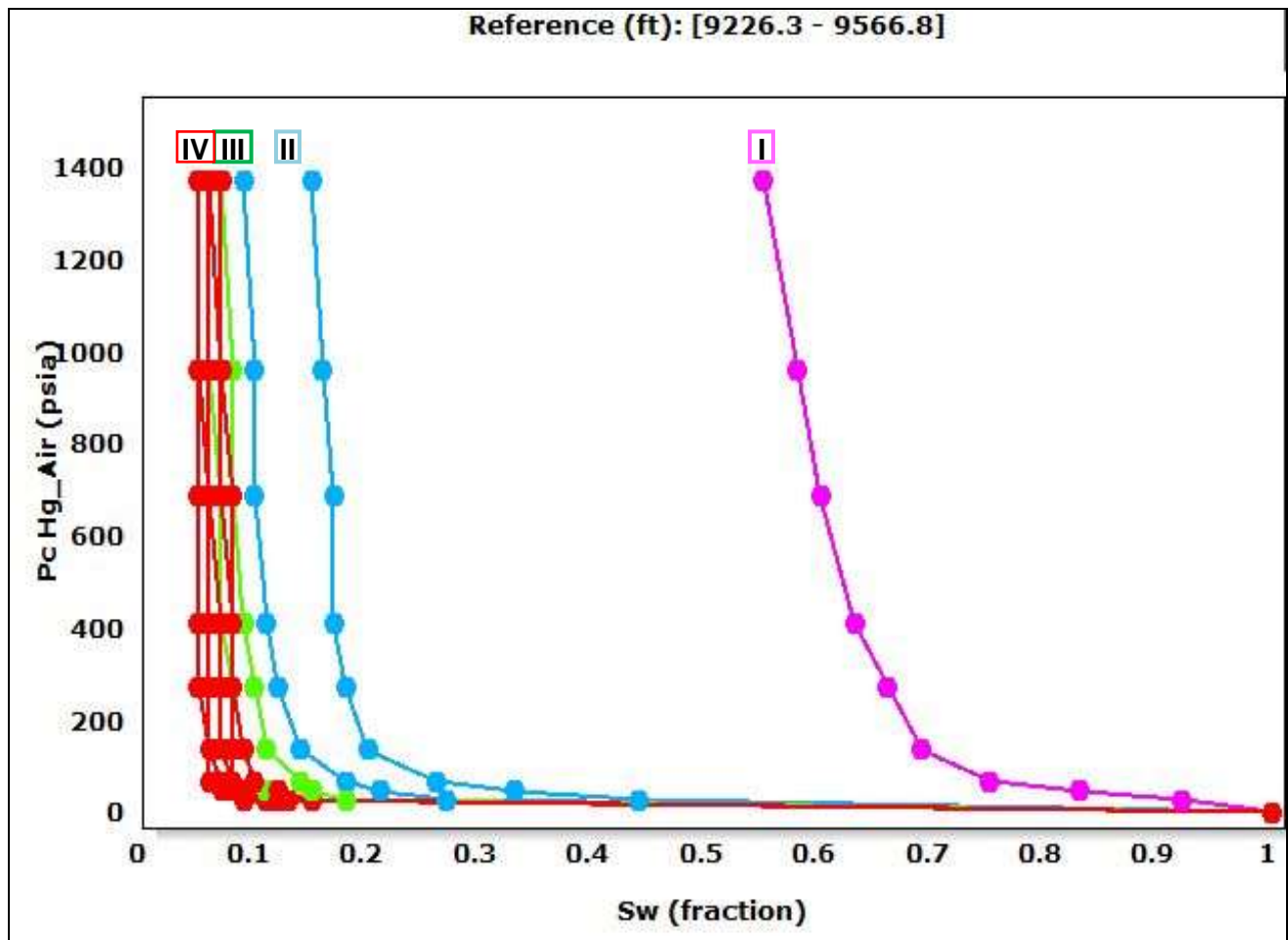


Figure 7.4: Plot of capillary pressure versus wetting phase saturation indicating the four (4) distinct genetic units with increasing macropores from rock unit I to IV, and decreasing reservoir quality from rock unit IV to I.

The modified-RQI concept based on a combination of $\overline{R_{tot}}$ and permeability data demonstrates efficacy for hydraulic flow unit delineation. A simple summation and normalization of the modified-RQI is sufficient for transforming rock-type-based reservoir zonation into petrophysically based flow units for input into a numerical flow simulator that honors the foot-by-foot characteristics at the wellbore. In such a plot consistent zones are characterized by straight lines with the slope of the line indicating the overall reservoir quality within a particular depth interval. The lower the slope of the normalized modified-RQI lines delineating each zone, the better the reservoir. The equation used for calculating the Normalized Cumulative Modified-RQI (NCMRQI), is as follows:

$$NCMRQI = \frac{\sum_{x=1}^i \sqrt{\frac{K_i}{R_{tot_i}}}}{\sum_{x=1}^n \sqrt{\frac{K_i}{R_{tot_i}}}} \quad [7.8]$$

where,

n = total number of data

i = number of individual data points

A plot of the NCMRQI versus depth demonstrates a possibility for delineating the reservoir into several zones by observing changes in the slope. Figures 7.5, 7.6 and 7.7 depict reservoir zones characterized by straight lines with changing slope indicating the overall reservoir quality within a particular depth interval. The straight line shows similar slope for respective facies unit association as depicted in figure 7, indicating consistency between the geologic rock classification and petrophysical units.

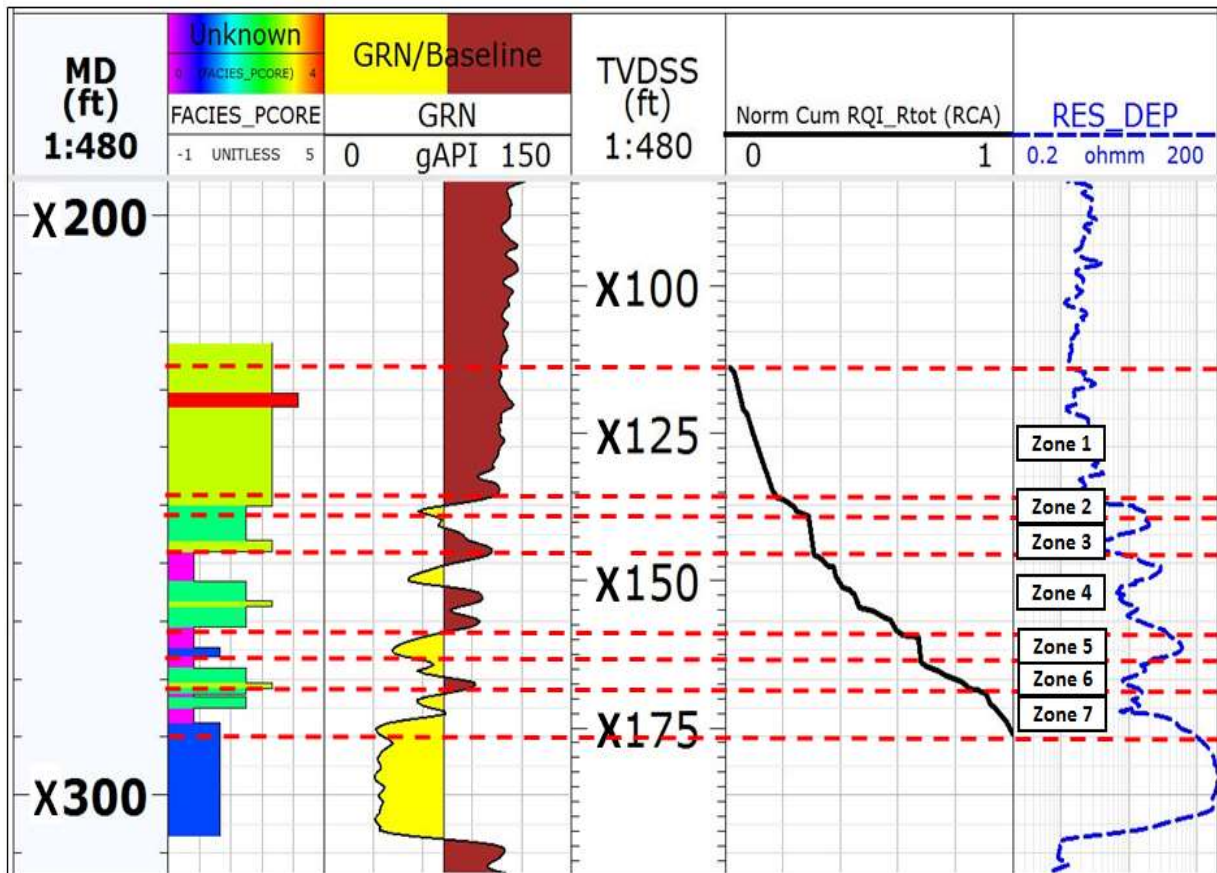


Figure 7. 5: PDL view for Zone 1 (Deep Water – Niger Delta). Track 3 presents the Normalized Modified RQI plot versus depth for flow zones delineation. This presents seven flow zones indicating consistency between the geologic rock facies classification and petrophysical units.

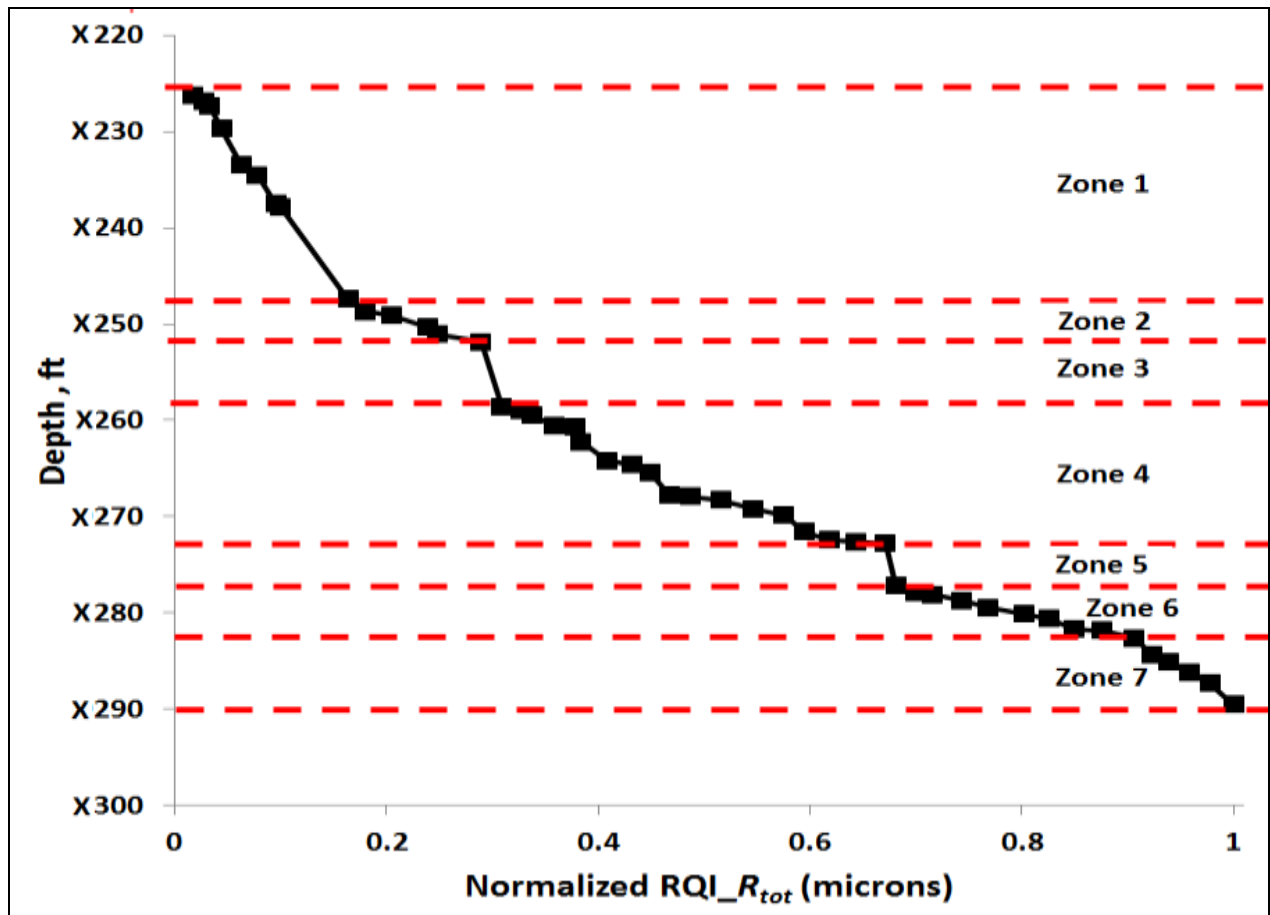


Figure 7. 6: Normalized Cumulative Modified RQI versus depth within the cored section indicating seven reservoir flow units.

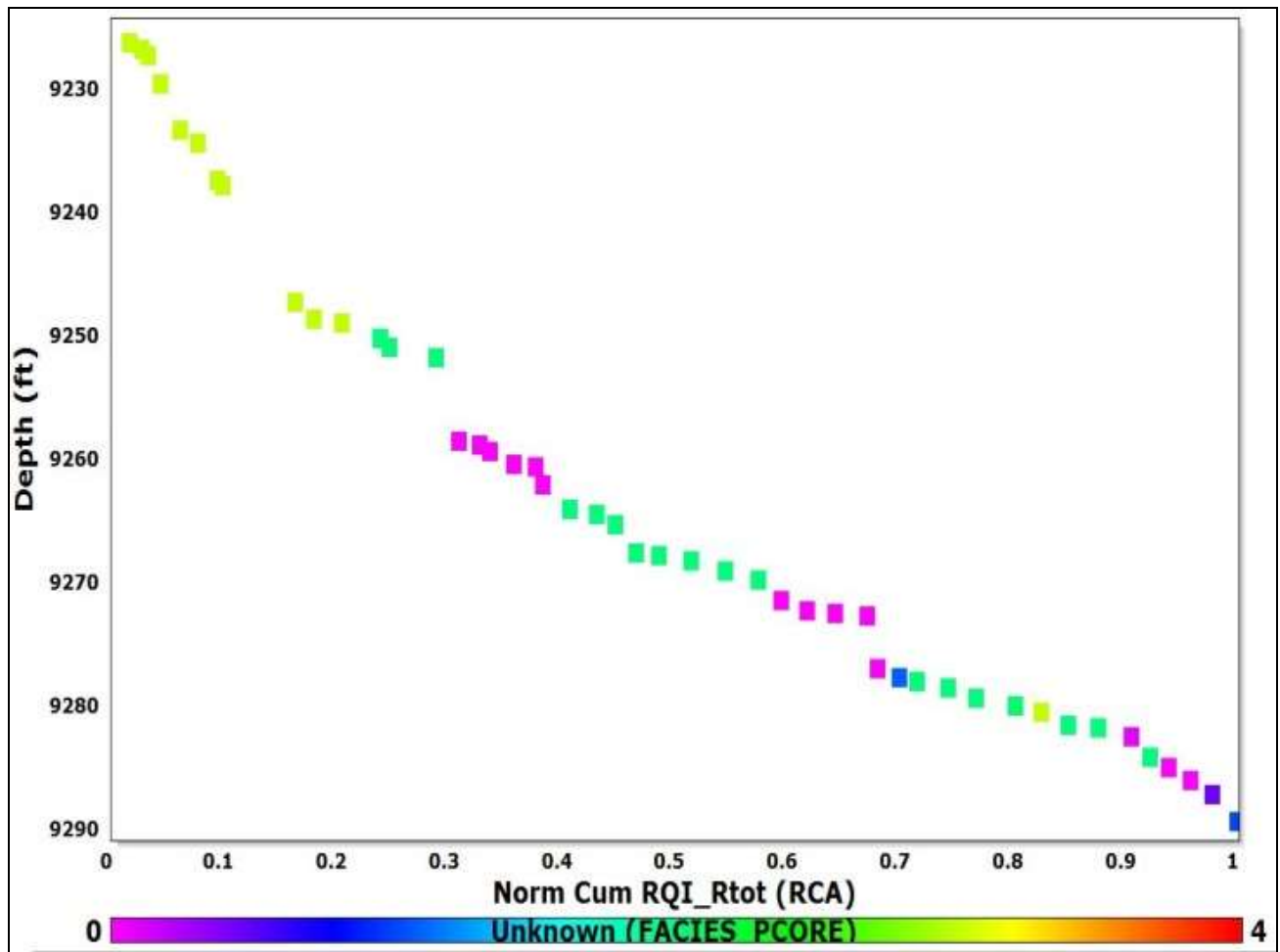


Figure 7. 7: Facies biased Normalized Cumulative Modified RQI versus depth within the cored section. This shows four units which bears correlation with the rock-type-based reservoir zonation and petrophysically based flow units.

The RQI method and the modified RQI approach were analyzed using dataset from the case study. The RQI method and the modified RQI approach was analyzed using dataset from the case study. Figures 7.8 and 7.9 present the efficacy of both methodologies for hydraulic flow unitization. FZI values ranged from 1.5 to 50 within the diagenetic sequence.

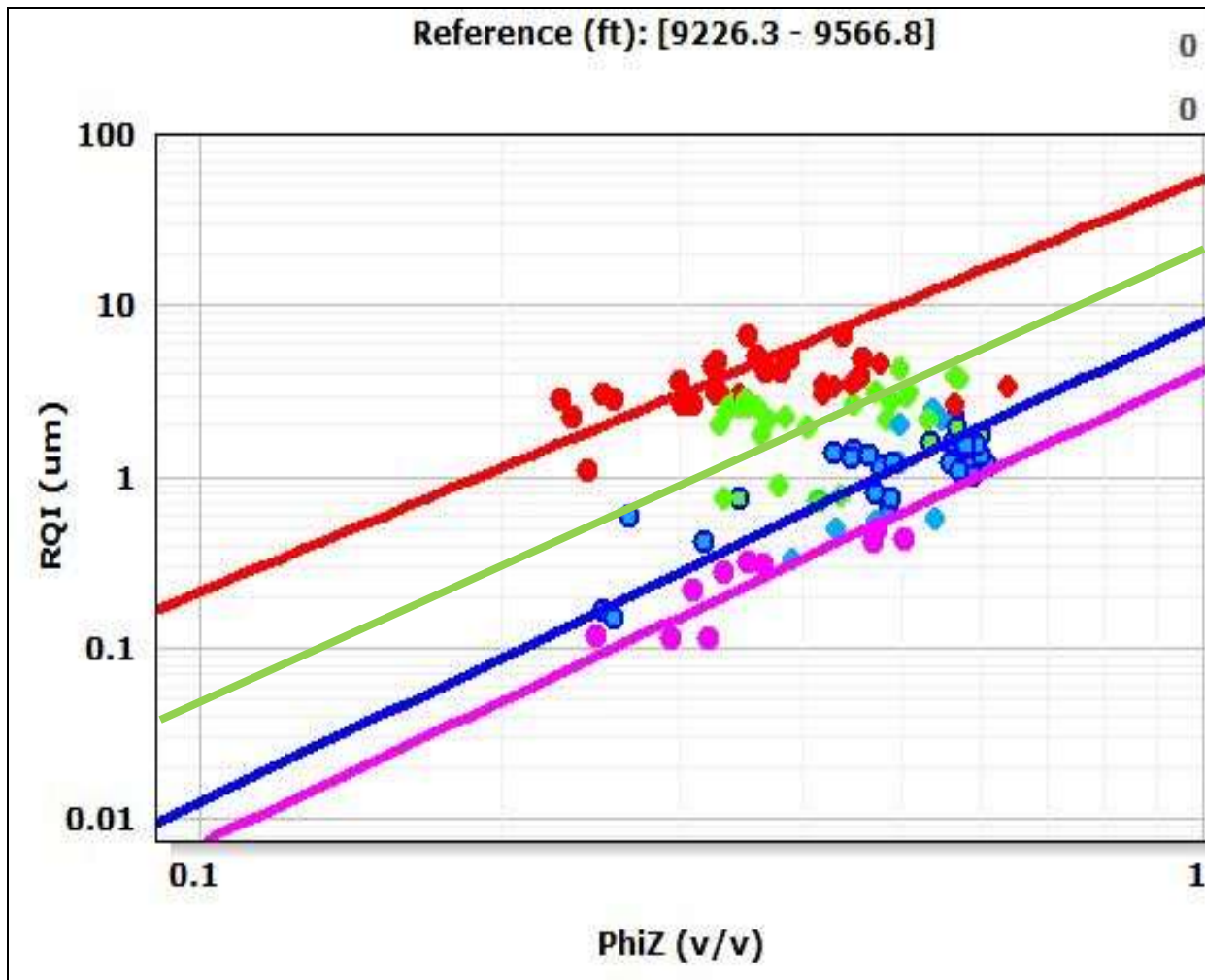


Figure 7.8: Log-log plot of RQI (after Aneafule *et al.*) versus ϕ_z for all samples, indicating their average FZI per unit as obtained from the intercept of each straight line at $\phi_z = 1$.

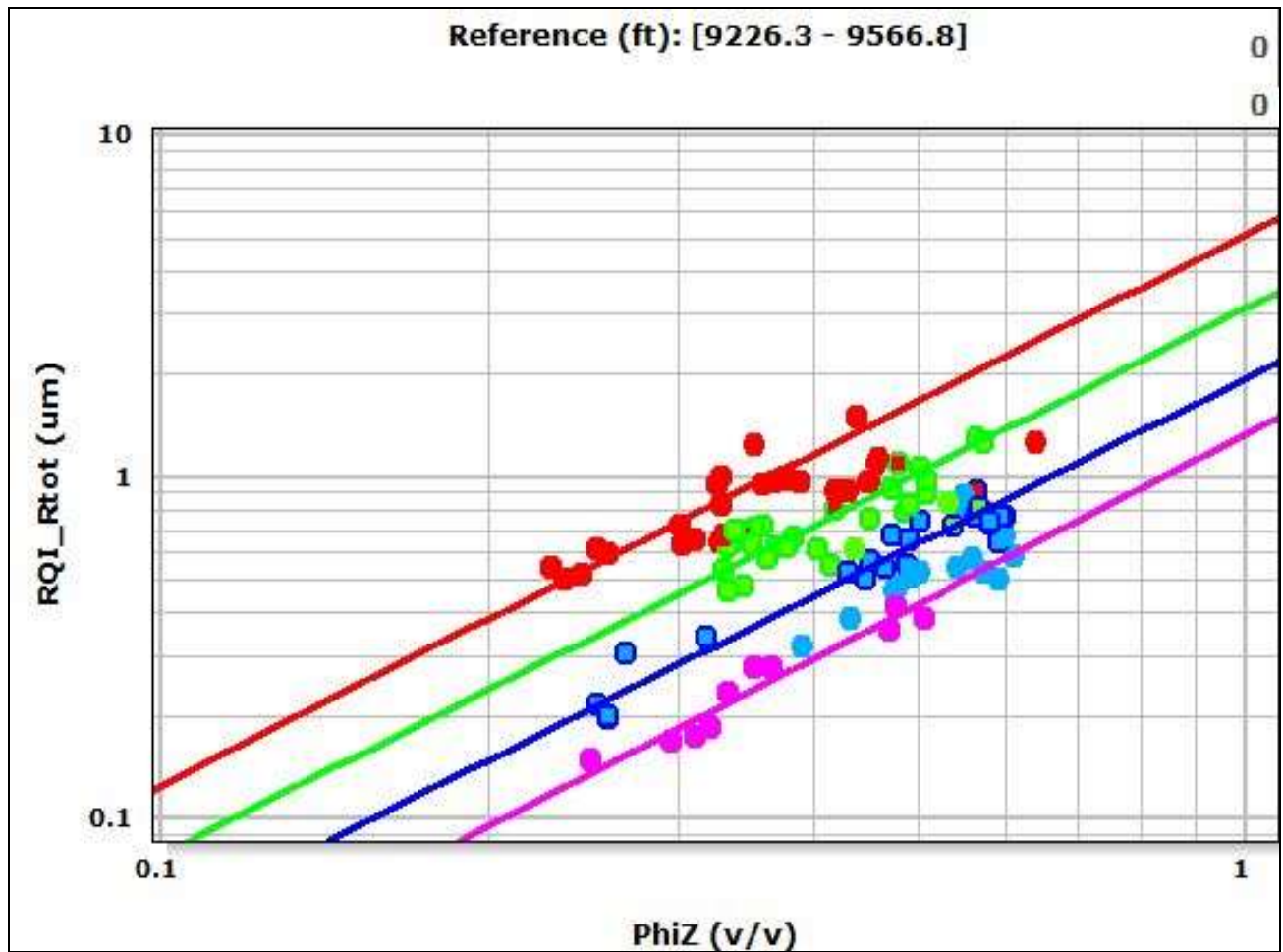


Figure 7.9: Log-log plot of $RQI_{R_{tot}}$ (proposed model) versus ϕ_z for all samples, indicating their average FZI per unit as obtained from the intercept of each straight line at $\phi_z = 1$.

The proposed model (figure 7.10B) demonstrates an improved capability in aligning all samples within same genetic reservoir units on same trend/straight line than existing RQI method (Ameafule *et al.*). This presents an improved hydraulic flow zone delineation method using the RQI concept.

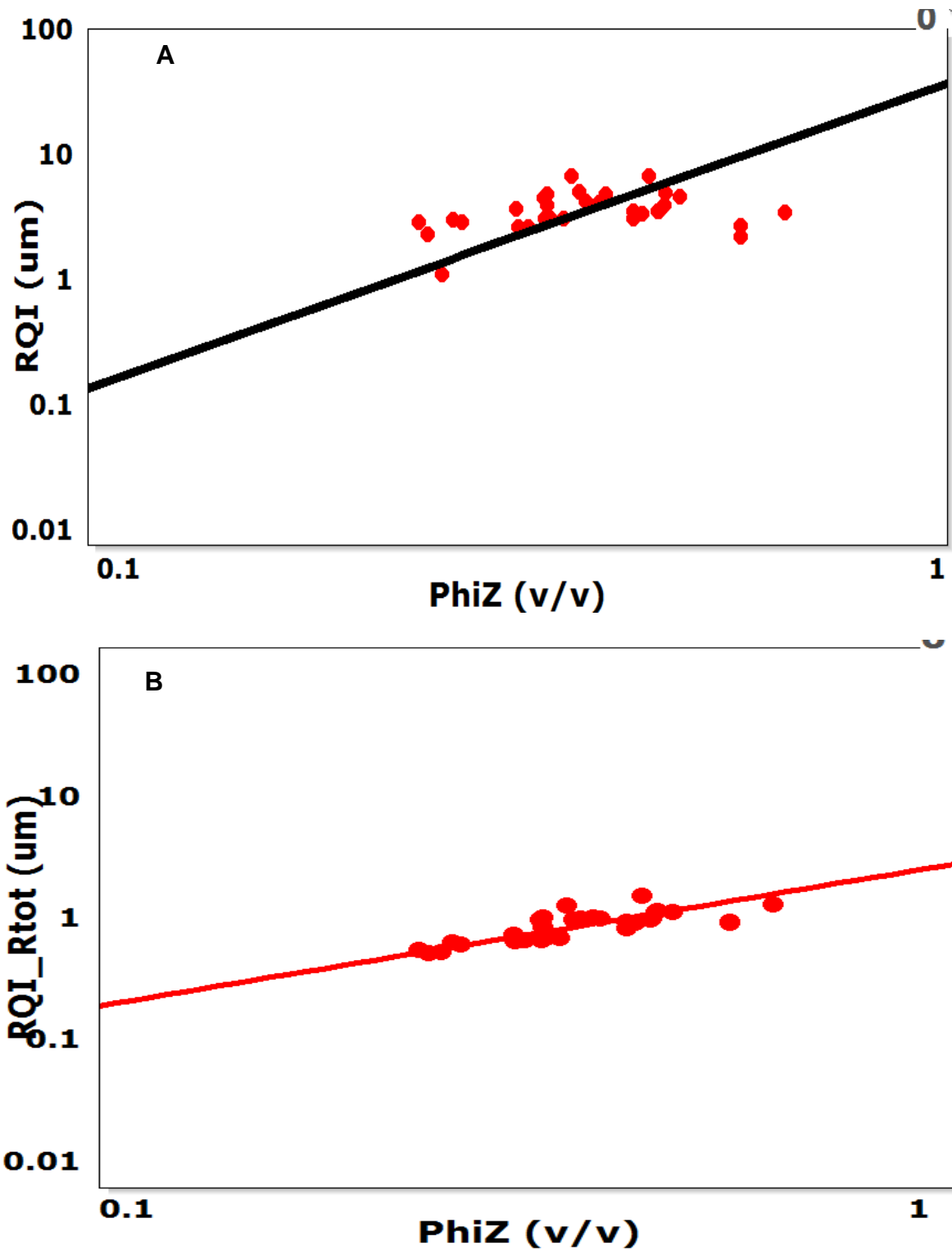


Figure 7.10: Log-log plot of RQI versus ϕ_z (top plot, A) and $RQI_{\overline{R_{tot}}}$ versus ϕ_z (bottom plot, B) for the Channel Storey Axis unit, indicating improved R^2 of 78% for the modified RQI over 31% indicates the efficacy of the proposed model for hydraulic flow zonation.

In addition, critical evaluation of individual genetic reservoir units for hydraulic flow unitization demonstrates an improvement in correlation coefficient as presented in figure 7.10. This shows a correlation coefficient of 78% from the proposed method over 31% for the existing RQI method after Aneafule *et al.*

Furthermore, figures 7.11 and 7.12 present plots of irreducible water saturation versus corresponding FZI values from ten (10) mercury injection capillary pressure samples obtained from the study area. It is expected that higher FZI values correspond to larger pore throats (diagenetic/textural fabric) and subsequently lower irreducible water saturation and vice versa as evident in the plots. The proposed modified RQI demonstrate an improved correlation between irreducible water saturation and FZI. The higher correlation coefficient of 76% for the modified RQI (figures 7.12) over 64% (figure 7.11) from the existing method indicates an improved efficacy of the proposed model for hydraulic flow zone characterization.

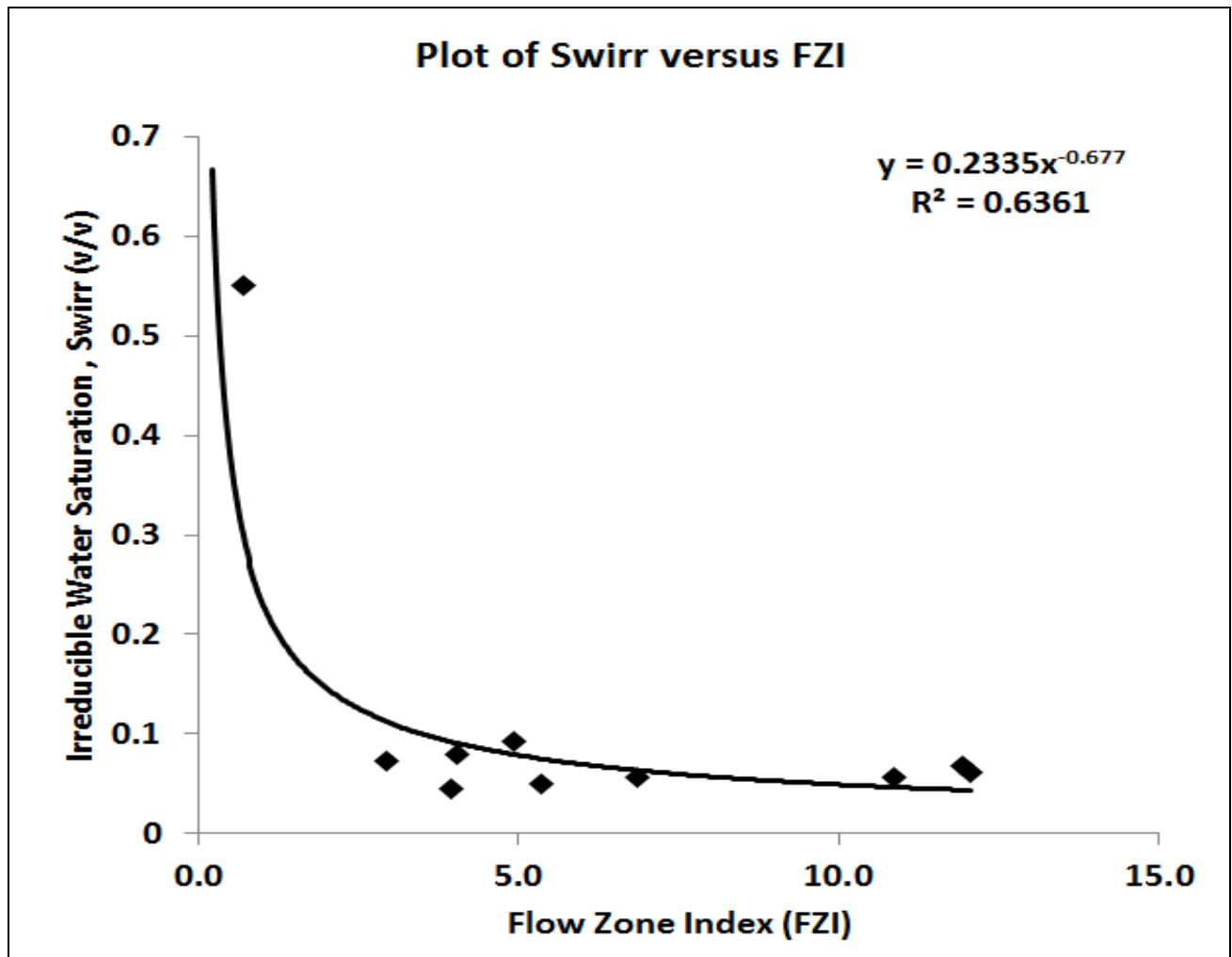


Figure 7.11: Plot of irreducible water saturation versus FZI (after Aamefule *et al.*) for all samples. Higher FZI's corresponds to rock units with megapores and lower irreducible saturation.

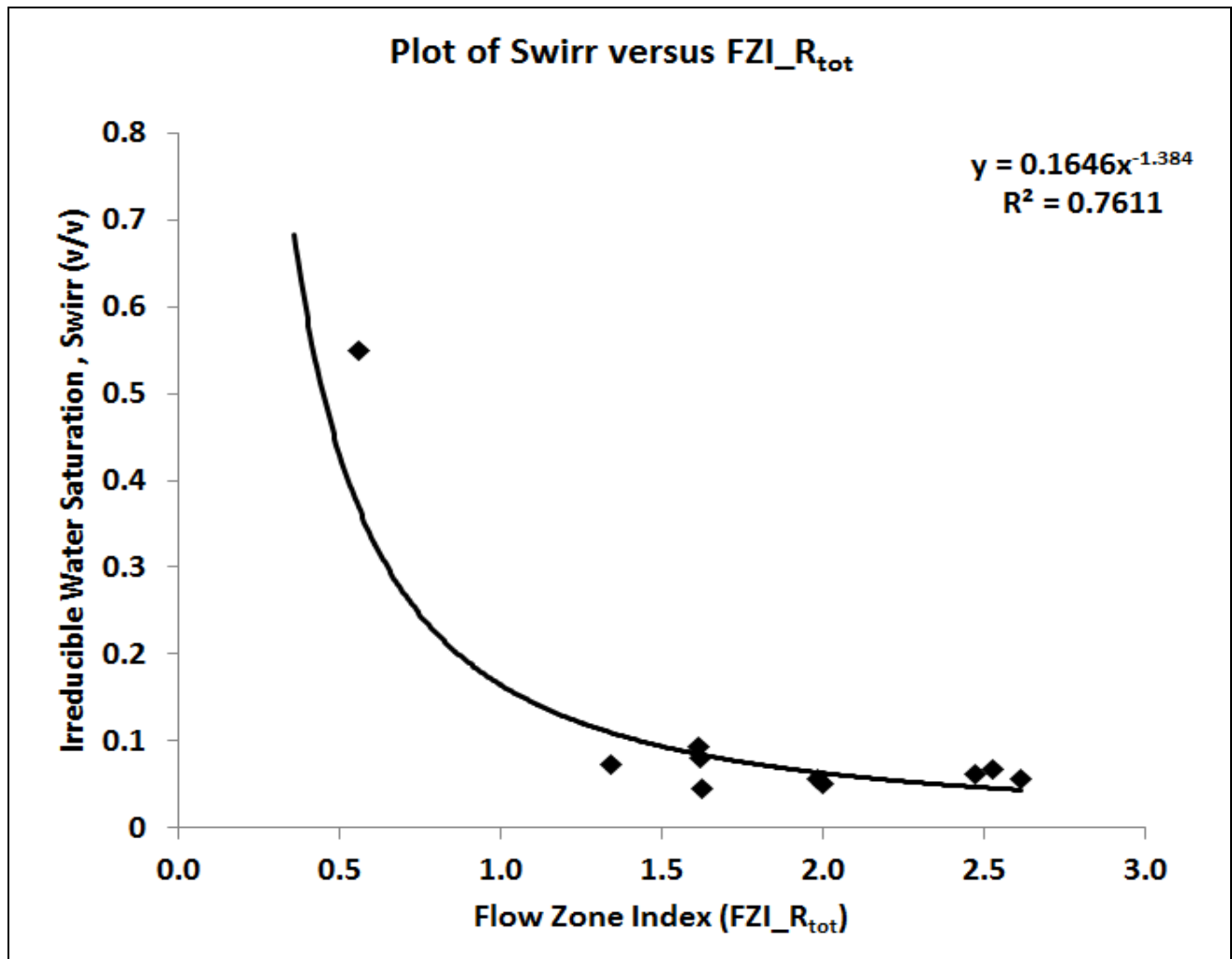


Figure 7.12: Plot of irreducible water saturation versus $FZI_{R_{tot}}$ (proposed modified RQI) for all samples. Higher FZI's correspond to rock units with megapores and lower irreducible water saturation.

7.2 The Leverett J-Function

Leverett (1941) proposed a general relationship for converting capillary pressure data to a universal curve from the standpoint of dimensional analysis. He defined the dimensionless function of saturation, by classifying various capillary curves considering their unique properties and similarities, and bearing in mind that capillary pressure depends on the porosity, interfacial tension, and mean pore radius.

The J-function is defined as:

$$J(S_w^*) = 0.2165 \frac{P_{c\ res}}{(\sigma \cos \theta)_{res}} \sqrt{\frac{k}{\phi}} \quad [7.9]$$

where: $J(S_w^*)$ = Leverett J-function

$P_{c\ res}$ = capillary pressure at oil-brine reservoir condition, psia

σ_{res} = oil-brine interfacial tension, dynes/cm

k = permeability, md

ϕ = porosity, fraction

θ_{res} = oil-brine fluid contact angle, degrees

A plot of $J(S_w^*)$ against the incremental normalized water saturation (S_w^*) demonstrate improved fluid saturation modelling, through generation of a set of curves for each single rock type.

The normalized water saturation (S_w^*) is defined as:

$$S_w^* = \frac{S_w - S_{wirr}}{1 - S_{wirr}} \quad [7.10]$$

where: S_w = water saturation at the *ith* pressure step (v/v)

S_{wirr} = irreducible water saturation

In general, pore geometry of the rock controls not only its permeability, but also its capillary pressure. Hence, fluid distribution in the reservoir is dependent on the pore attributes of the rocks. Nevertheless, it is a common practice to generate a single capillary pressure curve as a function of the water saturation to model the fluid distribution of the reservoir. This approach is too simplistic and usually leads to erroneous results, especially in highly heterogeneous reservoirs.

It is worthy of note that there are significant differences in correlating the J-function with water saturation for various formations, and as such no universal curve can be obtained. Hence, the classical J-function is not adequate for differentiating various hydraulic units. This is because the J-function only normalizes capillary pressures with respect to porosity, permeability and tortuosity, but doesn't include the effect of surface area. Improvements in reservoir characterization with the J-function concept relies on a facies/genetic units based normalization. Various rock units within a reservoir are usually modelled with individual J-function curves.

7.2.1 Integrating the R_{tot} with the Leverett J-Function

The relationship for pseudo averages of normalized pore throat radius is defined as:

$$R_{tot} = \overline{R_{tot}} \varphi_n ;$$

where: $\overline{R_{tot}}$ = genetic units averages of pore throat radius for the various depositional environments within the Niger Delta system; and

$$\varphi_n = 0.3 \left(\frac{1-\varphi}{\varphi} \right)$$

Substituting for R_{tot} in the J-function formulation results in:

$$J(S_W^*) = 0.2165 \frac{P_{c\ res}}{(\sigma \cos \theta)_{res}} \sqrt{\frac{K}{R_{tot}}} \quad [7.11]$$

7.2.2 Case Study of the Clastic Turbidite Reservoirs

Dataset from the Niger Delta Deep water system was also employed for validating the proposed modified Leverett J-function (equation 7.11) for modelling fluid saturation and normalizing data from different samples belonging to distinct genetic reservoir units. Figure 7.4 presents the mercury injection data, demonstrating the existence of a distinctive profile of capillary pressure versus water saturation for each of the four genetic reservoir units. Figure 7.13 and 7.14 presents the J-function plots for both methods. The modified Leverett J-function ($J\text{-function}_{R_{tot}}$) plot (figure 7.14) shows an improved potential in delineating the various rock units and in particular the Mud Rich Thin Beds (MRTB) from the Inter-Channel Thin Beds (ICTB).

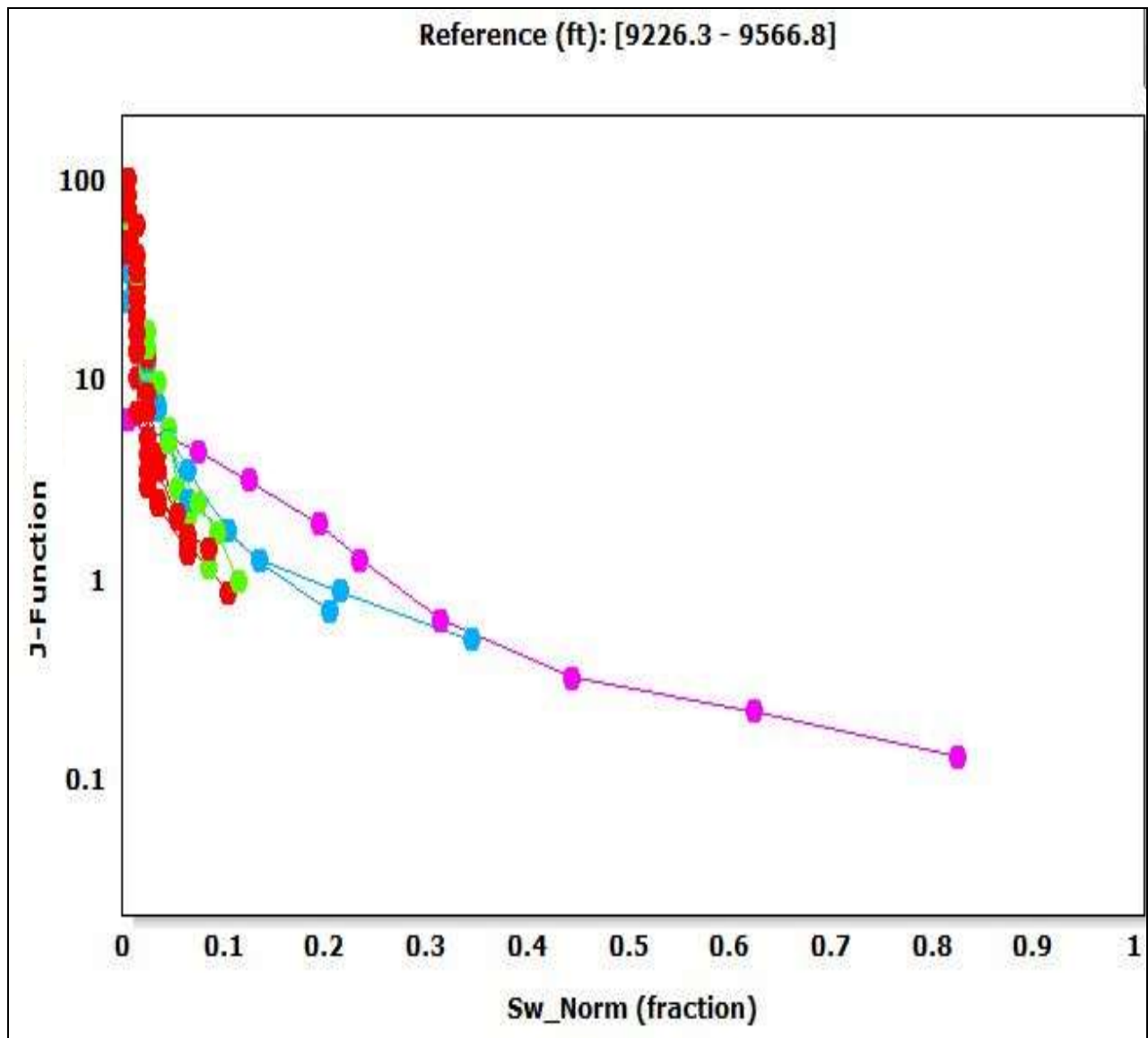


Figure 7.13: Plot of J-function (after Leverett J.) versus normalized wetting phase saturation for all samples, with color codes indicating the four (4) genetic unit classifications. Plot demonstrates deficiency in delineating the various facies association within the complex turbidites.

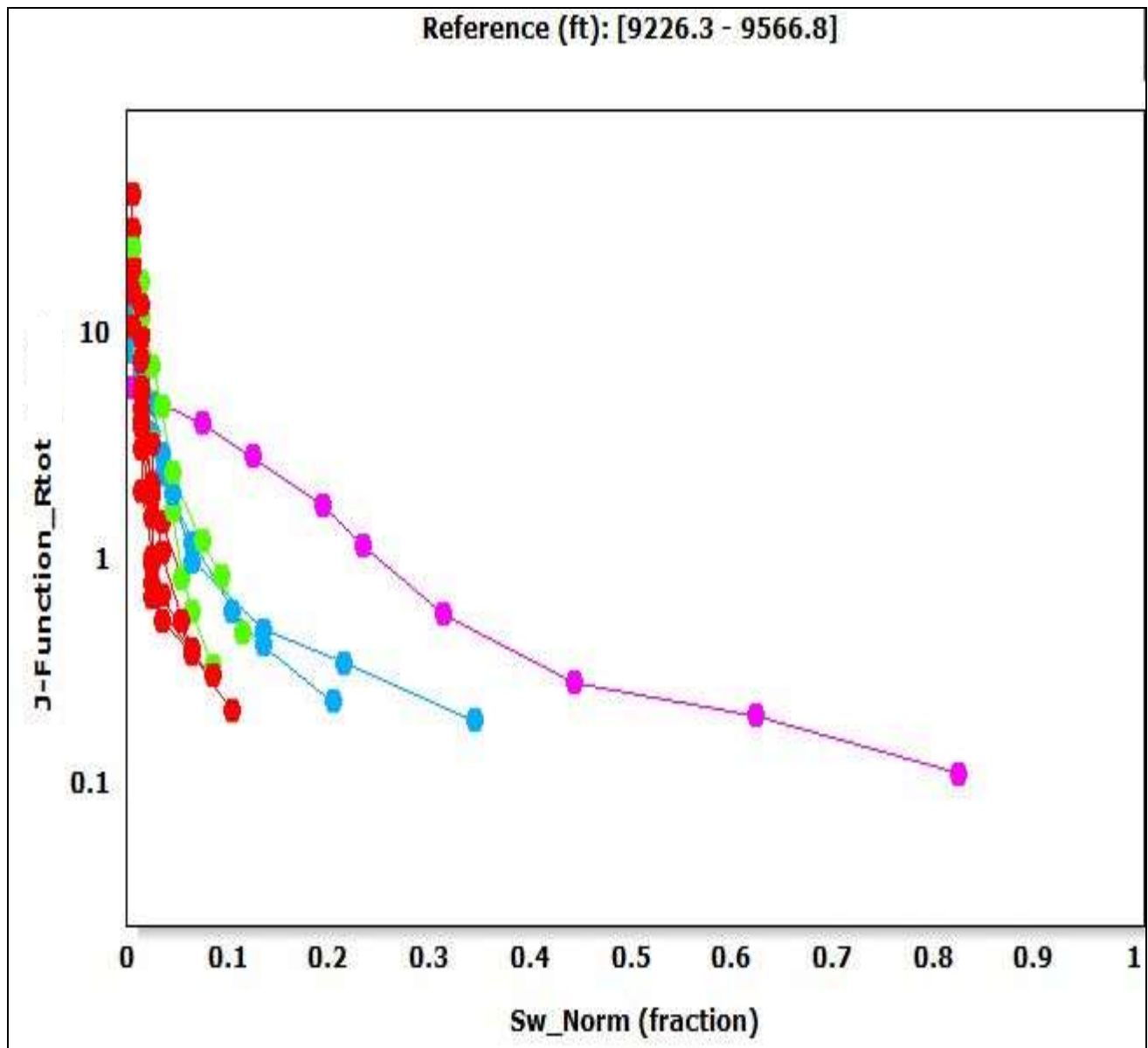


Figure 7.14: Plot of modified J-function (proposed model) versus normalized wetting phase saturation for all samples, with color codes indicating the four (4) genetic unit classifications. Plot demonstrates the capability of the proposed model in delineating various facies association within the turbiditic system.

The correlations established between the modified J-function and water saturation for each of the four genetic reservoir units can be applied to model fluid distribution in uncored reservoir intervals with similar genetic unit assemblage. Percentages of megapores for each of the hydraulic flow unit were considered from the drainage MICP datasets before converting to reservoir conditions for J-function evaluation. Table 7.1 presents averages of FZI values from the existing and modified approach for the rock types. The influence of diagenesis has modified the original depositional fabric and resulting in multiple hydraulic flow units.

Table 7. 1: Summaries of FZI's and HFU's for turbiditic shaley-sand system

Rock Unit	Description	% Megapore	FZI Average	Modified FZI Average	Swirr (%)
I	MRTB	<25	5	1.5	55.0
II	ICTB	30 - 80	8	2.2	9.3
III	CSM	80 - 90	22	3.5	8.0
IV	CSA	> 90	60	5.9	5.7

Furthermore, the Leverett J-function is an excellent indicator of a reservoir diagenetic/textural fabric. For capillary pressure data of a constant pore geometry (*i.e.* a fixed value of FZI), the relation between the values of $J(S_w^*)$ and normalized water saturation (S_w^*) is given by:

$$J(S_w^*) = J^* (S_w^*)^{-\frac{1}{\lambda}} \quad [7.12]$$

A log-log plot of $J(S_w^*)$ versus S_w^* gives a straight line for different rock units within a given reservoir. Equation 11 presents a linearized J-function relationship:

$$\log J(S_w^*) = -\frac{1}{\lambda} \log(S_w^*) + \log J^* \quad [7.13]$$

The term J^* is known as the lithology index and its obtained from the intercept at $S_w^* = 1$; and λ as the pore size distribution index, obtained from the reciprocal of the slope.

Figures 7.15 and 7.16 present log-log plot of J-function and the modified J-function versus normalized water saturation respectively. The proposed model delineates and defines the pore throat distribution index (λ) for the MRTB and ICTB efficiently than the existing J-function. Qualitatively, a higher value of the pore throat distribution index (λ) corresponds to rocks units with coarse and well sorted grains, lower surface areas, lower shape factor and tortuosity with corresponding high FZI's values and vice versa.

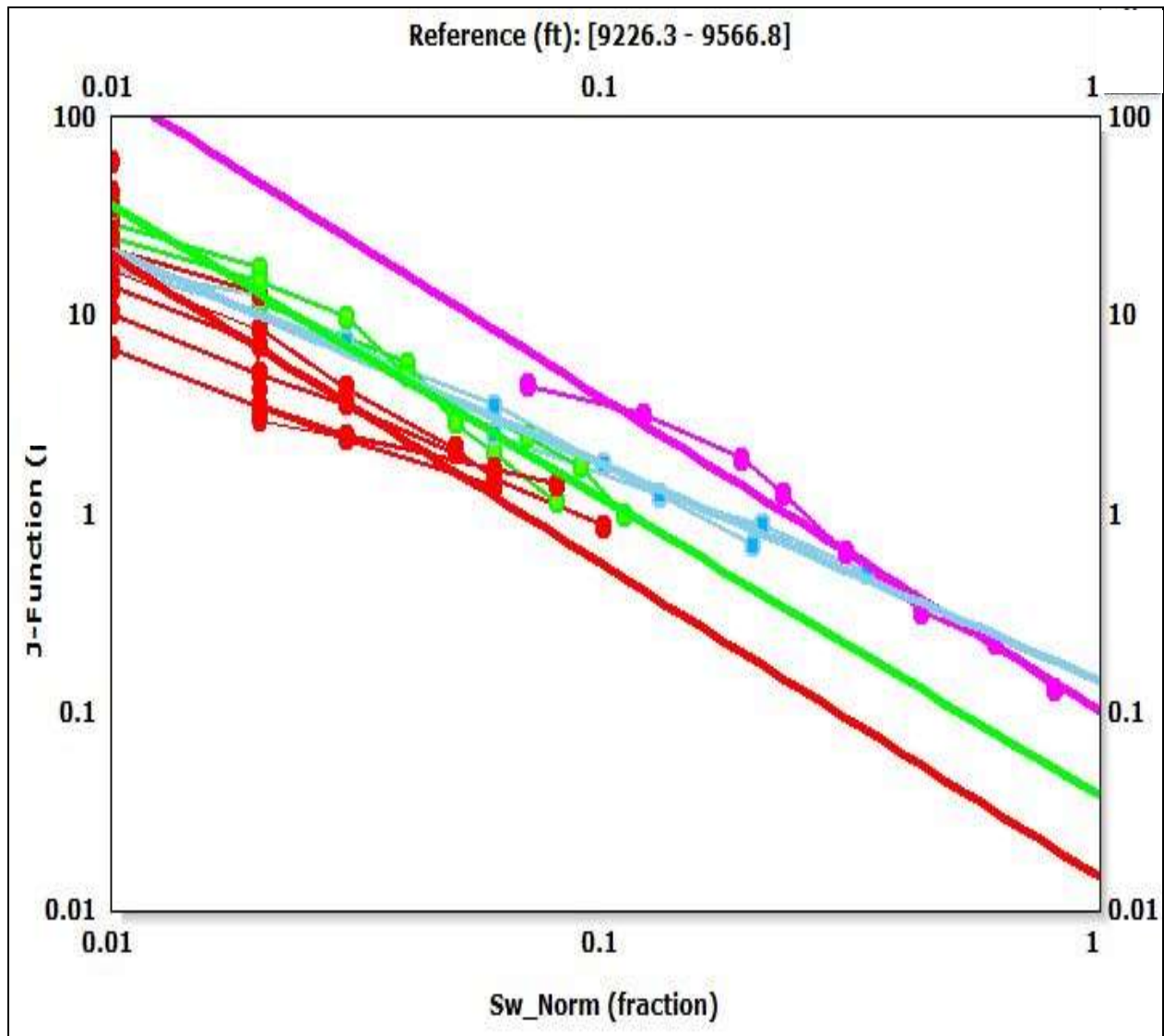


Figure 7.15: Log-log plot of J-function (after Leverett J.) versus normalized wetting phase saturation for all samples, indicating the pore size distribution index (λ) for the four (4) genetic units. The figure indicates difficulty in delineating the MRTB from the ICTB rock units.

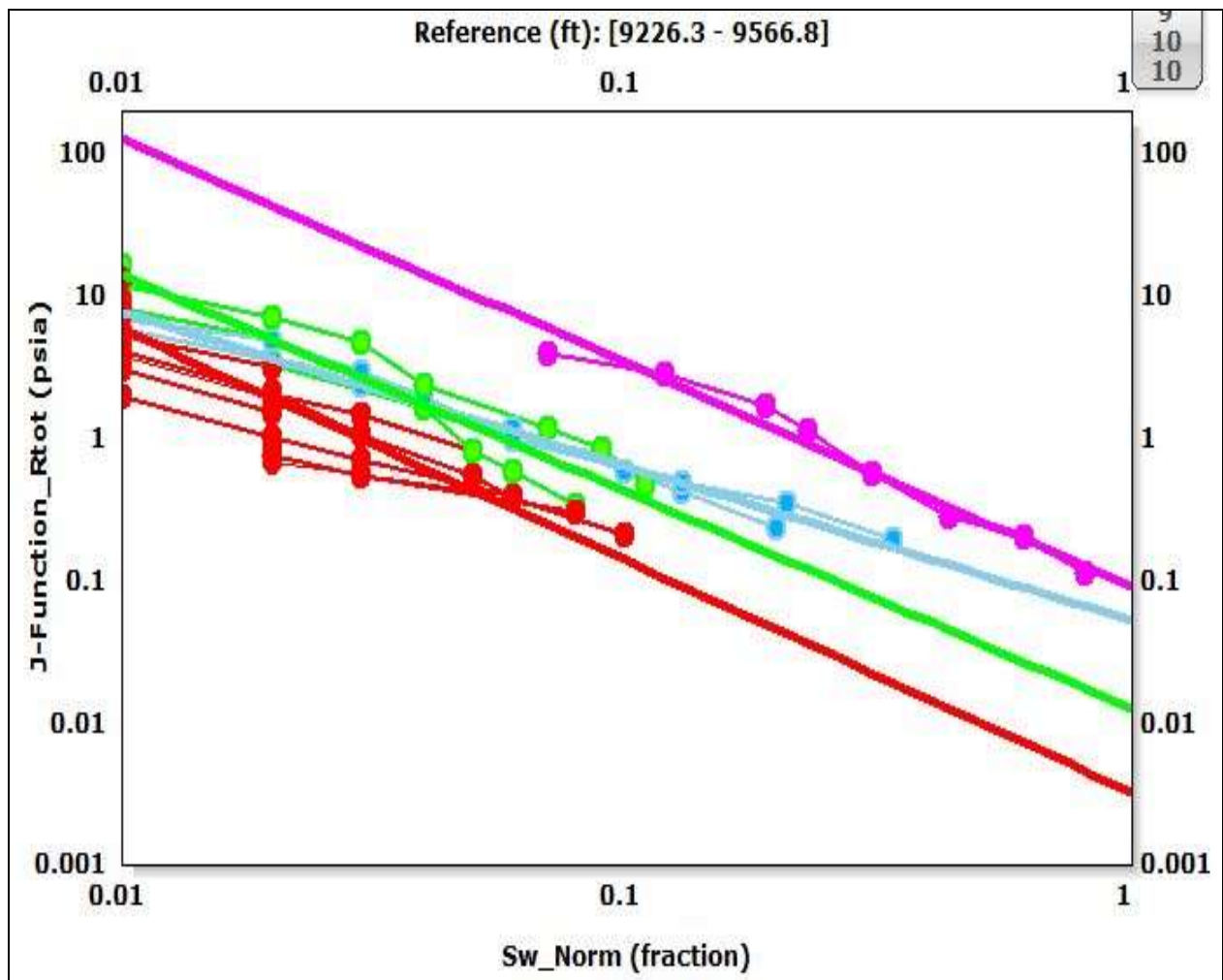


Figure 7.16: Log-log plot of Modified J-function (proposed model) versus normalized wetting phase saturation for all samples, indicating the pore size distribution index (λ) for the four (4) genetic units. Plot indicates a differentiation between the MRTB and ICTB rock units.

Table 7.2 presents a relationship between FZI, J^* and λ from the modified J-function. This demonstrates an increasing reservoir rock quality from I to IV. Pore throat distribution index (λ) less than 1 and a lithology index less than 0.1 for all rock units depicts the dataset for the turbidite sandstone system as a heterogeneous pore size distribution with poorly connected pore system, typical of complex deep water turbidites.

Table 7.2: Summaries of FZI's, J^* and λ for turbiditic shaley-sand dataset

Rock Unit	Description	Modified FZI Average	Swirr (%)	Lithology Index (J^*)	Pore Size Distribution Index (λ)
I	MRTB	1.5	55.0	0.091	0.534
II	ICTB	2.2	9.3	0.052	0.595
III	CSM	3.5	8.0	0.012	0.633
IV	CSA	5.9	5.7	0.003	0.662

7.3. Improved Stratigraphic Modified Lorenz Plot (SMLP) Concept

Using the Proposed Normalized Pore Throat (R_{tot}) Model

A quantitative approach aimed at transforming rock-type-based reservoir zonation into petrophysically based flow units for input into a numerical flow simulator is employed to validate the proposed normalized pore throat genetic units based model. This method provides a tool for improved reservoir characterization and determination of the minimum number of flow units as input into a numerical flow simulator that honors the foot-by-foot characteristics at the wellbore. Five graphical methods are used to quantify hydraulic flow units based on geologic framework, petrophysical rock/pore types, reservoir storage capacity and flow capacity, and the reservoir process speed.

These are: genetic units based porosity-permeability cross plot, Winland R35 porosity-Permeability cross plot, Stratigraphic Flow Profile (SFP), Stratigraphic Modified Lorenz Plot (SMLP) and Flow zone indicator.

Figures 7.17 and 7.18 presents the stratigraphic flow profiles of dataset obtained from the Continental-Fluvial depositional environment used for demonstrating the efficacy of the proposed model for hydraulic flow unit characterization. These dataset include conventional well logs and 445 special core and routine core analysis including detailed core description for genetic unit characterization, core porosities and permeabilities.

The proposed normalized pore throat relation is used to determine the reservoir's flow capacity, storage capacity and flow unit speed. Distinct flow units were referenced to existing Modified Stratigraphic Lorenz Plot (G. W Gunter *et al.*, 1997) and FZI based hydraulic flow unit characterization (J. O. Amaefule *et al.*, 1993) to validate the applicability of the proposed model for hydraulic flow unit characterization.

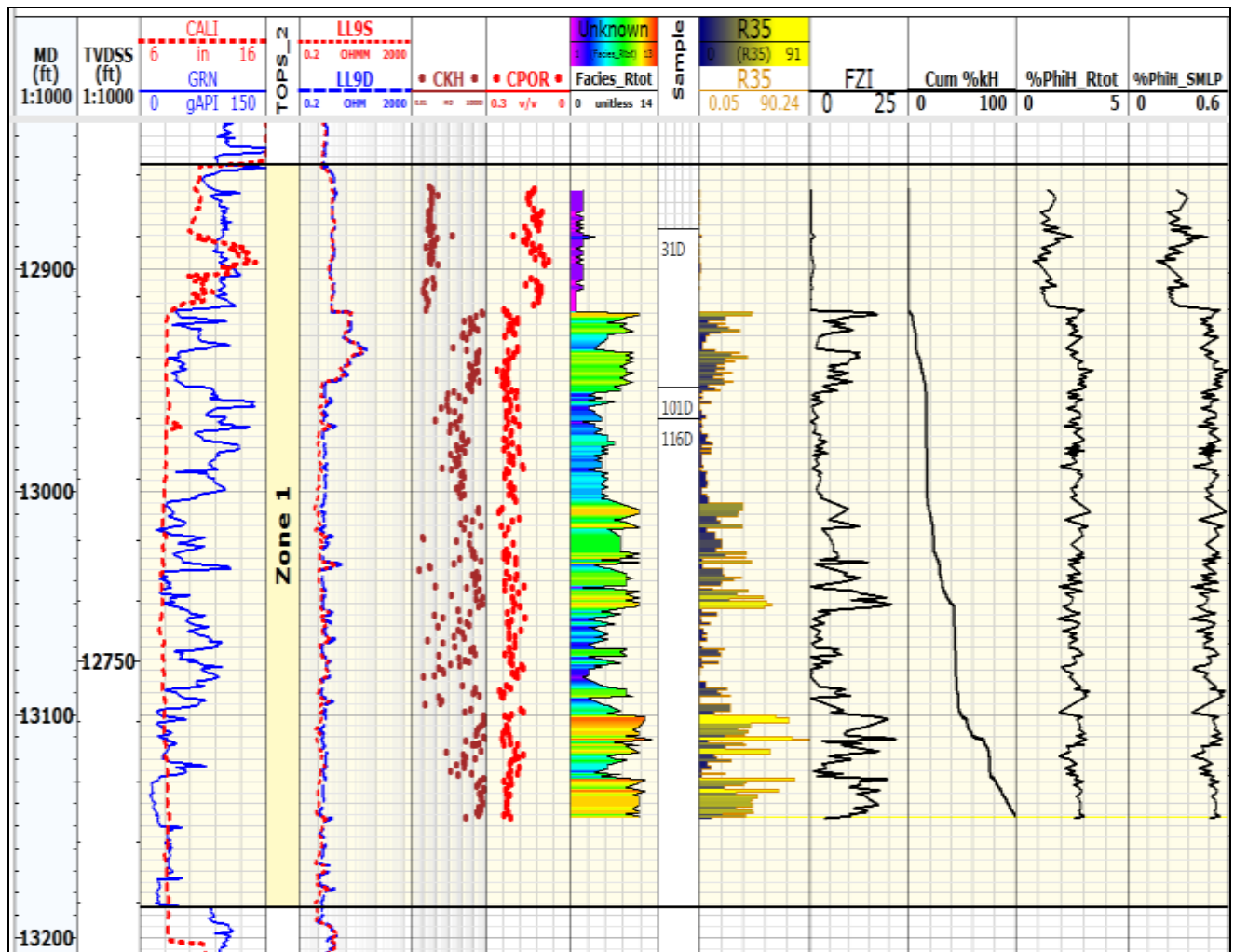


Figure 7.17: Stratigraphic Flow Profile for Zone 1 (Continental/Fluvial Environment) – Field “K” indicating a low resistive and low contrast pay reservoir with cored interval and facies association. The flow capacity track indicates multiple hydraulic units which is evident from the GR signature depicting a complex diagenetic effect.

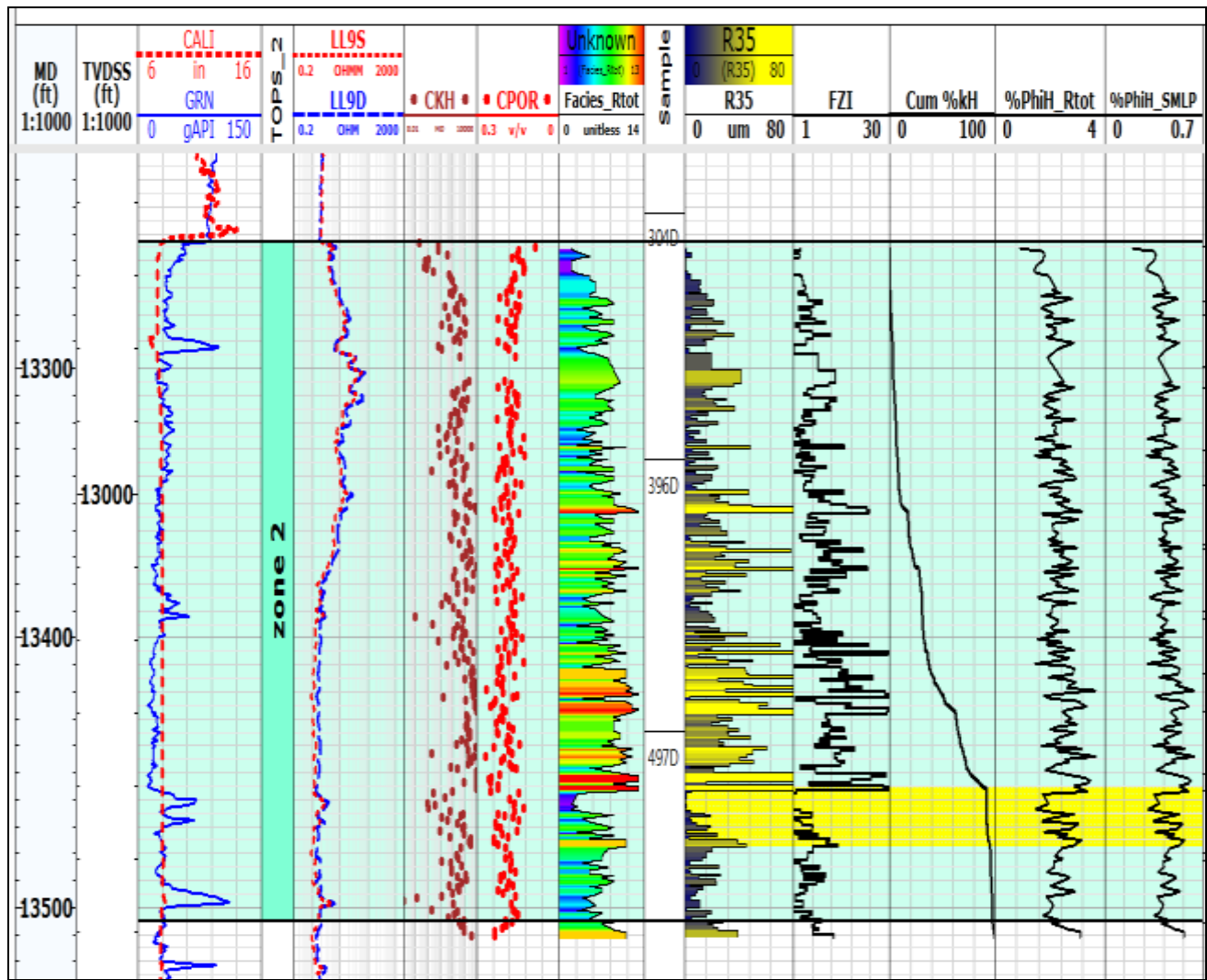


Figure 7.18: Stratigraphic Flow Profile for Zone 2 (Continental/Fluvial Environment) – Field “K” indicating the cored interval and multiple hydraulic units; and sand-shale intercalation evident of possible flow baffles within the highly permeable reservoir.

7.3.1 Methodology for Hydraulic Flow Units Characterization Using the SMLP

The hydraulic flow unit (HFU) concept has been developed to identify and characterize rock types, based on geological and physical parameters at pore scale. The stratigraphic modified Lorenz plot (SMLP) can be used to determine the number of HFUs, it is a plot of flow capacity and storage capacity, the change in slope indicates a new flow unit, while a flat trend can be treated as a barrier where no flow occurred. Five critical steps which honors the geologic framework and, maintain the foot-by-foot character of the data was employed for hydraulic unit characterization. These are:

1. Firstly, the rock types are defined using cross plots of measured porosity versus permeability and capillary attributes constrained to genetic reservoir units' classifications. It is beyond the scope of this work to describe the full Rock Typing workflow. Skalinski *et al.* (Skalinski *et al.*, 2005) and Rebelle *et al.* (Rebelle *et al.*, 2009) demonstrated typical Rock Typing workflows defined at core scale and methodology for migrating into log-based evaluation and cell-based 3D modeling. A unique definition for the term "Rock Type" runs into problems of semantics and context. But for clarity purposes, a Rock Type is here defined as a representative unit or volume of rock that contains a distinctive pore type network whose spatial distribution is related to one or a combination of genetic processes and whose petrophysical character is predictably expressed in terms of porosity, permeability and capillary properties. Hence both geological (spatial) and petrophysical criteria are used to define a Rock Type. Ultimately, Rock Type definition is something of an iterative process, taking into account geological and petrophysical considerations and at the same time views the wider reservoir engineering considerations of what matters most for fluid flow and recovery.

2. The SMLP is a plot of the cumulative percent flow capacity (permeability thickness) and cumulative percent storage capacity (porosity thickness). Both parameters are computed on a foot per foot basis. The reservoir flow capacity and storage capacity are measured in mD-feet or mD-meters and feet or meters respectively. When summed across a reservoir and normalized between 0 and 100%, it is called the cumulative flow capacity or KH% curve and cumulative storage capacity plot or $\phi H\%$. These parameters translates directly into estimated productivity and ultimately into cash flow.
3. A cross plot of the cumulative percent flow capacity (KH%) and cumulative percent storage capacity ($\phi H\%$) is employed to delineate preliminary flow unit intervals based on inflection points as presented in the subsequent subsections. The KH% curve is presented with 0% at the left and 100% on the right. This will match the shape of a spinner survey from a flowmeter, with zero production capacity at base of pay and 100% at top of pay. The shape of the stratigraphic curve is indicative of the flow performance and various hydraulic units. Segments with steep slopes have a greater percentage of the reservoirs' flow capacity relative to storage capacity, and by definition, have a high reservoir process speed. *They are called speed zones*. Segments with flat behavior have storage capacity but little flow capacity and are typically *reservoir baffles* if laterally extensive. Segments with neither flow nor storage capacity are *seals*, if laterally extensive.
4. The log responses, and reservoir quality for the vertical rock sequence in each rock type and genetic units classifications are brought together and correlated as presented in figures 7.17 and 7.18). This present typical petrophysical data log

from two environments of deposition within the Niger Delta employed for this study. The continuous (foot-by-foot) cumulative percent flow capacity (track 8) demonstrates a depth-wise inflection points which defines various rock units. Within each genetic reservoir units' interval as defined from core description and lithofacies association as depicted from the gamma ray and spontaneous potential signatures, the cumulative flow and storage capacities are grouped together as a specific rock type This defines the petrophysical data log that captures the lithological attributes, stratigraphic flow profile with correlation curve, porosity, permeability, k/ϕ ratio, R35, percent storage capacity and percent flow capacity curves, stratigraphic modified Lorenz plot (SMLP) and the flow zone index (FZI).

5. Finally, the delineated hydraulic flow units are validated using the relationship between rock quality and pore throat characterization from capillary attributes: irreducible water saturation, transition zone and pore entry pressures.

Two case studies from the tidal channel sandstone and the fluvial channel sandstone is presented in the following subsections to demonstrate the highlighted methodology for Hydraulic Flow Units Characterization Using the SMLP.

7.3.2 Case Study 1 of the Tidal Channel Sandstone Reservoir (Zone 1)

Figure 7.17 presents the petrophysical data log view of Zone 1 found to be hydrocarbon bearing with no primary gas cap. The sand is composed of three channel sand facies complexes (Sand, Heterolithic and Shale) characterized by variable degrees of incision into the Upper and Lower Shoreface setting. The Tidal Channel genetic unit dominates the base of the reservoir. The amount of tidal channel deposits reduces upward and tends to be replaced by shoreface deposits. These in turn are capped by very fine laminated bioturbated shaley sand, the offshore heterolith. Nine genetic reservoir units (figure 7.19) have been delineated based on core description. The identified rock units' possess distinct depositional fabric which generally controls porosity and permeability relationship as well as capillary pressures. After genetic unit identification, hydraulic flow units are defined to upscale this geologic and petrophysical framework for 3D reservoir simulation. Figure 7.20 presents a log-log plot of reservoir quality indicator (RQI) versus normalized porosity (ϕ_z), indicating eight distinct hydraulic units within the cored interval. Each hydraulic unit is characterized by a different average FZI value as depicted by the varying color codes on the plot.

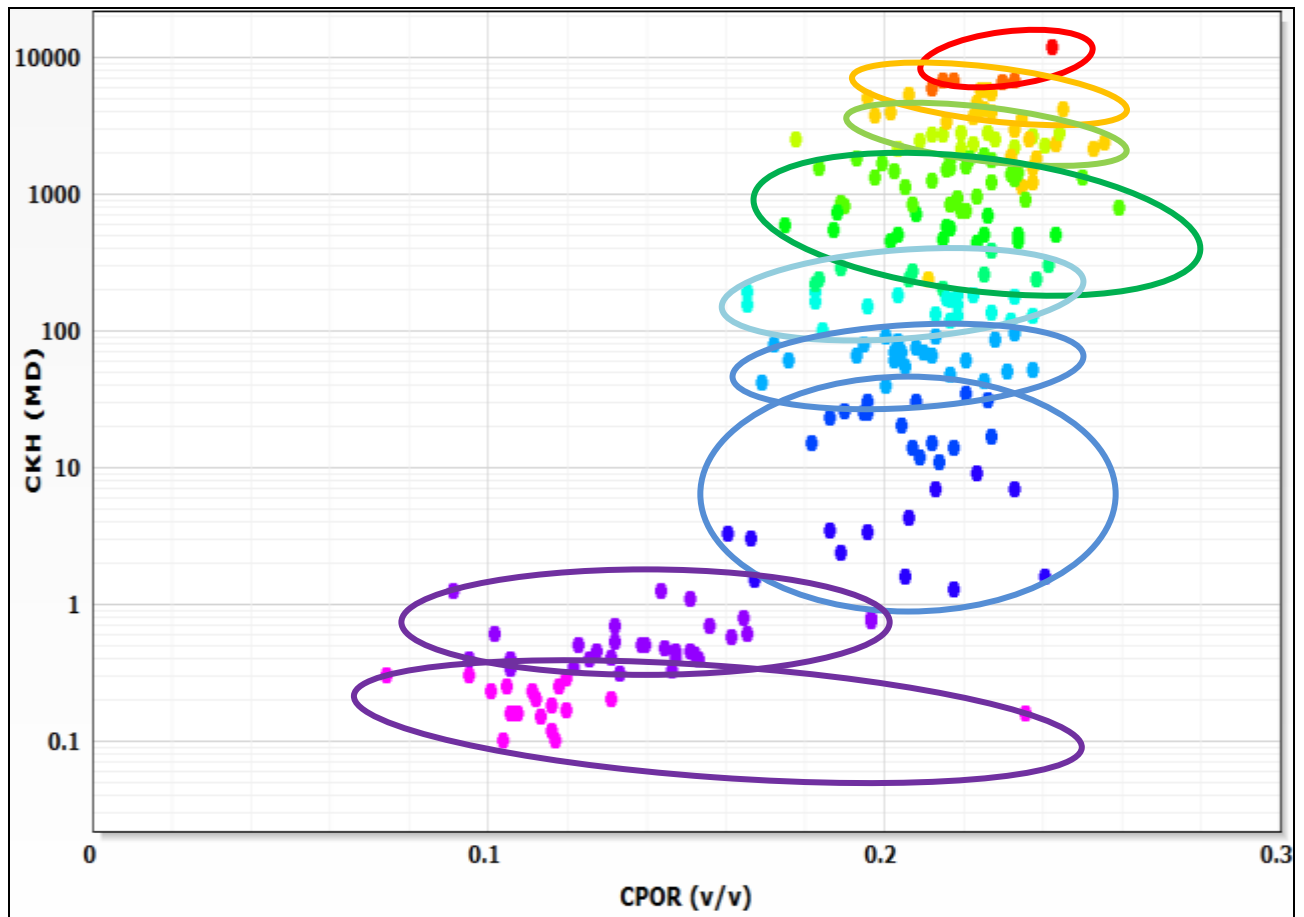


Figure 7.19: Porosity-Permeability plot for various genetic reservoir units for Zone 1 – Field “K” indicating nine (9) genetic reservoir units based on core description.

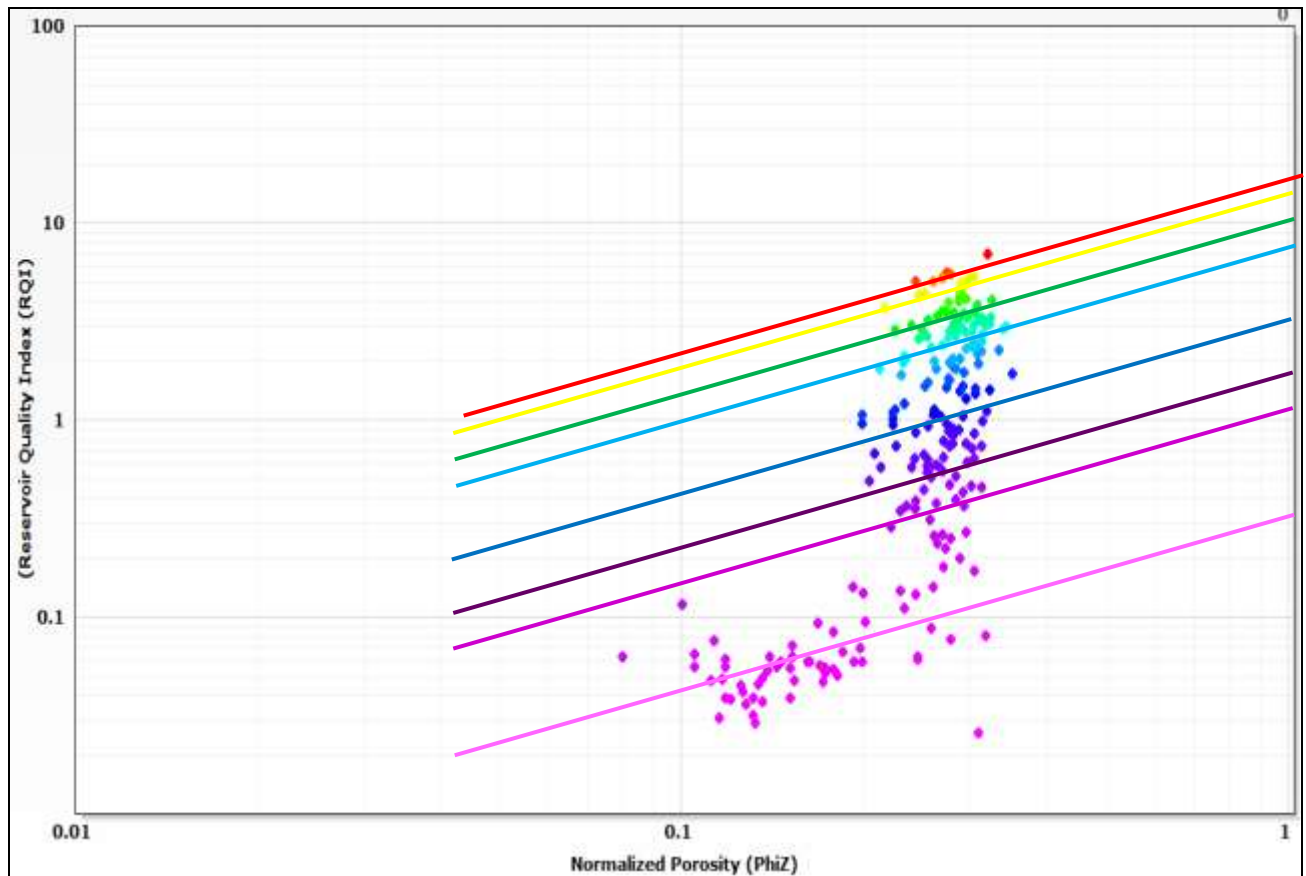


Figure 7.20: Log-log plot of RQI versus normalized porosity indicated various flow units for Zone 1 indicating eight (8) hydraulic flow units.

Figure 7.21 presents a plot of cumulative percent storage capacity versus cumulative percent flow capacity for zone 1 indicating eight (8) hydraulic flow units. The proposed model based normalized pore throat is captured in blue while the stratigraphic modified Lorenz plot is captured in black.

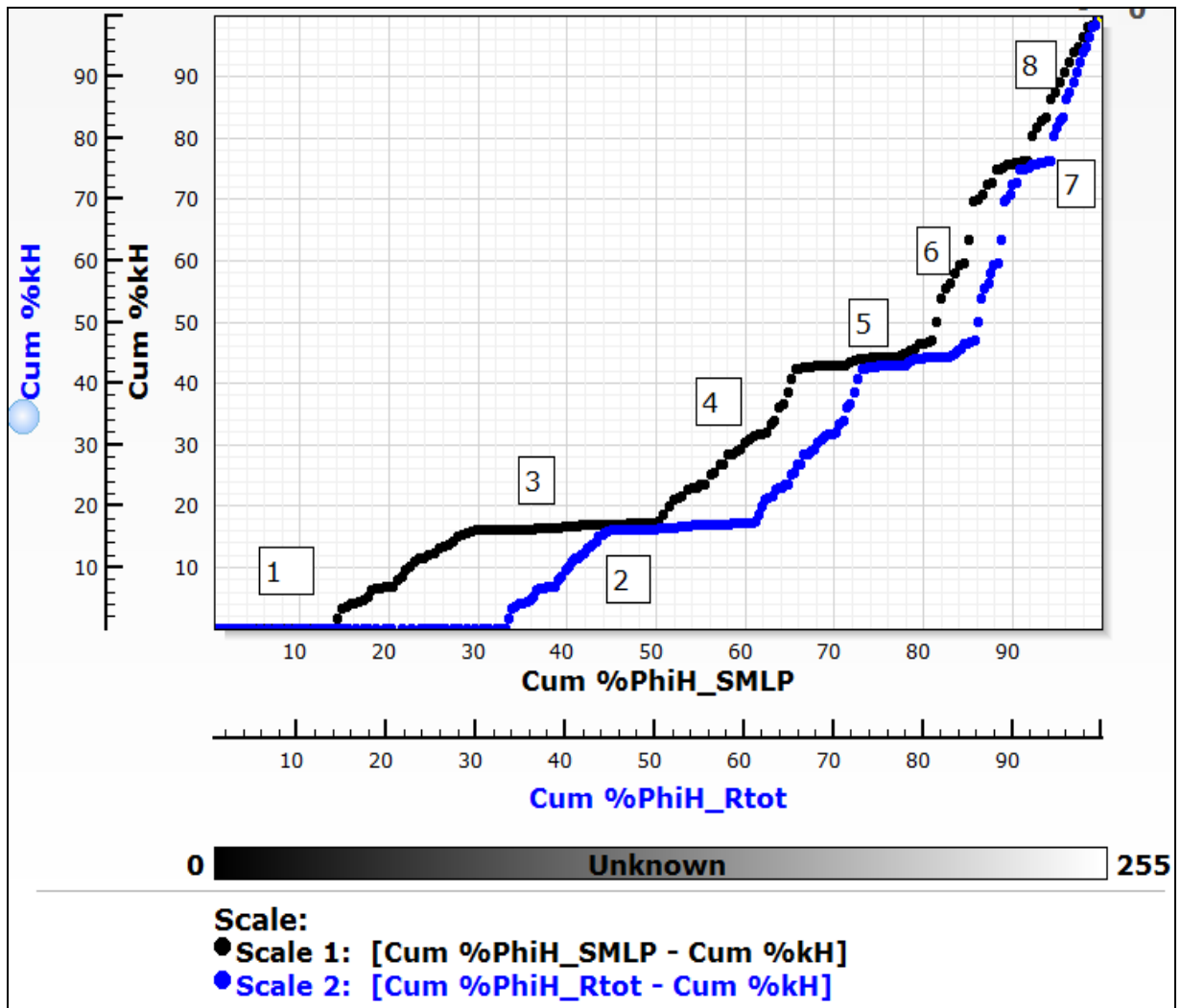


Figure 7.21: Stratigraphic Plot demonstrating hydraulic flow unit results from the proposed approach (blue color) and SMLP (black color) for Zone 1 – Field “K”.

A comparative assessment of the efficacy of the proposed model for hydraulic flow unit characterization was evaluated using figure 7.22. A correlation between the various flow units and genetic grouping depicts that the proposed model captures flow barrier/seals better than SMLP for optimal reservoir modelling. Flow unit 1 characterized by a flat behavior having storage capacity but no flow capacity (typically reservoir baffles), are highly under-predicted by the SMLP method as captured by the green and red coloration on both plots (flow unit 1). Flow units 2, 4, 6 and 8 have a greater percentage of the reservoirs' flow capacity relative to storage capacity as depicted by a steep slope.

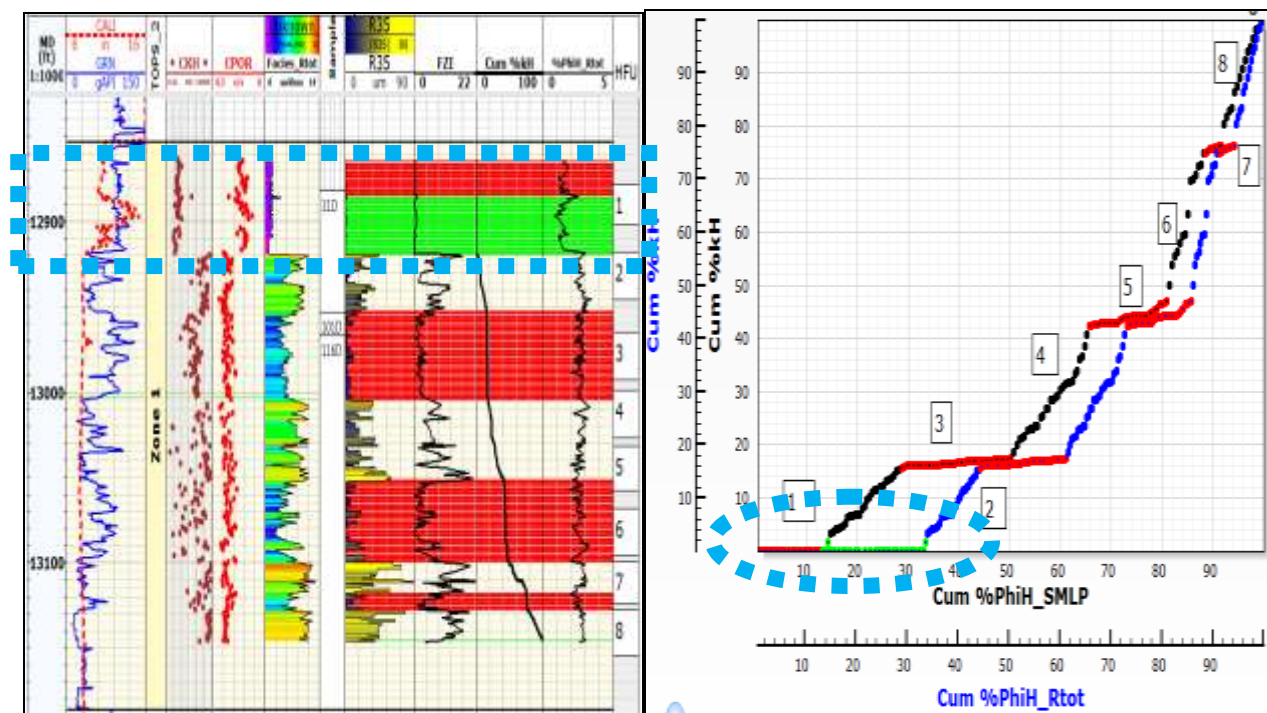


Figure 7.22: Plots of Stratigraphic flow profile (left) and SMLP (right) demonstrating hydraulic flow unit results from the proposed approach and SMLP for Zone 1 – Field “K”. Highlighted in red are reservoir seals. The green highlight demonstrates the efficacy of the modified SMLP in delineating the reservoir seal beyond the resolution of the existing SMLP method. This evidently captures the geologic control on flows on flow properties.

Mercury injection capillary pressures were incorporated in the analysis to calculate pore size distribution to check the consistency between the rock units differentiated by the proposed method, mean of the FZI, SMLP and the pore size measurements. Figure 7.23 presents the capillary pressure versus the wetting phase saturation of the samples and the corresponding pore throat size distribution. As it is observed, two different rock types corresponding to flow units 1 and 3 are identified based on the irreducible wetting phase saturation, the shape of the curve and the pore size distribution.

They are composed of poorer rock facies with high percentage of micropores (less than 10 microns). This is also typical of their longer transition zones.

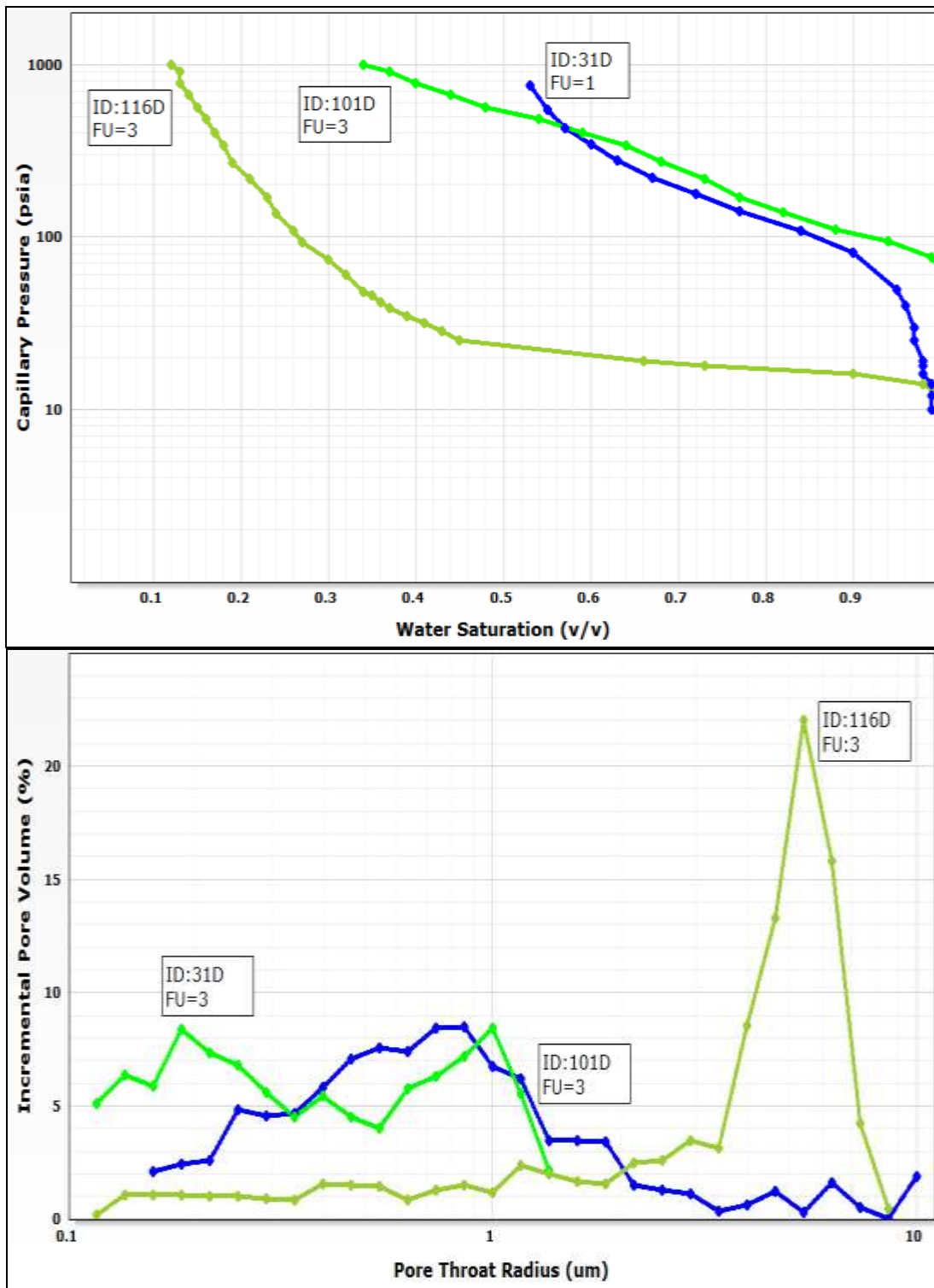


Figure 7.23: Plot of mercury injection capillary pressure curves (top) and Pore Throat Size Distribution (bottom) obtained within Zone 1 – Field “K”, showing relationship between plot as a function of identified flow units.

7.3.3 Case Study of the Fluvial Channel Sandstone Reservoir (Zone 2)

Similar workflow was applied for the deeper hydrocarbon bearing sand (zone 2). From core and analogue studies, the unit is interpreted to have been deposited in a Lower to Upper Shoreface (Sand/Shale Facies) setting, on top of remnant deposits of a tide dominated delta. The shoreface is incised by an active laterally migrating tidal regime that deposited tidal channels (Sand, Heterolith and Shale facies). These have coalesced into a massive tidal channel sequence of 200 – 300 ft. Intervening channel heteroliths, separating individual genetic units, are also prevalent. Figure 7.24 presents a porosity-permeability relationship with color coded variation, demonstrating the various genetic units analyzed from core description.

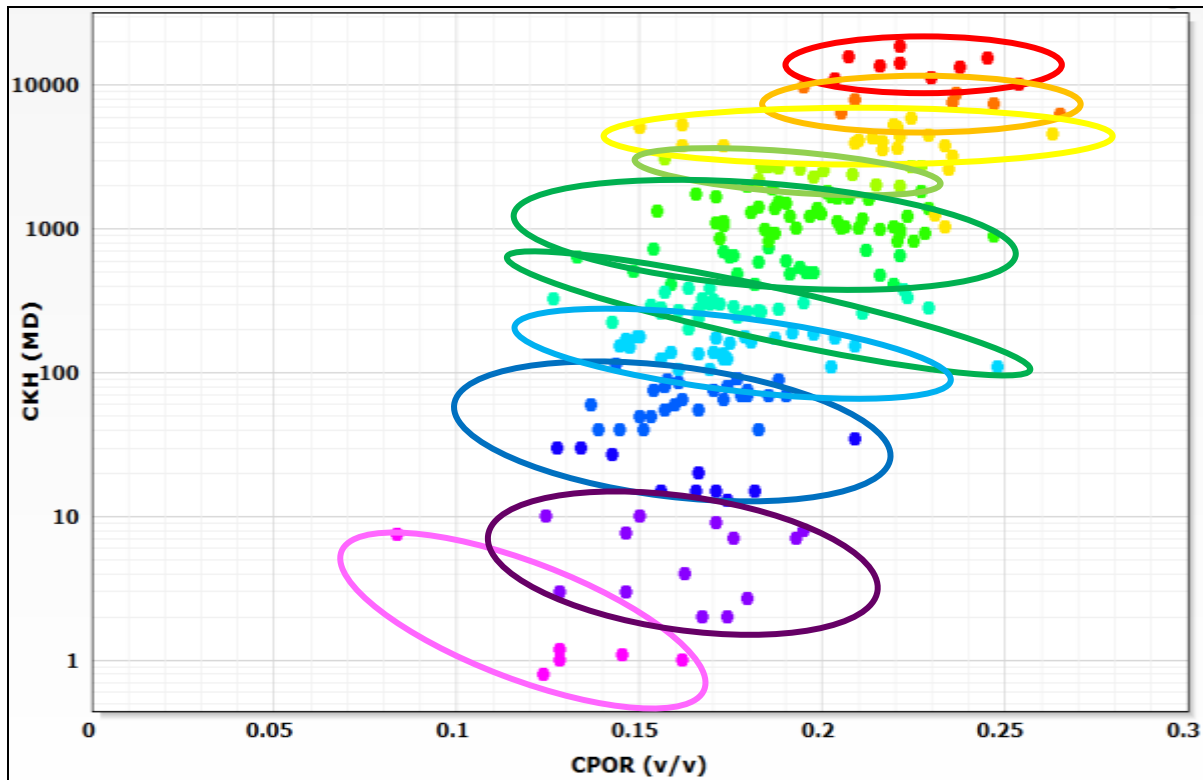


Figure 7.24: Porosity-Permeability plot for various genetic reservoir units for Zone 2 – Field “K” indicating ten (10) genetic units as interpreted from detailed core description.

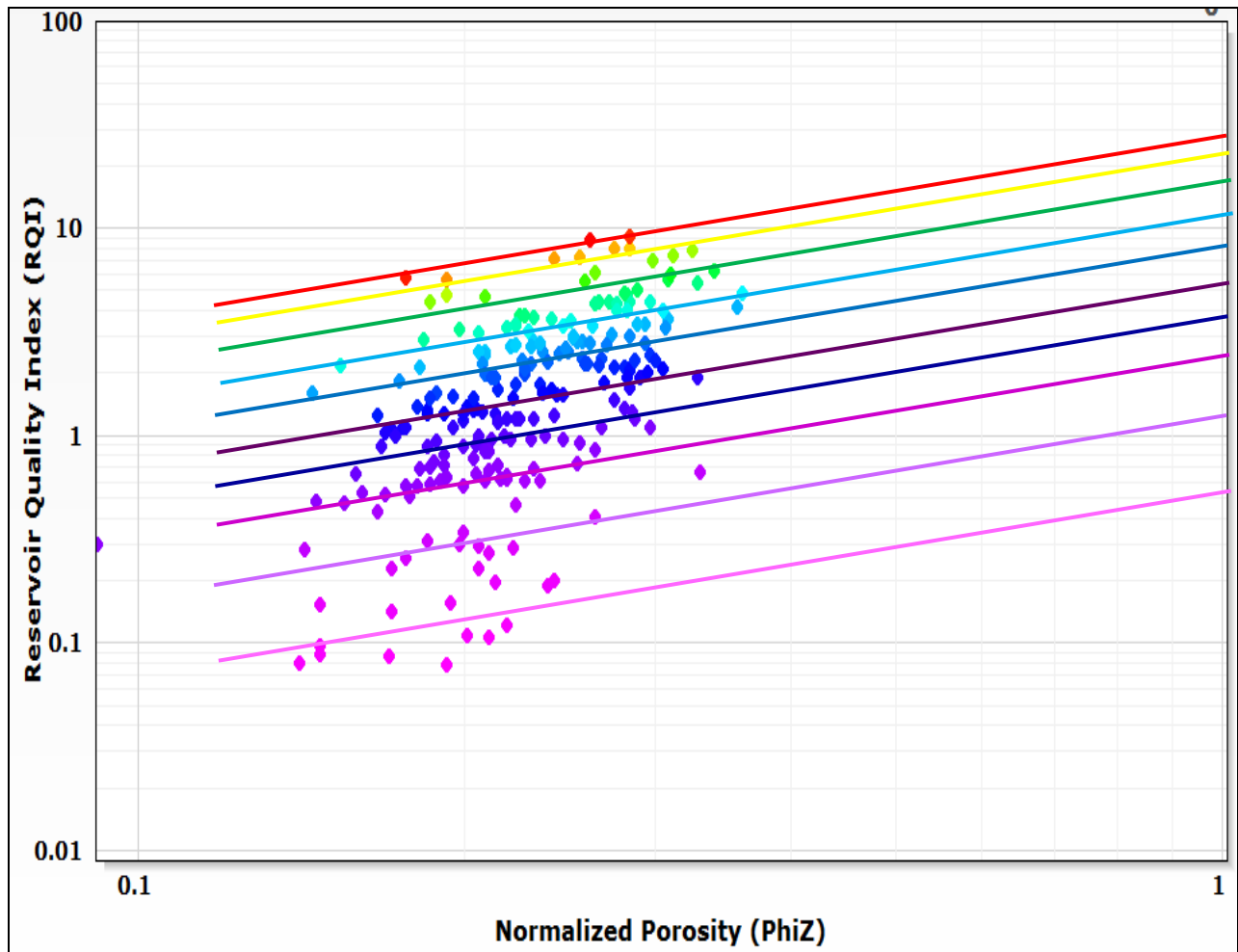


Figure 7.25: Log-log plot of RQI versus normalized porosity indicating various flow units for Zone 2, indicating ten (10) flow units with distinct FZI value, where normalized porosity = 1.

Figure 7.25 presents a log-log plot of reservoir quality indicator (RQI) versus normalized porosity (ϕ_z), indicating 10 distinct hydraulic units within the cored interval. This demonstrates a typical intercalated clastic fabric with permeability streaks. Each hydraulic unit is characterized by a different average FZI value as depicted by the varying color codes on the plot.

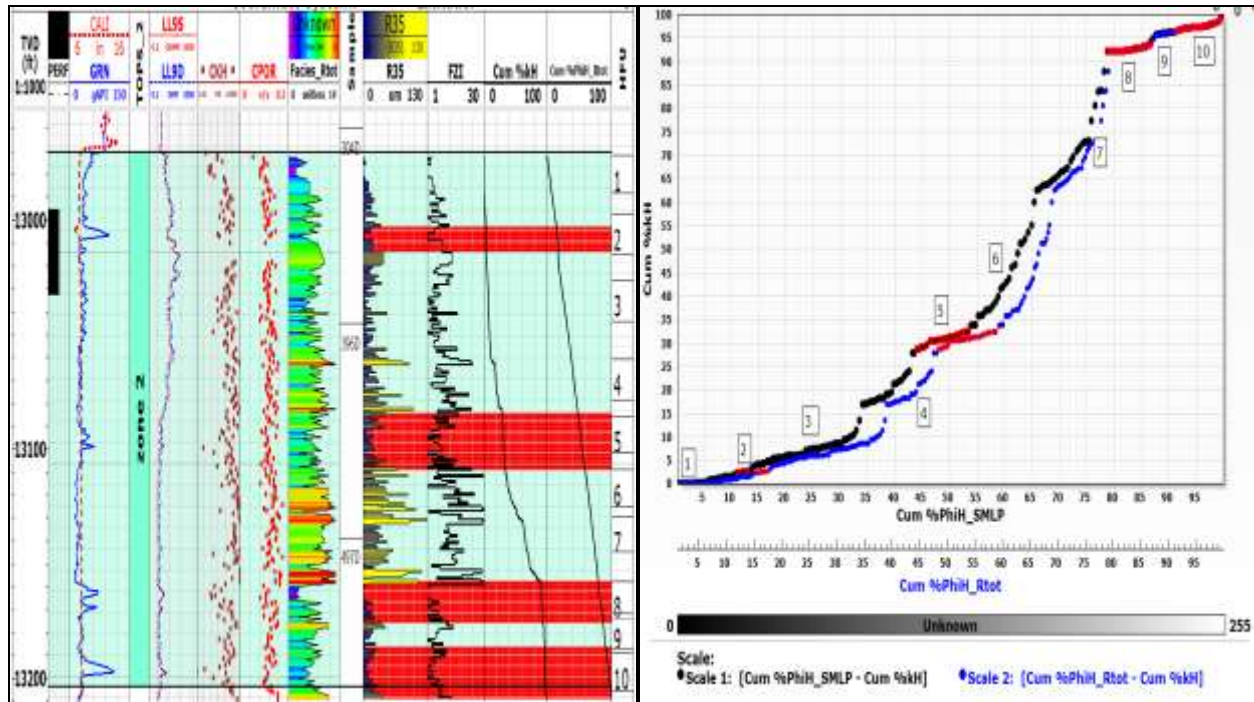


Figure 7.26: Plots of stratigraphic flow profile (left) and SMLP (right) demonstrating hydraulic flow unit results from the proposed approach and SMLP for Zone 2 – Field “K”, indicating the presence of ten (10) hydraulic units within the reservoir system.

Figure 7.26 presents a plot of cumulative percent storage capacity versus cumulative percent flow capacity for zone 1 indicating ten (10) hydraulic flow units. The proposed model based normalized pore throat is captured in blue while the stratigraphic modified Lorenz plot is captured in black

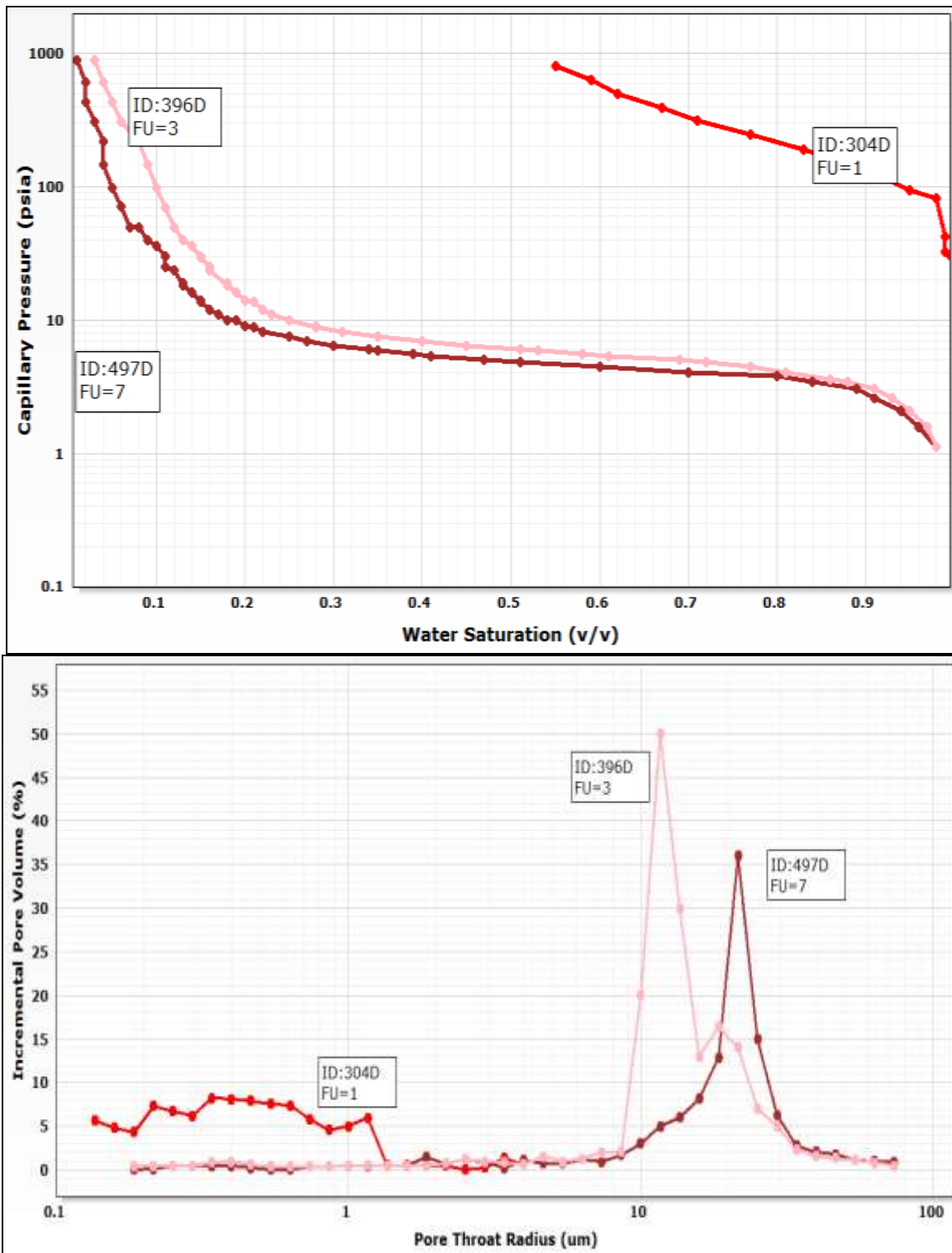


Figure 7.27: Plot of mercury injection capillary pressure curves (top) and Pore Throat Size Distribution (bottom) obtained within Zone 2 – Field “K”, showing relationship between plot as a function of identified flow units.

Figure 7.26 present plots used for hydraulic flow unit characterization. This indicates the existence of ten (10) flow units within zones 2. Flow units 3, 6 and 7 demonstrate excellent speed zones. This is demonstrated by their steep slope indicating high flow capacity compared to their storage potential. Figure 7.26 present plot of mercury injection capillary pressure versus saturation and their corresponding pore throat distribution. Higher values of irreducible water saturation and entry pressure usually defines pore rock facies and vice versa. Capillary curves with sample ID: 396D and 497D obtained from flow unit 3 and 7 respectively possess macropores between 10 and 100 microns. This demonstrates good reservoir parameters, storage potential and speed zones for fluid flow. As highlighted in figure 7.26, the correlation between the stratigraphic flow profile and flow unit plots demonstrate the proposed model capabilities in delineating flow barriers/seals in micro-scale (flow unit 2). Capillary Pressure plot with ID: 304D displays attributes of a typical poorer marine shale facies (high entry/displacement pressure, transition and irreducible water saturation) and this is evident on the stratigraphic flow units plot (left), defined by a flat behavior.

7.4 Application of the Normalized Pore Throat Methodology in 3D Reservoir Characterization Studies

7.4.1 Field Overview and Location of Study Area

3D modelling of the Fluvial Dominated Channel Sandstone reservoir was carried out through series of integrated geological and reservoir engineering studies. The case study area – Field "A" is located in the eastern part of the Cenozoic Niger Delta. Figure 7.28 present a 2D base map indicating the coordinate locations of the field and wells. A total of ten wells (9 conventional, 1 side-track) were drilled in the field.

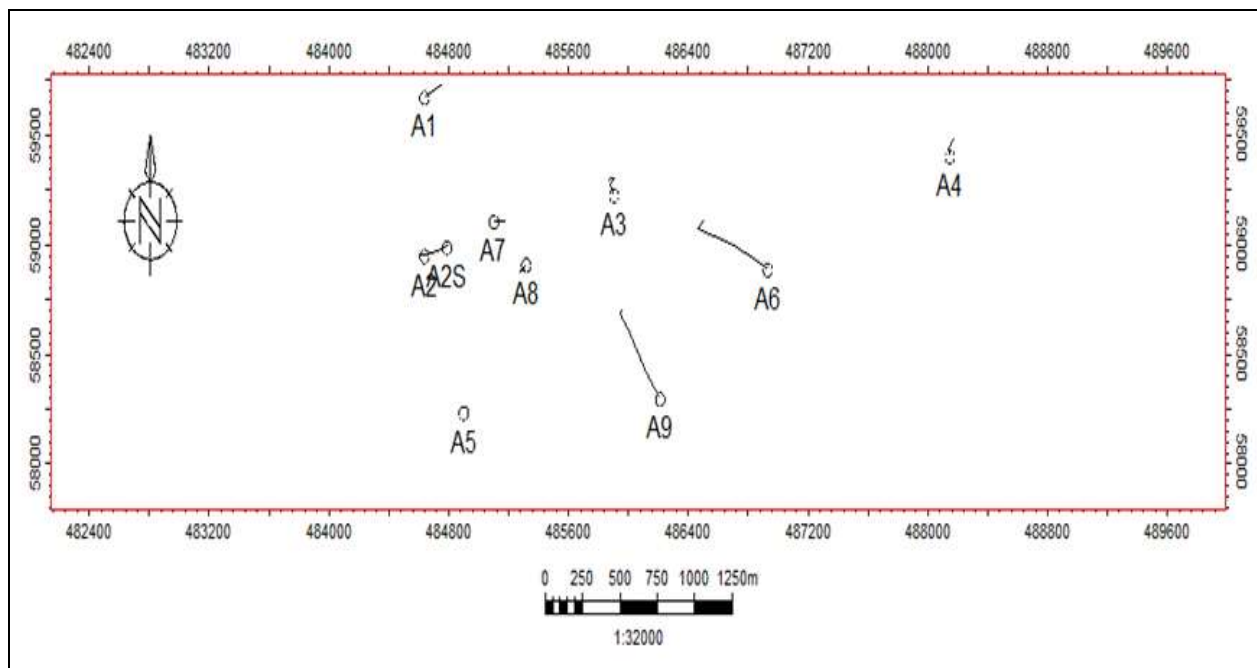


Figure 7.28: Base map of the study area with well locations.

Well A1-drilled in 1965, was off structure and encountered no hydrocarbon bearing sands, hence it was abandoned. Dataset from eight (8) wells was used for both geologic and reservoir description and characterization

7.4.2 Reservoir and Fluid Characterization of the Study Area

Four (4) major lithofacies units (figure 7.29) were distinguished by integrating all available core descriptions, core measurements, well logs, and petrophysical evaluations; for 3D geological facies modelling.

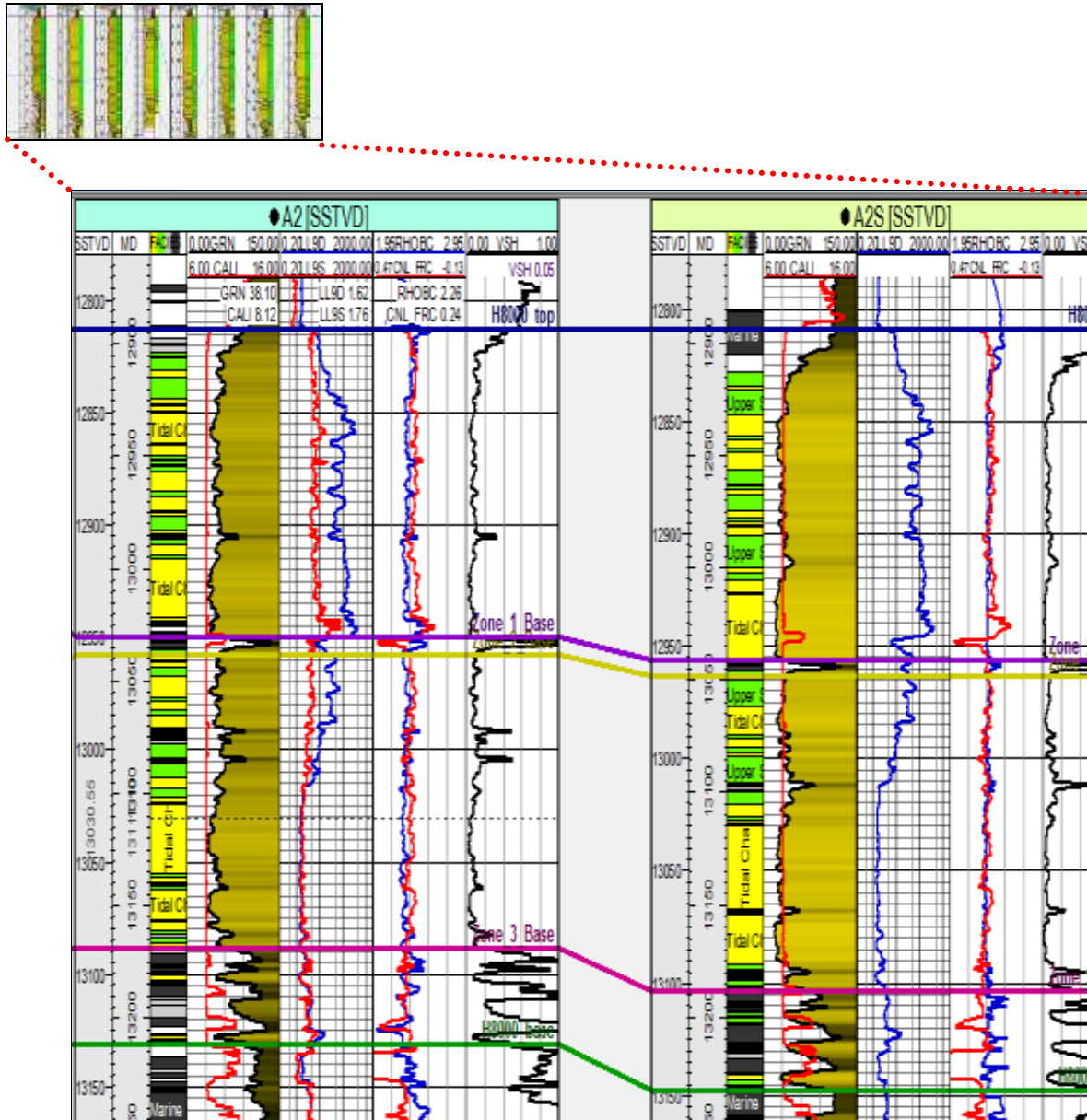


Figure 7.29: Lithostratigraphic correlation indicating the four (4) facies assemblage interpreted from core description, ditch cuttings analysis and well logs for the shoreface reservoir.

The shoreface is incised by an active laterally migrating tidal regime that deposited tidal channels (Sand, Heterolith and Shale facies). Intervening channel heteroliths, separating individual genetic units, are also prevalent. These are not correlatable across the reservoir (see figure 7.26 – top map), and as such, there is need for high resolution hydraulic unit characterization for efficient flow barrier/seal delineation and proper 3D reservoir modelling.

Oil and water gradient was estimated from RFT measurements as 0.274 psi/ft and 0.433 psi/ft respectively (see figure 7.30). The original oil water contact (OOWC) of 13,030 ftss (RFT from Well A2) & 13,026 ftss (log) was obtained from same well. Reservoir pressure at OOWC =13,030 ft was estimated to be 5,635 psia. Figure 7.31 presents a field wide interpreted OOWC per well for the reservoir used for reserves estimation.

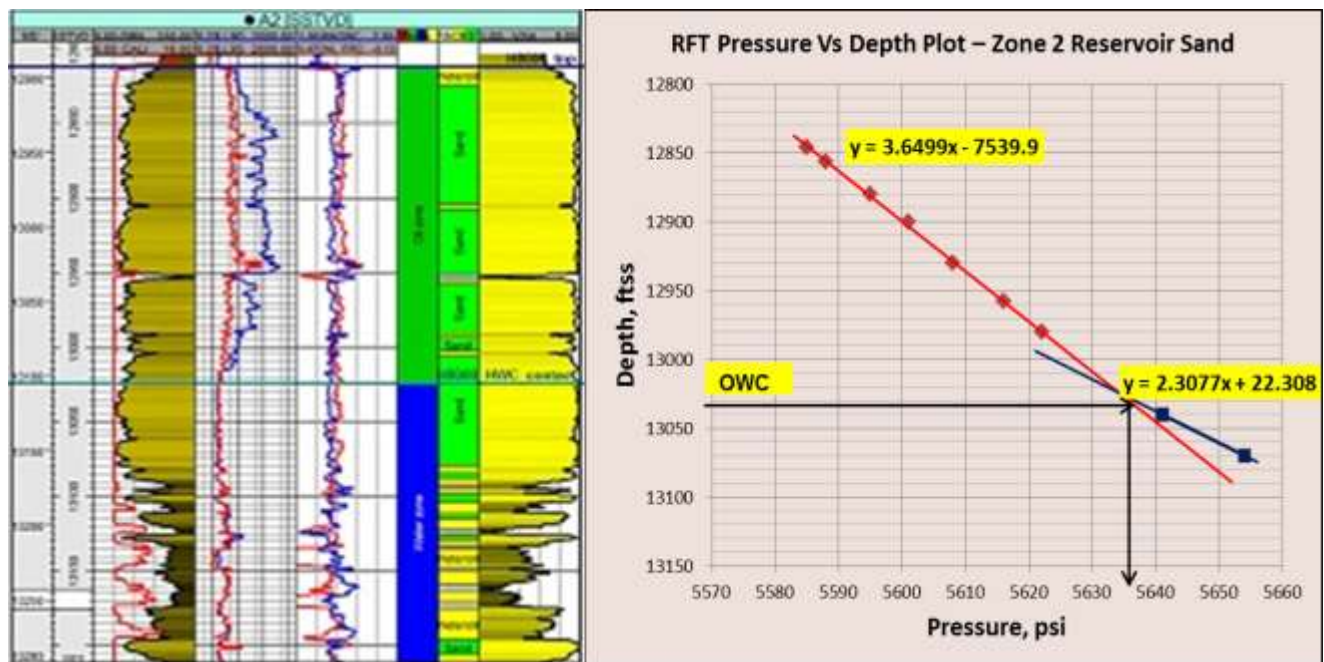


Figure 7.30: Fluid differentiation plot indicating OOWC established from interplay between resistivity and density/neutron logs, and correlating with RFT fluid gradient analysis.

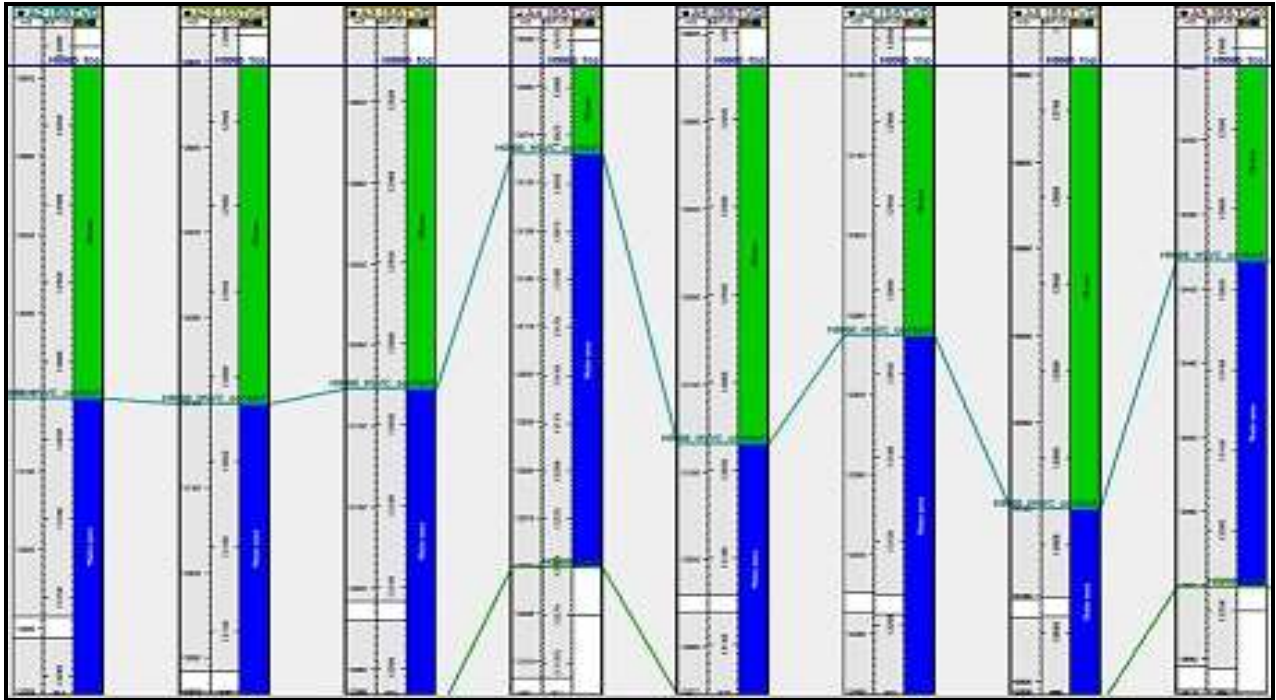


Figure 7.31: Field wide fluid differentiation plot indicating OOWC established from interplay between resistivity and density/neutron logs.

The reservoir performance studies indicate current pressure depletion is about 3% with average water cut of 4%. No primary gas cap and producing under bottom water drive. Four wells have produced water, while four remained dry. Based on a booked STOIP of 277 MMstb and Ultimate Recovery (UR) of 131 MMstb, the production figures suggest current recoveries of 7% STOIP & 14% UR. Table 7.3 present a summary of the reservoir and fluid properties obtained from laboratory assessment

Table 7.3: Reservoir and PVT properties obtained from Well A-002 indicating an under-saturated black oil reservoir.

PROPERTY	VALUE	UNITS
Datum Depth	13,026	ftss
OOWC	13,030	ftss
Initial reservoir pressure, P_i	5577	Psia
Bubble point pressure, P_b	2,874	Psia
Initial Oil FVF, B_{oi} @ P_i	1.636	rb/stb
R_{si}	0.855	Mscf/stb
Reservoir Oil Density	0.61	g/cc
Oil Viscosity	0.5	cp
Reservoir Temperature	224	°F
Rock Compressibility	3.00E-06	psia ⁻¹
Stock Tank Oil Density	40.9	°API
Gas Gravity (air = 1)	0.89	unitless

3D geological model of Zone 2 was built for this study, as part of the reserve quantification project. After construction of the structural model and gridding, the litho-types (facies) were propagated in the 3D model. Table 7.4 presents the project and model dimensions established from the available 3D pre and post stack-migrated seismic volume covering the block.

Table 7.4: Project (top) and Model (bottom) dimensions obtained from the interpreted seismic segy volume post stack migrated.

Axis	Min	Max	Delta
X	0.00	493,604.01	493,604.01
Y	0.00	68,337.12	68,337.12
Depth	-28,194.40	2,000	30,194.40

Axis	Min	Max	Delta
X	481,856.79	489,4518.84	7,595.05
Y	56,686.51	60,365.01	3,678.50
Z (Depth)	-13,595.01	-6,471.99	7,123.01
Cells (ni x nj x nk)	76 X 37 X 54		
Total number of 3D cells	151,848		

The reservoir properties including PHIE, VSH, S_w , and permeability were propagated as “conditioned to facies”, to consider the facies as the leading parameter in 3D space. The proposed normalized pore throat method for the permeability prediction and the Flow Zone Indicator (FZI) method were implemented and ten distinctive hydraulic units were identified. These flow units were compared and further validated with the capillary measurements and pore throat size distributions. In order to propagate the properties measured on cores into the 3D model, the relationship between those properties and the petrophysical properties, i.e. effective porosities (PHIE), shale volume (VSH), and water saturation (S_w) were investigated and properly correlated. This step is necessary as core data are usually very limited compared to log data and the reservoir volume. In general, due to the different resolutions of core and log data, this step includes most of the uncertainty, particularly in the heterogeneous reservoirs.

7.4.3 Results and Analysis

Table 7.5 presents histogram and function plot analysis for both permeability models.

Statistical parameter depicts higher correlation coefficients and lower covariance of the modified approach over the existing FZI based methods for all zones.

Table 7.5: Histogram and Function Plot Analysis of the FZI Model and the Proposed Normalized Pore Throat (R_{tot}) Method.

STATISTICAL ANALYSIS:- ZONE 1						
Property	Minimum	Maximum	Mean	Standard Dev.	Variance	Sum
PERM_ R_{tot} (mD)	0.04	2,311	1,082	677	457,970	57,980,536
PERM_ FZI (mD)	1.04	4,978	3,814	1,371	1,880,664	204,361,178
STATISTICAL ANALYSIS:- ZONE 2						
Property	Minimum	Maximum	Mean	Standard Dev.	Variance	Sum
PERM_ R_{tot} (mD)	0.02	1,131	388	79	6,175	693,252
PERM_ FZI (mD)	0.28	3,042	1,142	1,416	20,050,230	2,038,731
STATISTICAL ANALYSIS:- ZONE 3						
Property	Minimum	Maximum	Mean	Standard Dev.	Variance	Sum
PERM_ R_{tot} (mD)	0.62	3,080	1,007	960	921,865	26,967,453
PERM_ FZI (mD)	0.35	4,922	3,029	1,594	2,539,334	81,139,540
STATISTICAL ANALYSIS:- ZONE 4						
Property	Minimum	Maximum	Mean	Standard Dev.	Variance	Sum
PERM_ R_{tot} (mD)	0.42	1,279	150	310	96,045	2,140,235
PERM_ FZI (mD)	0.89	4,540	1,259	1,647	2,712,233	17,984,867
Function Analysis (PERM VERSUS PHIE): Zone2 (Intra-Reservoir Shale)						
Property	Correlation Coefficient (R^2)		Covariance			
PERM_ R_{tot} (mD)	0.723		1.34			
PERM_ FZI (mD)	0.305		10.17			

Regional studies as well as geophysical & geologic evaluation using amplitude seismic spectral decomposition, instantaneous phase and sweetness volume, depicts Zone 2 as discontinuous intra-reservoir marine shale. AVO analysis also demonstrates very poor rock properties within the zone. This is typical of reservoir baffles within the clastic environment. As evident from table 7.5, the proposed (R_{tot}) model captures these

uncertainties with permeability as low as 0.02 mD and a mean value of 388 mD compared to the FZI approach with 0.28 mD and 1,142 mD respectively.

The function plot also demonstrates the efficacy of the proposed model over the existing with higher correlation between the interconnected pore network (PHIE) and permeability to flow with a 72% for the proposed R_{tot} method and 31% for the FZI-based approach.

As demonstrated in previous sections, both the existing and modified FZI methods indicate better correlation with lithologic types and VSH than PHIE, and as a result, FZI was propagated in the 3D model using the regression equations fitted over FZI and combinations of lithologic types and VSH.

Using the above mentioned integrated methodology, the reservoir permeabilities were propagated in the 3D geological models, through most representative relationships established between the core and log data. PHIE and Sw were also distributed in the 3D grid cells using stochastic methods. Stochastic volume estimation demonstrates a strong correlation between the book reserves and methodology developed for this study as presented in table 7.6. A permissible 0.72% discrepancy between the booked and study estimated STOIP indicate a representative model further reservoir characterization study.

The static model was initialized and hydraulically equilibrated using a dynamic simulator (ECLIPSE®). Table 7.7 presents volumetric estimates indicating the initialized parameters and STOIP. A comparative evaluation of STOIP estimated from the stochastic static model and equilibrated dynamic model indicates appreciable match with less than 1% discrepancy (table 7.8).

Table 7.6: Volumetric comparison between the booked STOIIP and model estimated STOIIP indicating reasonable percentage difference.

	Bulk Volume (*10 ³ acre.ft)	STOIIP (MMSTB)
Static Model Based	372	275
Geologic Map Based	368	277
Percent Difference (%)	1.08	0.72

Table 7.7: Reservoir model Initialization indicating STOIIP and average reservoir properties.

```

=====
:                FIELD TOTALS                :
:                PAV =      5618.74  PSIA      :
:                PORV=  2595033804.  RB        :
: (PRESSURE IS WEIGHTED BY HYDROCARBON PORE VOLUME:
: PORE VOLUMES ARE TAKEN AT REFERENCE CONDITIONS):
:----- OIL STB -----:-- WAT STB --:----- GAS MSCF -----:
: LIQUID VAPOUR TOTAL : TOTAL : FREE DISSOLVED TOTAL :
:-----:-----:-----:-----:-----:-----:
:CURRENTLY IN PLACE : 278433497. : 278433497.: 302477325. : 306001827. : 580243308. : 886245136.:
:-----:-----:-----:-----:-----:-----:
: OUTFLOW THROUGH WELLS : : 0.: 0. : : 0.:
: WELL MATERIAL BAL. ERROR: : 0.: 0. : : 0.:
: FIELD MATERIAL BAL. ERROR: : 0.: 0. : : 0.:
:-----:-----:-----:-----:-----:-----:
:ORIGINALLY IN PLACE : 278433497. : 278433497.: 302477325. : 306001827. : 580243308. : 886245136.:
=====

: FIPNUM REGION AVERAGED GRID QUANTITIES :
: ( WEIGHTED BY PORE VOLUMES ) :
: AT REFERENCE CONDITIONS ) :
:-----:-----:-----:-----:-----:-----:
: REGION : PERMX : PERMY : PERMZ : PORO : D2 :
:-----:-----:-----:-----:-----:-----:
: FIELD : 1680.001 : 1680.001 : 84.000 : 0.18727 : 23.84 :
=====

```

Table 7.8: Relationship between Volumetric Estimation Methods Assessed in the Study.

	Bulk Volume (*10 ³ acre.ft)	STOIIP (MMSTB)
Geologic Map Based	461	277
Static Model Based	453	275
Dynamic Model Based	453	278

Relative permeability, PVT and MBAL were analyzed for the case study, and both the FZI and the R_{tot} based permeability models were simulated to validate their efficacy for fluid transmissibilities, recoveries, ease to history matching and meaningful production forecast. Figure 7.32 presents a cumulative oil production (FOPT) versus time plot using Proposed Model (red color code) and FZI (blue color code), indicate improved fluid RF and reduction is number of convergence issues and simulation time.

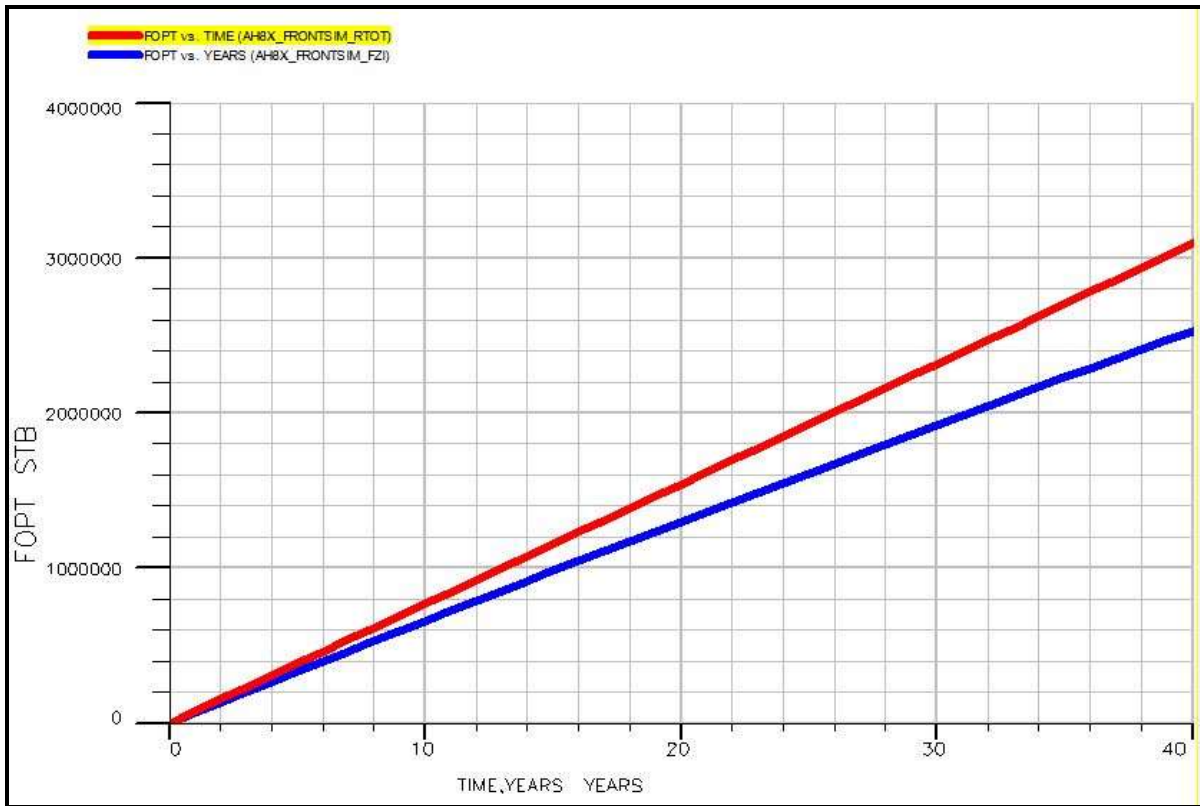


Figure 7. 32: Plot of oil production rates (FOPR) versus time (years) obtained from dynamic reservoir modelling, with proposed model (red) and FZI-based method (blue).

Finally, histogram and cross plot analysis proves the proposed model to be more realistic and honors the depositional/diagenetic fabric as well as flow potential of the shaley sandstone system. Analysis of zone 2, composed of intra reservoir marine shale, indicates that the facies based FZI approach over predicts the dynamic capability of the zone with an average and maximum permeability of 1,400 and 3,042 mD respectively.

The proposed model is quite conservative within this zone having an average permeability of 388 mD and maximum permeability of 1,142 mD due to the sand shale intercalation typical of the Niger Delta reservoirs. Analysis of the function plot for both permeability models versus effective porosities, throw more emphasis on the applicability of the proposed models as indicated by their R^2 values and covariance within the shaley-sandstone reservoir. The covariance of 1.34 for the proposed model validates the effectiveness of the model compared to the FZI based model with a covariance of 10.17. The FZI based method overestimates permeabilities in such units and invariably lead to inaccurate and misleading reservoir. The lower standard deviations from the mean value also substantial the efficacy of the proposed model to existing facies based model.

Analysis of the histogram and function plots based on hydraulic flow (HFU's) as well as genetic reservoir units have proved the proposed model to be more realistic and honors the depositional fabric and hydraulic conductivity of the Tertiary shaley sandstone system.

As a result, the FZI based permeability model suffers much convergence issues during simulation and subsequently a higher simulation run time. Also the proposed model gave improved recovery efficiency as demonstrated on figure 7.29.

7.4.4 Implication of the $\overline{R_{tot}}$ based Modified RQI Methodology in 3D Simulation Studies

3D reservoir model was built to validate the applicability of the proposed normalized pore throat methodology beyond well centric view in 3D scale for mature field performance studies. The case study is built from dataset obtained from the Tertiary Niger Delta Deep-Water depositional belt. A total of fourteen wells (7 deviated, 2 side-tracks and 5 horizontal) were drilled in the field. The reservoir is a black oil system with API gravity of 29°. Table 7.9 presents the reservoir rock and fluid properties.

Table 7. 9: Reservoir and Fluid Properties.

Property	Value
Datum Depth	4,600 ftss
Initial Reservoir Pressure, Pi	2,010 psia
Bubble Point Pressure, Pb	1,998 psia
FBHP(06,16)	1,912 psia
Reservoir Oil Density	0.61 g/cc
Reservoir Oil Viscosity	0.5 cp
Proven Oil Column	170 ft
Boi @ Pi	1.636 rb/stb
Initial Solution GOR, Rsi	298 scf/stb
Reservoir Temperature	167 °F
Stock Tank Oil Density	28.9 °API
Gas Gravity (air=1)	0.89
Rock Compressibility	3.00E-06
Average Porosity	0.28 v/v
Average Water Saturation, Sw	0.2 v/v
Average Permeability, K	3,100 mD
STOIP	201.0 MMSTB
Np (06/16)	84.3 MMSTB
RF (06/16)	41.9 %

Stratigraphic modelling was done to establish the geologic framework of the Reservoir. This entailed well correlation, intra-reservoir correlation and facies interpretation. The combination of log suites (GR, density, neutron, and resistivity) and petrophysical evaluation results (VSH, PHIT/PHIE, SW) were used in validating the tops and bases of the reservoir. The reservoir is characterized by clean, well sorted sands with some silt and shale intercalations. Log and core observations suggest a 'barrier bar' depositional model with fairly uniform and homogeneous shoreface sand.

Figure 7.33 presents the lithostratigraphic correlation indicating four (4) key facies assemblage as interpreted from core description, ditch cuttings analysis and well logs for the shoreface reservoir.

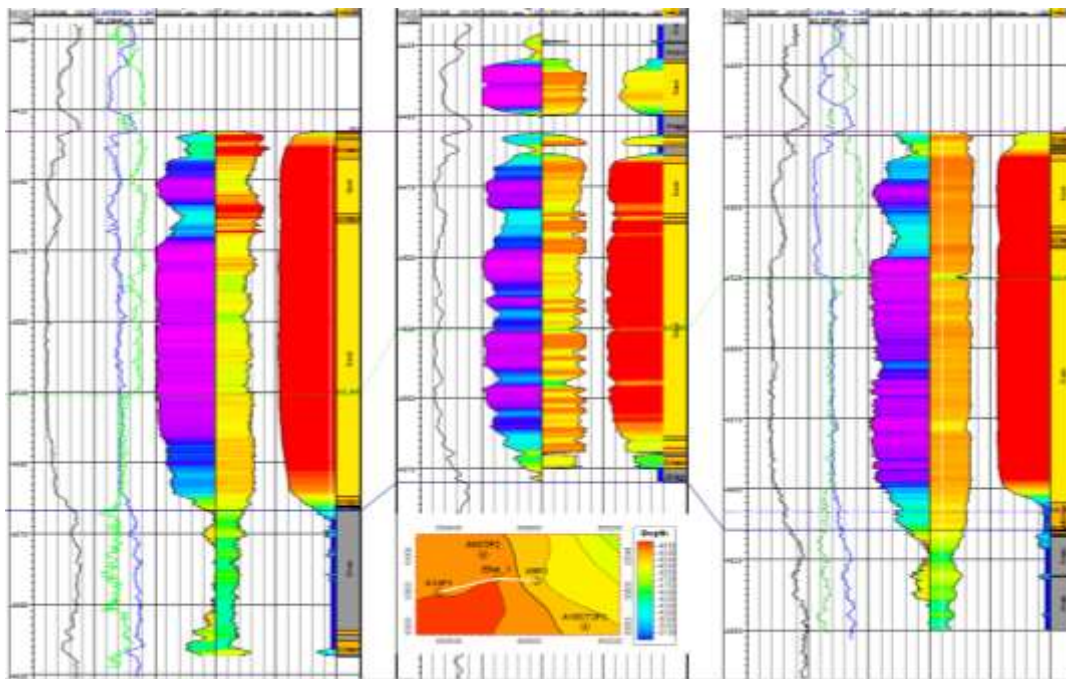


Figure 7.33: Lithostratigraphic correlation presenting a fairly homogeneous setting. Inset map underneath indicates line of cross-section E–W.

Review of the core reports depicts the availability of 254 core analysis data samples obtained from Well-A2 covering the reservoir interval. Figure 7.34 presents a plot of the measured permeabilities versus porosities for the shoreface sand unit. The petrophysical summary is as highlighted demonstrating excellent reservoir properties:

- 224 PERMX: 1.3 – 10,260 mD; [AVE: 4,029]
- 30 PERMZ: 0.33 – 6,900 mD; [AVE: 2,150.8]
- 249 PORO: 19.2 – 37.3 %; [AVE: 30.6]

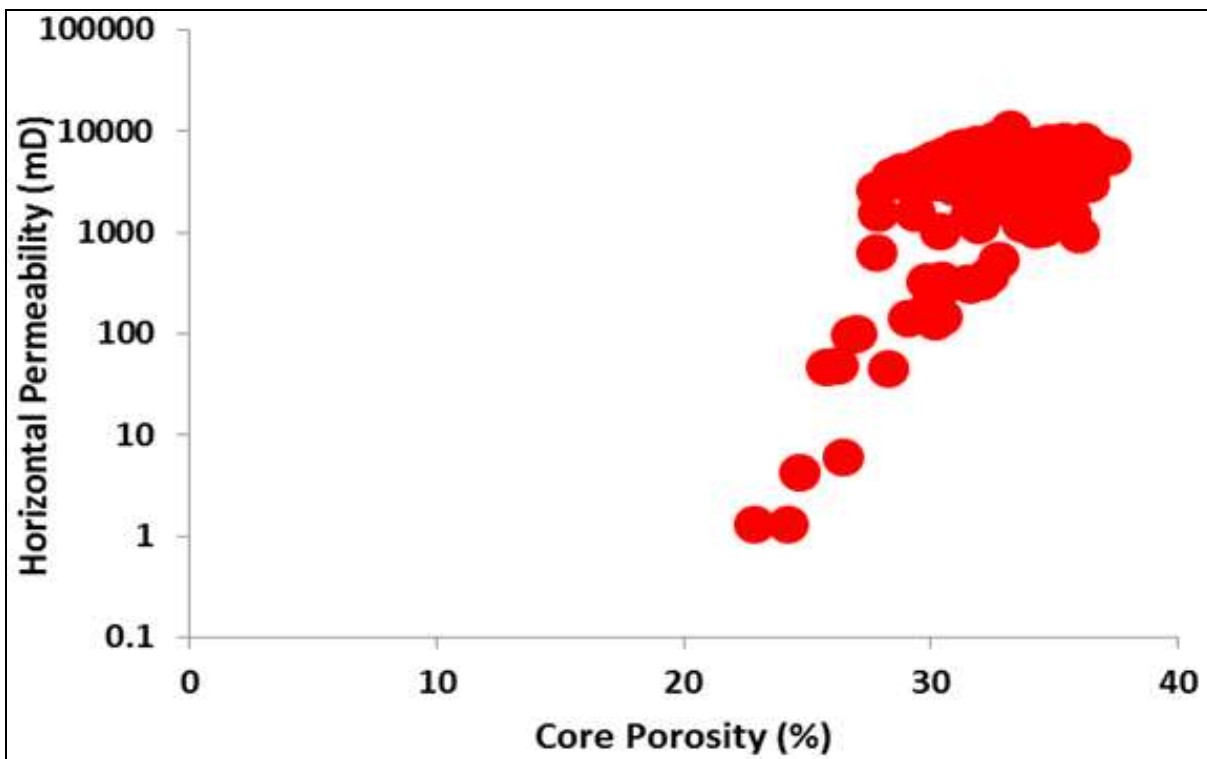


Figure 7. 34: Plot of core derived permeability versus porosity from the reservoir interval indicating excellent reservoir quality.

A preliminary quality check of the existing dynamic reservoir model depicts a highly pessimistic permeability estimates using the Timur-Coates approach compared with available corrected air permeabilities. Table 7.10 presents this assertion compared to the result summaries from figure 7.34. This indicates a need to re-calibrate the model to measured core dataset.

Table 7. 10: Initialized reservoir properties from existing model after Timur-Coates.

: FIPNUM REGION AVERAGED GRID QUANTITIES :						
: (WEIGHTED BY PORE VOLUMES :						
: AT REFERENCE CONDITIONS) :						
: REGION :	PERMX :	PERMY :	PERMZ :	PORO :	DZ :	:
: FIELD :	533.002 :	533.002 :	373.101 :	0.29915 :	3.77 :	:

The proposed genetic units based normalized pore throat and the Timur-Coates methods were implemented for permeability modelling for the field. Figure 7.35 shows preliminary evaluation of both models and their comparison to measured core dataset. Track 5 presents the permeability models after Timur-Coates (red), proposed normalized pore throat method (green) and laboratory measured core permeability (black dotted). This demonstrates higher correlation coefficient (R^2) of 94% between the core permeability and the genetic units based normalized pore throat permeability (PERM_Rtot) compared to existing Timur-Coates permeability model (PERM_TC) with R^2 of 56%. This was applied to all the seven (7) wells and lithostratigraphic correlation is presented in figure 7.36. This shows a consistent increase in permeability for all wells.

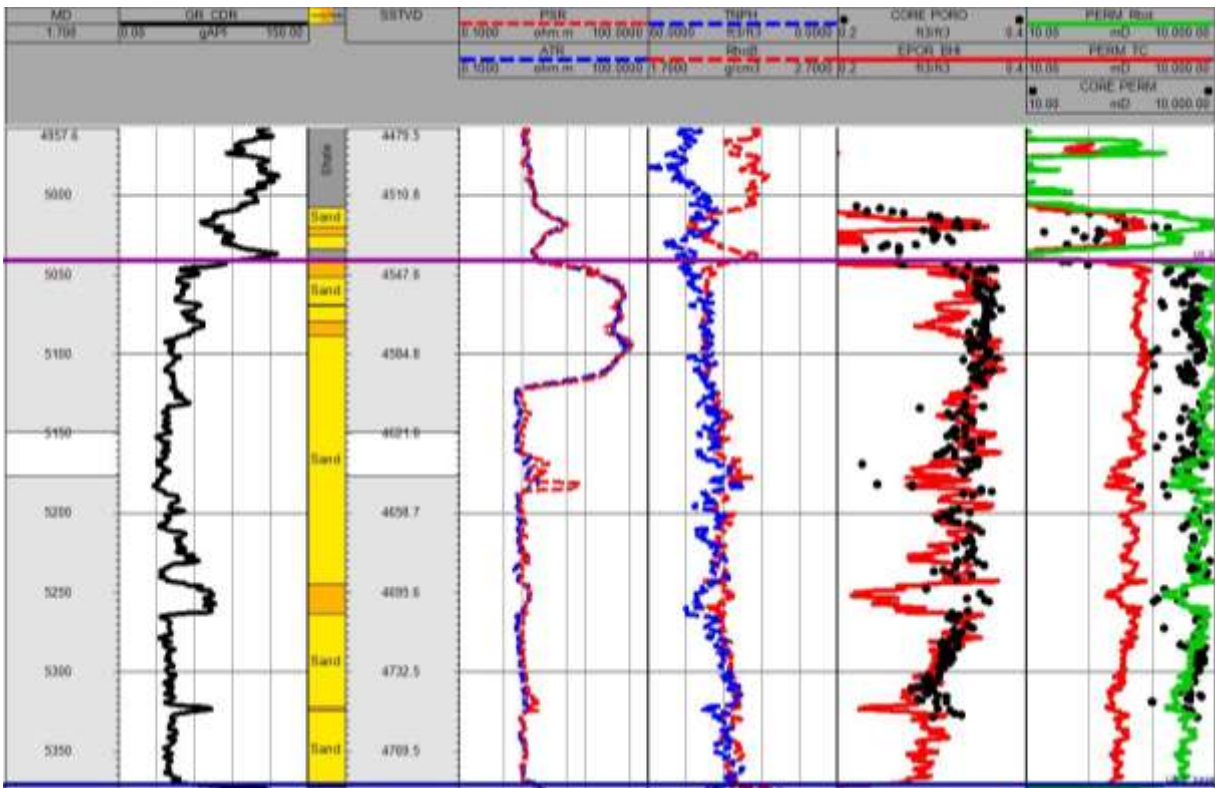


Figure 7. 35: Petrophysical Data Log View indicating improved correlation between the measured dataset and proposed model (green) with Timur-Coates (red).



Figure 7. 36: Lithostratigraphic correlation of the reservoir unit indicating variation between the proposed methodology (green) and Timur-Coates approach (red). Highlighted in red presents preliminary model calibration to measured data.

An estimated base case STOIP of 201 MMSTB and GIIP of 4.6 BSCF was established from detailed geological reservoir characterization study. The field has produced approximately 84 MMSTB, achieving 42% field wide recovery. Production peaked at a 28.7 MBOPD (2001) with average water cut at approximately 80%. The structural interpretation depicts the subsurface reservoir as a fault-assisted closure within the deep water turbiditic environment. The reservoir properties were propagated as “conditioned to facies”, to consider the facies as the leading parameter in 3D space. In order to propagate the properties measured on cores into the 3D model, the relationship between those properties and the petrophysical properties, i.e. effective porosities (PHIE), shale volume (VSH), and water saturation (Sw) were investigated and properly correlated. This step is necessary as core data are usually very limited compared to log data and the reservoir volume.

A numerical flow simulation was performed by integrated all requisite reservoir and fluid data to demonstrate model reliability for future reservoir management practices. Two model cases were established with only the permeability models (PERM-X, -Y, -Z) as variables to validate the applicability of the proposed methodology for permeability modelling and hydraulic flow unitization. The proposed $\overline{R_{tot}}$ permeability model and the Timur-Coates methods were implemented. Both models were constrained to RESV for material/energy balance (pressure match) and ORAT for saturation match.

Figure 7.37 presents results from the simulations runs using the normalized pore throat methodology. The black dots and continuous curves represent models responses for observed/historical and proposed method respectively. The results demonstrate the efficacy of the proposed methodology for improved reservoir characterization.

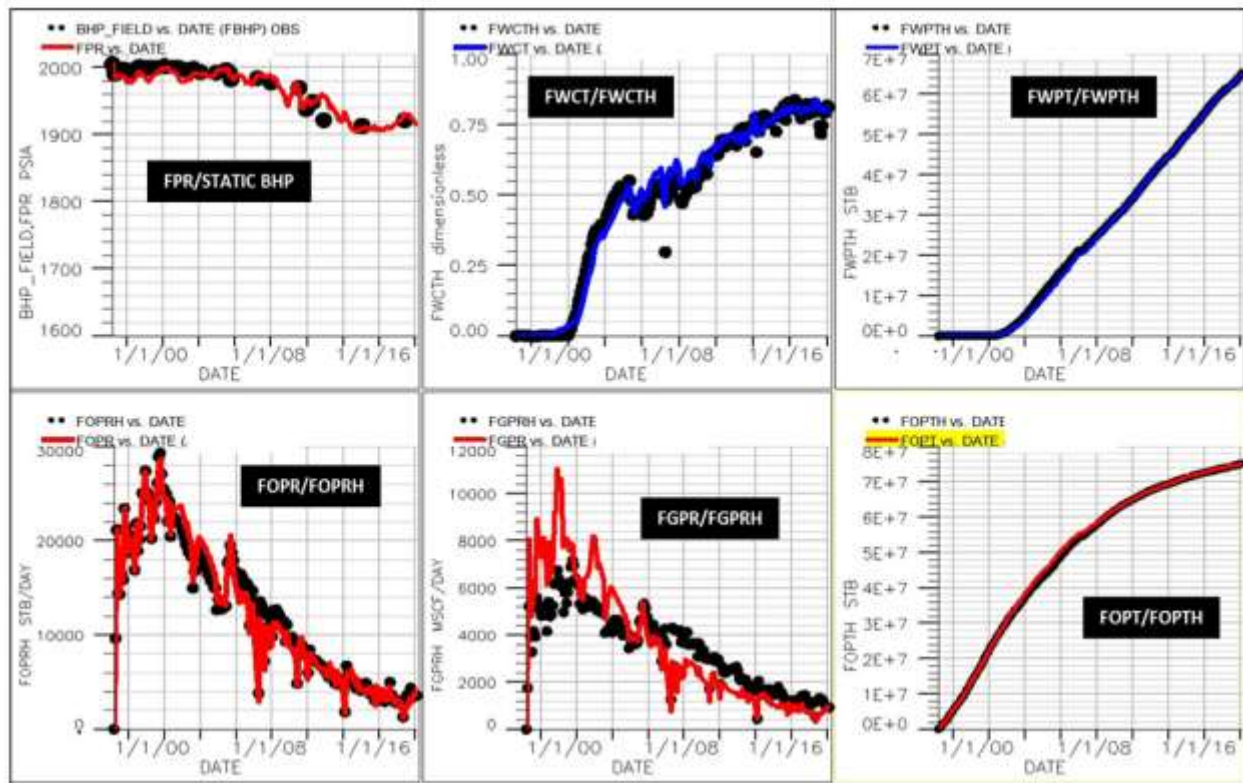


Figure 7. 37: 3D dynamic simulation results for pressures and saturation match.

A comparative assessment of proposed model and Timur-Coates model is presented in figure 7.38. The black dots, blue curves, and red curves are models responses for observed/historical, Timur-Coates and proposed method respectively. The result presents improvement over the Timur-Coates model for efficient and robust reservoir characterization for material/energy balance assessment and saturation match.

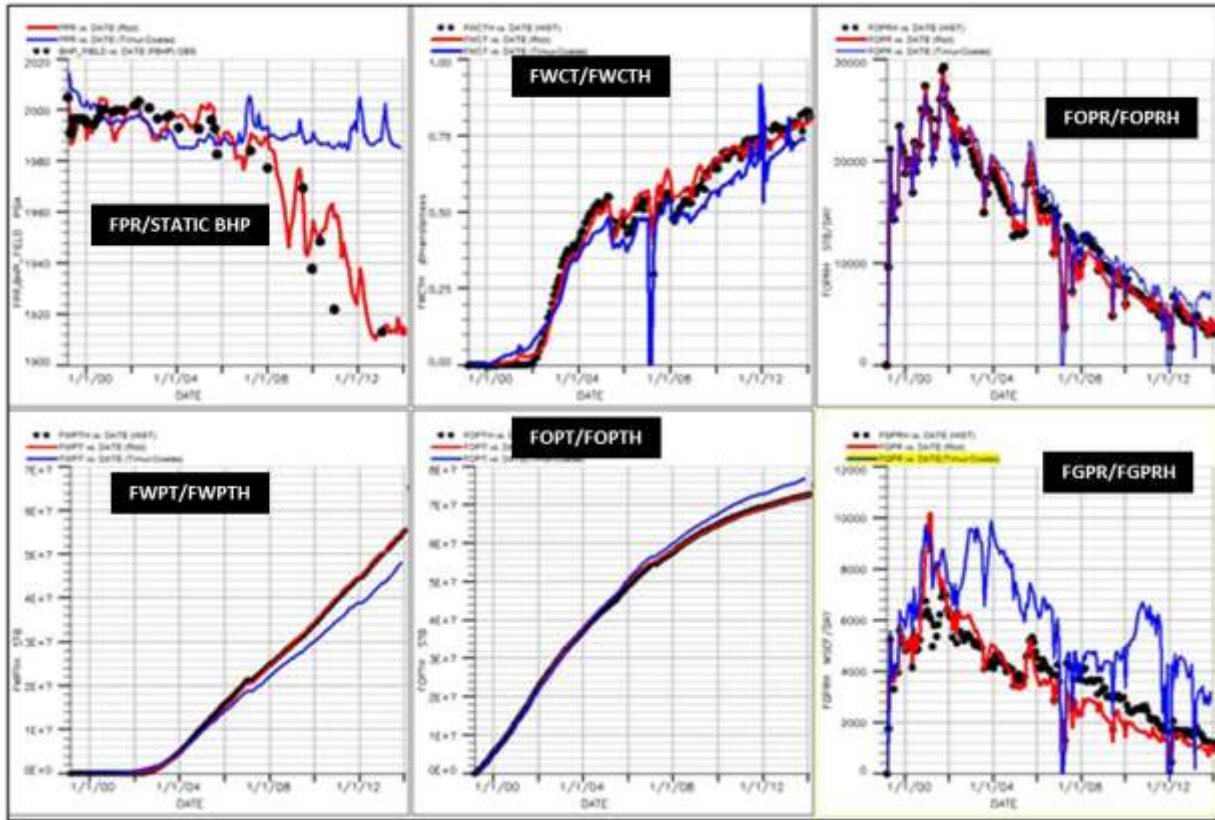


Figure 7. 38: 3D dynamic simulation results for pressures and saturation match. The black dots, blue and red lines represents historical/measured data, Timur Coates and the proposed (\overline{R}_{tot}) results respectively. The proposed model indicate appreciable match than the Timur Coates model.

Plot 1 of figure 7.38 presents the energy/material balance plot. This indicates that the proposed method calibrates effectively to the static bottom hole pressures compared to the Timur-Coates based model. The pessimistic Timur-Coates permeability model shows a highly energized system. In all scenarios for pressure and saturation match, the proposed model outperforms the Timur-Coates model.

Table 7. 11: Simulation Result Comparison for Cumulative Oil and Water Production.

Simulation End:October 2013					
Proposed Normalized Pore Throat Model			Timur - Coates Model		
Parameter	Cum. Volume	Difference	Parameter	Cum. Volume	Difference
FWPTH	53,875,056	62,284	FWPTH	53,115,136	5,006,208
FWPT	53,812,772		FWPT	48,108,928	

Simulation End:October 2013					
Proposed Normalized Pore Throat Model			Timur - Coates Model		
Parameter	Cum. Volume	Difference	Parameter	Cum. Volume	Difference
FOPTH	72,291,280	-62,280	FOPTH	71,877,712	-5,000,000
FOPT	72,353,560		FOPT	76,877,712	

Plots 5 and 6 in figure 7.38 presents the cumulative production rates for both models compared to the measured history data. Discrepancies in cumulative production rates for oil and water was used to evaluate the validity of the history matching process and reliability of results for future reservoir management campaigns. As presented in table 7.12 above, a cumulative difference of approximately 62,000 bbls from the proposed normalized pore throat methodology and 5 MMbbls from the Timur-Coates model presents further validation of the efficacy of the proposed model for reservoir characterization purposes.

CHAPTER 8

Contribution to Knowledge

8.1 Major Contributions

This research work has contributed to the pool of knowledge in the following ways:

1. Development of a novel statistically-derived genetic reservoir units-based normalized pore throat radius ($\overline{R_{tot}}$) methodology for permeability modelling for the clastic system. This captures the complex variation in pore geometry within the different lithofacies association necessary for improved reservoir description and ultimate reserves exploitation. The final form of the proposed model allows us to compute absolute permeability as a function of porosity, the incremental pore volume, and basic pore size characteristics.
2. Saturation height modelling and capillary pressure modelling depicts lambda model as most applicable to the Niger Delta dataset.
3. A new method for relating permeability to pore throat sizes that is more versatile than the existing methods of Swanson and Pittman is also presented, in that it can be employed for all types of pore throat size distribution – unimodal or multimodal.
4. The alternative kappa based approach for NMR T_2 distributions and capillary pressure calibration after Volokitin *et al.*, has been tested in the Niger Delta Deep Water turbidite field and compared to mercury injected capillary pressure (MICP) data from a full-bore core across the reservoir. The research work demonstrates and proved that a single kappa calibration factor of 3 after Volokitin *et al.* and 10 after Olubunmi and Chike is insufficient in modeling challenging clastic system.

A novel hydraulic flow unit based workflow for modelling capillary pressure curves from NMR T_2 transversal relaxation time in the absence of core dataset is been proposed based on genetic unit averages of kappa. This demonstrates that kappa vary as a function of diagenetic imprints within the clastic system.

5. Development of genetic unit averages of pseudo normalized pore throat radius as input parameter to the proposed model for improved petrophysical evaluation.
6. Various methodologies for validating petrophysical models with references to existing NMR based works of Schlumberger-Doll-Research group (SDR) and Coates; and FZI based methodology using dataset from the six (6) depositional belts within the Tertiary Niger Delta.
7. Novel methodology for hydraulic flow unitization using the normalized pore throat radius. This resulted in the modification of existing flow unit definition methodologies: RQI, Leverett J-function and SMLP. Results demonstrate the efficacy of the modified methods using the normalized pore throat approach.

8.2 Published research articles

The following contributions have been made to the field of petroleum reservoir characterization:

1. **O. M. Haruna, D. O. Ogbe, C. Nwosu**; Genetic Units Based Permeability Prediction for Clastic Reservoirs using Normalized Pore Throat Radius (Niger Delta as Case Study). *International Journal of Petroleum Engineering (IJPE)*, Inderscience Publishers. Volume 1, Issue 4, (2015). IJPE-93178 (2015).
2. **O. M. Haruna, A. O. Akeem, D. O. Ogbe**; Genetic Unit Averages of Pseudo-

Normalized Pore Throat Radius for Improved Permeability Predictions (Niger Delta as Case Study). *Journal of Petroleum Exploration & Production Tech. (JPEPT)*, Springer Publishers. Volume 5, Issue 2, pp 147-155, (2015). DOI – 10.1007/s13202-015-0167-9 (2015).

3. **O. M. Haruna**, D. O. Ogbe, C. Nwosu; Reservoir Characterization for Improved Petrophysical Properties Predictability & Validations: Capillary Pressures and Permeability (N. Delta Province as Case Study). *2013 Reservoir Characterization & Simulation Conference (RCSC)*, Abu Dhabi, **SPE 165958**.
4. **O. M. Haruna**, O. Badaru, L. Ramin; Evaluating the Applications of Magnetic Resonance Image Logging Technology in Thin-Bed Reservoir Analysis. *32nd Nigerian Asso. of Petroleum Explorationist (NAPE) Annual Conference and Exhibition*, (2014).

8.3 Publications In-view

The following publications are In-view:

1. **O. M. Haruna**, D. Tiab, D. O. Ogbe; Improved Hydraulic Flow Unitization Using the Normalized Pore Throat Methodology (Niger Delta field as Case Study). *Journal of Petroleum Exploration & Production Tech. (JPEPT)*, Springer Publishers. (2016). *JPEPT-XXXXXX (2016)*.
2. **O. M. Haruna**, A. Igbokoyi, D. O. Ogbe; Genetic Units Averages of Kappa for Capillary Pressure Estimation from NMR transversal T_2 distributions (Niger Delta as Case Study). *International Journal of Petroleum Engineering (IJPE)*, Inderscience Publishers. (2016). *IJPE-XXXXXX (2016)*.

CHAPTER 9

Summary, Conclusions and Recommendations

9.1 Summary and Conclusions

In today's economic climate with an increasing challenge to find new prospects/reserves in the frontier deep water setting which are usually characterized by complex rock fabric; it is more important than ever to emphasize the value petrophysics adds to our business. Accurate reservoir characterization is imperative for mature field re-development through structured workover/intervention operations for efficient field management & production optimization. This study addressed the issues of reservoir characterization and formation evaluation in challenging clastic environment, to develop improved workflows/methodologies at core plug scale for improved petrophysical and formation evaluation using the normalized pore throat radius concept and the Tertiary Niger Delta depositional belts as field case study. In line with the set objectives, the summary of the derivatives of this study is provided as follows:

- i. A quantitative procedure for analyzing multimodal capillary pressures has been developed for the Niger Delta Province. A central part of the results focuses on how to derive parameters that go beyond sample specific features—thereby focusing on genetic reservoir units.
- ii. On the basis of a 2 *micron* pore throat cut-off for modal separation using a dataset of around 300 MICP samples, an attempt has also been made in permeability modelling for the clastic reservoirs based on capillary pressure characterization. The coefficients: “a” and “b” defines the generalized proposed model which describes the linear relationship between permeability and normalized pore throat radius that can be used as a predictor over six (6) orders

of magnitude in permeability for all the genetic reservoir units examined, for all pore throat size distribution.

- iii. The increasing numeric value of the constant “A” which characterizes the normalized pore throat radius as a function of increasing rock properties for the clastic system analyzed, captures the effect of the expansive clay minerals within the various units. The lowest value is associated with the Channel Heterolithic unit – characterized by a dominant micropores with positively skewed pore throat distribution suggesting a high percentage of clay minerals; and the highest value associated with the Fluvial Channel Sand unit as depicted by its unimodal, macropores and negatively skewed distribution; indicative of reduction in smectite/illite group. This present the capability of the proposed model for hydraulic flow units characterization
- iv. Statistical analysis of the coefficient for each genetic reservoir units analyzed has proven that the sample statistic is statistically significant and therefore the test’s null hypothesis is rejected based on an α -value of 0.05.
- v. A constant scaling factor for kappa is insufficient in modelling subsurface capillary pressures from NMR T_2 logs.
- vi. I present improved methodologies for estimating primary drainage capillary pressure curves from NMR T_2 transversal distribution using a genetic unit based kappa scaling factor.
- vii. Kappa scaling factor for capillary pressure and NMR logs calibration vary as a function of pore size/grain sorting, rock types (petro-facies) and influence of thermal gradient on clay diagenesis within the clastic system.
- viii. NMR derived capillary pressure curve does not necessarily match the measured

curve due to the root mean square (RMS) average of saturation differences.

Additional curve fitting procedure is required for accurate capillary pressure modelling. This can be obtained by either using a fitting procedure that gives an average scaling factor for matching with measured data or the proposed modification after Guodong J. *et al.*, (2012).

- ix. I presented genetic unit averages of pseudo normalized pore throat radius as input parameter to the proposed model for improved permeability modelling has been developed for applications in the absence of core and NMR log dataset.
- x. The proposed $\overline{R_{tot}}$ model has been validated using approximately 1,000 corrected routine core analysis and corresponding well logs dataset at same formation depth interval. The lower mean value of 1.34 indicative of the product of the deviation between the proposed permeability model and effective porosities from its average value; validates the effectiveness of the model compared to the FZI based model with a covariance of 10.17.
- xi. Improved hydraulic flow unit characterization over existing methods: RQI, Leverett J-Function, SMLP for delineating the number of hydraulic units required for a robust reservoir modelling.
- xii. The proposed normalized pore throat permeability model demonstrates improved reservoir characterization and reduced errors compared to existing NMR based methods of Coates and SDR, and FZI based methodology after Aneafule *et al.*
- xiii. The proposed model possesses the capability of modelling extreme value of connections. This results in improved prediction of permeability and permeability distributions from wireline logs in partially cored/uncored intervals and adjacent wells for improved completions and enhanced recovery decisions.

9.2 Recommendations

There is scope for further development in the area of parameter estimation from capillary pressures based on NMR T_2 spectrum developed by Volokitin *et al.* (Volokitin, 1999). Progress in this area has been limited due to insufficient data. In practice parameter estimation should be genetic unit based. Upscaled model will require further testing on field data before being recommended for wide application.

Further simulation studies for streamline, water flooding and history matching for future reservoir management decisions is recommended to validate the flow connectivities as highlighted earlier. An efficient permeability model should require little or no permeability or transmissibility multipliers for an acceptable and robust history match. This is aimed at corroborating the influence of flow baffles typical in shaly sandstone system in terms of fluid recovery factors, pressure maintenance, ease to history matching and meaningful production forecast for each of the development scenarios.

Nomenclature

F_s = shape Factor, dimensionless

$F_s \tau^2$ = Kozeny Constant

K = permeability, mD (μm^2)

ϕ_e = effective porosity, dimensionless

ϕ_n = normalized grain volume-to-pore volume ratio

ϕ_z = normalized pore volume-to-grain volume ratio

S_{gv} = surface area per unit grain volume

τ = tortuosity, dimensionless

J = J-Leverett function, dimensionless

$P_{C_{res}}$ = capillary pressure at reservoir conditions, psi

$P_{C_{lab}}$ = capillary pressure at laboratory conditions, psi

P_{C_e} (P_e) = Entry/Displacement capillary pressure (fitting parameter), psi

CPMG – Carr-Purcell-Meiboom-Gill

T_1 – Longitudinal relaxation time

T_2 – Transverse relaxation time

T_{2i} – i th T_2 component

$T_{2_{cutoff}}$ – T_2 component for differentiating bound from movable fluid

$T_{2_{min}}$ – Minimum T_2 component

$T_{2_{max}}$ – Maximum T_2 component

ϕ_T – Total porosity

- κ = Volokitin's proportionality constant for pore body/pore throat relationship
- σ = Interfacial tension between two phases, dynes/cm
- θ = contact angle between two phases, degrees
- S_w = water Saturation, %
- S_{wet} = wetting phase saturation, %
- S_{wirr} = irreducible Water Saturation (fitting parameter), %
- S_w^* = normalized saturation of wetting phase, %
- S_{wi} = incremental pore volume at the i -th capillary pressure step, %
- R_{pi} = incremental pore throat radius at the i -th capillary pressure step, μm
- N, λ = pore size distribution index (fitting parameter)
- r = pore throat radius, μm
- d = grain diameter, μm
- $\overline{R_{Mac}}$ = normalized pore throat radius greater than 2 μm
- $\overline{R_{mic}}$ = normalized pore throat radius less than/equal to 2 μm
- $\overline{R_{tot}}$ = total normalized porosity, μm
- GR = gamma ray, °API
- $RhoB$ = bulk density, g/cc
- NMR = nuclear magnetic resonance, (v/v)
- $MICP$ = mercury injection capillary pressure, psi

CC = closure, insitu-stress and CBW corrected

CPOR = measured core porosity

CKH = measured core permeability

RQI = reservoir quality index, μm

FZI = flow zone indicator, μm

FFI = free fluid index

BWT = total bound water

BVF = bulk volume fluid

CBW = clay bound water

CPM = capillary pressure model

PTR/r = pore throat radius, μm

QC = quality control

CSA = channel storey axis

CSM = channel storey margin

ICTB = inter-channel thin beds

MRTB = mud-rich thin beds

API = American petroleum institute units

BCF = Billion cubic feet

BCM = Billion cubic meters

FMI = Fullbore micro imager

PSM = Pore scale modeling

PVT = Pressure volume temperature

SHF = Saturation height function

XRD = X-ray diffraction

V_{sh} = Volume of shale

P_d = Threshold pressure

a, b, A, B, C = Fitting parameters

e = Exponential

h = Height above the free water level

h_d = Height above the free water level at the entry pressure

J-function = Leverett dimensionless function

lab = Laboratory conditions

Res = Reservoir conditions

m = Cementation exponent from the composite system

n = Saturation exponent

Ref. = Reference

Rp35 or rp35 = Pore throat radius at 35% mercury saturation

R_t = True formation resistivity

S_b = Bulk mercury saturation, ratio of mercury volume and bulk volume

$S_{b\infty}$ = Bulk mercury saturation at infinite pressure assumed equal to porosity

References

- Hani H. Qutob, Abdelaziz Khlaifat, and Mohamed S. Efnik, "When a Good History-Matched Model Results in a Bad Forecast; Question your Petrophysical Data" (September 2013). SPE 166056.
- Nadeau, P.H., Bjorkum, P.A., and Walderhaug, O., (2005) "Petroleum system analysis: impact of shale diagenesis on reservoir fluid pressure, hydrocarbon migration, and biodegradation risk". Northwest Europe and Global Perspectives – Proceedings of the 6th Petroleum Geology Conference, Geological Society, London, 1267–1274.
- Nadeau, P.H., Walderhaug, O., Bjorkum, P.A., and Oelkers, E.H., "Fundamental particle size analysis: Application to hydraulic conductivity models in shales/mudstones". Conference of the European Clay Groups Association: Cracow, Program Abstracts, p. 115, 1999.
- Ejedawe, J.E., Coker, S.J., Lambert-Aikhionbare, D.O., Alofe, K.O., Adoh, F.O., 1984. "Evolution of oil-generative window and oil and gas occurrence in Tertiary Niger Delta basin. AAPG Bulletin 68, 1744–1751.
- Knox, G.J., Omatsola, E.M., 1989. "Development of the Cenozoic Niger Delta in Terms of the "Escalator regression" Model and Impact on Hydrocarbon Distribution". Proceedings KNGMG Symposium, Coastal Lowlands, Geology, and Geotechnology. Dordrecht, Kluwer. 181-202.
- Hulea I.N. and Nicholls C.A. (2012) "Carbonate rock characterization and modelling– Capillary pressure and permeability in multimodal rocks – a look beyond sample specific heterogeneity." AAPG Bulletin, September, v. 96, p. 1627-1642.
- Swanson, B.F. "A Simple Correlation between Permeability and Capillary Pressures." JPT 33 (12): pp. 2498-2504, Dec. 1981.

- Edward D. Pittman. "Relationship of porosity and permeability to various parameters derived from mercury injection-capillary pressure curves for sandstone". AAPG Bulletin, February 1992, v. 76 (2), p. 191-198
- Volokitin, Y, Looyestijn, W. J., Slijkerman, W. F. J., and Hofiiian, J.P., Constructing capillary pressure curves from NMR log data in the presence of hydrocarbons, 39th Annual Logging Symposium Transactions: SPWLA, 1999.
- Purcell, W.R. (1949) "Capillary Pressures-Their measurement using Mercury and the calculation of Permeability therefrom." JPT, TRANS AIME, February vol. 186, (2): Pp. 39-48. SPE-949039-G.
- Thomeer, J.H. (March 1960). Introduction of a pore Geometrical Factor defined by Capillary Pressure Curve. Journal of Petroleum Technology (JPT), TRANS AIME 219, 73-77.
- Thomeer, J.H. (April 1983). "Air Permeability as a Function of Three Pore Network Parameters". JPT 35 (4) 275, 809-818, April. SPE-10922-PA.
- McGeogh, S.L. & Kemper, M., "Saturation Height Mapping in CPS-3 Using SHMAP," Shell Expro 92.003, 1992.
- C.C. Huet, J.A. Rushing, K.E. Newsham, and T.A. Blasingame, SPE. A Modified Purcell/Burdine Model for Estimating Absolute Permeability from Mercury-Injection Capillary Pressure Data. IPTC 10994, November 2005.
- Markwell, P., "A review of existing Sirikit capillary pressure data", Thai Shell note for file EPP/43-040/88.
- Washburn, E.W., (1921). The dynamics of capillary flow. Physical Review 17, 273–283
- Van Brakel, J., Modry, S., Svata, M., (1981). Mercury porosimetry: State of the art. Powder Technology 29, 1–12

Katz, A.J. and Thompson, A.H., (1986). Quantitative Prediction of Permeability in Porous rock, *Physical Review B*, Vol.34, No. 11, pp. 8179-8181.

Katz, A.J. and Thompson, A.H., (1987). Prediction of Rock Electrical Conductivity from Mercury Injection Measurements", *Journal of Geophysical Research*, Vol.92, No.B 1, pp. 599-607.

Brown, Henry W. (1951). Capillary Pressure Investigations. *Trans. AIME* 192, 67-74.

Juhasz, I., "The Central Role of Qv and Formation-Water Salinity in the Evaluation of Shaly Formations." *Proc. SPWLA 20th Annual Log Symposium*, Tulsa, 1979

Hill, H.J., Shirley, O.J., Klein, G.E., (1979) "Bound Water in Shaly Sands-Its relation to Qv and other formation properties", *SPWLA*, Issue 03, vol. 20, May.

Leverett, M. C. (1941) Capillary Behaviour in porous Solids. *Trans. AIME* 142, 152-69

Walter Rose and Bruce, W.A. (1949), Evaluation of Capillary Characters in Petroleum Reservoir Rocks *JPT SPE-949127-G*.

Brooks, R. H., and Corey, A. J. 1964. Hydraulic proprieties of porous media. *Hydrology*. Pap. 3, Colo. State Univ., Fort Collins.

Swanson, B. F., 1981, A simple correlation between permeabilities and mercury capillary pressures: *Journal of Petroleum Technology*, Dec., p. 2488-2504.

Seeburger, D. A., and Nur, A., (1984). A Pore Space Model for Rock Permeability and Bulk Modulus. *Journal of Geophysical Research*, Vol.89, Issue.B 1, pp. 527-536

Amaefule J.O., Njoku RF.A, Egbogah E.O., Keelan D.K., Rasolovoahangy R.K. and Udegbulam E.O. (1997). Mature Niger Delta Reservoirs: Integration of Core and Log Data for flow unit zonation and Permeability Prediction. *SPENC 97*

Timur, A. (1968). An Investigation of Permeability, Porosity, and Residual Water Saturation Relationship for Sandstone Reservoirs, *The Log Analyst*, Vol. 9, No. 4,

- C.I. Uguru, U.O. Onyeagoro, J. Lin, J. Okkerman and I.O. Sikiru, "Permeability Prediction Using Genetic Unit Averages of Flow Zone Indicators (FZIs) and Neural Networks" (August 2005). SPDC. SPE 98828.
- Kleinberg, R.L., (1996), Utility of NMR T_2 distributions, connection with capillary pressure, clay effect, and determination of the surface relaxivity parameter r_2 : Magnetic Resonance Imaging, v. 14, p. 761-767.
- Kenyon, W.E., (1997), Petrophysical principles of applications of NMR logging: The Log Analyst, v. 38, no. 2, p. 21-43.
- Altunbay M., Martain R., Robinson M., (2001). Capillary Pressure Data from NMR Logs and Its Implications on Field Economics: SPEJ.
- Haruna, O. M., Olusegun B., Ramin L. (2014); Reducing the risk in developing thin bedded reservoirs using the magnetic resonance imaging in turbidite formations in the Niger Delta. 32nd Annual Nigerian Association of Petroleum Explorationist (NAPE) Conference.
- Freedman R., and Heaton N., (2004). Fluid Characterization Using Nuclear Magnetic Resonance Logging, Petrophysics 45, No. 3, 241.
- Olubunmi Arogun, SPE and Chike Nwosu, SPE; SNEPCO Nigeria, SPE (2011). Capillary Pressure Curves from Nuclear Magnetic Resonance log Data in a Deepwater Turbidite Nigeria Field – A Comparison to Saturation Models from SCAL Drainage Capillary Pressure Curves
- Dulien, F. A. L., "Porous media: Fluid transport and pore structure". Academic Press, San Diego, CA, 574 pp., 1992
- Cantrell, D.L. and R.M. Hagerty. (2003). Reservoir rock classification, Arab-D reservoir, Ghawar Field, Saudi Arabia. GeoArabia, v. 8, no. 3, p. 435-462.

- Mark Skalinski and Jeroen A. M. Kenter. (2005). Carbonate petrophysical rock typing: integrating geological attributes and petrophysical properties while linking with dynamic behaviour
- Oomkens, E. Lithofacies relations in the Late Quaternary Niger Delta complex. *Sedimentology* 21, 195–222. 1974
- Weber, K.J. (1971). Sedimentologic aspects of oil fields in the Niger Delta. *Geologie en Mijnbouw* 50, 559–576
- Archie, G.E. (1948). Progress Report in Capillary Pressure and Permeability of Drill Cuttings, S.O.C Progress report. Houston.
- Haruna, O. M., Ogbe, D. O., Nwosu, C., (2013). Reservoir Characterization for Improved Petrophysical Properties Predictability & Validations: Capillary Pressures and Permeability (Niger Delta Province as Case Study). SPE 165958
- Haruna, O. M., Ogbe, D. O., Nwosu, C., (2015). Genetic Units Based Permeability Prediction for Clastic Reservoirs using Normalized Pore Throat Radius (Niger Delta as Case Study). *International Journal of Petroleum Engineering (IJPE)*, Inderscience Publishers. Volume 1, Issue 4, (2015). IJPE-93178 (2015).
- Finney, J., (1970). Random packing and the structure of simple liquids (The geometry of random close packing), *Proceedings of the Royal Society*, 319A, 479
- Haruna, O. M., Akeem, A. O., Ogbe, D. O., (2015). Genetic Unit Averages of Pseudo-Normalized Pore Throat Radius for Improved Permeability Predictions (Niger Delta as Case Study). *Journal of Petroleum Exploration & Production Technology. (JPEPT)*, Springer publishers. Volume 5, Issue 2, pp 147-155, (2015).
- Jude O. Amaefule, Mehmet Altunbay, Djebbar Tiab, David G. Kersey and Dare K. Keelan (1997). Enhanced Reservoir Description: Using Core and Log Data to

Identify Hydraulic (Flow) Units and Predict Permeability in Uncored Intervals/Wells.

SPE 26436

G. W. Gunter, J. M. Finneran, D. J. Hartmann and J. D. Miller. Early Determination of Reservoir Flow Units Using an Integrated Petrophysical Method. SPE 38679

S.E.D.M Desouky. A New Method for Normalization of Capillary Pressure Curves. Oil & Gas Science and Technology Journal, Vol. 58 (2003), No. 5, pp. 551-556.

Djebbar Tiab and Erle C. Donaldson. Theory and Practice of Measuring Reservoir Rock and Fluid Transport Properties, Second Edition. Gulf Professional Publishing

Coates, G.; Xiao, L.; Prammer, M. "NMR Logging: Principles and Applications". Halliburton Energy Services. Houston. (1999).

Sørland, G.H.; Djurhuus, K.; Widerøe, H. C.; Lien, J.R.; and Skauge, A. "Absolute Pore Size Distributions from NMR". Journal for the Basic Principles of Diffusion Theory, Experiment and Application; Diffusion Fundamentals 5 (2007) 4.1 - 4.15.

Chen, S., Ostroff, G., and Georgi, D.T. "Improving Estimation of NMR Log T_2 Cutoff Value with Core NMR and Capillary Pressure Measurements". SCA International Symposium, The Hague, SCA-9822, (1998).

Guodong Jin, Artem Manakov, Jinhong Chen, and Jilin Zhang. "Capillary Pressure Prediction from Rock Models Reconstructed Using Well Log Data". SPE Annual Technical Conference & Exhibition, Texas, USA. SPE 159761, (2012).

Appendix A

A1: Sample Dataset for Model Development

Conversion Parameters				
	air/Hg	air/water	air/oil	oil/water
Mercury Contact Angle	140			
Mercury IFT	485			
Laboratory Contact Angle		0	0	30
Laboratory IFT		70	24	35
Reservoir Contact Angle		0		30
Reservoir IFT		50		25
Laboratory TcosTheta		30.3	24	30.3
Reservoir TcosTheta		21.7		21.7

Fluid Densities at 220°F

Water:	0.433
Oil:	0.346
Gas:	0.100

IFT * Cosine Contact Angle:			371.5	
σ	485	dynes/cm	7.03433E-03	lb/in
θ	140	degrees	2.443	radians
Conversion factor		10000		
Sample Type	injection Pressure psia	Mercury Saturation Hg Sat, %	Core Porosity %	Air Permeability mD
SCAL	134.15	26	8.8	15
SCAL	213.61	41.4	8.8	15
SCAL	267.27	51.8	8.8	15
SCAL	314.23	60.9	8.8	15
SCAL	353.96	68.6	8.8	15
SCAL	386.98	75	8.8	15
SCAL	120.74	23.4	9.7	31
SCAL	226.51	43.9	9.7	31
SCAL	300.3	58.2	9.7	31
SCAL	349.31	67.7	9.7	31
SCAL	393.69	76.3	9.7	31
SCAL	423.1	82	9.7	31
SCAL	125.9	24.4	10.6	15
SCAL	216.71	42	10.6	15
SCAL	293.59	56.9	10.6	15
SCAL	344.67	66.8	10.6	15
SCAL	388.01	75.2	10.6	15
SCAL	399.88	77.5	10.6	15
SCAL	134.15	26	10.4	110
SCAL	252.31	48.9	10.4	110

SCAL	326.09	63.2	10.4	110
SCAL	358.08	69.4	10.4	110
SCAL	396.27	76.8	10.4	110
SCAL	414.33	80.3	10.4	110
SCAL	29.93	5.8	9.7	6.4
SCAL	131.06	25.4	9.7	6.4
SCAL	228.58	44.3	9.7	6.4
SCAL	298.23	57.8	9.7	6.4
SCAL	344.67	66.8	9.7	6.4
SCAL	372.53	72.2	9.7	6.4
SCAL	22.19	4.3	7.4	1
SCAL	41.28	8	7.4	1
SCAL	125.38	24.3	7.4	1
SCAL	218.77	42.4	7.4	1
SCAL	297.72	57.7	7.4	1
SCAL	346.73	67.2	7.4	1
SCAL	146.54	28.4	12.8	257.8
SCAL	261.08	50.6	12.8	257.8
SCAL	351.89	68.2	12.8	257.8
SCAL	385.43	74.7	12.8	257.8
SCAL	415.87	80.6	12.8	257.8
SCAL	431.87	83.7	12.8	257.8
SCAL	120.22	23.3	12.4	107.5
SCAL	217.74	42.2	12.4	107.5
SCAL	301.84	58.5	12.4	107.5
SCAL	337.96	65.5	12.4	107.5
SCAL	389.04	75.4	12.4	107.5
SCAL	405.55	78.6	12.4	107.5
SCAL	0	0	11.2	1.1
SCAL	12.38	2.4	11.2	1.1
SCAL	49.02	9.5	11.2	1.1
SCAL	89.26	17.3	11.2	1.1
SCAL	145.5	28.2	11.2	1.1
SCAL	192.46	37.3	11.2	1.1
SCAL	0	0	14.3	2.7
SCAL	23.22	4.5	14.3	2.7
SCAL	74.3	14.4	14.3	2.7
SCAL	133.12	25.8	14.3	2.7
SCAL	187.3	36.3	14.3	2.7
SCAL	223.42	43.3	14.3	2.7
SCAL	8.02	0.1	18	239.29
SCAL	9.04	0.3	18	239.29
SCAL	9.94	0.4	18	239.29
SCAL	11.93	1.2	18	239.29
SCAL	13.84	8.4	18	239.29
SCAL	14.02	9.9	18	239.29
SCAL	15.6	24.2	18	239.29

SCAL	16.01	28.9	18	239.29
SCAL	16.95	38.7	18	239.29
SCAL	17.79	45.9	18	239.29
SCAL	18.02	48.2	18	239.29
SCAL	18.82	53.8	18	239.29
SCAL	18.97	54.9	18	239.29
SCAL	19.85	59.8	18	239.29
SCAL	20.94	63.8	18	239.29
SCAL	22.13	67	18	239.29
SCAL	23.34	69.8	18	239.29
SCAL	24.64	72	18	239.29
SCAL	25.01	72.7	18	239.29
SCAL	29.91	75.6	18	239.29
SCAL	34.56	77.6	18	239.29
SCAL	39.78	79.6	18	239.29
SCAL	40.07	79.6	18	239.29
SCAL	45.4	81	18	239.29
SCAL	50.41	82	18	239.29
SCAL	68.93	84.3	18	239.29
SCAL	90.64	86	18	239.29
SCAL	122.16	87.6	18	239.29
SCAL	184.34	89.2	18	239.29
SCAL	288.87	90.8	18	239.29
SCAL	458.07	92.1	18	239.29
SCAL	792.09	93.6	18	239.29
SCAL	998.05	93.9	18	239.29
SCAL	1907.68	95.1	18	239.29
SCAL	1999.25	95.2	18	239.29
SCAL	2991.63	96	18	239.29
SCAL	3988.58	96.7	18	239.29
SCAL	4987.74	97.2	18	239.29
SCAL	5994.78	97.7	18	239.29
SCAL	6976.07	98.1	18	239.29
SCAL	7994	98.7	18	239.29
SCAL	8996.5	98.9	18	239.29
SCAL	9968.15	99.3	18	239.29
SCAL	19943.07	100	18	239.29
SCAL	29910.3	100	18	239.29
SCAL	39916.08	100	18	239.29
SCAL	49873.67	100	18	239.29
SCAL	54739.68	100	18	239.29
SCAL	24.93	0.5	12	0.87
SCAL	29.99	0.7	12	0.87
SCAL	40.07	0.9	12	0.87
SCAL	49.91	1.4	12	0.87
SCAL	80.69	2.3	12	0.87
SCAL	108.4	3	12	0.87

SCAL	141.74	4.9	12	0.87
SCAL	177.06	10	12	0.87
SCAL	219.96	17.7	12	0.87
SCAL	276.11	25.3	12	0.87
SCAL	345.92	31.2	12	0.87
SCAL	424.06	35.3	12	0.87
SCAL	546.43	39.1	12	0.87
SCAL	747.82	42.3	12	0.87
SCAL	1004.49	44.7	12	0.87
SCAL	1588.09	47.4	12	0.87
SCAL	1993.08	48.8	12	0.87
SCAL	2986.68	51.6	12	0.87
SCAL	3919.95	54.7	12	0.87
SCAL	3992.6	54.9	12	0.87
SCAL	4869	58.4	12	0.87
SCAL	4984.91	58.8	12	0.87
SCAL	5942.5	62.6	12	0.87
SCAL	5998.4	62.8	12	0.87
SCAL	6937.19	66.3	12	0.87
SCAL	6989.24	66.5	12	0.87
SCAL	7962.75	69.8	12	0.87
SCAL	8913.12	72.8	12	0.87
SCAL	8986.37	73	12	0.87
SCAL	9981.11	75.3	12	0.87
SCAL	11862.63	79.5	12	0.87
SCAL	14418.91	83.7	12	0.87
SCAL	17358.86	87.4	12	0.87
SCAL	19853.49	90	12	0.87
SCAL	19974.95	90.2	12	0.87
SCAL	23986.82	93	12	0.87
SCAL	29311.6	95.3	12	0.87
SCAL	29895.74	95.6	12	0.87
SCAL	38208.77	97.7	12	0.87
SCAL	39876.4	98.1	12	0.87
SCAL	49880.94	99.3	12	0.87
SCAL	54931.29	100	12	0.87
SCAL	9.94	0.1	18	198.56
SCAL	11.93	0.8	18	198.56
SCAL	13.84	5.2	18	198.56
SCAL	14.02	6.1	18	198.56
SCAL	15.6	17.2	18	198.56
SCAL	16.01	20.1	18	198.56
SCAL	16.95	26.9	18	198.56
SCAL	17.79	32.2	18	198.56
SCAL	18.02	34.1	18	198.56
SCAL	18.82	39.4	18	198.56
SCAL	18.97	40.7	18	198.56

SCAL	19.85	46.9	18	198.56
SCAL	20.94	53.7	18	198.56
SCAL	22.13	59.9	18	198.56
SCAL	23.34	64.8	18	198.56
SCAL	24.64	69	18	198.56
SCAL	25.01	70.2	18	198.56
SCAL	29.26	71.5	18	198.56
SCAL	33.88	73.4	18	198.56
SCAL	39.07	75.6	18	198.56
SCAL	39.35	75.8	18	198.56
SCAL	44.66	77.5	18	198.56
SCAL	49.65	78.8	18	198.56
SCAL	66.12	81.6	18	198.56
SCAL	89.8	83.8	18	198.56
SCAL	121.29	85.6	18	198.56
SCAL	183.44	87.6	18	198.56
SCAL	287.95	89.5	18	198.56
SCAL	457.11	91.2	18	198.56
SCAL	791.12	92.8	18	198.56
SCAL	997.07	93.3	18	198.56
SCAL	1906.67	94.8	18	198.56
SCAL	1998.24	94.9	18	198.56
SCAL	2990.6	96.1	18	198.56
SCAL	3987.53	96.9	18	198.56
SCAL	4986.68	97.6	18	198.56
SCAL	5993.71	98.3	18	198.56
SCAL	6975	98.7	18	198.56
SCAL	7992.92	99.1	18	198.56
SCAL	8995.42	99.3	18	198.56
SCAL	9967.07	99.6	18	198.56
SCAL	19941.99	100	18	198.56
SCAL	29909.22	100	18	198.56
SCAL	39915	100	18	198.56
SCAL	49872.59	100	18	198.56
SCAL	54738.61	100	18	198.56
SCAL	4.57	0.4	16.4	1184.04
SCAL	5.08	1.2	16.4	1184.04
SCAL	5.58	3.8	16.4	1184.04
SCAL	6.08	10.4	16.4	1184.04
SCAL	6.57	18.2	16.4	1184.04
SCAL	7.07	27.1	16.4	1184.04
SCAL	7.07	27.6	16.4	1184.04
SCAL	7.56	35.1	16.4	1184.04
SCAL	7.55	35.1	16.4	1184.04
SCAL	8.04	41.3	16.4	1184.04
SCAL	8.04	41.4	16.4	1184.04
SCAL	8.52	47	16.4	1184.04

SCAL	9.01	51.6	16.4	1184.04
SCAL	9	51.6	16.4	1184.04
SCAL	9.48	55.1	16.4	1184.04
SCAL	10.06	58.8	16.4	1184.04
SCAL	10.06	58.8	16.4	1184.04
SCAL	10.62	61.6	16.4	1184.04
SCAL	11.19	64.2	16.4	1184.04
SCAL	11.86	66.7	16.4	1184.04
SCAL	12.05	67.4	16.4	1184.04
SCAL	12.83	70	16.4	1184.04
SCAL	13.67	72.9	16.4	1184.04
SCAL	14.02	73.9	16.4	1184.04
SCAL	15.02	76.3	16.4	1184.04
SCAL	15.91	77.9	16.4	1184.04
SCAL	17.23	79.7	16.4	1184.04
SCAL	17.99	80.4	16.4	1184.04
SCAL	19.05	81.3	16.4	1184.04
SCAL	21.55	82.9	16.4	1184.04
SCAL	24.99	84.2	16.4	1184.04
SCAL	30.03	85	16.4	1184.04
SCAL	39.86	85.9	16.4	1184.04
SCAL	49.89	86.7	16.4	1184.04
SCAL	90.93	88.4	16.4	1184.04
SCAL	133.46	89.3	16.4	1184.04
SCAL	185.91	90.1	16.4	1184.04
SCAL	241.98	90.8	16.4	1184.04
SCAL	311.96	91.3	16.4	1184.04
SCAL	391.13	92.2	16.4	1184.04
SCAL	495.67	92.6	16.4	1184.04
SCAL	631.9	93	16.4	1184.04
SCAL	807.16	93.4	16.4	1184.04
SCAL	999.14	94.1	16.4	1184.04
SCAL	1304.21	94.9	16.4	1184.04
SCAL	1697.48	95.4	16.4	1184.04
SCAL	1991.79	96.3	16.4	1184.04
SCAL	2578.49	96.8	16.4	1184.04
SCAL	2988.15	97.6	16.4	1184.04
SCAL	3692.7	97.9	16.4	1184.04
SCAL	3994.52	98.4	16.4	1184.04
SCAL	4853.09	98.6	16.4	1184.04
SCAL	5009.82	98.9	16.4	1184.04
SCAL	5931.83	99.1	16.4	1184.04
SCAL	6008.95	99.3	16.4	1184.04
SCAL	6945.9	99.3	16.4	1184.04
SCAL	6999.88	99.5	16.4	1184.04
SCAL	7961.9	99.6	16.4	1184.04
SCAL	8962.47	99.7	16.4	1184.04

SCAL	9959.19	99.9	16.4	1184.04
SCAL	12264.95	100	16.4	1184.04
SCAL	15139.44	100	16.4	1184.04
SCAL	19542.76	100	16.4	1184.04
SCAL	19957.25	100	16.4	1184.04
SCAL	26303.89	100	16.4	1184.04
SCAL	29889.78	100	16.4	1184.04
SCAL	39872.45	100	16.4	1184.04
SCAL	49780.64	100	16.4	1184.04
SCAL	54848.36	100	16.4	1184.04
SCAL	29.98	6.8	16.3	22.54
SCAL	35.11	18.3	16.3	22.54
SCAL	39.22	25.2	16.3	22.54
SCAL	40.21	26.4	16.3	22.54
SCAL	43.45	30.3	16.3	22.54
SCAL	47.22	33.9	16.3	22.54
SCAL	49.91	36.2	16.3	22.54
SCAL	62.83	43.5	16.3	22.54
SCAL	79.23	48.5	16.3	22.54
SCAL	97.57	51.7	16.3	22.54
SCAL	121.38	54.2	16.3	22.54
SCAL	158.02	57	16.3	22.54
SCAL	200.88	59.4	16.3	22.54
SCAL	246.88	61.5	16.3	22.54
SCAL	299.97	63.6	16.3	22.54
SCAL	360.25	65.6	16.3	22.54
SCAL	436.83	67.7	16.3	22.54
SCAL	528.25	69.7	16.3	22.54
SCAL	632.48	71.8	16.3	22.54
SCAL	752.3	73.6	16.3	22.54
SCAL	884.33	75.6	16.3	22.54
SCAL	996.93	76.8	16.3	22.54
SCAL	1182.3	78.5	16.3	22.54
SCAL	1369.76	80.2	16.3	22.54
SCAL	1587.43	81.5	16.3	22.54
SCAL	1845.42	83	16.3	22.54
SCAL	1993.05	83.8	16.3	22.54
SCAL	2351.61	85.5	16.3	22.54
SCAL	2787.46	86.8	16.3	22.54
SCAL	2993.25	87.3	16.3	22.54
SCAL	3511.35	88.9	16.3	22.54
SCAL	3969.99	90.2	16.3	22.54
SCAL	3998.88	90.2	16.3	22.54
SCAL	4904.22	92	16.3	22.54
SCAL	4999.71	92.3	16.3	22.54
SCAL	5944.59	93.5	16.3	22.54
SCAL	6015.92	93.6	16.3	22.54

SCAL	6970.21	94.8	16.3	22.54
SCAL	8011.26	95.9	16.3	22.54
SCAL	8996.4	96.7	16.3	22.54
SCAL	9989.25	97.4	16.3	22.54
SCAL	15252.38	99.1	16.3	22.54
SCAL	19975.72	99.5	16.3	22.54
SCAL	29885.1	100	16.3	22.54
SCAL	39966.06	100	16.3	22.54
SCAL	49761.71	100	16.3	22.54
SCAL	54741.46	100	16.3	22.54
SCAL	40.87	0.2	15.4	3.43
SCAL	44.17	0.5	15.4	3.43
SCAL	47.99	1	15.4	3.43
SCAL	50.71	1.3	15.4	3.43
SCAL	63.67	6.1	15.4	3.43
SCAL	80.08	10.2	15.4	3.43
SCAL	98.39	15.2	15.4	3.43
SCAL	122.15	20.4	15.4	3.43
SCAL	158.7	27.4	15.4	3.43
SCAL	201.46	33.8	15.4	3.43
SCAL	247.42	39.2	15.4	3.43
SCAL	300.46	44	15.4	3.43
SCAL	360.7	48	15.4	3.43
SCAL	437.26	51.5	15.4	3.43
SCAL	528.65	54.7	15.4	3.43
SCAL	632.86	57.7	15.4	3.43
SCAL	752.66	60.4	15.4	3.43
SCAL	884.67	63.3	15.4	3.43
SCAL	997.25	65.2	15.4	3.43
SCAL	1182.6	68.3	15.4	3.43
SCAL	1370.04	71	15.4	3.43
SCAL	1587.68	73.8	15.4	3.43
SCAL	1845.64	76.7	15.4	3.43
SCAL	1993.26	78.1	15.4	3.43
SCAL	2351.8	81.2	15.4	3.43
SCAL	2787.61	84.1	15.4	3.43
SCAL	2993.39	85	15.4	3.43
SCAL	3511.47	87.4	15.4	3.43
SCAL	3970.11	89	15.4	3.43
SCAL	3998.99	89.2	15.4	3.43
SCAL	4904.31	91.9	15.4	3.43
SCAL	4999.81	92	15.4	3.43
SCAL	5944.68	93.9	15.4	3.43
SCAL	6016.01	93.9	15.4	3.43
SCAL	6970.29	95.2	15.4	3.43
SCAL	8011.33	96.5	15.4	3.43
SCAL	8996.47	97.2	15.4	3.43

SCAL	9989.33	97.9	15.4	3.43
SCAL	15252.46	99.4	15.4	3.43
SCAL	19975.79	100	15.4	3.43
SCAL	29885.17	100	15.4	3.43
SCAL	39966.14	100	15.4	3.43
SCAL	49761.78	100	15.4	3.43
SCAL	54741.54	100	15.4	3.43
SCAL	8.03	0.2	11.5	7.13
SCAL	9.03	0.5	11.5	7.13
SCAL	10.03	0.7	11.5	7.13
SCAL	11.91	1	11.5	7.13
SCAL	14.02	1.4	11.5	7.13
SCAL	16.05	1.9	11.5	7.13
SCAL	17.97	2.2	11.5	7.13
SCAL	18.96	2.4	11.5	7.13
SCAL	24.93	3.1	11.5	7.13
SCAL	29.86	3.1	11.5	7.13
SCAL	39.93	3.9	11.5	7.13
SCAL	49.75	5.1	11.5	7.13
SCAL	80.44	9.6	11.5	7.13
SCAL	108.01	15.9	11.5	7.13
SCAL	141.23	22.7	11.5	7.13
SCAL	176.56	28.2	11.5	7.13
SCAL	219.54	32.8	11.5	7.13
SCAL	275.79	36.6	11.5	7.13
SCAL	345.68	40	11.5	7.13
SCAL	423.85	42.7	11.5	7.13
SCAL	546.26	45.1	11.5	7.13
SCAL	747.67	47.5	11.5	7.13
SCAL	1004.36	49.4	11.5	7.13
SCAL	1587.97	52	11.5	7.13
SCAL	1992.96	53.3	11.5	7.13
SCAL	2986.57	55.4	11.5	7.13
SCAL	3919.89	57.1	11.5	7.13
SCAL	3992.53	57.3	11.5	7.13
SCAL	4868.99	58.6	11.5	7.13
SCAL	4984.92	58.8	11.5	7.13
SCAL	5942.57	60	11.5	7.13
SCAL	5998.48	60	11.5	7.13
SCAL	6937.33	61.2	11.5	7.13
SCAL	6989.38	61.4	11.5	7.13
SCAL	7962.94	62.7	11.5	7.13
SCAL	8913.35	64.3	11.5	7.13
SCAL	8986.81	64.6	11.5	7.13
SCAL	9981.37	66	11.5	7.13
SCAL	11862.91	69.6	11.5	7.13
SCAL	14419.18	74.2	11.5	7.13

SCAL	17359.1	79	11.5	7.13
SCAL	19853.71	82.4	11.5	7.13
SCAL	19975.16	82.7	11.5	7.13
SCAL	23987	87	11.5	7.13
SCAL	29311.74	90.8	11.5	7.13
SCAL	29895.88	91.6	11.5	7.13
SCAL	38208.87	95.4	11.5	7.13
SCAL	39876.48	96.4	11.5	7.13
SCAL	49861	98.6	11.5	7.13
SCAL	54931.33	100	11.5	7.13
SCAL	62.08	0.1	18.3	2.72
SCAL	75.82	1	18.3	2.72
SCAL	94.22	6.5	18.3	2.72
SCAL	110.54	12.2	18.3	2.72
SCAL	137.58	18.4	18.3	2.72
SCAL	169.76	22.7	18.3	2.72
SCAL	216.89	27.4	18.3	2.72
SCAL	271.1	32.2	18.3	2.72
SCAL	337.05	36.5	18.3	2.72
SCAL	403.12	41.2	18.3	2.72
SCAL	479.78	46.5	18.3	2.72
SCAL	566.13	51.7	18.3	2.72
SCAL	667.71	56.3	18.3	2.72
SCAL	775.58	59.9	18.3	2.72
SCAL	900.81	63.4	18.3	2.72
SCAL	993.13	65.7	18.3	2.72
SCAL	1000.84	65.8	18.3	2.72
SCAL	1152.42	68.9	18.3	2.72
SCAL	1326.34	71.7	18.3	2.72
SCAL	1534.33	74.4	18.3	2.72
SCAL	1767.7	76.9	18.3	2.72
SCAL	1985.83	78.8	18.3	2.72
SCAL	2007.03	79	18.3	2.72
SCAL	2361.38	81.4	18.3	2.72
SCAL	2754.13	83.7	18.3	2.72
SCAL	3005.05	84.8	18.3	2.72
SCAL	3529.04	86.9	18.3	2.72
SCAL	3965.24	88.5	18.3	2.72
SCAL	4007.18	88.6	18.3	2.72
SCAL	4760.47	90.5	18.3	2.72
SCAL	5023.59	91.1	18.3	2.72
SCAL	5968.82	92.9	18.3	2.72
SCAL	6001.59	92.9	18.3	2.72
SCAL	6969.36	94.2	18.3	2.72
SCAL	7966.08	95.2	18.3	2.72
SCAL	8987.83	95.9	18.3	2.72
SCAL	10007.67	96.6	18.3	2.72

SCAL	13589.65	98.2	18.3	2.72
SCAL	19915.05	99.4	18.3	2.72
SCAL	29920.82	100	18.3	2.72
SCAL	39820.56	100	18.3	2.72
SCAL	49791.84	100	18.3	2.72
SCAL	54727.05	100	18.3	2.72
SCAL	9.97	0.1	23.3	286.12
SCAL	12.06	0.5	23.3	286.12
SCAL	14	2.3	23.3	286.12
SCAL	16	9.9	23.3	286.12
SCAL	18.02	27.4	23.3	286.12
SCAL	18.93	34.3	23.3	286.12
SCAL	24.99	55.4	23.3	286.12
SCAL	28.37	57.2	23.3	286.12
SCAL	31.49	59.4	23.3	286.12
SCAL	34.93	61.2	23.3	286.12
SCAL	38.44	62.7	23.3	286.12
SCAL	41.97	64	23.3	286.12
SCAL	45.82	65.1	23.3	286.12
SCAL	47.97	65.7	23.3	286.12
SCAL	60.19	68.3	23.3	286.12
SCAL	73.88	70.5	23.3	286.12
SCAL	92.35	72.7	23.3	286.12
SCAL	108.78	74.1	23.3	286.12
SCAL	135.92	75.9	23.3	286.12
SCAL	168.16	77.5	23.3	286.12
SCAL	215.36	79.2	23.3	286.12
SCAL	269.65	80.7	23.3	286.12
SCAL	335.67	82.1	23.3	286.12
SCAL	401.82	83.1	23.3	286.12
SCAL	478.59	84.1	23.3	286.12
SCAL	565.05	85.1	23.3	286.12
SCAL	666.72	85.9	23.3	286.12
SCAL	774.68	86.7	23.3	286.12
SCAL	899.95	87.5	23.3	286.12
SCAL	992.31	87.9	23.3	286.12
SCAL	1000.02	87.9	23.3	286.12
SCAL	1151.66	88.6	23.3	286.12
SCAL	1325.64	89.3	23.3	286.12
SCAL	1533.67	89.9	23.3	286.12
SCAL	1767.08	90.6	23.3	286.12
SCAL	1986.24	91.1	23.3	286.12
SCAL	2006.45	91.2	23.3	286.12
SCAL	2360.84	91.9	23.3	286.12
SCAL	2753.63	92.6	23.3	286.12
SCAL	3004.56	93	23.3	286.12
SCAL	3528.58	93.8	23.3	286.12

SCAL	3964.8	94.3	23.3	286.12
SCAL	4006.75	94.4	23.3	286.12
SCAL	4760.06	95.3	23.3	286.12
SCAL	5023.19	95.6	23.3	286.12
SCAL	5966.43	96.6	23.3	286.12
SCAL	6001.21	96.6	23.3	286.12
SCAL	6968.99	97.1	23.3	286.12
SCAL	7965.7	97.7	23.3	286.12
SCAL	8987.47	98.2	23.3	286.12
SCAL	10007.31	98.6	23.3	286.12
SCAL	13589.32	99.4	23.3	286.12
SCAL	18914.72	100	23.3	286.12
SCAL	29920.5	100	23.3	286.12
SCAL	39820.24	100	23.3	286.12
SCAL	49791.32	100	23.3	286.12
SCAL	54726.74	100	23.3	286.12
SCAL	21.55	0.2	11.1	1.41
SCAL	24.99	0.5	11.1	1.41
SCAL	32.21	0.7	11.1	1.41
SCAL	42.04	1.2	11.1	1.41
SCAL	82.09	1.9	11.1	1.41
SCAL	93.1	4.8	11.1	1.41
SCAL	135.52	10.1	11.1	1.41
SCAL	187.82	17.1	11.1	1.41
SCAL	243.76	23.2	11.1	1.41
SCAL	313.62	28.7	11.1	1.41
SCAL	392.69	33.3	11.1	1.41
SCAL	497.13	37.7	11.1	1.41
SCAL	633.28	41.3	11.1	1.41
SCAL	808.47	44.9	11.1	1.41
SCAL	1000.4	47.6	11.1	1.41
SCAL	1306.4	51	11.1	1.41
SCAL	1698.62	54.1	11.1	1.41
SCAL	1992.9	56	11.1	1.41
SCAL	2579.54	59.4	11.1	1.41
SCAL	2988.16	61.6	11.1	1.41
SCAL	3693.65	65	11.1	1.41
SCAL	3996.44	66.4	11.1	1.41
SCAL	4853.93	70	11.1	1.41
SCAL	5010.66	70.5	11.1	1.41
SCAL	5932.6	73.9	11.1	1.41
SCAL	6009.71	74.2	11.1	1.41
SCAL	6946.6	76.8	11.1	1.41
SCAL	7000.58	77.1	11.1	1.41
SCAL	7962.55	79	11.1	1.41
SCAL	8963.07	81.2	11.1	1.41
SCAL	9959.76	82.9	11.1	1.41

SCAL	12265.42	86.5	11.1	1.41
SCAL	15189.82	90.6	11.1	1.41
SCAL	19543.05	94	11.1	1.41
SCAL	19957.54	94.2	11.1	1.41
SCAL	26304.1	96.6	11.1	1.41
SCAL	29889.95	97.8	11.1	1.41
SCAL	39872.65	99.3	11.1	1.41
SCAL	49760.71	99.3	11.1	1.41
SCAL	54848.41	100	11.1	1.41
SCAL	1.11	2.3	20.7	10949.2
SCAL	1.11	2.3	20.7	10949.2
SCAL	1.56	4.4	20.7	10949.2
SCAL	2.08	6.3	20.7	10949.2
SCAL	2.6	8.6	20.7	10949.2
SCAL	3.04	11	20.7	10949.2
SCAL	3.45	16.1	20.7	10949.2
SCAL	3.8	19.8	20.7	10949.2
SCAL	4.06	30.1	20.7	10949.2
SCAL	4.05	30.1	20.7	10949.2
SCAL	4.45	40.1	20.7	10949.2
SCAL	4.45	40.3	20.7	10949.2
SCAL	4.85	49.4	20.7	10949.2
SCAL	5.06	53.1	20.7	10949.2
SCAL	5.4	58.7	20.7	10949.2
SCAL	5.55	60.6	20.7	10949.2
SCAL	5.9	65	20.7	10949.2
SCAL	6.03	66.3	20.7	10949.2
SCAL	6.47	69.9	20.7	10949.2
SCAL	6.47	70	20.7	10949.2
SCAL	6.97	73.1	20.7	10949.2
SCAL	6.98	73.1	20.7	10949.2
SCAL	7.47	75.4	20.7	10949.2
SCAL	7.47	75.5	20.7	10949.2
SCAL	8.07	77.6	20.7	10949.2
SCAL	8.07	77.6	20.7	10949.2
SCAL	8.77	79.4	20.7	10949.2
SCAL	9.06	80.1	20.7	10949.2
SCAL	9.95	81.5	20.7	10949.2
SCAL	9.95	81.6	20.7	10949.2
SCAL	11.06	82.9	20.7	10949.2
SCAL	11.93	83.7	20.7	10949.2
SCAL	13.6	84.9	20.7	10949.2
SCAL	14.04	85.2	20.7	10949.2
SCAL	16	86.2	20.7	10949.2
SCAL	18.01	86.9	20.7	10949.2
SCAL	18.94	87.2	20.7	10949.2
SCAL	23.44	88.3	20.7	10949.2

SCAL	24.95	88.6	20.7	10949.2
SCAL	29.75	89.4	20.7	10949.2
SCAL	30.02	89.4	20.7	10949.2
SCAL	36.14	90	20.7	10949.2
SCAL	39.91	91	20.7	10949.2
SCAL	49.59	91.8	20.7	10949.2
SCAL	49.75	92.8	20.7	10949.2
SCAL	70.47	93.7	20.7	10949.2
SCAL	98.63	94.6	20.7	10949.2
SCAL	145.34	95.6	20.7	10949.2
SCAL	216.49	96.5	20.7	10949.2
SCAL	307.03	97.2	20.7	10949.2
SCAL	432.95	97.9	20.7	10949.2
SCAL	608.76	98.1	20.7	10949.2
SCAL	880.25	99	20.7	10949.2
SCAL	1004.11	99.2	20.7	10949.2
SCAL	1646.24	99.6	20.7	10949.2
SCAL	2007.55	99.8	20.7	10949.2
SCAL	2988.36	99.9	20.7	10949.2
SCAL	3981.07	99.9	20.7	10949.2
SCAL	5004.24	100	20.7	10949.2
SCAL	5980.13	100	20.7	10949.2
SCAL	6980.7	100	20.7	10949.2
SCAL	7977.42	100	20.7	10949.2
SCAL	8968.36	100	20.7	10949.2
SCAL	9968.94	100	20.7	10949.2
SCAL	19914.96	100	20.7	10949.2
SCAL	29853.27	100	20.7	10949.2
SCAL	39855.21	100	20.7	10949.2
SCAL	49766.52	100	20.7	10949.2
SCAL	54759.78	100	20.7	10949.2